METALLOPHTHALOCYANINES: VERSATILE PROBES FOR MICROBIAL PHOTOINACTIVATION AND FOR POLLUTANT DEGRADATION AS PHOTOCATALYSTS, BOTH MOLECULAR OR SUPPORTED FORM

A thesis submitted in fulfillment of the requirements for the degree of

DOCTOR OF PHILOSOPHY

Of

RHODES UNIVERSITY

By

AZOLE SINDELO

OCTOBER 2023

Acknowledgements

I would like to express my gratitude to my PhD supervisor, to Distinguished Prof T. Nyokong. Thank you, Prof Nyokong, for your support, encouragement, and patience in good and bad times. Thank you for being a great mentor to me over the years. For giving me opportunities to grow as a researcher, learn how to operate various instrumentations, and adapt to different environments, for sending me to the University of Ottawa in Canada for three months, and for public speaking at different conferences. Thank you, Prof, for teaching me never to give up and celebrating the small successes every time. I would like to thank Prof Mack and Dr Britton for their support and assistance throughout my studies. I would like to also thank Ms Gail Cobus for her assistance and great administrative work.

To all the administrative, technical, and supporting staff of the Chemistry department (Rhodes University), thank you. The Department of Science and Technology (DST) and the National Research Foundation (NRF), thank you for your funding. I also extend my gratitude to Marvin Randall and the Electron Microscopy Unit at large.

I am grateful to the entire S22 research group, past, and present, especially, Dr. Donovan Mafukidze, Dr Balaji Babu, and Dr Pinar Sen for being supportive, encouraging, and entertaining. To the lab manager through my studies, thank you for lending a helping hand. To my parents, siblings, extended family, and my awesome friends, thank you so much for everything, your support is invaluable. I love you guys.

"*Victoria Concordia Crescit*"

Abstract

This thesis investigates the synthesie of metallophthalocyanines for potential use as photosensitizers in two applications: photodynamic antimicrobial chemotherapy and the photodegradation of organic pollutants. To achieve this, phthalocyanines with morpholine (substituted at alpha and beta position, to imine), ethyl and propyl pyrrolidine Schiff bases, asymmetrical mercaptobenzothiazole and morpholine substituents were synthesized for the first time. All nitrogen containing phthalocyanines were methylated to form cationic derivatives. Asymmetrical mercaptobenzothiazole were covalently linked to spherical and pyramidal zinc oxide nanoparticles, while the asymmetrical morpholine were conjugated to polyacrylonitrile (PAN) nanofibers, chitosan modified PAN and glass wool, while carboxylic acid containing phthalocyanines were also linked to glass wool. Various characterization techniques, including electronic spectroscopy, mass spectroscopy, nuclear magnetic resonance (NMR), Fourier-transform infrared (FT-IR), elemental analysis, X-ray photoelectron spectroscopy (XPS), transmission electron microscopy (TEM), scanning electron microscope (SEM), and time-resolved fluorescence measurements were employed to characterize all the phthalocyanine composites.

The research aimed to establish general trends in fluorescence quantum yields, triplet and singlet oxygen generation, photodegradation rates, and fluorescence and triplet state lifetimes of the complexes. Notably, the presence of zinc oxide nanoparticles increased the triplet quantum yield of phthalocyanines, however, the singlet oxygen quantum yield decreased.

The study also examined the photodynamic inactivation of various planktonic cells and biofilms using all photosensitizers. The photodynamic antimicrobial chemotherapy

activities were dose-dependent, and all cationic photosensitizers were highly effective in completely inactivating the microbes in both forms, as opposed to non-charged photosensitizers. For the supports, the chitosan modified PAN showed high efficacy due to improved hydrophilicity.

Furthermore, the research was conducted on the photodegradation of 4-chlorophenol, methyl orange and methylene blue using Pc-anchored PAN and glass wool supports. The immobilized photosensitizers demonstrated a strong capacity for generating singlet oxygen in aqueous media, with the cationic Pc-PAN removing methylene blue more efficiently due to its adsorption and photodegradation abilities. All supports were recoverable, showing potential application for future use in the removal of microbes and organic pollutants.

Table of Contents

List of Symbols

Δ_{AT}	=	Changes in the triplet state absorbance
Δ_{AS}	=	Changes in the singlet state absorbance
k_d	=	Decay constant of singlet oxygen
τ_F	=	Fluorescence lifetime
Φ_F	=	Fluorescence quantum yield
$t_{1/2}$	=	Half-life
I_{abs}	=	Light intensity
ε	=	Molar extinction coefficients
α	=	Non-peripheral position
k_{obs}	=	Observed rate constant
β	=	Peripheral position
Φ_{ADMA}	=	Quantum yield of ADMA
k_a	=	Rate constant for the reaction of ADMA with singlet oxygen
n	=	Refractive index
Φ_Δ	=	Singlet oxygen quantum yield
ε_S	=	Singlet state molar extinction coefficients
t	=	Time
τ_T	=	Triplet lifetime
Φ_T	=	Triplet quantum yield
ε_T	=	Triplet state molar extinction coefficients
λ	=	Wavelength

List of Abbreviations

^{1}H NMR	=	Proton nuclear magnetic resonance
ADMA	=	Anthracene-9,10-bis-methylmalonate
APTES	=	3-Aminopropyltriethoxysilane
BET	=	Brunauer-Emmett-Teller
$CDCl_3$	=	Deuterated chloroform
CS	=	Chitosan
DBU	=	1,8-diazabicyclo[5.4.0]undec-7-ene
DCC	=	Dicyclohexylcarbodiimide
DMF	=	Dimethylformamide
DMS	=	Dimethyl sulfate
DMSO	=	Dimethyl sulfoxide
DMSO-d_6	=	Deuterated dimethyl sulfoxide
DPBF	=	Diphenylisobenzofuran
EDX	=	Energy dispersive X-ray spectroscopy
FT-IR	=	Fourier-Transform Infrared
GW	=	Glass wool
HOMO	=	Highest occupied molecular orbital
IC	=	Internal conversion
IRF	=	Instrument response function
ISC	=	Intersystem crossing
LUMO	=	Lowest unoccupied molecular orbital
MALDI	=	Matrix–Assisted Laser Desorption/Ionization
MS	=	Mass Spectrometer

Nd–YAG	=	Neodymium–doped Yttrium Aluminum Garnet
NPs	=	Nanoparticles
PACT	=	Photodynamic antimicrobial chemotherapy
PAN	=	Polyacrylonitrile
PBS	=	Phosphate buffer saline
Pcs	=	Phthalocyanines
PDT	=	Photodynamic therapy
ROS	=	Reactive oxygen species
SEM	=	Scanning electron microscope
Std	=	Standard
TCSPC	=	Time-correlated single photon counting
TEM	=	Transmission electron microscope
THF	=	Tetrahydrofuran
ToF SIMS	=	Time-of-flight-secondary ion mass spectrometry
UV–Vis	=	Ultraviolet–Visible
XPS	=	X–ray Photoelectron Spectroscopy
XRD	=	X–ray Diffraction

Preamble

This thesis presents the syntheses and photophysiocochemical properties of neutral and cationic metallophthalocyanines (MPcs). The effects of substituents and symmetry will be investigated. The asymmetrical photocatalysts will be covalently linked to zinc oxide nanospheres (ZnONSps), and nanopyramids (ZnONPys), polyacrylonitrile (PAN) and glass wool (GW) to enhance photophysical properties and the recoverability of the materials. The PAN polymer was further coupled with chitosan, to increase the hydrophilicity of the polymer. The prepared photocatalysts are applied for the photo-elimination of gram-positive, and gram-negative bacteria as well as fungi in their planktonic and biofilm forms. This study also investigates the removal of 4-chlorophenol (4-CP), methyl orange (MO) and methylene blue (MB) from water through photo-transformation or photodegradation.

Chapter 1

Introduction

1. Introduction

Water pollution can be defined as the contamination of various water resources such as lakes, rivers, and groundwater by liquid and solid wastes. This challenge leads to the inaccessibility of clean and safe water. The major sources of water pollution are caused by domestic sewage, industries, population growth and plastic waste [1-4]. The presence of water pollutants such as insecticides, heavy metals, dyes, and micro-organisms could lead to adverse effects such as toxicity, carcinogenesis, and infections [5-8]. It is reported that unsafe water sickens about 14 000 people daily, and 3.1 % of people have succumbed to poor-quality water worldwide [9,10]. These pollutants may be removed via different remediation techniques such as reverse osmosis, filtration, ion exchange, distillation, electrolysis, biosand, precipitation, adsorption and electrodialysis [11-14]. These conventional treatment techniques may not be suitable for removing or converting all types of pollutants to less toxic compounds [15]. Moreover, the ability to remove multiple contaminants simultaneously is essential to improve removal efficiency, one of the methods to achieve this is through photosensitization. In this work, micro-organisms and organic pollutants are removed via photodynamic antimicrobial chemotherapy (PACT) and photocatalysis using phthalocyanines.

1.1 Phthalocyanines

Phthalocyanines (Pcs) are classified as second-generation photosensitizers (PS) containing a planar conjugated π-electron aromatic system with four isoindole units interconnected by aza nitrogens, **Figure 1.1** [16, 17]. In the past few decades, these heterocyclic compounds have been extensively studied in different fields including semiconducting materials, photocatalysis, liquid crystals, laser printing systems, chemical and electronic sensors, optical disks, dyes, photovoltaic, photoconductivity,

catalysis, solar cells, photodynamic therapy, and photodynamic antimicrobial chemotherapy [18-28]. Pcs are desirable complexes due to their ease of preparation on a large scale, affordability, and chemical and thermal stability. Unsubstituted Pcs are known to have low solubility in common organic solvents. Several modifications can be made in the macrocycle by inserting different metal atoms, these are known as metallophthalocyanines (MPcs) or by incorporating different functional groups on the non-peripheral (α), peripheral (β) positions and by adding axial ligands for some metals. At the same time, metal-free Pc exists with two hydrogen atoms in the centre (H_2Pc), as shown in **Figure 1.1**.

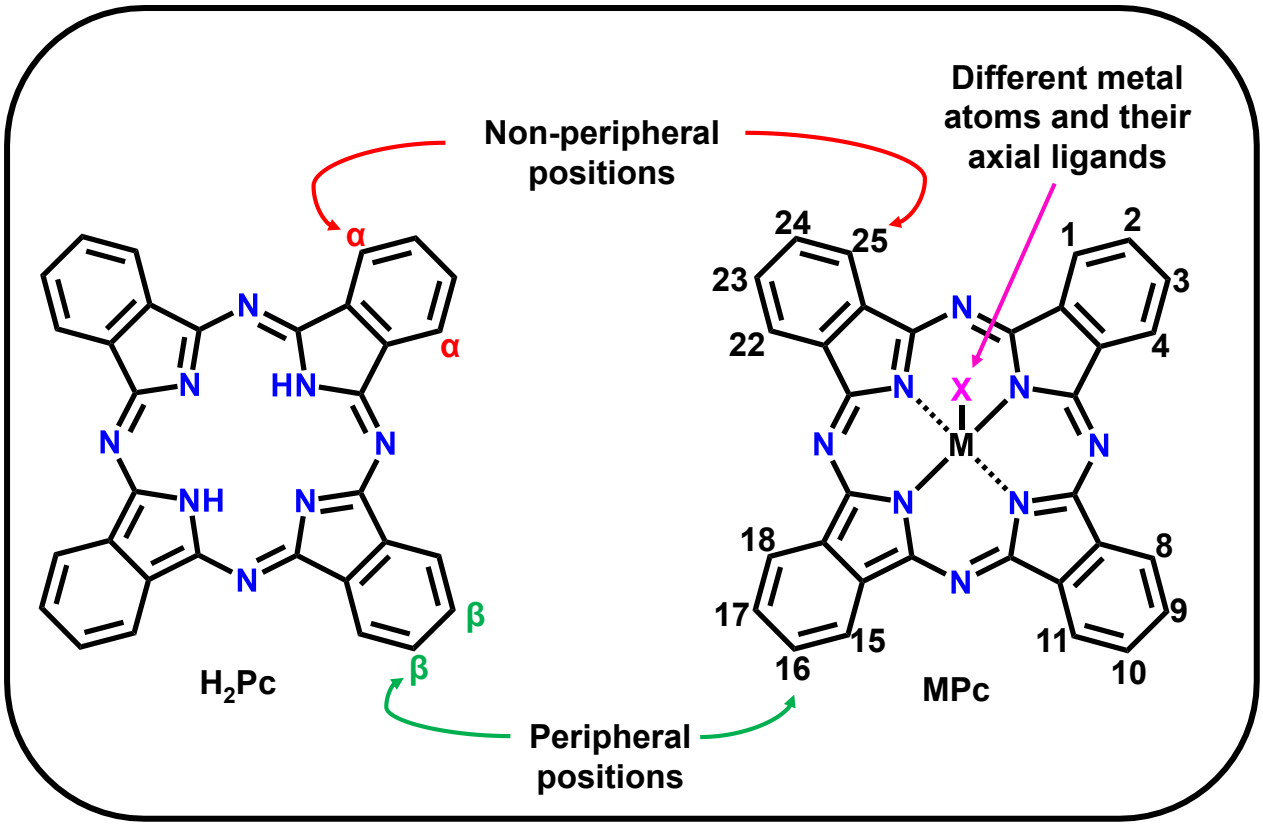

Figure 1.1: General structure of metal-free phthalocyanine (H2Pc) and MPc with possible substitution at non-peripheral (α) and peripheral (β) positions.

1.1.1 Synthesis of symmetrical and asymmetrical Pcs

The synthesis of Pcs is based on the cyclotetramerization of easily accessible precursors such as phthalonitriles, phthalic acids, or phthalic anhydrides in the absence (for H_2Pcs) or presence of metal salts (for MPcs) and a basic catalyst. Non-peripherally (α) and peripherally (β) substituted symmetrical MPcs can be prepared in a single step using a mono-substituted 3-nitrophthalonitrile and/or 4-nitrophthalonitrile as precursors. Tetrasubstituted α- and β-substituted MPcs consist of four constitutional isomers: C_s, C_{2v}, C_{4h}, and D_{2h}, respectively [**29**].

Asymmetrical (low symmetry) Pcs have been reported to improve photophysical properties by introducing the distortion of the phthalocyanine macrocycle leading into changes in the electronic states [**30**, **31**]. Moreover, the asymmetrical Pcs enables specific conjugation or coordination to desired molecules, making such Pcs more favoured than symmetrical Pcs [**31**, **32**]. Asymmetrical Pcs can be synthesized via statistical mixed condensation method, polymeric-support synthetic route and the sub-phthalocyanine approach [**33-35**]. In this work, statistical mixed condensation method was employed due to simplicity. The method involves reacting two differently substituted phthalonitrile producing three identical and unidentical isoindole sub-units (A_3B). The two phthalonitriles may be combined to a molar ratios of 3:1 up to 9:1 (A:B) depending upon the reactivity of the substituents [**36**]. Theoretically, this synthetic route results in six possible products; A_4, A_3B, two A_2B_2, AB_3 and B_4 as shown in **Scheme 1.1**, which can be isolated via column chromatography.

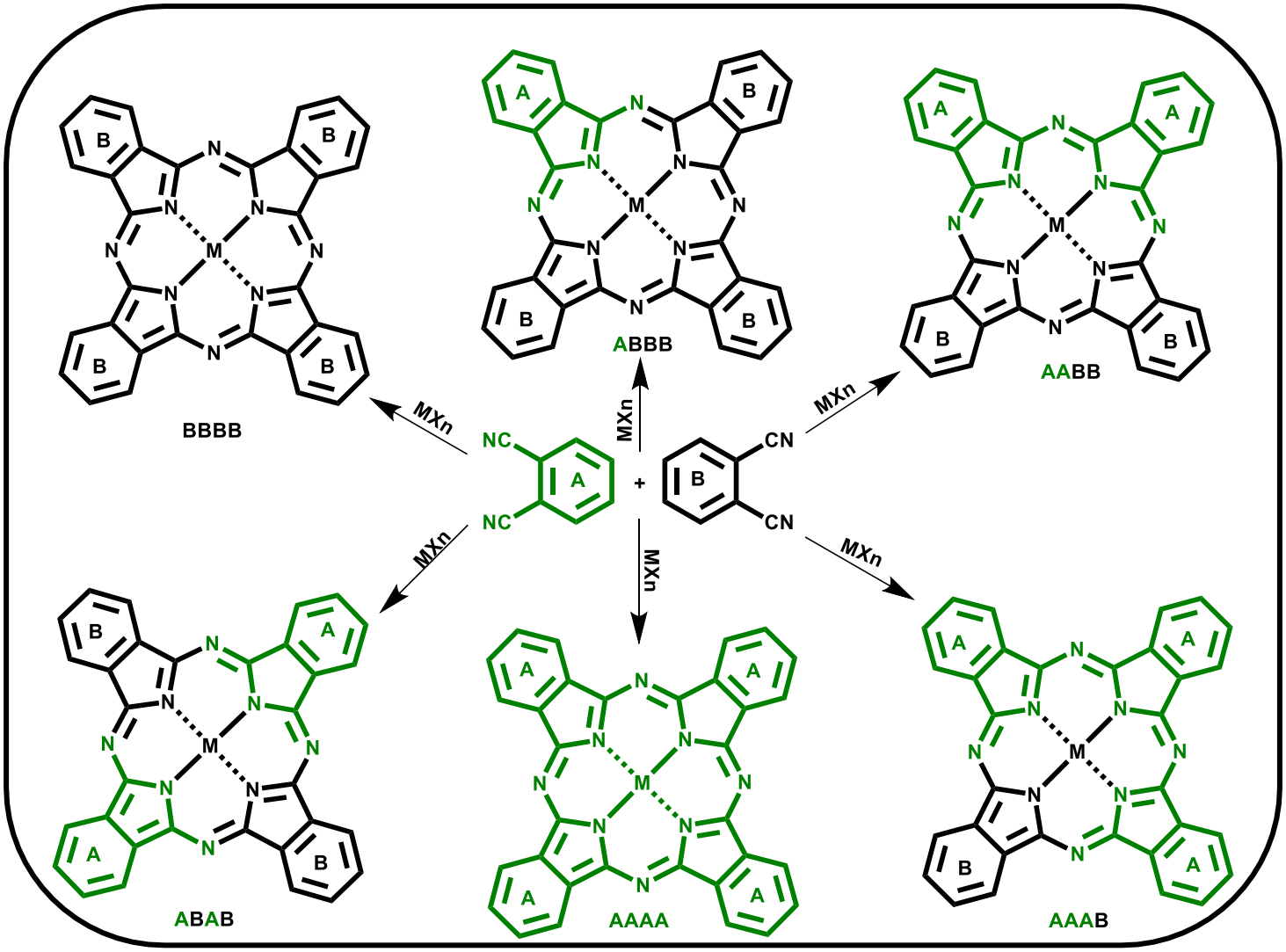

Scheme 1.1: Six possible phthalocyanine from the statistical mixed condensation synthetic route.

1.1.2 Electronic absorption spectra

The ground-state electronic absorption spectra of phthalocyanines consists of two distinct absorption regions; the B-band located in the near ultraviolet (300-400 nm) and the Q-band in the visible region (>650 nm, depending on metal and substituent) **Figure 1.2**. Several factors can influence the changes in the UV/vis absorption spectrum. These include changes in central metal, substituents attached, symmetry,

the position of the substituent (alpha versus beta), solvent, charge and ring expansion [37-42].

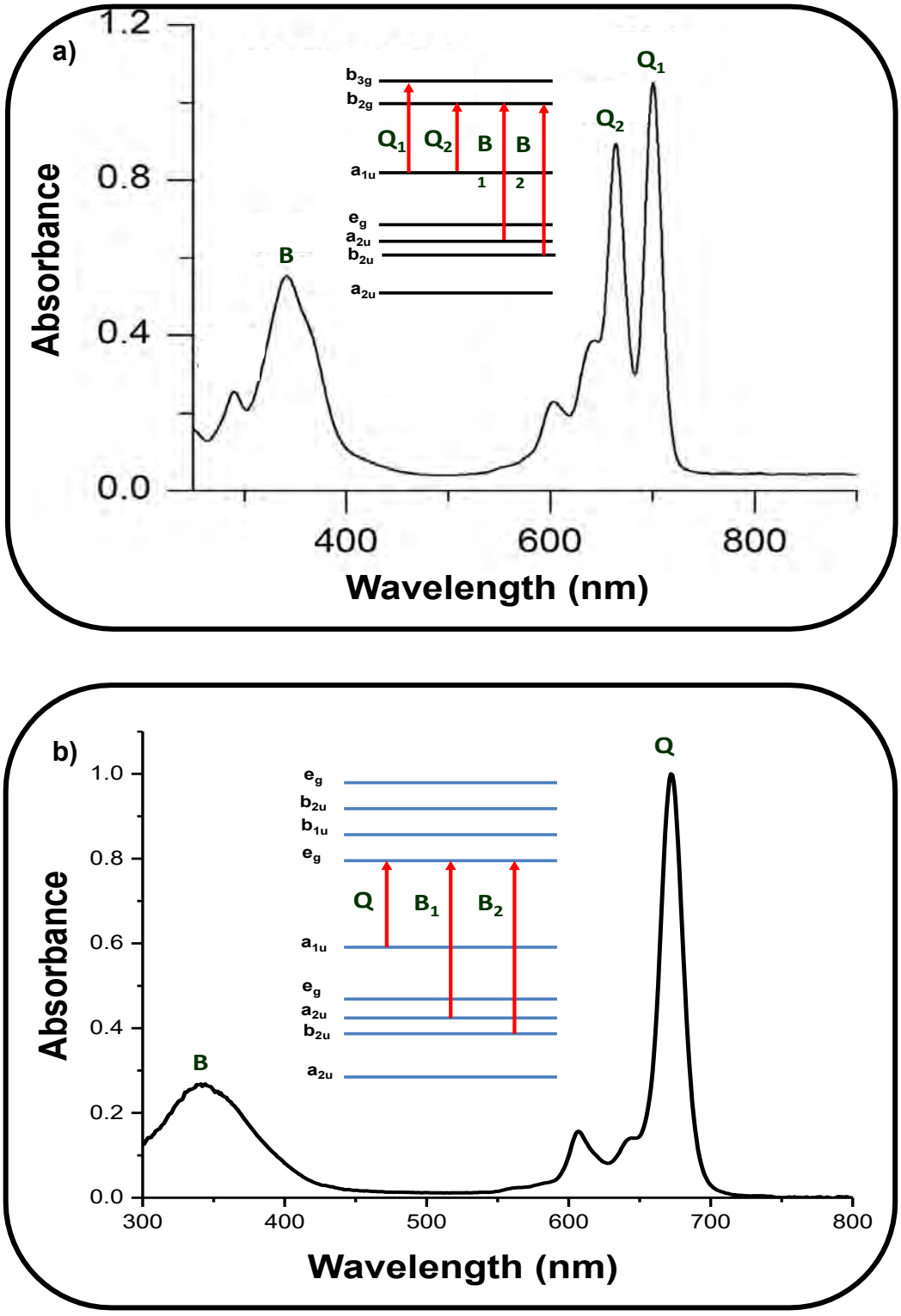

Figure 1.2: Typical electronic absorption spectrum of a) H_2Pc [37] in chloroform and b) MPc in DMSO [41].

The absorption spectrum of Pcs can be explained using Gouterman's four orbital model [43]. The H_2Pcs consist of split Q-bands in the visible range (**Figure 1.2a**), Q_1 and Q_2 arising from the π-π* transition between the a_{1u} of the highest occupied molecular orbital (HOMO) to b_{2g} and b_{3g} of the lowest unoccupied molecular orbital (LUMO) as shown in the insert in **Figure 1.2**. The split Q-band is observed due to the low symmetry (D_{2h}) of H_2Pcs. However, for MPcs, a single intense band (**Figure 1.2b**) is observed as a result of their D_{4h} symmetry which arises from the transition from the a_{1u} of the HOMO to e_g of the LUMO. The B-band emerge from the overlapping of B_1 and B_2 bands originating from π-π* transitions from HOMO a_{2u} and b_{2u} to the LUMO e_g for MPcs (**Figure 1.2**, insert) [44-47].

1.1.3 Phthalocyanine complexes synthesised in this work

The structures and names of Pcs used in this work are given in **Table 1.1**. Herein, the synthesis of symmetrical and asymmetrical zinc or indium metalated Pcs is presented. The metals used in this thesis were selected based on the fact that they are diamagnetic, which promotes intersystem crossing from the excited singlet state to the triplet state [48-50]. This process is essential in producing cytotoxic singlet oxygen and other reactive oxygen species [50]. Complexes **1-7** are novel compounds reported for the first time in this study while complexes **8-10** have been reported before [51, 52].

Table 1.1: Phthalocyanines reported in this thesis.

	Complex name and number	R	Application/ supporting material(s)
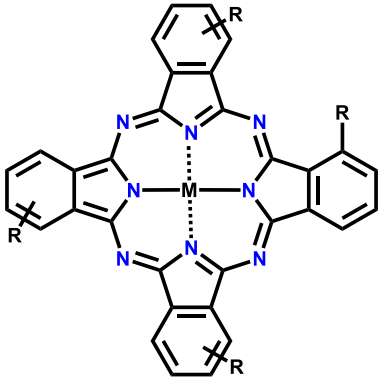	**1-H_2** – 1(4),8(11),15(18),22(25)-Tetrakis-(morpholino) phthalocyanine (**new**) **1-Zn** – 1(4),8(11),15(18),22(25)-Tetrakis-(morpholino) phthalocyaninato zinc(II) (**new**) **1-In** – 1(4),8(11),15(18),22(25)-Tetrakis-(morpholino) phthalocyaninato indium(III) chloride (**new**)	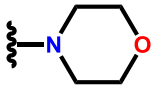	**PACT – Planktonic/** None
	1-ZnQ–1(4),8(11),15(18),22(25)-Tetrakis-(N-methylmorpholino) phthalocyaninato zinc(II) (**new**) **1-InQ**–1(4),8(11),15(18),22(25)-Tetrakis-(N-methylmorpholino) phthalocyaninato indium(III) chloride (**new**)	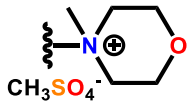	

Table 1.1 continued:

	Complex name and number	R	Application/ supporting material(s)
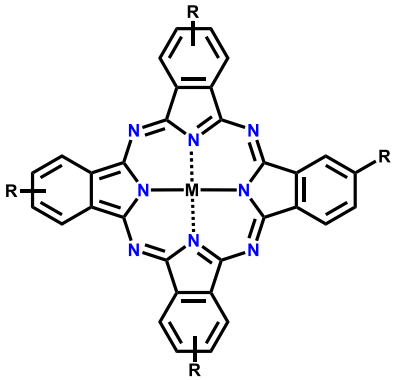	**2-H₂** – 2(3),9(10),16(17),23(24)-Tetrakis-(morpholino) phthalocyanine (**new**) **2-Zn** – 2(3),9(10),16(17),23(24)-Tetrakis-(morpholino) phthalocyaninato zinc(II) (**new**) **2-In** – 2(3),9(10),16(17),23(24)-Tetrakis-(morpholino) phthalocyaninato indium(III) chloride (**new**)	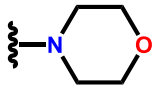	**PACT – Planktonic/** None
	2-ZnQ – 2(3),9(10),16(17),23(24)-Tetrakis-(N-methylmorpholino) phthalocyaninato zinc(II) (**new**) **2-InQ** – 2(3),9(10),16(17),23(24)-Tetrakis-(N-methylmorpholino) phthalocyaninato indium(III) chloride (**new**)	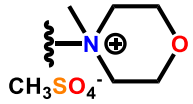	

Table 1.1 continued:

	Complex name and number	R	Application/ supporting material(s)
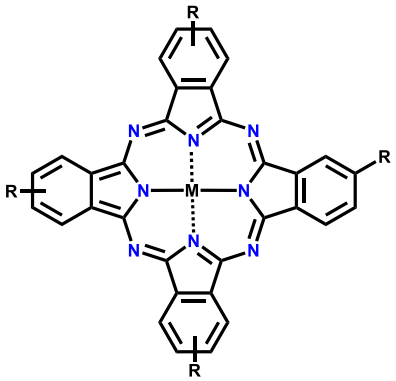	**3-Zn** –2(3),9(10),16(17),23(24)-Tetrakis-(4-phenoxy(((2-(morpholino)ethyl)imino) methyl))phthalocyaninato zinc(II) (**new**) **3-In** – 2(3),9(10),16(17),23(24)-Tetrakis-(4-phenoxy(((2-(morpholino)ethyl)imino) methyl)) phthalocyaninato indium(III) chloride (**new**)	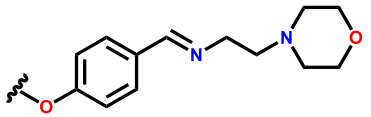	**PACT – Planktonic/** None
	3-ZnQ – 2(3),9(10),16(17),23(24)-Tetrakis-(4-phenoxy(((2-(N-methylmorpholino)ethyl)imino) methyl))phthalocyaninato zinc(II) (**new**) **3-InQ** – 2(3),9(10),16(17),23(24)-Tetrakis-(4-phenoxy(((2-(N-methylmorpholino)ethyl)imino) methyl))phthalocyaninato indium(III) chloride (**new**)	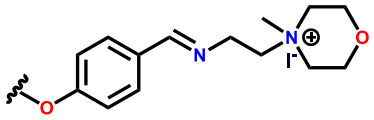	

Table 1.1 continued:

	Complex name and number	R	Application/ supporting material(s)
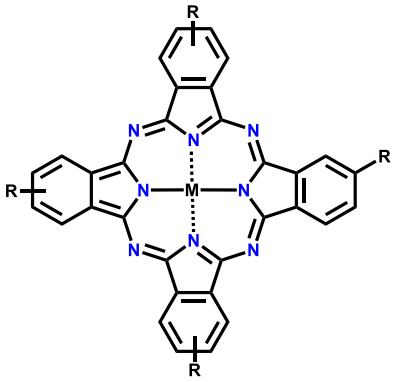	**4-Zn** – 2(3),9(10),16(17),23(24)-Tetrakis-(4-phenoxy(((2-(pyrrolidin-1-yl)ethyl)imino) methyl))phthalocyaninato zinc(II) (**new**) **4-In** – 2(3),9(10),16(17),23(24)-Tetrakis-(4-phenoxy(((2-(pyrrolidin-1-yl)ethyl)imino) methyl))phthalocyaninato indium(III) chloride (**new**)	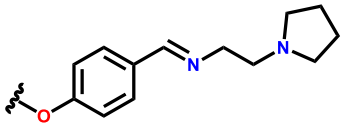	**PACT – Planktonic/** None
	4-ZnQ – 2(3),9(10),16(17),23(24)-Tetrakis-(4-phenoxy(((2-(N-methylpyrrolin-1-yl)ethyl)imino) methyl))phthalocyaninato zinc(II) (**new**) **4-InQ** – 2(3),9(10),16(17),23(24)-Tetrakis-(4-phenoxy(((2-(N-methypyrrolin-1-yl)ethyl)imino) methyl))phthalocyaninato indium(III) chloride (**new**)	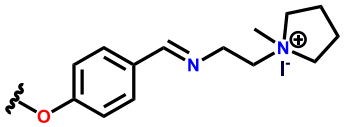	

Table 1.1 continued:

	Complex name and number	R	Application/ supporting material(s)
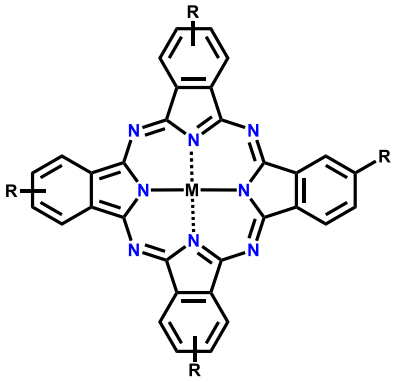	**5-Zn** – 2(3),9(10),16(17),23(24)-Tetrakis-(4-phenoxy(((3-(pyrrolidin-1-yl)propyl)imino) methyl)) phthalocyaninato zinc(II) (**new**) **5-In** – 2(3),9(10),16(17),23(24)-Tetrakis-(4-phenoxy(((3-(pyrrolidin-1-yl)propyl)imino) methyl)) phthalocyaninato indium(III) chloride (**new**)	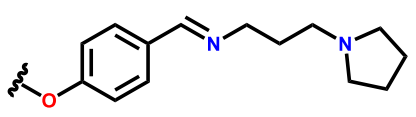	**PACT – Planktonic/** None
	5-ZnQ – 2(3),9(10),16(17),23(24)-Tetrakis-(4-phenoxy(((3-(N-methylpyrrolin-1-yl)propyl)imino) methyl))phthalocyaninato zinc(II) (**new**) **5-InQ** – 2(3),9(10),16(17),23(24)-Tetrakis-(4-phenoxy(((3-(N-methypyrrolin-1-yl)propyl)imino) methyl))phthalocyaninato indium(III) chloride (**new**)	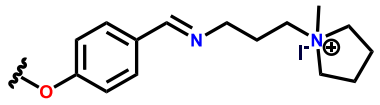	

Table 1.1 continued:

	Complex name and number	R_1	R_2	Application/ supporting material(s)
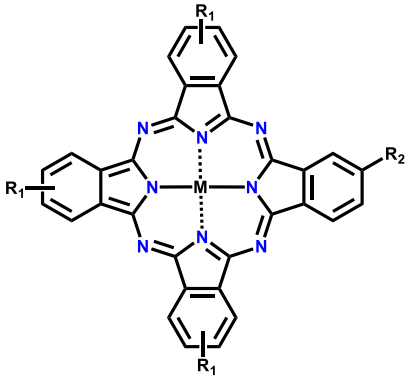	**6-Zn** – 2-(4-carboxyphenoxy)-9(10),16(17),23(24)-tris(benzo[*d*]thiazol-2-ylthio) phthalocyaninato zinc(II) (**new**) **6-In** – 2-(4-carboxyphenoxy)-9(10),16(17),23(24)-tris(benzo[*d*]thiazol-2-ylthio) phthalocyaninato indium(III) chloride (**new**)	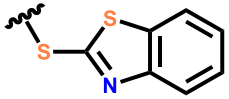	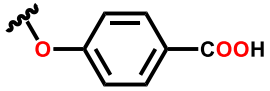	**PACT – Planktonic and biofilm/** (**6-Zn**–ZnONSps, **6-Zn**–ZnONPys, **6-In**–ZnONSps, **6-In**–ZnONPys)
	6-ZnQ – 2-(4-carboxyphenoxy)-9(10),16(17),23(24)-tris(benzo[*d*]thiazol-2-ylthio)phthalocyaninato zinc(II) (**new**) **6-InQ** – 2-(4-carboxyphenoxy)-9(10),16(17),23(24)-tris(benzo[*d*]thiazol-2-ylthio)phthalocyaninato indium(III) chloride (**new**)	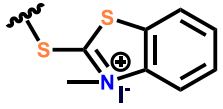	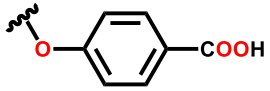	**PACT – Planktonic and biofilm/** (**6-ZnQ**–ZnONSps, **6-ZnQ**–ZnONPys, **6-InQ**–ZnONSps, **6-InQ**–ZnONPys)

Table 1.1 continued:

	Complex name and number	R_1	R_2	Application/ supporting material(s)
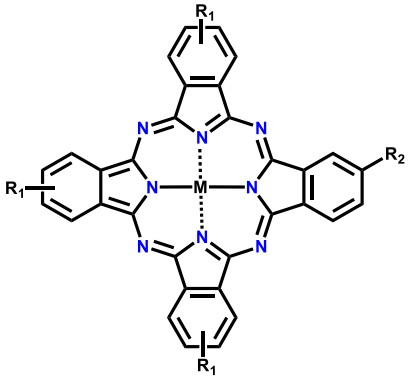	**7-Zn** – 2-(4-carboxyphenoxy)-9(10),16(17),23(24)-tris(morpholino)phthalocyaninato zinc(II) (**new**) **7-In** – 2-(4-carboxyphenoxy)-9(10),16(17),23(24)-tris(morpholino)phthalocyaninato indium(III) chloride (**new**)	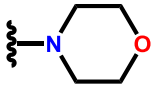	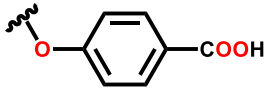	**PACT – Planktonic and Photodegradation – 4-CP, MO and MB**/(**7-Zn** -PAN, **7-In** -PAN, **7-Zn** -PAN-CS, **7-In** -PAN-CS **7-Zn** -GW, and **7-In** -GW)
	7-ZnQ – 2-(4-carboxyphenoxy)-9(10),16(17),23(24)-tris(N-methylmorpholino)phthalocyaninato zinc(II) methyl sulfate (**new**) **7-InQ** – 2-(4-carboxyphenoxy)-9(10),16(17),23(24)-tris(N-methylmorpholino)phthalocyaninato indium(III) chloride methyl sulfate (**new**)	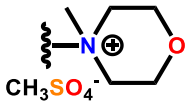	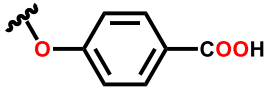	**PACT – Planktonic and Photodegradation – 4-CP, MO and MB**/(**7-ZnQ** -PAN, **7-InQ** -PAN, **7-ZnQ** -PAN-CS, **7-InQ** -PAN-CS **7-ZnQ** -GW, and **7-InQ** -GW)

Table 1.1 continued:

	Complex name and number	R_1	R_2	Application/ supporting material(s)
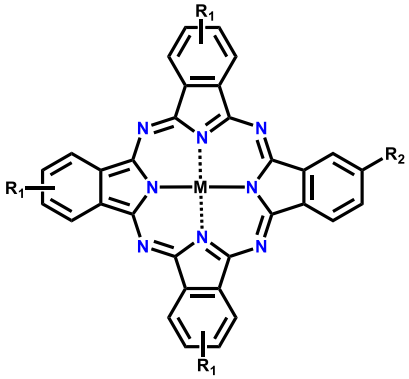	**8-Zn** – 2(3)-mono-(4-carboxyphenoxy) phthalocyaninato zinc(II) [**51**]	**H**	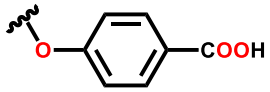	**PACT – Planktonic and photo-degradation** – **MO**/**8-Zn**-GW, **9-Zn**-GW, **10-Zn**-GW
	9-Zn – 2(3),9(10),16(17),23(24)-Tetrakis-(4-carboxyphenoxy) phthalocyaninato zinc(II) [**51**]	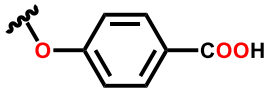	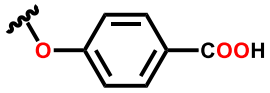	
	10-Zn – 2(3),9(10),16(17),23(24)–Tetrakis-((5-phenoxy)-isophthalic acid) phthalocyaninato zinc(II) [**52**]	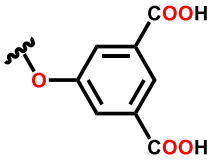	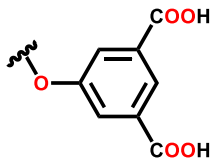	

Q – quaternized, PACT – photodynamic antimicrobial chemotherapy, NSp – nanosphere, NPy – nanopyramid, GW – glass wool, MO – methyl orange, PAN - polyacrylonitrile, CS – chitosan, 4-CP – 4-chlorophenol, MB – methylene blue.

Phthalocyanines containing morpholine (complexes **1**-**3** and **7**), pyrrolidine (complexes **4**, **5**), and mercaptobenzothiazole (complex **6**) substituents were employed due to their antibacterial and antifungal properties of these substituents [53-58]. These complexes also contain nitrogen atoms which enable quaternization to form cationic Pcs. Complexes **1**,**2** were substituted in either the peripheral or non-peripheral position. Their properties and antimicrobial activities are compared in this thesis. The pyrrolidine and morpholine moiety were attached to imine groups to form Schiff base Pcs (complexes **3**, **4**, and **5**), in order to enhance the antimicrobial activities and improve the photophysical properties of the Pc complexes [59, 60]. Furthermore, carboxylic acid-containing complexes (complexes **6**-**10**) were used for specific conjugation to supports such as zinc oxide nanoparticles, polymers, and glass wool.

1.2 Photodynamic antimicrobial chemotherapy (PACT)

Photodynamic antimicrobial chemotherapy (PACT) is an antimicrobial treatment modality based on using light of a specific wavelength in combination with a photosensitizer, leading to a phototoxic reaction that induces micro-organism destruction, known as the photodynamic effect [28]. PACT is expected to eradicate micro-organisms through the photosensitized production of toxic reactive oxygen species (ROS) including singlet oxygen in the presence of molecular oxygen [61], as shown in **Figure 1.3**. This method is adapted from photodynamic therapy (PDT), a form of cancer therapy, but recently has been proposed as an antimicrobial therapy. This approach is preferred for selectively terminating micro-organisms over mammalian cells [62], protein-inactivation [63], and irreversible cell membrane damage preventing resistance against PACT [64, 65].

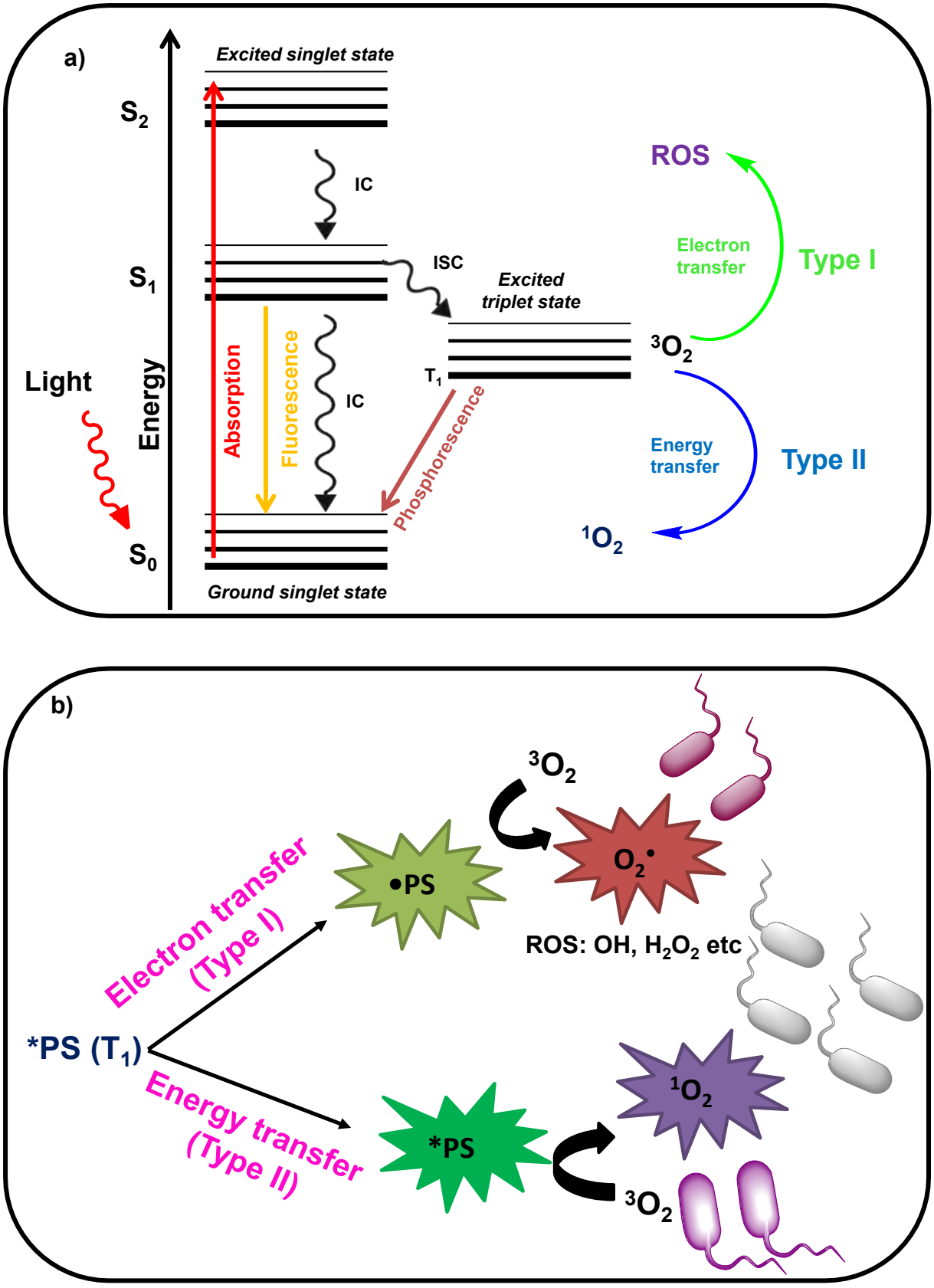

Figure 1.3: a) The Jablonski diagram illustrating the photochemical process of photosensitizers (PS) upon activation and b) typical ROS generation in PACT.

In PACT, the molecules absorb light to the first excited state (S_1) and can further undergo a spin conversion through intersystem crossing (ISC) from S_1 to long-lived triplet state (T_1) where they either emit photons through phosphorescence or can undertake other chemical reactions known as either type I or type II pathways. In type I, ROS such hydroxyl radical ($^{\bullet}OH$), hydrogen peroxide (H_2O_2), and superoxide anion ($O_2^{-\bullet}$) radicals are generated through electron transfer from the PS in the triplet state to $^3O_2$. In the type II reaction, the activated PS transfers energy to the $^3O_2$ forming $^1O_2$. Both pathways can occur simultaneously and are responsible for the inactivation of multiple pathogens, with the most dominant pathway being largely dependent on the photosensitizer (PS) used [**66**, **67**].

An ideal photosensitizer (PS) should exhibit high photochemical reactivity, which is essential in producing ROS. The PS should have a high absorption coefficient, be photostable, have thermal- and chemical-stability. The PS should be able to produce high triplet quantum yields and long triplet lifetime to allow for efficient energy transfer to ground-state oxygen [**66**, **68**]. Various photosensitizers have been used to generate $^1O_2$, some shown in **Figure 1.4**. These PSs can be classified into two categories, porphyrinoids and nonporphyriniods. Porphyrinoids are aromatic tetrapyrrole macrocycles derived from natural pigments such as chlorophyll. They can be subdivided into first, second and third generations based on the evolution of the photosensitizer. Porphyrinoids include porphyrin, chlorin, phthalocyanine, bacteriochlorin, porphycene, texaphyrins, and sapphyrins [**69**, **70**]. The nonporphyriniods refer to aromatic dyes that can generate singlet oxygen, including methylene blue, rose bengal, 4,4-difluoro-4-bora-3a,4a-diaza-s-indacene (BODIPY), eosin blue and erythrosine B [**70**, **71**].

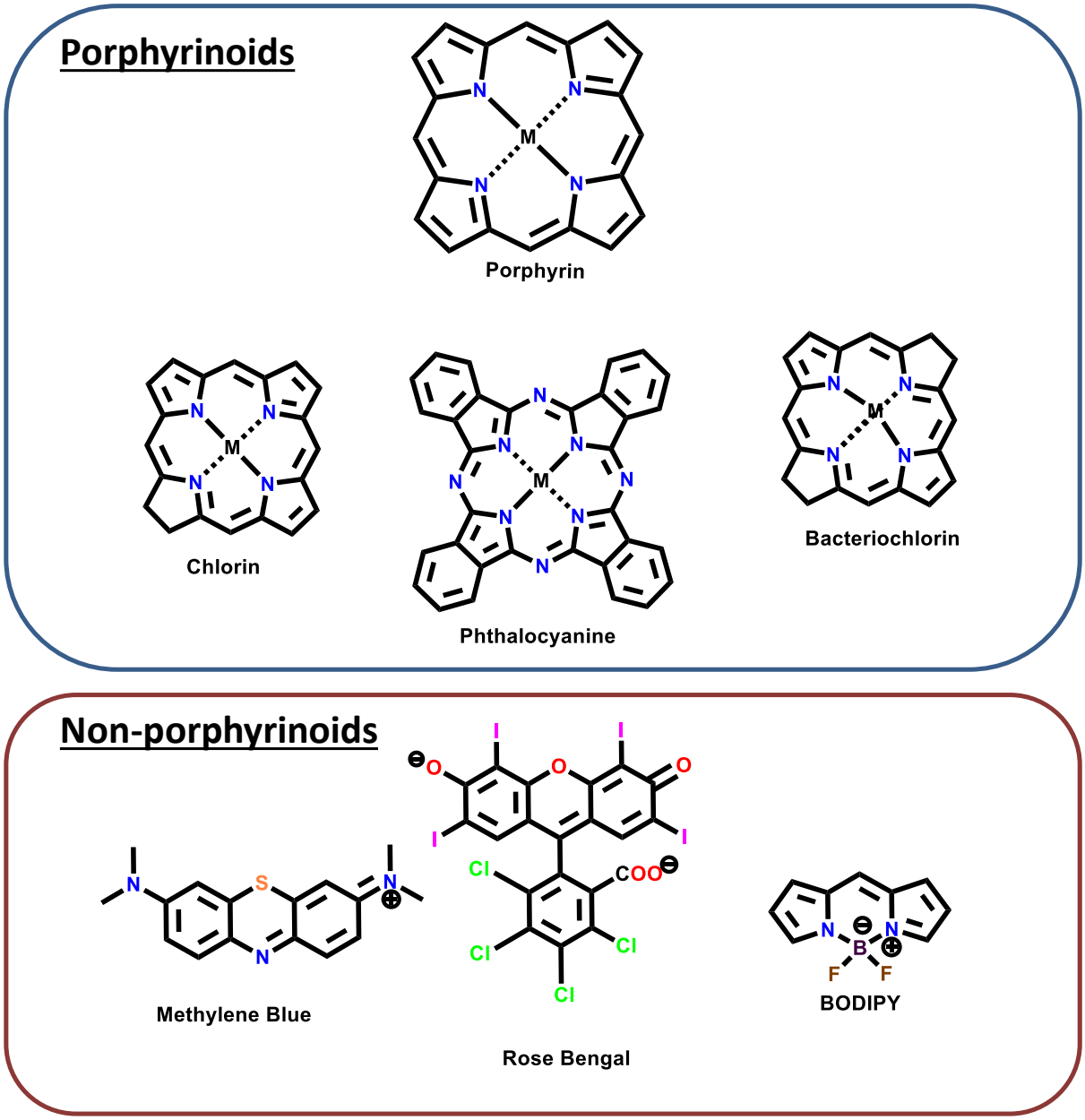

Figure 1.4: Chemical structures of common photosensitizers.

Preventing resistance is very crucial in microbial treatment. Over the years, micro-organisms have developed resistance to traditional antibiotics due to misuse and overuse. The World Health Organization (WHO) has listed the following as high-priority pathogens in urgent need of drug development [72]: Methicillin-resistant *Staphylococcus aureus* (MRSA), a *Staphylococcus aureus* (*S. aureus*) strain that possesses the methicillin resistance gene *mecA* which has a low affinity for β-lactams [73, 74] and vancomycin-resistant *Enterococcus faecium* (VREF) with VanA and VanB glycopeptide resistance operons present [75] amongst other prevalent micro-organisms.

In this thesis, the PACT activity of all phthalocyanine complexes (in the presence and absence of supporting materials) was assessed using gram-positive bacteria: *S. aureus*, MRSA, and VREF, gram-negative bacteria: *Escherichia coli* (*E. coli*), *Klebsiella pneumoniae* (*K. pneumoniae*), and *Salmonella enterica* subspecies *enterica serovar Choleraesuis* (*S. choleraesuis*) and fungi: *Candida albicans* (*C. albicans*) in their planktonic forms. These micro-organisms were chosen based on their physiological and morphological differences. Gram-positive bacteria consist of a moderately permeable outer membrane with a thick peptidoglycan covering the plasma membrane. Both the gram-negative bacteria and fungi have much more complex cell wall structures with more permeability barriers, such as two membranes for gram-negative bacteria and beta-glucans and chitin protecting the cell membrane for fungi. The structures of the cell wall of gram-positive bacteria, gram-negative bacteria and fungi are shown in **Figure 1.5**, adapted from [76, 77]. The ability to permeate the cell wall is one of the most critical requirements of a PS, and this is to allow the production of $^1O_2$ inside the cell.

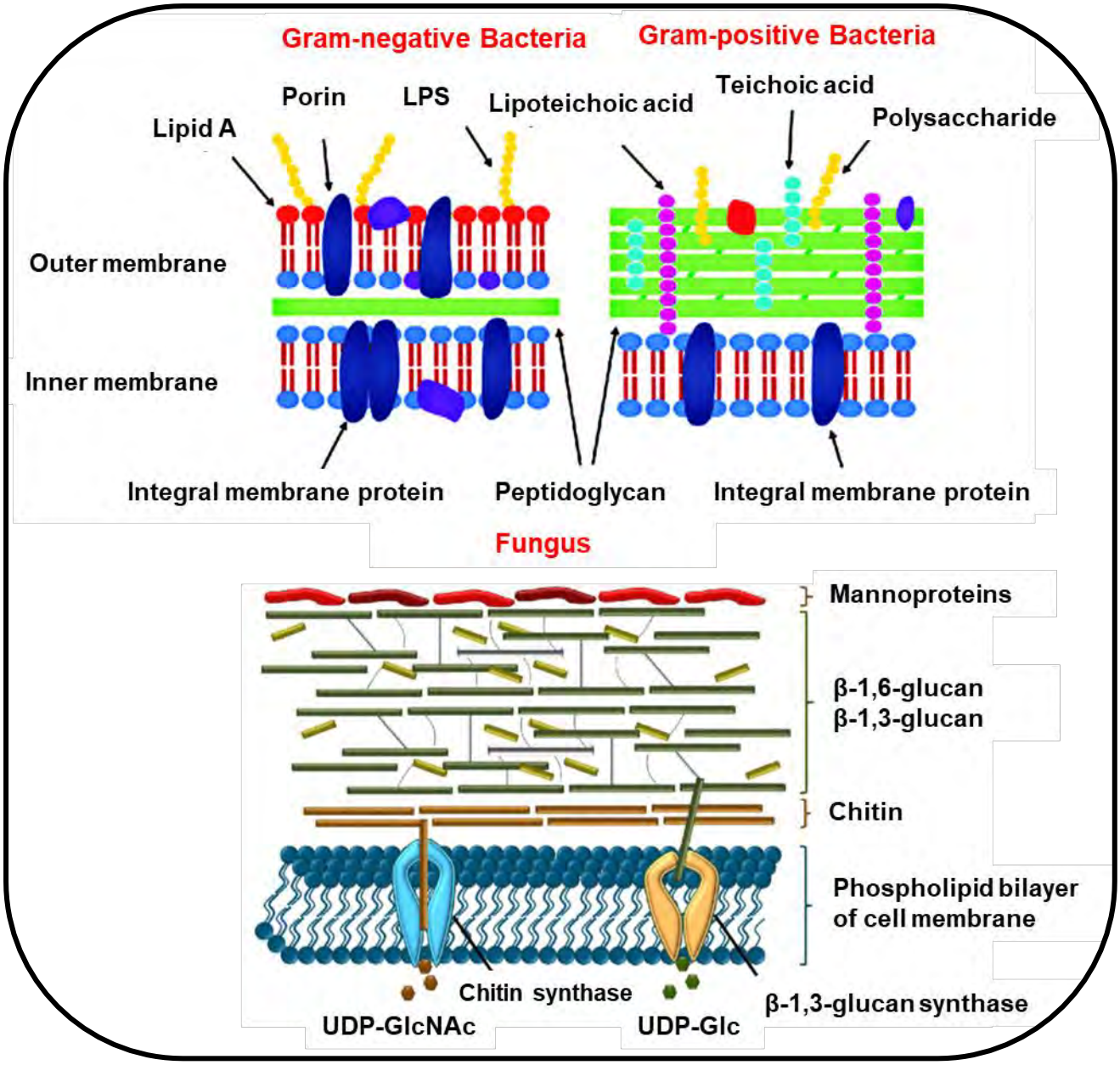

Figure 1.5: Structures of the cell walls of gram-negative bacteria, gram-positive bacteria and fungus as adapted from [76, 77]. LPS - lipopolysaccharides, UDP-Glc - uridine diphosphate-N-glucose, UDP-GlcNAc - uridine diphosphate-N-acetylglucosamine

Another form of treatment resistance is the formation of biofilms which is prevalent on the surface of medical devices such as catheters, artificial heart valves, and other biomaterials leading to the development of chronic infection [78, 79]. Biofilms are more resistant than planktonic cells as they possess an exopolysaccharide matrix and undergo changes in their gene expression. Hence, the studies on the removal of biofilms using PACT are few.

Table 1.2 [80-89] summarizes the micro-organisms that have been photo-eradicated using Pcs alone and when conjugated to nanoparticles or supports. Cationic Pcs have shown good efficiency against gram-positive and gram-negative bacteria due to improved permeability [80, 82-83, 85]. In this thesis, the evaluation of the PACT activity of neutral and cationic Pcs in various states, including planktonic, homogenous, and mixed biofilm forms is undertaken. Herein, the effect of the position of the substituent, the increase in the hydrocarbon length, and introduction of the imine group on PACT is investigated. Pcs can be incorporated into nanoparticles to enhance PACT activity [83, 84, 86]. Complexes **6** were conjugated to spherical and pyramidal zinc oxide nanoparticles as **Table 1.1** shows; it is the first time that Pcs are conjugated to pyramidal zinc oxide nanoparticles and applied for PACT studies. For practical use, Pcs can be embedded in supporting materials such as polymers [81, 87-89]. In this thesis, Pcs (**7**, **8**) were anchored on polyacrylonitrile-chitosan polymer and glass wool, and this is the first the PAN-CS polymer is being reported. As indicated in Table 1.2, there is no prior record of PACT studies conducted using Pc-glass wool conjugates; therefore, these studies will be presented for the first time in this thesis.

Table 1.2: Phthalocyanines previously reported for PACT.

	Central metal and R groups	Microorganism(s)/Support	Ref.
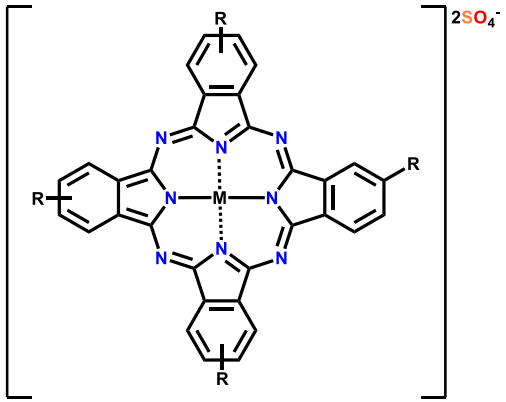	M =In(III)Cl, R = 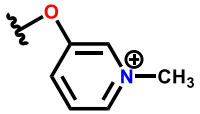 1(4)-tetrakis-(3-methylpyridyloxy)phthalocyaninato indium(III) chloride	***E. coli****/None*	[80]
	M = Si(IV)2OH, R = 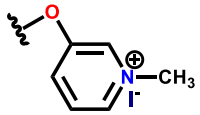 2(3),9(10),16(17),23(24)-Tetrakis-(N-methylpyridyloxy)phthalocyaninato silicon(IV) dihydroxy	***E. coli (planktonic and biofilm cultures)****/* Poly(vinyl alcohol) film	[81]

Table 1.2 continued:

	Central metal and R groups	Microorganism(s)/ Support	Ref.
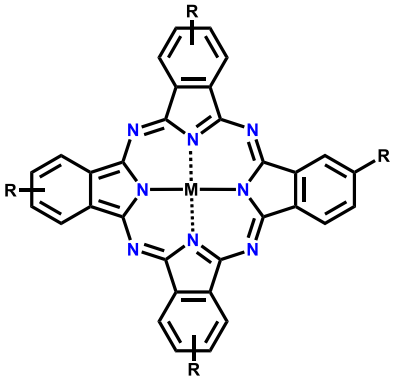	M = Zn(II), R = 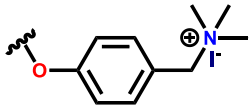 2(3),9(10),16(17),23(24)-Tetrakis-(((2-aminoethylamino)methyl)phenoxy)phthalocyaninoto zinc (II)	***S. aureus***/None	[82]
	M = In(III)Cl, R = 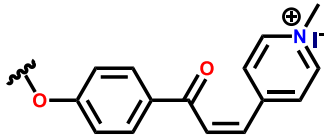 2(3),9(10),16(17),23(24)-Tetrakis-(E)-4-(4-(3-(N-methyl-pyridin-4-yl)acryloyl)phenoxy)phthalocyaninato indium(III)	***S. aureus* and *E. coli* (planktonic and biofilm cultures)**/ Detonated nanodiamonds	[83]
	M = Al(III)Cl, R = H Chloroaluminum(III) phthalocyanine	***S. mutans* (biofilm)**/Chitosan nanoparticles	[84]

Table 1.2 continued:

	Central metal and R groups		Microorganism(s)/ Support	Ref.
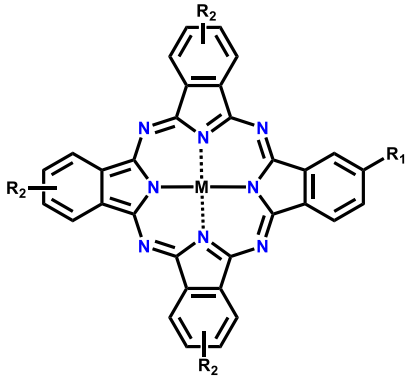	M = Zn(II), R_1 = 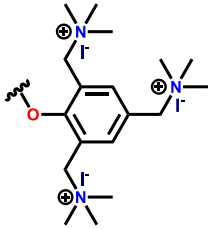	R_2 = H	**MRSA**/None	[85]
	tri-cationic monosubstituted zinc(II) phthalocyanine			
	M = Zn(II), R_1 = 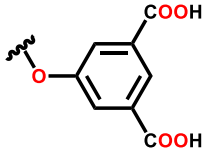	R_2 = 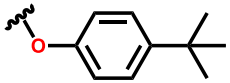	***S. aureus***/Silver and iron oxide nanoparticles	[86]
	2(3)-Mono-isophthalic acid-9(10),16(17),23 (24)-tri (*tert*-butylphenoxy)phthalocyaninato zinc(II)			
	M = Pb(II), R_1 = 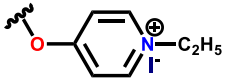	R_2 = 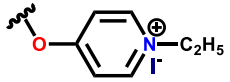	***E. coli***/ Polystyrene nanofibers	[87]
	2,9,16,23-Tetrakis[4-(N-ethylpyridyloxy)]-phthalocyaninato lead(II)			

Table 1.2 continued:

	Central metal and R groups	Microorganism(s)/ Support	Ref.
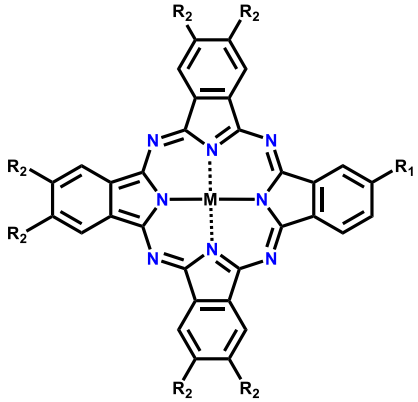	M = Zn(II), R_1 = 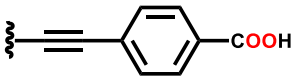 R_2 = 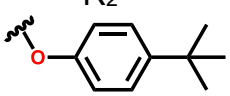 Zinc (II) 9,10,16,17,23,24-hexa(4´-tert-butylphenoxy)- 2-[2´-(4´´-carboxyphenyl)ethynyl] phthalocyaninato (2-)- N29, N30, N31,N32	***S. aureus***/Titanium dioxide nanoparticles	[88]
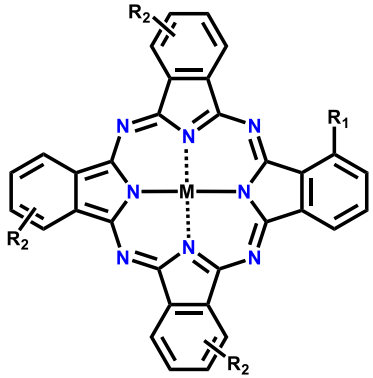	M = Zn(II), R_1 = 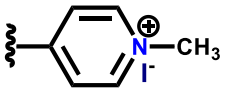 R_2 = 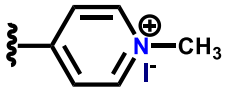 Tetrakis(N-methylpyridinium-4-yl)phthalocyaninato zinc(II)	***E. coli* and *Acinetobacter baylyi* *(A. baylyi)***/Paper	[89]

1.3 Nanoparticles

Nanoparticles (NPs) are defined as small particles with a size in the range of 1-100 nm [90]. Particles in this nano range show significantly different properties than in their bulky form [91]. The properties of nanoparticles can change based on dimensions, morphology, and composition [92]. Due to their differing properties, nanoparticles have gained interest in different research areas such as bioimaging, biomedicine, cosmetics, coating, pollution remediation, drug delivery and photodynamic therapies [93-99]. Nanoparticles possess a large surface area to volume ratio, and the ease of surface modification allows for the immobilization of the particles to other molecules. In this study, spherical and pyramidical zinc oxide nanoparticles (ZnONPs) capped with 3-aminopropyl)triethoxysilane (APTES) were covalently linked to asymmetrical MPcs (complexes **6**) to enhance the PACT activity against planktonic and biofilm cultures.

Zinc oxide nanoparticles are metal oxide nanoparticles with interesting characteristics, including lack of toxicity, biocompatibility, and antimicrobial activity [100]. The antimicrobial activity of ZnONPs is size-correlated, and dependant on the biological system they interact with as they induce intracellular uptake [92]. ZnONPs are non-specific and have been reported to have various antimicrobial mechanisms. ZnONPs can generate harmful ROS through a series of oxidation-reduction reactions caused either photochemically or through surface defects of the nanoparticle [101]. Another antimicrobial mechanism is through the release of Zn^{2+} ions by the ZnONPs. The free-flowing Zn^{2+} ions may decrease the amino acids metabolism and disturb the enzymatic system of the microbe and therefore result in higher antimicrobial activity [102]. Lastly, the ZnONPs can exhibit toxicity by interacting with the cell wall resulting in the microbe's integrity loss [103]. This interaction increases membrane permeability

allowing for the accumulation of ZnONPs in the micro-organism cell membrane. ZnONPs can cause changes in the environment close to the microbe. Herein, the ZnONPs will be investigated using two differently shaped ZnONPs; zinc oxide nanospheres (ZnONSps) and zinc oxide nanopyramids (ZnONPys). ZnONSps were selected due to their high surface area-to-volume ratio and are known to enhance antimicrobial activity against circular micro-organisms [104]. ZnONPys has yet to be extensively explored; however, non-spherical silver NPs have shown improved antimicrobial activity [105, 106]; hence ZnONPys are studied in this work. The combination of ZnONPs and MPcs is expected to improve the PACT activity against both planktonic and biofilm culture due to the synergetic effect of the two antimicrobial agents.

1.4 Support

Phthalocyanines and nanoparticles are promising photocatalysts on their own. However, for water treatment applications, they need to be recoverable. Hence, introducing them to supports such as nanofibers, polymer membranes, gels, and glass wool will improve their recoverability, thus introducing recyclability [107-116]. Photocatalysts are immobilized onto the support via mixing, self-assembly and covalent linkage [109-114]. In this study, Pcs are covalently linked to polyacrylonitrile nanofibers and glass wool to avoid possible photocatalyst leaching during application.

1.4.1 Nanofibers

Polymer nanofibers (NF) are solid fibers with a small diameter, a high surface area to volume ratio, high porosity with minimal pore size and flexibility in surface functionalities. These properties make NF ideal candidates for many applications such as tissue engineering, drug delivery, filters, water treatment and wound dressing [117-

121]. Various methods, such as drawing, template synthesis, self-assembly, phase separation and electrospinning, have been used to prepare nanofibers [**122-126**]. Electrospinning is preferred due to the production of ultrafine, uniform nanofibers. The electrospinning process is cost-effective and does not require expensive purification methods [**127**].

Rayleigh invented electrospinning in 1879 [**128**]. In the 1930s, the experimental set-up and apparatus used were presented and patented by Formalas [**129**, **130**]. The formation of nanofibers relies on three components; a high-voltage power supply, a needle attached to a syringe and a collector [**131**]. In an electrospinning process, a high voltage is applied to a polymer solution to create a strong electric field between the needle and the collector. This results in a conically shaped droplet caused by the surface charge created on a polymer fluid [**132**]. The conical droplet, known as the Taylor cone [**127**], is ejected due to the electrostatic force exceeding the surface tension of the polymer, as shown in **Figure 1.6**.

Phthalocyanines have been embedded and covalently linked to electrospun nanofibers [**87**, **107**, **111**, **112**]. In this study, polyacrylonitrile (PAN) polymer is applied due to its mechanical strength and chemical stability [**133**, **134**]. However, PAN is hydrophobic and tends to be fouled by micro-organisms, decreasing the efficiency of the polymer support over time [**135**]. To overcome this, the PAN polymer was chemically modified with chitosan (CS). Chitosan is a natural polymer with antimicrobial activity [**136**, **137**]. Chitosan alone is challenging to electrospin due to poor solubility in common organic solvents or the formation of highly viscous solutions [**127**, **138**].

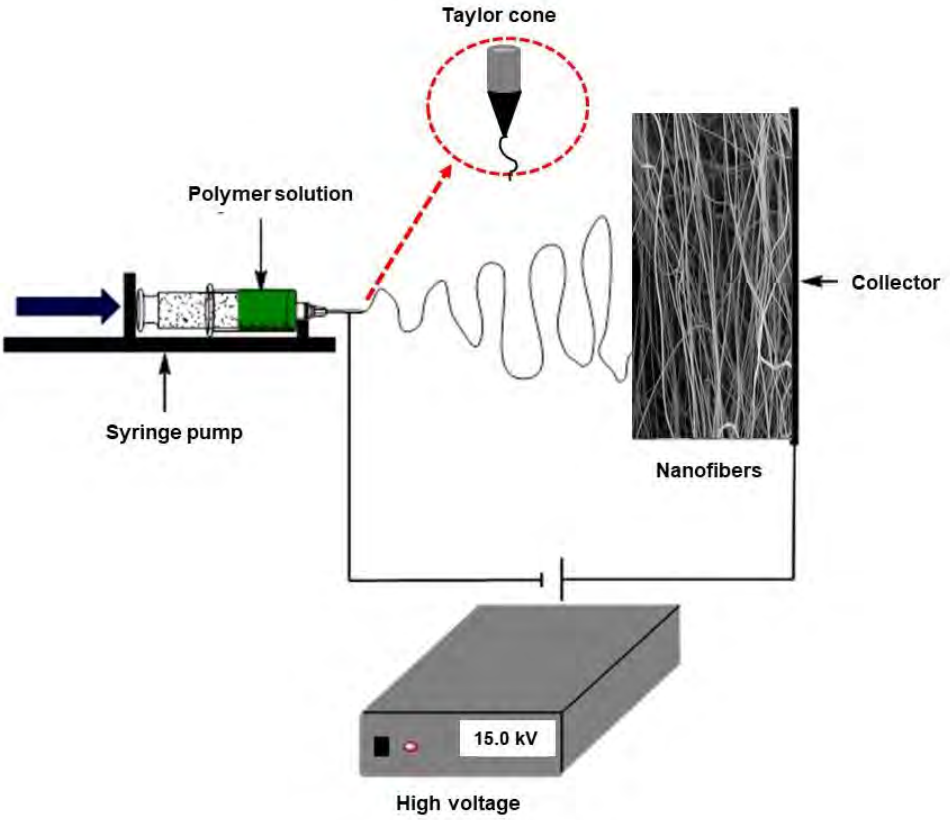

Figure 1.6: Electrospinning set-up [127, 128].

The PAN and PAN-CS nanofibers will be linked to neutral and cationic Pcs. Linking cationic Pcs to the polymers alters the surface of the polymers from hydrophobic to hydrophilic. This will be the first time that PAN is linked with CS and Pc. The PACT activity of these composites was evaluated. Furthermore, the neutral and cationic Pc-PAN composites were also applied for photodegradation studies of pollutants.

1.4.2 Glass wool (GW)

Glass wool, also known as glass fibers, has wide applications such as thermal and sound insulators, filtration mats and adsorbent beds [139-141]. This material is known to be inexpensive, widely available, inert, and robust towards numerous chemicals and is stable in different pH levels [110, 139]. GW has been used to immobilize antibodies

and culture biofilms [142, 143]. However, the material has not been previously used as supports in antimicrobial studies. The composite was modified with APTES to allow a covalent linkage with Pcs, and this is the first time Pcs are linked to GW. This study compares GWs' efficiency to NFs as photocatalysts in PACT and photodegradation applications.

1.5 Photo-oxidation of environmental pollutants

As stated above environmental pollution is a growing problem due to increased industrial activities. Organic pollutants being deposited into the environment, especially bodies of water, is one of the leading causes of environmental issues [144]. It has been reported that about 20% of synthetic dyes such as methyl orange, methylene blue, and many other dyes are discharged to water bodies without treatment and further exacerbating the environmental pollution issue [145]. Methyl orange (MO) is an anionic azo dye, and methylene blue (MB) is a cationic thiazine dye. Both dyes are toxic, carcinogenic, and non-biodegradable [146, 147]. Apart from dyestuff, chlorophenols are one of the organic pollutants listed as a priority due to their toxicity and low biodegradability. 4-Chlorophenol (4-CP) is primarily used as a pesticide, and it is regarded as mutagenic [148].

Wastewater treatment technologies are divided into physical (adsorption [149], sedimentation [150], membrane separation [151]), biological (aerobic [152] and anaerobic [153] processes), chemical (oxidation [154], electrolysis [155], and advanced oxidation process [156]) methods. However, the physical methods have difficulties removing organic pollutants [157], and the biological methods have high operation costs and long pre-preparation cycles [158]. In contrast, chemical methods can wholly and efficiently degrade organic pollutants [159].

Amongst chemical methods, advanced oxidation processes (AOPs) are one of the popular techniques as they only use oxygen and generate non-toxic by-products [**149**]. Photocatalysis is one of the AOPs for organic pollutant degradation. In this study, MO, MB, and 4-CP are photodegraded or photo-transformed using laser or sunlight. The photochemical transformation of 4-CP, MB, and MO using symmetrical and asymmetrical phthalocyanine embedded in fibers has been reported [**107, 160-164**]. This work reports for the first time on the use of asymmetrical cationic phthalocyanine covalently linked to electrospun nanofibers and glass wool for the degradation of 4-CP, MO and MB. The PACT activity of the supports was also examined and compared.

1.6 Summary of aims of thesis

The aims of this thesis include:

1. Synthesize and characterize symmetrical, asymmetrical, alpha, beta, charged and neutral zinc and indium phthalocyanines.
2. Synthesize and characterize differently shaped zinc oxide nanoparticles
3. Fabricate and characterize polyacrylonitrile nanofibers and covalently link the polymer to chitosan.
4. Modify glass wool with 3-aminopropyltriethoxysilane.
5. Covalently link phthalocyanines with nanoparticles, polymers, and glass wool.
6. Study the photophysical and photochemical properties of the phthalocyanines alone or when anchored on support in organic and/or aqueous media.
7. Investigate the PACT activity of the prepared photocatalyst against planktonic and biofilm cultures.
8. Assess the photocatalytic degradation or transformation of pollutants; 4-chlorophenol, methyl orange and methylene blue using neutral and cationic Pc-PAN and Pc-GW composites.

Chapter 2

Experimental

2. Experimental

2.1 Materials

2.1.1 General reagents and solvents

Dimethylsulfoxide (DMSO), dimethylformamide (DMF), dichloromethane (DCM), tetrahydrofuran (THF), deuterium oxide, chloroform, methanol, diethyl ether, ethanol, and ethyl acetate were purchased from Merck, while deuterated chloroform and acetonitrile were purchased from Associated Chemical Enterprises. Deuterated dimethyl sulfoxide (DMSO-d_6), dithranol, triton-X and α-cyano-4-hydroxycinnamic acid were purchased from Sigma Aldrich. Ultra-pure water from a Milli-Q Water system (Millipore Corp, Bedford, MA, USA) or in ultra-pure Type II water obtained from Elga PURELAB chorus 2 (RO/ DI) system. All solvents were dried using molecular sieves.

2.1.2 Reagents for phthalonitrile precursors, phthalocyanine syntheses

Zinc (II) acetate ($Zn(OAc)_2$), indium (III) chloride, 1,8-diazabicycloundec-7-ene (DBU), 1-pentanol, methyl iodide, sodium carbonate, morpholine, 4-(2-aminoethyl)morpholine, 4-nitrophthalonitrile, 3-nitrophthalonitrile, 1-(2-aminoethyl)pyrrolidine, and 1-(3-aminopropyl)pyrrolidine were purchased from Sigma Aldrich, while dimethyl sulphate was bought from Riedel-de Haen. The tetrakis[4-formylphenoxy]phthalocyaninato zinc(II) (**A**) [165] and tetrakis[4-formylphenoxy]phthalocyaninato indium(III) (**B**) chloride [166] were prepared according to literature. The synthesis of phthalonitriles, 4-(benzo[*d*]thiazol-2-ylthio)phthalonitrile (**i**) [167] and 4-(3,4-dicyanophenoxy)benzoic acid (**ii**) [168] were completed as reported in the literature.

2.1.3 Reagents for zinc oxide nanoparticles, polymer nanofibers and glass wool syntheses, modification, and conjugation

3-Aminopropyltriethoxysilane (APTES), polyacrylonitrile (PAN, MW = 150 000 Da), chitosan (MW = 50 000 - 190 000 Da), non-treated glass wool Aldrich catalog #: 20384, N,N'-dicyclohexylcarbodiimide (DCC), 1-ethyl-3-(3-dimethylaminopropyl)carbodiimide (EDC), hydrazine, N-hydroxysuccinimide (NHS) were procured from Sigma. The synthesis of ZnONSps [169], ZnONPys, and [170] PAN-COOH [171] were as reported before.

2.1.4 Chemicals and reagents for photophysicochemical studies

1,3-Diphenylisobenzofuran (DPBF), anthracene-9,10-bis-methylmalonate (ADMA), methylpiperidone (TEMP), 5,5-dimethyl-1-pyrroline-*N*-oxide (DMPO), sodium azide, zinc (II) phthalocyanine (ZnPc) were purchased from Sigma Aldrich.ClAlPcSmix (containing a mixture of differently sulfonated Pc) was synthesized as reported in literature [172] and used as a standard for singlet oxygen determinations in aqueous media.

2.1.5 Reagents for bacterial and photodegradation studies

Phosphate-buffered saline (PBS) solution pH 7.4 was prepared using appropriate amounts of Na_2HPO_4 and NaOH in ultra-pure water. Nutrient agar, ampicillin, and agar bacteriological BBL Muller Hinton broth were purchased from Merck, *E. coli* (ATCC 25922), *K. pneumoniae* (ATCC 13883) were obtained from Microbiologic. *S. aureus* (ATCC 25923), MRSA (ATCC 700699), *S. choleraesuis* (ATCC 10708), VREF (ATCC 51299) and *C. albican* (ATCC 24433) were from Davies Diagnostics. Crystal violet, methicillin, sodium dodecyl sulfate (SDS), 4-chlorophenol (4-CP), methylene blue (MB), methyl orange (MO), and tryptic soy broth were purchased from Sigma Aldrich.

2.2 Equipment

i. Electronic absorption spectra of solutions were recorded on a Shimadzu UV-2550 spectrophotometer using 3 cm quartz cell cuvette.

ii. Solid-state UV-Vis was performed in Perkin Elmer Lambda 950 UV–Vis NIR spectrophotometer using the holmium reference to convert reflectance measurements to equivalent absorption spectra.

iii. Infrared (IR) spectra were recorded on a Bruker Alpha IR (100 FT-IR) spectrophotometer.

iv. Elemental analyses were carried out on a Vario EL III MicroCube CHNS Analyzer.

v. Mass spectra data were collected with a Bruker AutoFLEX III Smartbeam TOF/TOF Mass spectrometer and with Bruker microTOF II mass spectrometer. The spectra were acquired using dithranol and α-cyano-4-hydroxycinnamic acid as the MALDI matrix.

vi. ^{1}H nuclear magnetic resonance spectra recorded on a Bruker AMX 600 MHz and 400 MHz NMR spectrometers.

vii. Fluorescence emission and excitation spectra were recorded on a Varian Eclipse spectrofluorimeter.

viii. Fluorescence decay lifetimes were measured using a time-correlated single photon counting (TCSPC) setup (FluoTime 300, Picoquant GmbH). The excitation source was a diode laser (LDH-P-670 driven by PDL 800-B, 670 nm, 20 MHz repetition rate, 44 ps pulse width, Pico quant GmbH).

ix. Triplet state quantum yields were determined using a laser flash photolysis system consisting of an LP980 spectrometer with a PMT-LP detector and an ICCD camera (Andor DH320T-25F03), **Figure 2.1**. The signal from a PMT

detector was recorded on a Tektronix TDS3012C digital storage oscilloscope. The excitation pulses were produced using a tunable laser system consisting of an Nd:YAG laser (355 nm, 135 mJ/4–6 ns) pumping an optical parametric oscillator (OPO, 30 mJ/3–5 ns) with a wavelength range of 420–2300 nm (NT-342B, Ekspla). The absorbance of solutions of the Pcs and the ZnPc standard were ~1.5 at Q band. The solution was introduced into a 1 cm path length UV-visible spectrophotometric cell and de-aerated using argon for 15 min. The maximum triplet absorption detection wavelength was obtained from the transient curve. Triplet state lifetimes were determined by exponential fitting of the kinetic curves using ORIGIN® 8 Professional software.

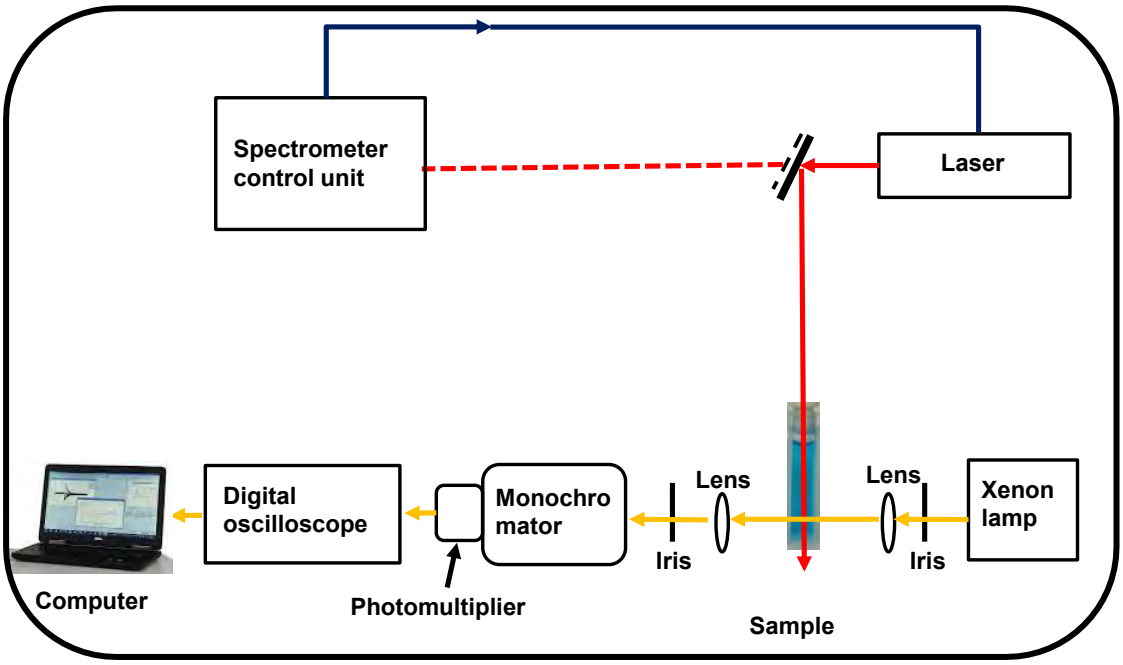

Figure 2.1: Schematic diagram of the laser flash photolysis set-up.

x. Photo-irradiations for singlet oxygen quantum yield determination, photostability and antimicrobial studies were performed using a General Electric Quartz lamp (300 W), 600 nm glass (Schott) and water filters were used to filter off ultra-violet and far infrared radiations (and in the absence of the filters for white light studies). Light intensities measured with a POWER MAX 5100

(Molelectron detector incorporated) power meter or Modulight ML7710–680/690-RHO laser system was employed, **Figure 2.2**. The system was equipped with a cylindrical output channel, aiming beams, foot/hand pedal switch, a calibration module, fiber sensors (subminiature version A) connectors, and safety interlocks.

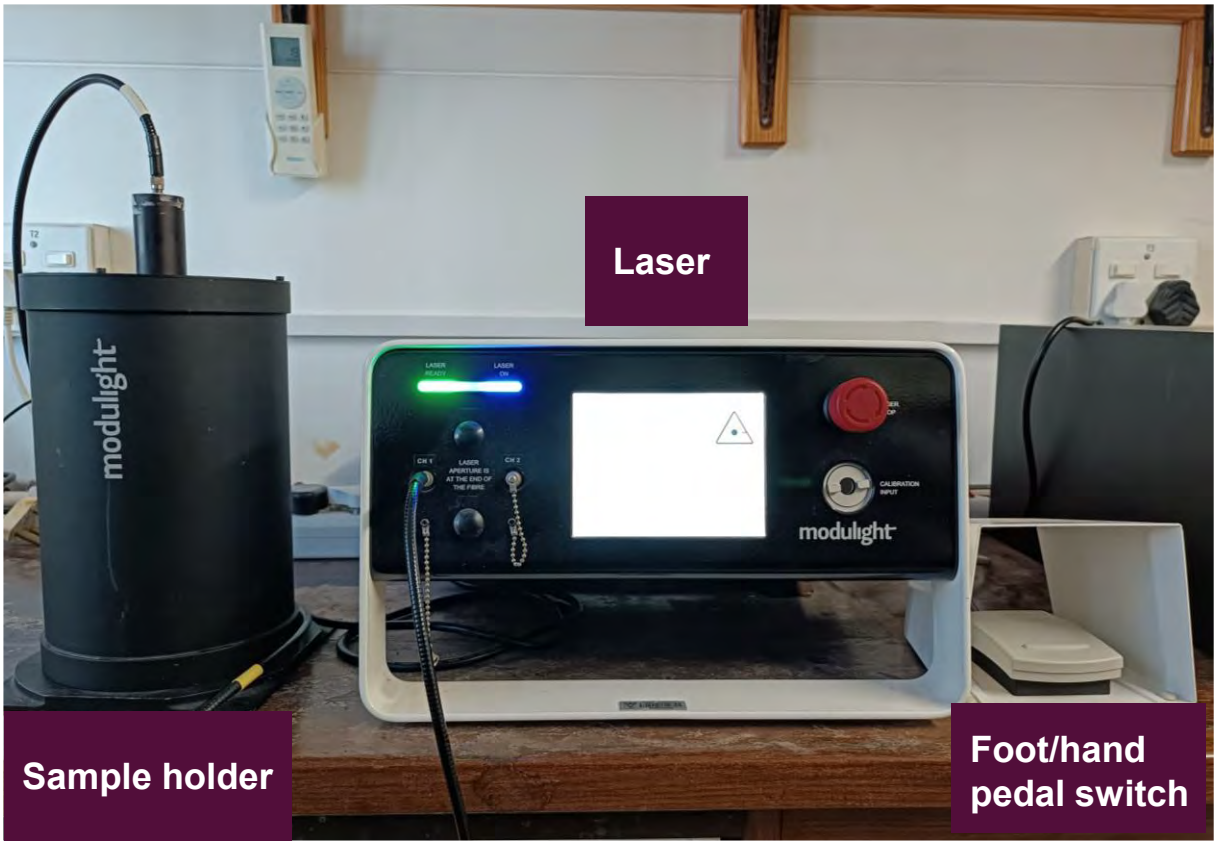

Figure 2.2: Experimental set-up of the Modulight ML7710–680/690-RHO laser system.

xi. The electron paramagnetic resonance (EPR) spectroscopy measurements were carried out using the Bruker EMX Plus EPR spectrometer, specifications: model number: EMP-9.5/12B/P. set at 0.632 mW for the microwave power, frequency 9.714 GHz, resolution 2048 points, at a center field of 3500 G and 200 G for the sweep width and time constant of 5.12.

xii. Sizes and morphologies of the nanoparticles and conjugates were determined by Transmission electron microscopy (TEM) using a Zeiss Libra 120 TEM operating at 80 kV.

xiii. X-ray powder diffraction (XRD) patterns were recorded using a Cu K radiation (1.5405 °A, nickel filter) on a Bruker D8 Discover equipped with a proportional counter and the X-ray diffraction data were processed using the Eva (evaluation curve fitting) software.

xiv. Zeta potential were determined using a Malvern Zetasizer Nanoseries, Nano-ZS90.

xv. Scanning electron microscope (SEM) micrograms were obtained using a JOEL JSM 840 scanning electron microscope.

xvi. Energy-dispersive X-ray spectrometer (EDX, INCA PENTA FET coupled with VAGA TESCAM operated at 20 kV) was used for elemental composition.

xvii. Time-of-flight-secondary ion mass spectrometer (ToF-SIMS) data were recorded with an ION TOF GmbH TOF SIMS 5–100 run in a micro-raster mode.

xviii. Thermal decomposition profiles of all compounds were recorded using Perkin Elmer TGA 8000 Thermogravimetric Analyzer, purged with nitrogen.

xix. Micrometrics ASAP 2020 Surface Area and Porosity Analyzer was employed for nitrogen adsorption/desorption isotherm.

xx. X-ray Photoelectron Spectroscopy (XPS) analysis was done using an AXIS Ultra DLD, with Al (monochromatic) anode equipped with a charge neutralizer, supplied by Kratos Analytical.

xxi. The optical densities of microbial culture were determined using the LEDETECT 96 from LABXIM PRODUCTS.

xxii. PRO VSM-3 Labplus Vortex mixer and HERMLE Z233M-2 centrifuge from LASIEC were used to mix the microbial solution.

xxiii. Scan 500 Automatic Colony Counter (Healthcare Technologies) was used for colony counting.

xxiv. The fluorescence intensity for the uptake studies were measured using CLARIOstar plus microplate reader from BMG Labtech.

xxv. A thermostatic oven was used to harvest the microbial cells.

xxvi. The pH values were measured using Metrohm Swiss 827 pH meter.

2.3 Syntheses

2.3.1 Syntheses of phthalonitriles

Three phthalonitriles (3- or 4-morpholinophthalonitrile and 2-((3,4-dicyanophenyl)thio)-N-methylbenzothiazolium iodide) are reported for the first time and their synthetics details are provided in this section.

Synthesis of 3-Morpholinophthalonitrile (iii) or 4-Morpholinophthalonitrile (iv) – Scheme 3.1

3-Nitrophthalonitrile or 4-nitrophthalonitrile (1.97 g, 10 mmol) and morpholine (3.9 g, 45 mmol) were dissolved in dry DMF (25 mL) and reacted with anhydrous Na_2CO_3 (3.12 g, 30 mmol). The mixture was stirred at 100 °C, for 18 h under inert conditions, using an oil bath to maintain the temperature. The products were precipitated using water, and the yellow precipitates formed were filtered under vacuum and recrystallized with methanol. The crude products were purified further by column chromatography using alumina and eluting with ethyl acetate. Both compounds are soluble in most organic compounds (DMF, DMSO, methanol, ethyl acetate, DCM, chloroform and THF).

3-Morpholinophthalonitrile (iii) - Yield: 22.78 % (0.56 g). FTIR (Attenuated Total Reflectance, ATR), v/cm^{-1}: 2967 (C-H), 2907 (CH_2), 2869 (CH_2), 2218 (C≡N), 1597, 1512 (C=C),1255, 1179, 1099 (C-O), 1038, 957, 866, 809, 723 (C-C). Elemental analysis: calc (%) for $C_{12}H_{11}N_3O$: C, 67.59 %; H, 5.20 %; N, 19.71 %, Found: C 67.68 %; H, 4.61 %; N, 19.74 %; ^{1}H NMR (600 MHz, $CDCl_3$): δ (ppm) 7.49 (d, *J* = 8.6 Hz, 1H), 7.14 (d, *J* = 7.6 Hz, 1H), 7.07-7.03 (m, 1H), 3.79 (d, *J* = 3.6 Hz, 4H, CH_2), 3.26 (d, *J* = 3.3 Hz, 4H, CH_2). MS (MALDI-TOF): *m/z* cald =213.09, found =214.10 $[M+1H]^+$.

4-Morpholinophthalonitrile (iv) - Yield: 48.56 % (1.18 g). FTIR (ATR), v/cm^{-1}: 3109 (C-H), 2909 (CH_2), 2864 (CH_2), 2221 (C≡N), 1592, 1507 (C=C),1257, 1179, 1110 (C-O), 1037, 951, 863, 817, 718 (C-C). Elemental analysis: calc (%) for $C_{12}H_{11}N_3O$: C, 67.59 %; H, 5.20 %; N, 19.71 %, Found: C 67.61 %; H, 4.98 %; N, 19.75 %; ^{1}H NMR (600 MHz, $CDCl_3$): δ (ppm) 7.60 (d, *J* = 8.0 Hz,1H), 7.15 (d, *J* = 8.1 Hz, 1H), 7.05-7.02 (m, 1H), 3.88 (d, *J* = 3.4 Hz, 4H, CH_2), 3.35 (d, *J* = 3.4Hz, 4H, CH_2). MS (MALDI-TOF): *m/z* cald =213.09, found =214.11 $[M+1H]^+$.

Synthesis of 2-((3,4-dicyanophenyl)thio)-N-methylbenzothiazolium iodide (v) – Scheme 3.1

A mixture of 4-(benzo[d]thiazol-2-ylthio)phthalonitrile (**i**, 1.0 g, 3.4 mmol) and methyl iodide (0.7 g, 5.1 mmol) in DMF (10 mL) was heated to reflux with stirring at 120 °C for 5 h. This was followed by precipitation using hexane, filtering under reduced pressure and recrystalization with methanol. The faint yellow precipitate was air dried. Yield: 59.5 % (0.88 g), FTIR (ATR) v/cm^{-1}: 2950, 2944 (Ar-H), 2231 (C≡N), 1585 (C=N), 1426 (Ar C=C), 1281 (CH3), 1233 (C-S), 1050 (Ar C-H), 785 (C-S). Elemental Analysis: calc (%) for $C_{16}H_{10}N_3S_2^+$: C, 62.31 %; H, 3.27 %; N, 13.63 %; S, 20.79 %; found: C, 62.01 %; H, 3.09 %; N = 13.89 %; S = 21.22 %. ^{1}H NMR (DMSO-d_6, 400

NMR δ (ppm) 8.40 (d, *J* = 8.2 Hz, 2H, Ar-H), 8.20 (d, *J* = 8.5 Hz, 1H, Ar-H), 7.85 (t, 8.5 Hz, 2H, Ar-H), 7.74 (t, 8.2 Hz, 2H, Ar-H), 4.12 (s, 3H, CH_3).

2.3.2 Syntheses of phthalocyanines

The preparation of seven new phthalocyanines is detailed below.

2.3.2.1 Synthesis of morpholino phthalocyanines (1 and 2) – Scheme 3.2

For **1-H_2** and **2-H_2**; 3-morpholinophthalonitrile (**iii**) and 4-morpholinophthalonitrile (**iv**) (0.20 g, 0.94 mmol) were each mixed with 5 mL of 1- pentanol and DBU (0.25 mL), followed by stirring for 20 min at 360 °C. The products were precipitated with dilute HCl. The green products were filtered and further washed with water, methanol, and acetonitrile. The products were further purified by column chromatography with silica gel and eluting with chloroform. Both complexes (**1-H_2** and **2-H_2**) are soluble in $CHCl_3$, THF, DCM, DMF and partially in DMSO.

The metalated derivatives, **1-Zn**, **1-In**, **2-Zn**, and **2-In** were prepared as follows; compounds **iii** or **iv** (0.30 g, 1.4 mmol) and 0.35 mmol of metal salt (0.097 g $Zn(OAc)_2$ and 0.12 g $InCl_3$) were mixed in 3 mL of dry 1-pentanol and 0.1 mL DBU. The mixtures were stirred for 8 h at 138 °C. The products were precipitated with 1:1 methanol: H_2O, filtered and washed with acetonitrile. The products were further purified by column chromatography with silica gel and eluting with chloroform. All the complexes were soluble in $CHCl_3$, THF, DCM, DMF and DMSO.

Quaternization of **1-Zn**, **1-In**, **2-Zn**, and **2-In** to form **1-ZnQ**, **1-InQ**, **2-ZnQ**, and **2-InQ** was as follows; Complexes **1-Zn**, **2-Zn** (0.010 g, 0.011 mmol) or **1-In** and **2-In** (0.010 g, 0.0099 mmol) and 5.05 mmol of dimethyl sulphate were mixed in 3 mL of dry DMF, followed by stirring for 4 h at 155 °C. The products were precipitated with acetone,

filtered, and washed with chloroform and diethyl ether. All the complexes were soluble in H_2O, DMF and DMSO.

1(4),8(11),15(18),22(25)-Tetrakis-(morpholino)phthalocyanine (1-H$_2$) - Yield: 7.0 % (0.013 g). UV–vis (dimethylformamide, DMF): λ_{max} (nm) (log ε) 323 (4.33), 644 (4.18), 682 (4.27), 745 (4.70), 775 (4.73). FTIR (ATR), v/cm^{-1}: 3282 (N-H), 3018 (C-H), 2949 (CH_2), 2811 (CH_2), 1564 (N-H), 1485 (C=C),1309, 1222, 1107 (C-O), 1022, 963, 864, 799, 736 (C-C). Elemental analysis: calc (%) for $C_{48}H_{46}N_{12}O_4$: C, 67.43 %; H, 5.42 %; N, 19.66 %; Found: C, 66.94 %; H, 5.08 %; N, 19.51 %; ^{1}H NMR (600 MHz, $CDCl_3$): δ (ppm) 8.98 (s, 2H, NH), 7.78 (s, 4H, Ar-H) 7.26 (dd, *J* = 8.5, 1.2 Hz, 8H, Ar-H), 4.20 (d, *J* = 5.7 Hz, 16H, CH_2), 3.48 (d, *J* = 5.6 Hz, 16H, CH_2). MS (MALDI-TOF): *m/z* cald =854.38, found =855.12 $[M+1H]^+$.

2(3),9(10),16(17),23(24)-Tetrakis-(morpholino)phthalocyanine (2-H$_2$) - Yield: 12.0 % (0.023 g). UV–vis (dimethylformamide, DMF): λ_{max} (nm) (log ε) 346 (4.42), 634 (4.38), 658 (4.41), 709 (4.58), 739 (4.62). FTIR (ATR), v/cm^{-1}: 3280 (N-H), 3104 (C-H), 2899 (CH2), 2804 (CH2), 1557 (N-H), 1473 (C=C),1311, 1199, 1102 (C-O), 1032, 947, 804, 781, 731 (C-C). Elemental analysis: calc (%) for $C_{48}H_{46}N_{12}O_4$: C, 67.43 %; H, 5.42 %; N, 19.66 %; Found: C, 67.34 %; H, 5.09 %; N, 18.26 %; ^{1}H NMR (600 MHz, $CDCl_3$): δ (ppm) 9.02 (s, 2H, NH), 8.24 (s, 4H, Ar-H), 7.70 (dd, *J* = 8.9, 1.1 Hz, 8H, Ar-H), 3.79 (d, *J* = 4.7 Hz 16H, CH_2), 3.26 (d, *J* = 5.0 Hz 16H, CH_2). MS (MALDI-TOF): *m/z* cald =854.38, found =855.99 $[M+2H]^+$.

1(4),8(11),15(18),22(25)-Tetrakis-(morpholino)phthalocyaninoto zinc(II) (1-Zn) - Yield: 23.0 % (0.05 g). UV–vis (dimethyl sulfoxide, DMSO): λ_{max} (nm) (log ε) 340 (4.53), 682 (4.21), 747 (4.96). FTIR (ATR), v/cm^{-1}: 3189 (CH), 2910 (CH_2), 2837 (CH_2), 1601 (C=C),1309, 1220, 1094 (C-O), 1019, 946, 879, 810, 734 (C-C). Elemental

analysis: calc (%) for $C_{48}H_{44}N_{12}O_4Zn$: C, 62.78 %; H, 4.83 %; N, 18.30 %; Found: C, 63.34 %; H, 4.09 %; N, 18.26 %; ^{1}H NMR (600 MHz, $CDCl_3$): δ (ppm) 7.60 (s, 4H, Ar-H), 7.06-6.93 (m, 8H, Ar-H), 3.83 (d, *J* = 6.2 Hz, 16H, CH_2), 3.36 (d, *J* = 5.9 Hz, 16H, CH_2). MS (MALDI-TOF): *m/z* cald =916.29, found =916.26 $[M]^+$.

1(4),8(11),15(18),22(25)-Tetrakis-(morpholino)phthalocyaninoto indium(III) chloride (1-In) - Yield: 19.8 % (0.043 g). UV–vis (DMSO): λ_{max} (nm) (log ε) 366 (4.08), 396 (3.94), 765 (4.71). FTIR (ATR), v/cm^{-1}: 3011 (C-H), 2948 (CH_2), 2849 (CH_2), 1493 (C=C),1330, 1225, 1104 (C-O), 1058, 985, 892, 777, 734 (C-C). Elemental analysis: calc (%) for $C_{48}H_{44}ClInN_{12}O_4$: C, 57.47 %; H, 4.42%; N, 16.75 %; Found: C, 56.83 %; H, 4.18 %; N, 16.32 %; ^{1}H NMR (600 MHz, $CDCl_3$): δ (ppm) 8.92 (s, 4H, Ar-H), 8.25-7.20 (m, 8H, Ar-H), 4.00 (d, *J* = 5.7 Hz, 16H, CH_2), 3.22 (d, *J* = 5.6 Hz, 16H, CH_2). MS (MALDI-TOF): *m/z* cald =1002.23, found =1002.49 $[M]^+$.

2(3),9(10),16(17),23(24)-Tetrakis-(morpholino)phthalocyaninoto zinc(II) (2-Zn) - Yield: 42.8 % (0.093 g). UV–vis (dimethyl sulfoxide, DMSO): λ_{max} (nm) (log ε) 364 (4.13), 644 (3.94), 717 (4.78). FTIR (ATR), v/cm^{-1}: 3175 (CH), 2906 (CH_2), 2824 (CH_2), 1608 (C=C),1298, 1214, 1102 (C-O), 1020, 952, 869, 808, 729 (C-C). Elemental analysis: calc (%) for $C_{48}H_{44}N_{12}O_4Zn$: C, 62.78 %; H, 4.83 %; N, 18.30 %; Found: C 62.94 %; H, 4.078 %; N, 18.81 %; ^{1}H NMR (600 MHz, $CDCl_3$): δ (ppm) 7.71 (s, 4H, Ar-H), 6.92-6.72 (m, 8H, Ar-H), 3.76 (d, *J* = 5.3 Hz, 16H, CH_2), 1.85 (d, *J* = 5.0 Hz, 16H, CH_2). MS (MALDI-TOF): *m/z* cald =916.29, found =916.26 $[M]^+$.

2(3),9(10),16(17),23(24)-Tetrakis-(morpholino)phthalocyaninoto indium(III) chloride (2-In) - Yield: 40.0 % (0.087 g). UV–vis (DMSO): λ_{max} (nm) (log ε) 363 (3.98), 665 (3.75), 736 (4.68). FTIR (ATR), v/cm^{-1}: 3023 (C-H), 2909 (CH_2), 2823 (CH_2), 1510 (C=C),1396, 1198, 1108 (C-O), 1078, 962, 871, 762, 727 (C-C). Elemental analysis:

calc (%) for $C_{48}H_{44}ClInN_{12}O_4$: C, 57.47 %; H, 4.42 %; N, 16.75 %; Found: C, 57.27 %; H, 4.34 %; N, 16.02 %; ^{1}H NMR (600 MHz, $CDCl_3$): δ (ppm) 7.75 (s, 4H, Ar-H), 7.62-7.58 (m, 8H, Ar-H), 4.25 (d, *J* = 5.7 Hz, 16H, CH_2), 3.90 (d, *J* = 5.3 Hz,16H, CH_2). MS (MALDI-TOF): *m/z* cald =1002.23, found =1002.89 $[M]^+$.

1(4),8(11),15(18),22(25)-Tetrakis-(N-methylmorpholino)phthalocyaninoto zinc(II) (1-ZnQ) - Yield: 34.0 % (0.003 g). UV–vis (DMSO): λ_{max} (nm) (log ε) 352 (4.84), 614 (4.53), 678 (5.20). FTIR (ATR), v/cm^{-1}: 3042 (CH), 2923 (CH_2), 1608 (C=C),1329, 1173, 1100 (C-O), 1041, 912, 850, 746 (C-C). Elemental analysis: calc (%) for $C_{52}H_{56}N_{12}O_{20}S_4Zn$: C, 45.83 %; H, 4.14 %; N, 12.33 %; S, 9.41 %; Found: C, 43.14 %; H, 4.52 %; N, 11.55 %; 9.72 %; ^{1}H NMR (600 MHz, D_2O): δ (ppm) 9.83 (s, 4H, Ar-H), 9.35-8.41 (m, 8H, Ar-H), 4.58-4.50 (m, 16H, CH_2), 4.28 (d, *J* = 6.2 Hz 16H, CH_2), 2.18 (s, 12H, CH_3).

1(4),8(11),15(18),22(25)-Tetrakis-(N-methylmorpholino)phthalocyaninoto indium(III) (1-InQ) - Yield: 27.0 % (0.003 g). UV–vis (DMSO): λ_{max} (nm) (log ε) 353 (4.51), 621 (4.17), 689 (4.90). FTIR (ATR), v/cm^{-1}: 3042 (CH), 2923 (CH_2), 1608 (C=C),1329, 1173, 1100 (C-O), 913, 861, 745 (C-C). Elemental analysis: calc (%) for $C_{52}H_{56}ClInN_{12}O_{20}S_4$: C, 43.15 %; H, 3.90 %; N, 11.61 %; S, 8.86 %; Found: C, 44.03 %; H, 4.02 %; N, 11.89 %; S, 9.06 %; ^{1}H NMR (600 MHz, D_2O): δ (ppm) 9.95 (s, 4H, Ar-H), 9.61-9.35 (m, 4H, Ar-H), 8.74-8.51 (m, 4H, Ar-H), 4.73-4.58 (m, 16H, CH_2), 4.29 (d, *J* = 5.4 Hz 16H, CH_2), 3.64 (s, 12H, CH_3).

2(3),9(10),16(17),23(24)-Tetrakis-(N-methylmorpholino)phthalocyaninoto zinc(II) (2-ZnQ) - Yield: 52.0 % (0.005 g). UV–vis (DMSO): λ_{max} (nm) (log ε) 343 (4.98), 610 (4.64), 673 (5.33). FTIR (ATR), v/cm^{-1}: 3038 (CH), 2919 (CH_2), 1598 (C=C),1317, 1181, 1201 (C-O), 1001, 888, 832, 768 (C-C). Elemental analysis: calc (%) for

$C_{52}H_{56}N_{12}O_{20}S_4Zn$: C, 45.83 %; H, 4.14 %; N, 12.33 %; S, 9.41 %; Found: C, 44.78 %; H, 4.07 %; N, 11.92 %; S, 9.35 %; ^{1}H NMR (600 MHz, D_2O): δ (ppm) 9.89 (s, 4H, Ar-H), 8.51-8.07 (m, 8H, Ar-H), 4.34-4.27 (m, 16H, CH_2), 4.05 (d, *J* = 4.0 Hz 16H, CH_2), 3.88 (s, 12H, CH_3).

2(3),9(10),16(17),23(24)-Tetrakis-(N-methylmorpholino)phthalocyaninoto indium(III) chloride (2-InQ) - Yield: 27.0 % (0.003 g). UV–vis (DMSO): λ_{max} (nm) (log ε) 356 (4.72), 616 (4.46), 684 (5.11). FTIR (ATR), v/cm^{-1}: 3039 (CH), 2927 (CH2), 1617 (C=C),1334, 1197, 1008 (C-O), 938, 817, 739 (C-C). Elemental analysis: calc (%) for $C_{52}H_{56}ClInN_{12}O_{20}S_4$: C, 43.15 %; H, 3.90 %; N, 11.61 %; S, 8.86 %; Found: C, 43.65 %; H, 4.11 %; N, 11.73 %; S, 9.07 %; ^{1}H NMR (600 MHz, D_2O): δ (ppm) 9.63 (s, 4H, Ar-H),), 9.45-9.27 (m, 4H, Ar-H), 9.03-8.78 (m, 4H, Ar-H), 4.52-4.41 (m, 16H, CH_2), 4.33 (d, *J* = 5.5 Hz 16H, CH_2), 3.22 (s, 12H, CH_3).

2.3.2.2 Synthesis of Schiff base morpholino phthalocyanines (3) – Scheme 3.3

The general procedure for the synthesis of neutral Schiff base morpholino phthalocyanines (**3-Zn** and **3-In**) is as follows: tetrakis[4-formylphenoxy]phthalocyaninato zinc(II) (**A**) [**165**] (0.2 g, 0.189 mmol) or tetrakis[4-formylphenoxy]phthalocyaninato indium(III) (**B**) [**166**] (0.2 g, 0.175 mmol) were added separately to dry tetrahydrofuran (THF, 20 mL). The precursor (4-(2-aminoethyl)morpholine, 4.4 eq) was added to the mixture, followed by stirring under reflux for 24 h. Thereafter, the mixtures were precipitated with ethanol, and the green products were washed with methanol and ethanol.

Quaternization of **3-Zn** and **3-In** to from **3-ZnQ** and **3-InQ** was as follows: Complex **3-Zn** (0.060 g; 0.040 mmol) and **3-In** (0.038 mmol) were separately mixed with methyl iodide (10 eq.) in dry dimethyl formamide (DMF, 5 mL). The mixtures were stirred in the dark for 4 h at 120 °C under inert conditions. The reaction mixtures were cooled to room temperature and precipitated with acetone and washed with diethyl ether. The solid products were separated by centrifugation and further washed with dichloromethane, and acetone and then air dried.

2(3),9(10),16(17),23(24)-Tetrakis(4-phenoxy(((2-(morpholino)ethyl)imino)methyl)) phthalocyaninato zinc (II) (3-Zn) **-** Yield: 31.6 % (0.09 g). UV–vis (DMSO): λ_{max} (nm) (log ε) 360 (4.08), 623 (3.86), 692 (4.74). FTIR (ATR), v/cm^{-1}: 3058 (C-H), 2991, 2896 (Aliph. C-H), 1650 (C=N), 1600 (C=C), 1448, 1368 (C-N), 1269 (Asym. C-O), 1164 (C-N), 1092 (C-O-C), 1049 (Sym. C-O), 862 (C=C). Elemental analysis: calc (%) for $C_{84}H_{80}N_{16}O_8Zn$: C 66.95 %; H 5.35 %; N 14.87 %, Found: C 66.09 %; H 4.62 %; N 14.27 %; ^{1}H NMR (600 MHz, DMSO-d_6): δ (ppm) 9.38 (s, 2H, -CH=N), 9.32 (s, 2H, -CH=N), 9.17 (d, *J* = 7.4 Hz, 8H, Ar-H), 9.12 - 9.04 (m, 4H, Ar-H), 8.80 – 8.67 (m, 4H, Ar-H), 8.17 (d, *J* = 9.3 Hz, 6H, Ar-H),), 7.79 – 7.67 (m, 6H, Ar-H), 3.99 – 3.92 (m, 16H, Aliph-H) 3.66 -3.59 (m, 16H, morpholine ring-H), 1.48 - 1.32 (m, 16H, morpholine ring-H). MS (MALDI-TOF): *m/z* cald =1504.56, found =1505.07 [M]$^+$.

2(3),9(10),16(17),23(24)-Tetrakis(4-phenoxy(((2-(morpholino)ethyl)imino)methyl))phthalocyaninato indium (III) chloride (3-In) **-** Yield: 46.7 % (0.13 g). UV–vis (DMSO): λ_{max} (nm) (log ε) 356 (4.10), 635 (3.66), 698 (4.69). FTIR (ATR), v/cm^{-1} 3069 (C-H), 2919, 2853 (Aliph. C-H), 1652 (C=N), 1598 (C=C), 1460, 1395 (C-N), 1227 (Asym. C-O), 1132 (C-N), 1078 (C-O-C), 1030 (Sym. C-O), 821 (C=C).Elemental analysis: calcd (%) for $C_{84}H_{80}ClInN_{16}O_8$: C 63.38 %; H

5.07 %; N 14.08 %, Found: C 62.60 %; H 5.34 %; N 13.65 %; ^{1}H NMR (600 MHz, DMSO-d_6): δ (ppm) 8.09 (s, 1H, -CH=N), 8.00 (s, 3H, -CH=N), 7.77 (dd, *J* = 8.2, 6.1 Hz, 8H, Ar-H), 7.65 – 7.59 (m, 6H, Ar-H), 7.29 (dd, *J* = 8.7, 2.4 Hz, 4H, Ar-H), 7.17 – 7.11 (m, 6H, Ar-H), 6.78 (d, *J* = 8.4 Hz, 4H, Ar-H), 3.83 – 3.22 (m, 16H, Aliph-H), 3.38 - 3.22 (m, 16H, morpholine ring-H), 3.11 (d, *J* = 4.8 Hz, 16H, morpholine ring-H).MS (MALDI-TOF): *m/z* cald =1590.51, found =1555.29 $[M\text{-}Cl]^+$.

2(3),9(10),16(17),23(24)-Tetrakis(4-phenoxy(((2-(N-methylmorpholino)ethyl)-imino)methyl))phthalocyaninato zinc (II) (3-ZnQ) **-** Yield: 76.3% (0.063 g). UV–vis (DMSO): λ_{max} (nm) (log ε) 361 (4.82), 612 (4.48), 680 (5.20). FTIR (ATR), v/cm^{-1} 3042 (C-H), 2991, 2907 (Aliph. C-H), 1664 (C=N), 1604 (C=C), 1442, 1372 (C-N), 1232 (Asym. C-O), 1102 (C-N), 1090 (C-O-C), 1052 (Sym. C-O), 881 (C=C). Elemental analysis: calcd (%) for $C_{88}H_{92}I_4N_{16}O_8Zn$: C 50.94 %; H 4.47 %; N 10.80 %, Found: C 49.59 %; H 4.08 %; N 10.92 %; ^{1}H NMR (600 MHz, DMSO-d_6): δ (ppm) 9.35 (s, 4H, -CH=N), .54 - 8.03 (m, 12H, Ar-H), 7.78 - 7.22 (m, 16H, Ar-H), 3.84 - 3.73 (m, 16H, Aliph-H), 2.78 (s, 12H, CH_3), 2.04 - 1.91 (m, 16H, morpholine ring-H), 1.31 (d, *J* = 6.3 Hz, 16H, morpholine ring-H). MS (MALDI-TOF): *m/z* cald =391.41, found =390.73 $[M]^{4+}$.

2(3),9(10),16(17),23(24)-Tetrakis(4-phenoxy(((2-(N-methylmorpholino)ethyl)-imino)methyl))phthalocyaninato indium (III) chloride (3-InQ) **-** Yield: 95.8% (0.078 g). UV–vis (DMSO): λ_{max} (nm) (log ε) 365 (4.74), 619 (4.44), 690 (5.06). FTIR (ATR), v/cm^{-1}: 3069 (C-H), 2925, 2853 (Aliph. C-H) 1646 (C=N), 1605 (C=C), 1455, 1395 (C-N), 1233 (Asym. C-O), 1132 (C-N), 1084 (C-O-C), 1066 (Sym. C-O), 892 (C=C). Elemental analysis: calcd (%) for $C_{88}H_{92}ClI_4InN_{16}O_8$: C 48.94 %; H 4.29 %; N 10.38 %, Found: C 49.47 %; H 3.51 %; N 9.75 %; ^{1}H NMR (600 MHz, DMSO-d_6): δ (ppm) 9.33 (s, 4H, -CH=N), 8.60 – 7.62 (m, 16H, Ar-H), 7.35 – 6.76 (m, 12H, Ar-H),

3.86 - 3.73 (m, 16H, Aliph-H), 2.77 (s, 12H, CH_3), 2.03 (d, *J* = 8.2 Hz, 16H, morpholine ring-H), 1.44 - 1.10 (m, 16H, morpholine ring-H). MS (MALDI-TOF): *m/z* cald =412.55, found = 414.44 $[M+1H]^{4+}$.

2.3.2.3 Syntheses of Schiff base pyrrolidine phthalocyanines (4 and 5) – Scheme 3.4

The synthesis of neutral phthalocyanines **4-Zn**, **4-In**, **5-Zn**, and **5-In** was completed as follows; complex **A** (0.2 g, 0.189 mmol) or complex **B** (0.2 g, 0.175 mmol) were added separately to dry tetrahydrofuran (THF, 20 mL) containing the precursors (1-(2-aminoethyl)pyrrolidine or 1-(3-aminopropyl)pyrrolidine, 4.5 eq). The mixtures were stirred under reflux for 24 h. After cooling, the resulting mixtures were precipitated out with ethanol, and the crude solid was washed with methanol and ethanol.

Quaternization for **4-ZnQ**, **4-InQ**, **5-ZnQ**, and **5-InQ** was done as follows; the metallophthalocyanine (0.060 g; 0.042 mmol for **4-Zn**, 0.039 mmol for **4-In**, 0.040 mmol for **5-Zn** and 0.038 mmol for **5-In**) and methyl iodide (10 eq.) were mixed in 5 mL of dry dimethylformamide (DMF). The mixtures were stirred in the dark for 4 h at 120 °C under inert conditions. The reaction mixtures were cooled to room temperature and precipitated and washed with diethyl ether. The solid products were separated by centrifugation, washed with dichloromethane, and then air dried.

2(3),9(10),16(17),23(24)-Tetrakis(4-phenoxy(((2-(pyrrolidin-1-yl)ethyl)imino) methyl))phthalocyaninato zinc (II) (4-Zn) - Yield: 48.1 % (0.13 g). UV–vis (DMSO): λ_{max} (nm) (log ε) 362 (4.68), 615 (4.29), 681 (4.88). FTIR (ATR), v/cm^{-1}: 3092 (Ar C-H), 2924 (Aliph. C-H), 2884 (Aliph. C-H), 1653 (C=N), 1598 (C=C), 1475–1393 (C-C), 1229 (Asymm. Ar-O), 1163 (C-N), 1088 (C-N), 1037 (Symm. Ar-O), 830. Elemental analysis: calc (%) for $C_{84}H_{80}N_{16}O_4Zn$: C 69.92 %; H 5.59 %; N 15.53 %, Found: C

69.64 %; H 4.70 %; N 14.68 %; ^{1}H NMR (600 MHz, DMSO-d_6): δ (ppm) 9.37 (s, 2H, -CH=N), 9.30 (s, 2H, -CH=N), 8.88 - 8.67 (m, 4H, Ar-H), 8.12 - 7.73 (m, 8H, Ar-H), 7.56 – 7.31 (m, 16H, Ar-H), 2.88 - 2.73 (m, 8H, Aliph-H), 2.46 - 2.19 (m, 24H, pyrrolidone ring-H and Aliph-H), 1.78 (d, *J* = 7.9 Hz,16H, pyrrolidone ring-H). MS (MALDI-TOF): *m/z* calc =1440.58, found =1440.86 $[M]^+$.

***2(3),9(10),16(17),23(24)-Tetrakis(4-phenoxy(((2-(pyrrolidin-1-yl)ethyl)imino) methyl))phthalocyaninato indium(III)* chloride (4-In)** - Yield: 37.4 % (0.10 g). UV–vis (DMSO): λ_{max} (nm) (log ε) 357 (4.66), 627 (4.34), 696 (4.84). FTIR (ATR), v/cm^{-1}: 3009 (Ar C-H), 2961 (Aliph. C-H), 2884 (Aliph. C-H), 1658 (C=N), 1597 (C=C), 1472–1396 (C-C), 1231 (Asymm. Ar-O), 1163 (C-N), 1087 (C-N), 1046 (Symm. Ar-O), 833. Elemental analysis: calc (%) for $C_{84}H_{80}ClInN_{16}O_4$: C 66.03 %; H 5.28 %; N 14.67 %, Found: C 65.03 %; H 5.03 %; N 13.62 %; ^{1}H NMR (600 MHz, DMSO-d_6): δ (ppm) 9.27 (s, 2H, -CH=N), 8.84 (s, 2H, -CH=N), 8.14 - 7.82 (m, 12H, Ar-H), 7.62 - 7.35 (m, 16H, Ar-H), 4.59 (d, *J* = 8.3 Hz, 8H, Aliph-H), 1.28 (d, *J* = 4.7 Hz, 16H, pyrrolidone ring-H) 1.13 - 1.04 (m, 8H, Aliph-H), 0.96 - 0.67(m, 16H, pyrrolidone ring-H). MS (MALDI-TOF): *m/z* calc =1526.5, found =1527.36 $[M]^+$, 1492.22 $[M\text{-}Cl]^+$.

2(3),9(10),16(17),23(24)-Tetrakis(4-phenoxy(((3-(pyrrolidin-1-yl)propyl)imino) methyl))phthalocyaninato zinc(II) (5-Zn) - Yield: 38.8 % (0.11 g). UV–vis (DMSO): λ_{max} (nm) (log ε) 346 (4.58), 614 (4.32), 682 (4.96). FTIR (ATR), v/cm^{-1}: 3085 (Ar C-H), 2918 (Aliph. C-H), 2853 (Aliph. C-H), 1655 (C=N), 1592 (C=C), 1466–1388 (C-C), 1225 (Asymm. Ar-O), 1161 (C-N), 1085 (C-N), 1039 (Symm. Ar-O), 825. Elemental analysis: calc (%) for $C_{88}H_{88}N_{16}O_4Zn$: C 70.50 %; H 5.92 %; N 14.95 %, Found: C 69.07 %; H 5.06 %; N 14.28 %; ^{1}H NMR (600 MHz, DMSO-d_6): δ (ppm) 9.36 (s, 2H, -CH=N), 8.78 (s, 2H, -CH=N), 7.89 (d, *J* = 12.2 Hz, 12H, Ar-H), 7.65 - 7.30 (m, 16H,

Ar-H), 4.62 (d, *J* = 6.0 Hz, 8H, Aliph-H), 2.01 – 1.86 (m, 8H, Aliph-H 1.75-1.65 (m, 16H, pyrrolidone ring-H), 1.29 (dd, *J* = 4.2, 3.8 Hz, 16H, pyrrolidone ring-H), 0.93-0.83 (m, 8H, Aliph-H). MS (MALDI-TOF): *m/z* calc =1496.65, found =1496.14 $[M]^+$.

2(3),9(10),16(17),23(24)-Tetrakis(4-phenoxy(((3-(pyrrolidin-1-yl)propyl)imino) methyl))phthalocyaninato indium(III) chloride (5-In) - Yield: 43.3% (0.12 g). UV–vis (DMSO): λ_{max} (nm) (log ε) 358 (4.68), 623 (4.36), 697 (4.82). FTIR (ATR), v/cm^{-1}: 3092 (Ar C-H), 2927 (Aliph. C-H), 2860 (Aliph. C-H), 1655 (C=N), 1593 (C=C), 1468–1393 (C-C), 1226 (Asymm. Ar-O), 1162 (C-N), 1085 (C-N), 1043 (Symm. Ar-O), 826. Elemental analysis: calc (%) for $C_{88}H_{88}ClInN_{16}O_4$: C 66.73 %; H 5.60 %; N 14.15 %, Found: C 65.47 %; H 5.34 %; N 13.69 %; ^{1}H NMR (600 MHz, DMSO-d_6): δ (ppm) 9.37 (s, 2H, -CH=N), 9.29 (s, 2H, -CH=N 8.90 – 8.63 (m, 4H, Ar-H), 7.89 – 7.80 (m, 8H, Ar-H), 7.55 – 7.30 (m, 16H, Ar-H), 4.66 - 4.42 (m, 8H, Aliph-H), 2.82 - 2.73 (m, 8H, Aliph-H), 1.87 – 1.74 (m, 16H, pyrrolidone ring-H), 1.29 (dd, *J* = 4.8,1.0 Hz, 16H, pyrrolidone ring-H), 0.97-0.80 (m, 8H, Aliph-H). MS (MALDI-TOF): *m/z* calc =1582.59, found =1547.47 $[M-Cl]^+$,1582.29 $[M]^+$.

2(3),9(10),16(17),23(24)-Tetrakis(4-phenoxy(((2-(N-methylpyrrolidin-1-yl)ethyl)imino)methyl))phthalocyaninato zinc(II) (4-ZnQ) - Yield: 85.3 % (0.072 g). UV–vis (DMSO): λ_{max} (nm) (log ε) 357 (4.52), 614 (4.28), 678 (4.79). FTIR (ATR), v/cm^{-1}: 3104 (Ar C-H), 2961 (Aliph. C-H), 2924 (Aliph. C-H), 1655 (C=N), 1603 (C=C), 1466–1386 (C-C), 1234 (Asymm. Ar-O), 1163 (C-N), 1091 (C-N), 1028 (Symm. Ar-O), 832. Elemental analysis: calc (%) for $C_{88}H_{92}I_4N_{16}O_4Zn$: C 52.53 %; H 4.61 %; N 11.15 %, Found: C 51.84 %; H 5.45 %; N 11.31 %; ^{1}H NMR (600 MHz, DMSO-d_6): δ (ppm) 9.36 (s, 2H, -CH=N), 9.28 (s, 2H, -CH=N 8.91 – 8.65 (m, 6H, Ar-H), 7.81 (dd, *J* = 10.2, 5.9 Hz, 8H, Ar-H), 7.64 – 7.24 (m, 14H, Ar-H), 3.57 (s, 12H, -CH_3), 2.81 (d, *J* = 4.5 Hz,

8H, Aliph-H), 2.38 (t, *J* = 6.6 Hz, 24H, pyrrolidone ring-H and Aliph-H), 1.78 (dd, *J* = 6.2, 1.2 Hz, 16H, pyrrolidone ring-H). MS (MALDI-TOF): *m/z* calc =375.17, found =373.54 $[M-H]^{4+}$.

***2(3),9(10),16(17),23(24)-Tetrakis(4-phenoxy(((2-(N-methylpyrrolidin-1-yl)ethyl)imino)methyl))phthalocyaninato indium(III)* chloride (4-InQ)** - Yield: 93.1 % (0.075 g). UV–vis (DMSO): λ_{max} (nm) (log ε) 360 (4.71), 627 (4.38), 691 (4.88). FTIR (ATR), v/cm^{-1}: 3114 (Ar C-H), 2948 (Aliph. C-H), 2898 (Aliph. C-H), 1656 (C=N), 1589 (C=C), 1474–1396 (C-C), 1231 (Asymm. Ar-O), 1148 (C-N), 1098 (C-N), 1044 (Symm. Ar-O), 846.Elemental analysis: calc (%) for $C_{88}H_{92}ClI_4InN_{16}O_4$: C 50.44 %; H 4.43 %; N 10.69 %, Found: C 50.08 %; H 3.46 %; N 10.59 %; ^{1}H NMR (600 MHz, DMSO-d_6): δ (ppm) 9.34 (s, 3H, -CH=N), 8.83 (s, 1H, -CH=N 8.07 - 7.84 (m, 12H, Ar-H), 7.63 - 7.37 (m, 16H, Ar-H), 4.75 - 4.45 (m, 8H, Aliph-H), 2.30 (s, 12H, CH_3), 1.80 (t, *J* = 5.8 Hz, 8H, Aliph-H), 1.63 - 1.42 (m, 32H, pyrrolidone ring-H). MS (MALDI-TOF): *m/z* calc =396.65, found =361.44 $[M-Cl]^{4+}$, 397.05 $[M]^{4+}$.

2(3),9(10),16(17),23(24)-Tetrakis(4-phenoxy(((3-(N-methylpyrrolidin-1-yl)propyl)imino)methyl))phthalocyaninato zinc(II) (5-ZnQ) - Yield: 82.2 % (0.068 g). UV–vis (DMSO): λ_{max} (nm) (log ε) 362 (4.59), 614 (4.38), 679 (4.92). FTIR (ATR), v/cm^{-1}: 3104 (Ar C-H), 2955 (Aliph. C-H), 2923 (Aliph. C-H), 1647 (C=N), 1560 (C=C), 1456–1399 (C-C), 1233 (Asymm. Ar-O), 1147 (C-N), 1046 (C-N), 1012 (Symm. Ar-O), 848. Elemental analysis: calc (%) for $C_{92}H_{100}I_4N_{16}O_4Zn$: C 53.46 %; H 4.88 %; N 10.84 %, Found: C 53.06 %; H 4.08 %; N 10.92 %; ^{1}H NMR (600 MHz, DMSO-d_6): δ (ppm) 8.93 (s, 2H, -CH=N), 8.80 (s, 2H, -CH=N), 8.07 - 7.82 (m, 12H, Ar-H), 7.72 - 7.14 (m, 16H, Ar-H), 4.76 - 4.36 (m, 8H, Aliph-H), 2.80 (s, 12H, CH_3), 1.98 – 1.70 (m, 16H, Aliph-H), 1.37 - 1.10 (m, 16H, pyrrolidone ring-H), 0.95 – 0.68 (m, 16H, pyrrolidone ring-H).MS (MALDI-TOF): *m/z* calc =389.68, found =389.25 $[M]^{4+}$.

2(3),9(10),16(17),23(24)-Tetrakis(4-phenoxy(((3-(N-methylpyrrolidin-1-yl)propyl)imino)methyl))phthalocyaninato indium(III) chloride (5-InQ) - Yield: 86.8% (0,071 g). UV–vis (DMSO): λ_{max} (nm) (log ε) 359 (4.64), 628 (4.31), 691 (4.89). FTIR (ATR), v/cm^{-1}: 3108 (Ar C-H), 2954 (Aliph. C-H), 2923 (Aliph. C-H), 1658 (C=N), 1597 (C=C), 1504–1395 (C-C), 1234 (Asymm. Ar-O), 1174 (C-N), 1088 (C-N), 1046 (Symm. Ar-O), 842. Elemental analysis: calc (%) for $C_{92}H_{100}ClI_4InN_{16}O_4$: C 51.35 %; H 4.68 %; N 10.42 %, Found: C 51.82 %; H 3.19 %; N 10.24 %; ^{1}H NMR (600 MHz, DMSO-d_6): δ (ppm) 9.36 (s, 2H, -CH=N), 9.29 (s, 2H, -CH=N), 8.88 - 8.69 (m, 4H, Ar-H), 7.91 (dd, *J* = 8.7, 4.8 Hz, 8H, Ar-H), 7.66 - 7.24 (m, 16H, Ar-H),), 4.64 (d, *J* = 5.6 Hz, 8H, Aliph-H), 2.83 - 2.73 (m, 8H, Aliph-H), 2.41 (s, 12H, CH_3), 1.68 (d, *J* = 4.4 Hz, 16H, pyrrolidone ring-H), 1.42 - 1.20 (m, 16H, pyrrolidone ring-H), 0.93 – 0.64 (m, 8H, Aliph-H). MS (MALDI-TOF): *m/z* calc =410.67, found =412.71 $[M+2H]^{4+}$.

2.3.2.4 General synthesis of tris benzothiazole phthalocyanine (6-Zn, 6-In, 6-ZnQ and 6-InQ) – Scheme 3.5

The neutral (**6-Zn and 6-In**) and quaternized (**6-ZnQ**, **6-InQ**) phthalocyanines were synthesized by a mixed condensation reaction. For neutral Pcs **6-Zn** and **6-In**, a mixture of 4-(benzo[*d*]thiazol-2-ylthio)phthalonitrile (**i**) (0.40 g, 1.36 mmol), 4-(3,4-dicyanophenoxy)benzoic acid (**ii**) (0.0388 g, 0.15 mmol), dry zinc(II) acetate (0.112 g, 0.5 mmol, for Pc **6-Zn**) or indium(III) chloride (0.113 g, 0.51 mmol, for Pc **6-In**) and DBU (0.5 mL) in 5 mL 1-pentanol was heated at reflux temperature for 12 h under inert conditions. The neutral Pcs (**6-Zn**, **6-In**) were precipitated in methanol, and the precipitated products were further washed with methanol and ethyl acetate. Pcs **6-Zn** and **6-In** were purified using column chromatography with chloroform:methanol mixture (9:1, v:v) as an eluent to give green products. The cationic Pcs **6-ZnQ** and **6-InQ** were synthesized following the same procedure as **6-Zn** and **6-In**, but using

phthalonitriles (**v**) (0.40 g, 1.30 mmol), (**i**) (0.0368 g, 0.14 mmol), dry zinc(II) acetate (0.107 g, 0.49 mmol, for **6-ZnQ**) or indium(III) chloride (108 mg, 0.49 mmol for **6-InQ**). The quaternized Pcs (**6-ZnQ**, **6-InQ**) were however precipitated out using acetone, the products were washed with acetonitrile through centrifugation and then air-dried.

2-(4-carboxyphenoxy)-9(10),16(17),23(24)-tris(benzo[d]thiazol-2-ylthio)phthalocyaninato zinc(II) (6-Zn) - Yield: 47.8 % (0.22 g). UV–vis (DMSO): λ_{max} (nm) (log ε) 352 (4.48), 615 (4.16), 683 (5.08). FTIR (ATR), v/cm^{-1}: 3393 (O-H stretch), 2928, 2851 (Ar-H), 1711 (C=O), 1597 (C=N), 1456 (Ar C=C), 1228(C-S), 1089 (Ar C-H), 788 (C-S). Elemental analysis: calc (%) for $C_{60}H_{29}N_{11}O_3S_6Zn.2H_2O$: C 57.85 %; H 2.65 %; N 12.38 %, S 15.42 %, Found: C 57.58 %; H 2.15 %; N 12.40 %; S 15.39 % ; ^{1}H NMR (400 MHz, DMSO-d_6): δ (ppm) 11.58 (s, 1H), 9.14-8.89 (m, 6H, Ar-H), 8.36 (d, *J* = 8.7 Hz, 4H, Ar-H), 8.07 (d, *J* = 6.9 Hz, 4H, Ar-H), 7.96-7.83 (m, 8H, Ar-H), 7.40 (dd, *J* = 8.9, 3.6 Hz, 6H, Ar-H). MS (MALDI-TOF): *m/z* calc =1207.01, found =1208.11 $[M+H]^+$.

2-(4-carboxyphenoxy)-9(10),16(17),23(24)-tris(benzo[d]thiazol-2-ylthio)phthalocyaninato indium(III) chloride (6-In) - Yield: 35.7 % (0.18 g). UV–vis (DMSO): λ_{max} (nm) (log ε) 352 (4.48), 615 (4.16), 683 (5.08). FTIR (ATR), v/cm^{-1}: 3395 (O-H stretch), 2923, 2853 (Ar-H stretch), 1713 (C=O), 1579 (C=N), 1421 (Ar C=C), 1239 (C-S), 1081 (Ar C-H), 757 (C-S). Elemental analysis: calc (%) for $C_{60}H_{29}ClInN_{11}O_3S_6.2H_2O$: C 54.16 %; H 2.48 %; N 11.58 %, S 14.43 %, Found: C 54.59 %; H 2.07 %; N 10.85 %; S 13.33 %; ^{1}H NMR (400 MHz, DMSO-d_6): δ (ppm) 11.49 (s, 1H), 9.14-8.89 (m, 6H, Ar-H), 8.36 (d, *J* = 8.7 Hz, 4H, Ar-H), 8.07 (d, *J* = 6.9 Hz, 4H, Ar-H), 7.96-7.83 (m, 8H, Ar-H), 7.40 (dd, *J* = 8.9, 3.6 Hz, 6H, Ar-H). MS (MALDI-TOF): *m/z* calc = 1292.95, found = 1293.05 $[M]^+$.

2-(4-carboxyphenoxy)-9(10),16(17),23(24)-tris(benzo[d]thiazol-2-ylthio)phthalocyaninato zinc(II) (6-ZnQ) - Yield: 32.7 % (0.16 g). UV–vis (DMSO): λ_{max} (nm) (log ε) 333 (4.53), 615 (4.35), 682 (5.22). FTIR (ATR), v/cm^{-1}: 3408 (O-H stretch), 2923, 2857 (Ar-H stretch), 1713 (C=O), 1603 (C=N), 1464 (Ar C=C), 1289.8 (CH_3), 1228 (C-S), 1087 (Ar C-H), 786.2 (C-S). Elemental analysis: calc (%) for $C_{63}H_{38}N_{11}O_3S_6I_3Zn$: C 46.27 %; H 2.34 %; N 9.42 %, S 11.76 %, Found: C 46.61 %; H 1.71 %; N 10.31 %; S 10.35 %; ^{1}H NMR (400 MHz, DMSO-d_6): δ (ppm) 9.40 (dd, *J* = 8.0, 5.8 Hz, 5H, Ar-H), 9.17 (dd, *J* = 6.8, 3.6 Hz, 6H, Ar-H), 8.91-8.90 (m, 5H, Ar-H), 8.23 (dd, *J* = 6.5, 3.0 Hz, 6H, Ar-H), 7.83 (d, *J* = 4.4 Hz, 6H, Ar-H), 3.71 (s, 9H, CH_3). MS (MALDI-TOF): *m/z* calc = 417.36, found = 420.48 $[M+3H]^{3+}$.

2-(4-carboxyphenoxy)-9(10),16(17),23(24)-tris(benzo[d]thiazol-2-ylthio)phthalocyaninato indium(III) chloride (6-InQ) - Yield: 30.4 % (0.17 g). UV–vis (DMSO): λ_{max} (nm) (log ε) 370 (4.49), 625 (4.11), 695 (5.14). FTIR (ATR), v/cm^{-1}: 3412 (O-H stretch), 2929, 2857 (Ar-H stretch), 1707 (C=O), 1603 (C=N), 1432 (Ar C=C), 1256 (CH_3), 1218 (C-S), 1075 (Ar C-H), 744 (C-S). Elemental analysis: calc (%) for $C_{63}H_{38}ClI_3InN_{11}O_3S_6$: C 43.98 %; H 2.23 %; N 8.96 %, S 11.18 %, Found: C 43.09 %; H 2.70 %; N 9.49 %; S 10.74 %; ^{1}H NMR (400 MHz, DMSO-d_6): δ (ppm) 8.57 (d, *J* = 3.5 Hz, 3H, Ar-H 8.24-8.20 (m, 8H, Ar-H), 8.10 (d, *J* = 5.8 Hz, 4H, Ar-H), 7.98 (d, *J* = 6.1 Hz, 4H, Ar-H), 7.56-7.54 (m, 4H, Ar-H), 7.48 (t, *J* = 6.0 Hz, 5H, Ar-H), 3.39 (s, 9H, CH_3). MS (MALDI-TOF): *m/z* calc = 446.01, found = 446.07 $[M]^{3+}$.

2.3.2.5 General synthesis procedure of the tris morpholino phthalocyanines (7) – Scheme 3.6

Neutral tris morpholino phthalocyanines **7-Zn** and **7-In** were synthesized as follows; in two separate round bottomed flasks, phthalonitriles (**ii**) (0.2 g, 0.94 mmol) and (**v**) (0.058 g, 0.22 mmol) were dissolved in n-pentanol (3 mL). The temperature of the mixtures was increased to 90 °C, followed by stirring for 30 min. $InCl_3$, (0.046 g, 0.36 mmol) and $Zn(OAc)_2$, (0.066 g, 0.36 mmol) were added separately to each flask together with DBU (0.3 mL, 2 mmol). The reaction mixtures were stirred for 8 h at 138 °C under inert conditions. The mixtures were then cooled to room temperature and poured into a water: methanol mixture (1:1, v:v). The precipitates were filtered and air-dried. Purification of the green crude products was achieved by column chromatography using silica gel as the stationary phase (mobile phase: dichloromethane (DCM) - methanol (9:1)).

Cationic phthalocyanines **7-ZnQ** and **7-InQ** were quaternized as follows; complexes **7-Zn** or **7-In** (0.020 g, 0.02 mmol or 0.018 mmol) and 5.05 mmol of dimethyl sulphate were mixed in 3 mL of dry DMF. The mixtures were stirred for 4 h at 155 °C under inert conditions. Then, the mixtures were cooled to room temperature and poured into a acetone: methanol (1:1, v: v) mixture. The products were filtered and washed with chloroform and diethyl ether.

2-(4-carboxyphenoxy)- 9(10),16(17),23(24)-tris(morpholino)phthalocyaninato zinc(II) (7-Zn) - Yield: 24.0 % (0.041 g). UV-Vis (DMSO), λ_{max} (nm) (log ε): 362 (4.91), 641 (4.66), 710 (5.27). FTIR (ATR), v/cm^{-1}: 3331 (O-H), 3072 (Ar-H), 2920 and 2857 (Al-H), 1702 (C=O), 1601, 1484, 1463 (C=C, C=N), 1237,1091 (C-O-C). Elemental analysis: calc (%) for $C_{51}H_{41}N_{11}O_6Zn$: C 63.19 %; H 4.26 %; N 15.90 %, Found: C 62.29 %; H 3.34 %; N 14.19 %; ^{1}H-NMR (600 MHz, DMSO-d_6): δ (ppm) 9.25 (dd, *J* =

8.6, 7.2 Hz, 4H, Ar-H), 9.08-8.88 (m, 4H, Ar-H), 8.25-8.05 (m, 8H, Ar-H), 4.08 (t, *J* = 5.9 Hz, 12H, $-CH_2$), 3.76 (t, *J* = 4.3 Hz, 12H, $-CH_2$); MALDI-TOF (*m/z*) calc = 967.25; found = 968.37$[M+1]^+$.

2-(4-carboxyphenoxy)- 9(10),16(17),23(24)-tris(morpholino)phthalocyaninato indium(III) chloride (7-In) **-** Yield: 17.0 % (0.033 g). UV-Vis (DMSO), λ_{max} (nm) (log ε): 378 (4.91), 656 (4.53), 727 (5.11). FTIR(ATR) v/cm^{-1}: 3377 (O-H), 3062 (Ar-H), 2952 and 2856 (Al-H), 1709 (C=O), 1600, 1489, 1444 (C=C, C=N), 1234, 1091 (C-O-C). Elemental analysis: calc (%) for $C_{51}H_{41}ClInN_{11}O_6$: C 58.11 %; H 3.92 %; N 14.62 %, Found: C 59.37 %; H 3.50 %; N 14.43 %; ^{1}H-NMR (600 MHz, DMSO-d_6) δ (ppm) 9.11 (dd, *J* = 7.4, 1.4 Hz, 4H, Ar-H), 9.02-8.86 (m, 4H, Ar-H), 8.63-8.49 (m, 5H, Ar-H), 8.25-8.17 (m, 3H, Ar-H), 4.21 (t, *J* = 5.0 Hz, 12H, $-CH_2$), 3.87 (t, 12H, $-CH_2$); MALDI-TOF (*m/z*): calc = 1053.20; found = 1054.08$[M+1]^+$.

2-(4-carboxyphenoxy)-9(10),16(17),23(24)-tris(N-methylmorpholino)phthalocyaninato zinc(II) (7-ZnQ) - Yield: 78% (0.035 g). UV-Vis (DMSO), λ_{max} (nm) (log ε): 368 (4.96), 610 (4.86), 675 (5.31). FTIR (ATR), v/cm^{-1}: 3373 (O-H), 3055 (Ar-H), 2958 and 2856 (Al-H), 1701 (C=O), 1599, 1484(C=C, C=N), 1229, 1090 (C-O-C). Elemental analysis: calc (%) for $C_{57}H_{59}N_{11}O_{18}S_3Zn$: C 50.80 %; H 4.41 %; N 11.43 %, Found: C 49.23 %; H 3.70 %; N 9.67 %; ^{1}H-NMR (600 MHz, D_2O) δ (ppm): 8.45 (d, *J* = 9.0 Hz, 4H, Ar-H), 8.50-8.30 (m, 4H, Ar-H), 8.28-8.10 (m, 8H, Ar-H), 4.11 (t, *J* = 5.2 Hz, 12H, $-CH_2$), 3.88 (t, *J* = 4.8 Hz, 12H, $-CH_2$), 3.22 (s, 9H, $-CH_3$).

2-(4-carboxyphenoxy)-9(10),16(17),23(24)-tris(N-methylmorpholino)phthalocyaninato indium(III) chloride (7-InQ) - Yield: 70% (0.027 g). UV-Vis (DMSO), λ_{max} (nm) (log ε): 374 (4.98), 622 (4.89), 689 (5.19).

FTIR(ATR), v/cm^{-1}: 3373 (O-H), 3040 (Ar-H), 2922 and 2853 (Al-H), 1695 (C=O), 1584, 1487, 1462 (C=C, C=N), 1221, 1079 (C-O-C). Elemental analysis: calc (%) for $C_{57}H_{59}ClInN_{11}O_{18}S_3$: C 47.79 %; H 4.15 %; N 10.79 %, Found: C 47.48 %; H 3.82 %; N 9.16 %; ^{1}H-NMR (600 MHz, D_2O) δ (ppm): 8.52 (m, 5H, Ar-H), 8.36 (dd, *J* = 6.0, 4.2 Hz, 3H, Ar-H), 8.38-8.22 (m, 6H, Ar-H), 8.06 (s, 2H, Ar-H), 4.21 (t, *J* = 5.8 Hz, 12H, $-CH_2$), 3.81 (t, *J* = 5.5 Hz, 12H, $-CH_2$), 3.68 (s, 9H, $-CH_3$).

2.3.3 Synthesis of APTES capped ZnONPs and covalent conjugation to Pcs

The synthesis of bare ZnONSps and ZnONPys were synthesized as reported in literature [**169**, **170**].

2.3.3.1 APTES capped ZnO nanoparticles, Scheme 3.7

The synthesis of APTES functionalized zinc oxide nanoparticles was achieved using the previously reported method [**173**] with modification. Typically, ZnONSps or ZnONPys (1.0 g each) were mixed with ethanol (40 mL), and the mixtures were stirred at room temperature for 20 min. Then, APTES (0.1 g, 0.45 mmol) was added to the mixtures followed by the addition of ethanol (65 mL) and water (45 mL), and the mixtures were left to stir at 24 °C for 7 h. The yellowish solutions were centrifuged at 4000 rpm, and then the pellet was washed several times with ethanol and dried at 80 °C overnight producing NH_2-ZnONSps and NH_2-ZnONPys.

2.3.3.2 Amide linkage of Pc complexes (6) to NH_2-ZnONPs, Scheme 3.8

The conjugation of phthalocyanine complexes (**6-Zn, 6-In, 6-ZnQ and 6-InQ**) to NH_2-ZnONSps and NH_2-ZnONPys was carried out as follows: Pc (**6-Zn**: 0.038 g, 0.03 mmol; **6-In**: 0.039 g, 0.03 mmol; **6-ZnQ**: 0.049 g, 0.03 mmol; **6-InQ**: 0.052 g, 0.03 mmol) were weighed into four separate flasks. Then, DMF (2 mL) and DCC (0.017 g,

0.082 mmol) were added to each flask. The reaction mixtures were allowed to stir for 24 h at room temperature. This was followed by addition of solutions of NH_2-ZnONSps or NH_2-ZnONPys (0.040 g each in DMF), followed by stirring for 48 h at room temperature. The milky green solutions were centrifuged at 4000 rpm and washed with methanol, THF, and ethanol. The conjugates were air-dried and are represented as **6-Zn**-ZnONSps, **6-In**-ZnONSps, **6-ZnQ**-ZnONSps, **6-InQ**-ZnONSps, **6-Zn**-ZnONPys, **6-In**-ZnONPys, **6-ZnQ**-ZnONPys and **6-InQ**-ZnONPys, with NH_2 left out from the ZnONPs for simplicity.

2.3.4 Synthesis of glass wool functionalization and covalent conjugation to Pcs

The introduction amino moiety on the glass wool is described below, the amino functionalization glass wool was then covalently linked to **7-Zn**, **7-ZnQ**, **7-In**, **7-InQ, 8-Zn**, **9-Zn**, and **10-Zn**. The synthesis of **88-Zn**, **9-Zn**, and **10-Zn** has been reported [**51**, **52**].

2.3.4.1 Glass wool functionalization, Scheme 3.9

A clean and clear 250 mL round-neck bottom flask was initially coated with APTES by adding 10% APTES in 200 mL HPLC grade toluene, and this solution was refluxed at 110 ºC for 18 h. The solution was decanted, and the milky round bottom flask was rinsed with toluene and acetone and dried in the oven. This promotes an interaction between the glass ware and APTES before reacting with GW, and this step is essential as it will increase the chances of the APTES interacting with GW rather than the glassware.

Then, to three pretreated round bottom flasks containing 200 mL of high-performance liquid chromatography grade toluene, GW (1.00 g) was added, followed by 2, 4, and

8 mL of APTES. The mixtures were refluxed at 110 °C for 18 h. The resulting APTES functionalized glass wools (GW-APTES) were vacuum filtered, washed with toluene and acetone, and dried in the oven at 100 °C overnight. The resulting glass wools are represented as GW-2-APTES, GW-4-APTES, and GW-8-APTES, for 2, 4, or 8 mL APTES.

2.3.4.2 Pc-GW conjugate synthesis, Scheme 3.10

APTES-GW (also referred to as GW-4-APTES, the reason for this choice will be discussed later) was conjugated to **7-Zn**, **7-ZnQ**, **7-In**, **7-InQ, 8-Zn**, **9-Zn**, and **10-Zn** via an amide bond. The Pcs (**7-Zn** (7.8 mg, 0.008 mmol), **7-In** (8.4 mg, 0.008 mmol), **7-ZnQ** (11.2 mg, 0.008 mmol), or **7-InQ** (11.8 mg, 0.008 mmol), **8-Zn** (5.7 mg, 0.008 mmol), **9-Zn** (8.9 mg, 0.008 mmol), **10-Zn** (10 mg, 0.008 mmol)), and DCC ((2.4 mg, 0.012 mmol, for **7-Zn**, **7-ZnQ**, **7-In**, **7-InQ**, and **8-Zn**), (9.7 mg, 0.048 mmol, for **9-Zn**) and (19.4 mg, 0.096 mmol, for **10-Zn**) were dispersed in dry DMF (5 mL) and stirred at room temperature for 24 h. After this time, the activated MPcs were separately added to beakers containing APTES-4-GW (100 mg) immersed in dry DMF (10 mL). The mixtures were stirred at room temperature for 72 h. Then, the reaction mixtures were filtered under a vacuum, and the glass wool was washed with methanol, THF, water, and acetone; and dried in the oven. The glass wool was further purified on a Soxhlet extractor using water to remove any unbound MPcs producing, **7-Zn-GW**, **7-ZnQ-GW**, **7-In-GW**, and **7-InQ-GW**, **8-Zn-GW**, **9-Zn-GW**, and **10-Zn-GW**.

2.3.5 Synthesis of functionalized polymer, chitosan-polymer and phthalocyanine-polymer conjugates

Carboxylic-functionalized polyacrylonitrile (**PAN-COOH**) was prepared according to literature [171].

2.3.5.1 Synthesis of amino-functionalized polymer (PAN-NH_2), Scheme 3.11

Amino-functionalized **PAN** (**PAN-NH_2**) was produced by forming an amide bond linkage between **PAN-COOH** and hydrazine as follows: **PAN-COOH** (0.25 g), EDC (0.3 g, 1.9 mmol), NHS (0.3 g, 2.6 mmol), and hydrazine (0.5 mL, 15 mmol) were dispersed in DMF (10 mL) and stirred at room temperature for 48 h. The resultant mixture was precipitated out in water, filtered, and washed with methanol to give **PAN-NH_2**.

2.3.5.2 Synthesis of polyacrylonitrile-chitosan conjugate (PAN-CS), Scheme 3.11

PAN-Chitosan (**PAN-CS**) conjugate was synthesized through a formation of an amide bond. **PAN-COOH** (0.5 g) and DCC (0.15 g, 0.7 mmol) were dissolved in dry DMF (10 mL) under nitrogen, and then chitosan (0.1 g) dispersed in DMF (5 mL) was carefully added. The solution was stirred at room temperature under nitrogen for 72 h. The product was filtered, and the filtrate was evaporated in a rotary evaporator. The residue was precipitated with diethyl ether, filtered, and washed with methanol.

2.3.5.3 Synthesis of Pc conjugates, Scheme 3.12

The conjugation of phthalocyanines to **PAN-NH_2** and **PAN-CS** was performed with modifications as previously described [174]. To form **Pc-PAN**, reaction mixtures containing 0.020 g each of (complex **7-Zn** (0.021 mmol) or complex **7-ZnQ** (0.014 mmol) or complex **7-In**, (0.019 mmol) or complex **7-InQ** (0.014 mmol)), DCC (0.0103 mg, 0.05 mmol) and NHS (0.0103 mg, 0.09 mmol) were prepared in dry DMF (5 mL), followed by stirring at room temperature for 24 h. A solution of **PAN-NH_2** (0.5 g) in 5 mL DMF was carefully added and the reaction was allowed to continue for a further 48 h. For **Pc-PAN-CS**, a similar protocol was followed whereby the same amount of Pc complexes (20 mg) were each dissolved in dry DMF (5 mL), then DCC (0.0103 mg,

0.05 mmol) and NHS (0.0103 mg, 0.09 mmol) were added to activate the carboxyl functional groups. The mixtures were stirred at room temperature for 24 h. Then, **PAN-CS** (0.5 g) was dissolved in dry DMF (5 mL) and added to the Pc solutions, followed by stirring at room temperature for a further 48 h. Both products were filtered, and the filtrates were added to acetonitrile dropwise. The resultant precipitates were collected by centrifugation and washed with methanol and THF. The conjugates are denoted as **7-Zn-PAN-CS**, **7-ZnQ-PAN-CS**, **7-In-PAN-CS, 7-InQ-PAN-CS** and **7-Zn-PAN**, **7-ZnQ-PAN**, **7-In-PAN**, and **7-InQ-PAN**.

2.3.6 Synthesis of nanofibers by electrospinning

Solutions for electrospinning were prepared as follows: 5 wt% (with respect to the weight of the solution) each of **Pc-PAN** and **Pc-PAN-CS** polymer were suspended in DMF, the samples were stirred at 60 ^{o}C until homogenous mixtures were formed. Then, the solutions were cooled to room temperature and pristine PAN was added gradually to make up a concentration of 20 wt%. The solutions were further stirred at 60 ^{o}C for 6h. For comparison, 20 wt% each of pristine **PAN** and **PAN-CS** were also prepared.

Each solution was placed in a 5 mL syringe fitted with a hypodermic needle (inner diameter of 0.5 mm) and the electrospinning of nanofibers was conducted at 15 kV, at a flow rate of 0.05 mL/ h, and a tip to collector distance of 12 cm at room temperature. The nanofibers were collected on aluminium foil covering the collector.

2.4 Procedures for photodynamic antimicrobial chemotherapy (PACT)

2.4.1. Preparation of micro-organisms

The micro-organisms used in this thesis were standard strains of *C. albicans* (ATCC 24433), *E. coli* (ATCC 25922), *K. pneumoniae* (ATCC 13883), *S. aureus* (ATCC 25923), *S. choleraesuis* (ATCC 10708), MRSA (ATCC 700699) and VREF (ATCC 51299). The micro-organisms were cultured in broth at 37 °C for 24 h and *C. albicans* was grown at 30 °C for 48 h. Each micro-organism was grown separately until it reached an optical density of 0.6 at 620 nm. And then, the pellets were isolated via centrifugation at 3000 rpm for 15 min and washed thrice with sterile phosphate-buffered saline (PBS). The pellets were further diluted to 1/100 in PBS to form a working stock microbial solution.

2.4.2. Dark toxicity and phototoxicity studies of planktonic cells

To conduct the experiments on phthalocyanine and nanoconjugates, the following procedure was followed; various concentrations of each Pc complexes and nanoconjugates were prepared in aqueous media containing ≤ 5% DMSO and were added to diluted microbial suspension. The suspensions were incubated in a shaker-equipped oven at an appropriate temperature for 30 min in the dark. After the incubation period, 100 µL of the suspensions were inoculated onto agar plates. The remaining suspensions were divided equally and added to two separate 24-well plates. One plate was exposed to light while the other plate was kept in the dark for the same duration. Aliquots of 100 µL of each suspension were inoculated on nutrient agar plates and afterwards, the plates were incubated overnight. The same procedure was followed for time-correlated studies, these were performed at 15 min intervals. The viable cells were determined by the colony count method by quantifying the log CFU/mL. Various controls were prepared, these included; a control containing

microbial suspension without photosensetizer kept in the dark or irradiated prepared in PBS, and at 5% DMSO. The experiments were prepared in triplicates.

In addition to the colony count method, the disc diffusion method was applied for complex **4** and **5** [175]. The sterile blank test discs were soaked with 20 µL of the Pc complexes (250 µM), the Pc-loaded disks were air-dried, and then placed onto nutrient agar plates inoculated with methicillin-sensitive *Staphylococcus aureus* (MSSA) or MRSA. Thereafter, the plates were irradiated for 1 h or kept in the dark, and the plates were subsequently incubated for 18 h at 37 °C. The zone of inhibition diameters was measured in mm and discs soaked in PBS, ampicillin (50 µM), and methicillin (50 µM) were used as blanks and controls.

For the glass wool and polymer nanofibers, three pieces of each support (10 mg) were individually weighed and placed in a 24-well plate containing 2.5 mL microbial solution. As the control, wells with unconjugated supports were prepared. The experiments were conducted for 1 h under light using the set-up described above and in dark conditions. Thereafter, 100 µL of each sample were diluted with 900 µl PBS and were spotted on agar plates using a micropipette and were incubated at the appropriate temperature.

2.4.3. Dark toxicity and phototoxicity studies of microbial biofilms

The mono and mixed biofilms used were prepared from the micro-organisms mentioned above. The mono biofilms were grown in 96-well plates using nutrient broth to a desired final concentration. The suspension was seeded at 37 °C (30 °C for *C. albicans*) for 48 h. After every 24 h, 200 µL of culture medium were removed from each well, the wells were gently washed with PBS and 200 µL of fresh tryptic soy broth was added after each wash. After 48 h, each well was washed gently with PBS three

times to remove unattached cells. Then, crystal violet (0.1%) staining was used for the quantification of biofilm biomass (OD = 570 nm). The plates were stained for 15 min, and were washed with PBS three times. Then, aliquots of 100 µL of Pcs at varying concentrations were added to the 96-well containing biofilms. The plates were incubated with shaking for 30 min in the dark at 37 °C (30 °C for *C. albicans*) and were irradiated with light. After irradiation, the suspensions were diluted serially in PBS and 100 µL were inoculated on an agar plate. The agar plates were incubated for 24 h at 37 °C (and at 48 h at 30 °C for *C. albicans*). The mixed biofilm was prepared by individually culturing each micro-organism to 2×10^9 separately, then 50 µL from each sample was added to one test tube, and the suspension was agitated for 30 min for homogeneity. Then, the same procedure stated above was repeated. The number of CFU/mL was counted and presented as log CFU. All experiments were performed in triplicates and all light studies were carried out with using the light set-up stated above.

2.4.4 Photosensitizer uptake studies

The uptake of Pc complexes **4** and **5** by both MRSA and MSSA were studied in different concentrations and time. Various concentrations of Pc complexes (0-250 µM) were added to the bacterial suspension and then incubated in dark for 1 h. Then, for the time studies, stock bacterial solution containing 5 µM Pc complexes were incubated with gentle agitation at 37 ºC for 0 to 24 h in the dark. For all uptake studies, the cells were isolated via centrifugation, rinsed thrice with PBS, and then extracted with 10% sodium dodecyl sulfate (SDS) for 24 h in the dark with gentle shaking [**176**]. The samples were further centrifuged, and the fluorescence in cells was measured using a microplate reader. The excitation wavelength used was 630 nm, and the emission was recorded at 690 nm. Calibration curves with fluorescence intensity were

obtained. The cellular uptake was determined by the number of incubated photosensitizers divided by the number of bacterial strains in incubated cells.

2.4.5 Statistical analysis

The data for CFU/mL were converted to logarithmic value and the values were presented in mean ± standard deviation. Values of p-value of 0.05 was considered significant.

2.5 Photodegradation studies

The photocatalytic effects of Pc-NF and Pc-GW were studied using model pollutant dyes; MO, 4-CP and MB. The studies were carried out separately, using either λ ~ 660 - 750 nm (red light) and λ ~ 380–750 nm (white light). The pollutant dye solutions were prepared at concentrations of 16.5 – 82.5 µM. Then, 10 mg of Pc-NF and Pc-GW were immersed in 3 mL of pollutant dye solutions. Each sample was irradiated at 15 min intervals, and the process was followed via UV-Vis spectroscopy at 470 nm, 667 nm and 305 nm for MO, MB and 4-CP, respectively. The reusability studies were conducted by washing the used material with deionized water followed by air-drying overnight, and the process was repeated twice

Publications

The results discussed in the following chapters have been published or submitted for publication in peer-reviewed journals.

1. **Sindelo, A**., Kobayashi, N., Kimura, M., & Nyokong, T. (2019). Physicochemical and photodynamic antimicrobial chemotherapy activity of morpholine-substituted phthalocyanines: effect of point of substitution and central metal. *J Photochem Photobiol A Chem*, *374*, 58-67.
2. **Sindelo, A**., Mafukidze, D. M., & Nyokong, T. (2022). Fabrication of asymmetrical morpholine phthalocyanines conjugated chitosan-polyacrylonitrile nanofibers for improved photodynamic antimicrobial chemotherapy activity. *Photodiagnosis Photodyn Ther*, *38*, 102760.
3. **Sindelo, A**., Nene, L., & Nyokong, T. (2022). Photodynamic antimicrobial chemotherapy with asymmetrical cationic or neutral metallophthalocyanines conjugated to amino-functionalized zinc oxide nanoparticles (spherical or pyramidal) against planktonic and biofilm microbial cultures. *Photodiagnosis Photodyn Ther*, *40*, 103160.
4. **Sindelo, A.,** Britton, J., Lanterna, A. E., Scaiano, J. C., & Nyokong, T. (2022). Decoration of glass wool with zinc (II) phthalocyanine for the photocatalytic transformation of methyl orange. *J Photochem Photobiol A Chem*, *432*, 114127.
5. **Sindelo, A**., Sen, P., & Nyokong, T. (2023). Photoantimicrobial activity of Schiff-base morpholino phthalocyanines against drug resistant micro-organisms in their planktonic and biofilm forms. *Photodiagnosis and Photodynamic Therapy*, *42*, 103519.

6. **Sindelo, A**., Sen, P., & Nyokong, T. (2023). Photodynamic inactivation of methicillin-resistant Staphylococcus aureus using pyrrolidinium containing Schiff base phthalocyanines. *J Photochem Photobiol A Chem*, *438*, 114535.
7. **Sindelo, A**., & Nyokong, T. (2024). Photoinactivation of microorganisms and photodegradation of pollutants using phthalocyanines supported on nanofibers and glass wool *J Photochem Photobiol A Chem*, *447*, 115236.

Chapter 3

Synthesis and Characterization

3. Synthesis and characterization

3.1 Phthalonitriles

The synthesis of phthalonitriles, 4-(benzo[*d*]thiazol-2-ylthio)phthalonitrile (**i**) and 4-(3,4-dicyanophenoxy)benzoic acid (**ii**) were carried out following the procedures outlined in literature [167,168]. The detailed synthesis and characterization of morpholino phthalonitriles **(iii), (iv)** and 2-((3,4-dicyanophenyl)thio)-N-methylbenzothiazolium iodide **(v)** is given below.

The synthetic pathway of morpholino phthalonitriles (**iii**), (**iv**) and 2-((3,4-dicyanophenyl)thio)-N-methylbenzothiazolium iodide (**v**) is illustrated in **Scheme 3.1**. The synthesis of phthalonitriles (**iii**) and (**iv**) involved a nucleophilic substitution reaction between the nitro group of 3- or 4-nitrophthalonitrile and the NH group of morpholine. This reaction was carried out at 100 °C in dry DMF with Na_2CO_3 used as a base catalyst. The reaction was conducted for 18 h under a N_2 gas atmosphere. While the cationic phthalonitrile **v** was synthesized via the methylation of 4-(benzo[d]thiazol-2-ylthio)phthalonitrile (**i**). This reaction has been effectively used in the preparation of cationic phthalonitrile [177].

The phthalonitriles were confirmed with FT-IR, ^{1}H NMR and elemental analysis. FTIR spectra confirmed the formation of the morpholinophthalonitriles (**iii** o**r iv**) where there was a presence of two sharp -CH_2 bands at 2907, 2869 and 2909, 2864 cm^{-1}, as well a strong -C≡N band at 2218 and 2221 cm^{-1} for **iii** and **iv**, respectively. The ^{1}H NMR showed aromatic protons peaks between 7.03 – 7.49 ppm for **iii** and between 7.02 – 7.60 ppm for

iv, and the CH_2 protons were observed between 3.24 – 3.80 ppm for **iii** and between 3.34 – 3.90 ppm for **iv**.

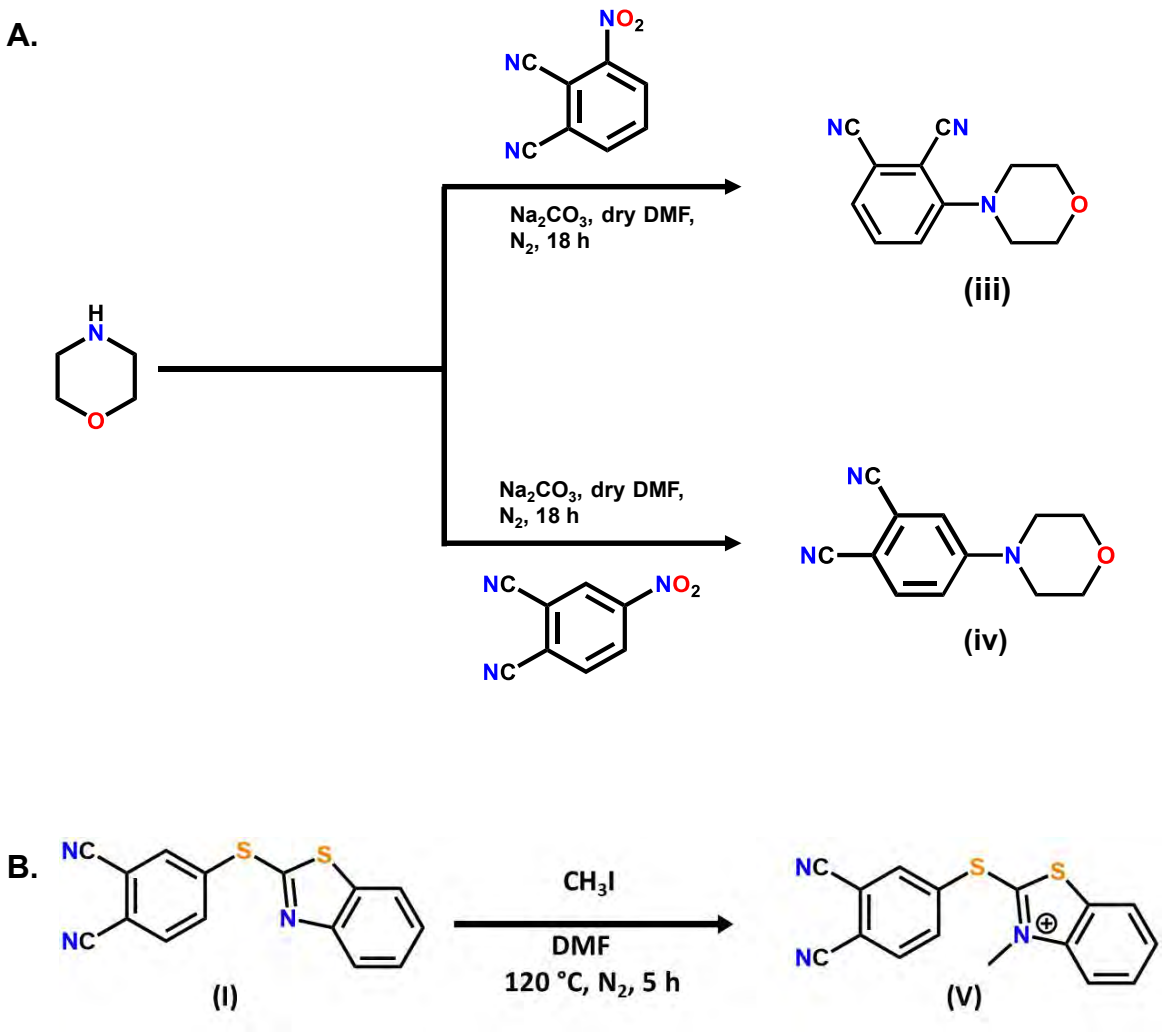

Scheme 3.1: Synthetic route for A. 3-morpholinophthalonitrile (**iii**), 4-morpholinophthalonitrile (**iv**) and B. 2-((3,4-dicyanophenyl)thio)-N-methylbenzothiazolium iodide **(v)**

^{1}H NMR of phthalonitrile **i** (**Figure 3.1a**) showed an aromatic peak between 7.70-7.29 ppm corresponding to the benzothiazole moiety. Upon the quaternization, an additional peak for phthalonitrile **v** was observed at 4.12 ppm, related to the presence of CH_3 (**Figure 3.1b**).

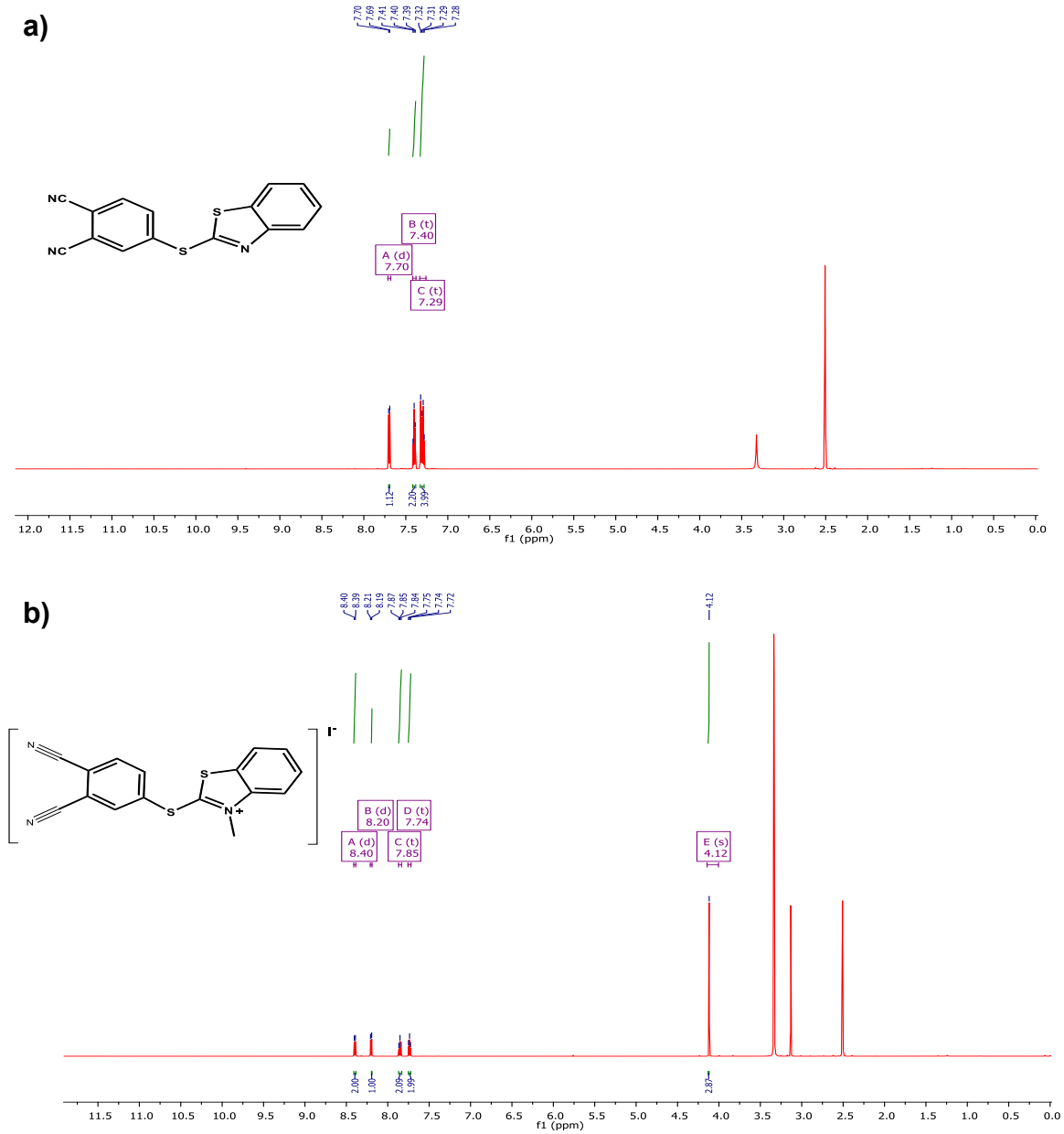

Figure 3.1: ^{1}H NMR spectrum of phthalonitriles (a) **i** and (b) **v** in DMSO-d_6.

3.2 Phthalocyanines (Pcs)

The synthesis and characterization of complexes **8-Zn**, **9-Zn**, and **10-Zn** have been previously reported [**51**, **52**]; hence they will not be covered in this study. However, the detailed characterization of the novel complexes **1-7** will be discussed below.

3.2.1 Metal-free (1-H2 and 2-H2), metalated (1-Zn, 2-Zn, 1-In and 2-In) morpholinophthalocyanine and their quaternization

The cyclotetramerization of (**iii**) or (**iv**) was performed in the presence of DBU and dry DMF producing the metal-free phthalocyanines **1-H_2** or **2-H_2** and with the addition of metal salts; $Zn(OAc)_2$, $InCl_3$ for **1-Zn, 1-In, 2-Zn** and **2-In**. The metallophthalocyanines were further quaternized using dimethyl sulfate (**Scheme 3.2**). IR spectra of the all Pcs showed the disappearance of the -C≡N band of the phthalonitriles on formation of the Pcs, with H_2Pcs (**1a** and **1b**) showing an additional –NH peak at 3282 and 3280 cm^{-1}, respectively. The compounds were further characterized using elemental analysis, ^{1}H NMR, mass spectroscopy, and UV-vis. The results obtained were comparable with the proposed structures.

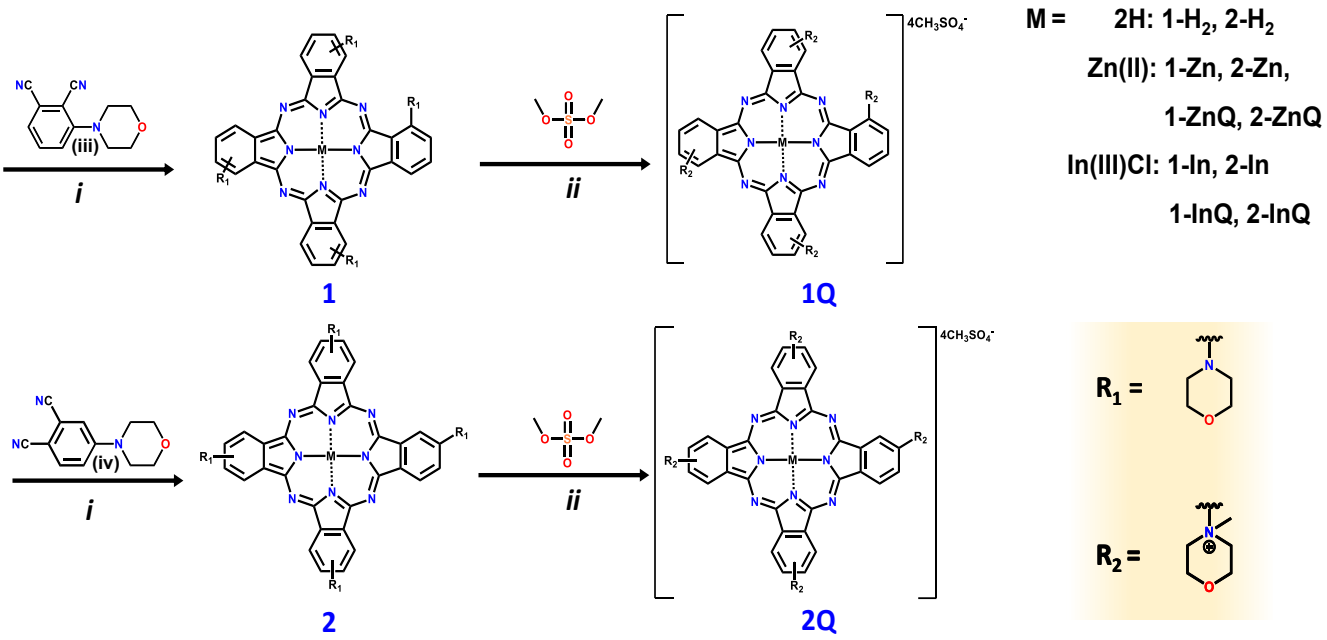

Scheme 3.2: Syntheses of complexes **1**, **2** and their quaternized counterparts using (i) N_2, n-pentanol, DBU, 138 °C, 8h, and or $Zn(OAc)_2$ or $InCl_3$ and (ii) dry DMF, 155 °C, 4 h.

^{1}H NMR was recorded in deuterated $CDCl_3$ for all the unquaternized compounds and D_2O for the quaternized compounds which gave the expected signals. For all the phthalocyanine complexes, the aromatic protons appeared between 9.95 and 6.72 ppm, and the -CH_2 protons between 4.58 and 1.59 ppm. The quaternized compounds had an additional sharp singlet upfield (δ = 3.88-2.18 ppm) from the additional –CH_3 protons. Compound **1-H₂** and **2-H₂**) had an additional singlet signal at 8.98 and 9.02 ppm, respectively, attributed to the presence of –NH. In mass spectroscopy, all the proposed structures were obtained with peaks at 855.15 $[M+1H]^+$, 916.26 $[M]^+$ and 1002.46 $[M]^+$ for

1-H_2, **1-Zn** and **1-In**, respectively (as examples). The molecular ion peaks for quaternized derivatives of complexes **1** and **2** was not observed due to lack of ionization.

3.2.2 Schiff base metallophthalocyanines

3.2.2.1 Schiff base morpholino phthalocyanines (3)

The syntheses of complexes **3-Zn** and **3-In** were achieved by reacting aldehyde substituted Pcs (**A** or **B**) with 4-(2-aminoethyl)morpholine (**Scheme 3.3**). Then, the tertiary amino groups of Pcs **3-Zn** and **3-In** were quaternized by methyl iodide to form cationic Pcs, **3-ZnQ** and **3-InQ**. The structures of **3** were determined by ^{1}H NMR, FT-IR, mass spectroscopy and elemental analysis.

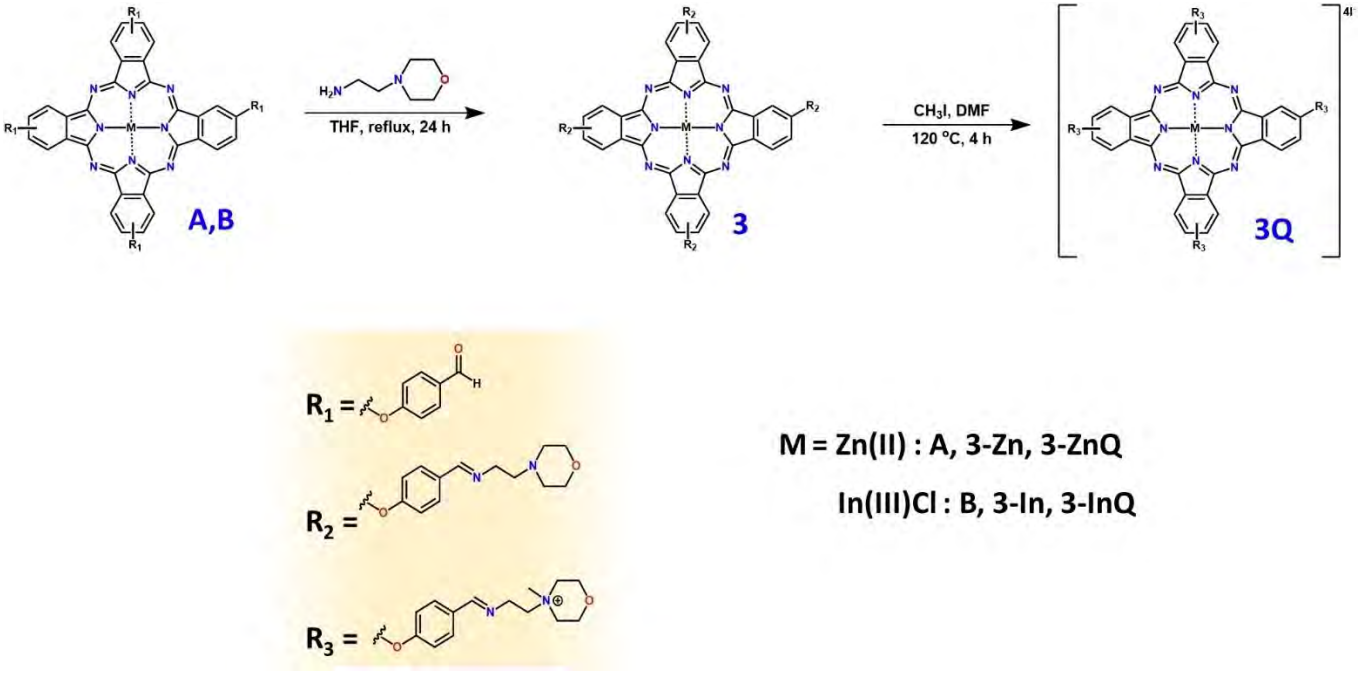

Scheme 3.3: Synthesis of complexes **3** under their respective conditions.

FT-IR spectra of the starting aldehyde substituted Pcs and all complexes are shown in **Figure 3.2**. Complexes **A** and **B** showed a carbonyl peak at 1710 cm^{-1}. Upon the formation of complexes **3**, there was an imine peak between 1650 and1652 cm^{-1}, confirming the successful preparation of the Schiff base Pcs and the peaks at ~1600 cm^{-1}, ~1400 cm^{-1} and ~1100 cm^{-1} were related to C=C, C-N and C-O-C stretching, respectively.

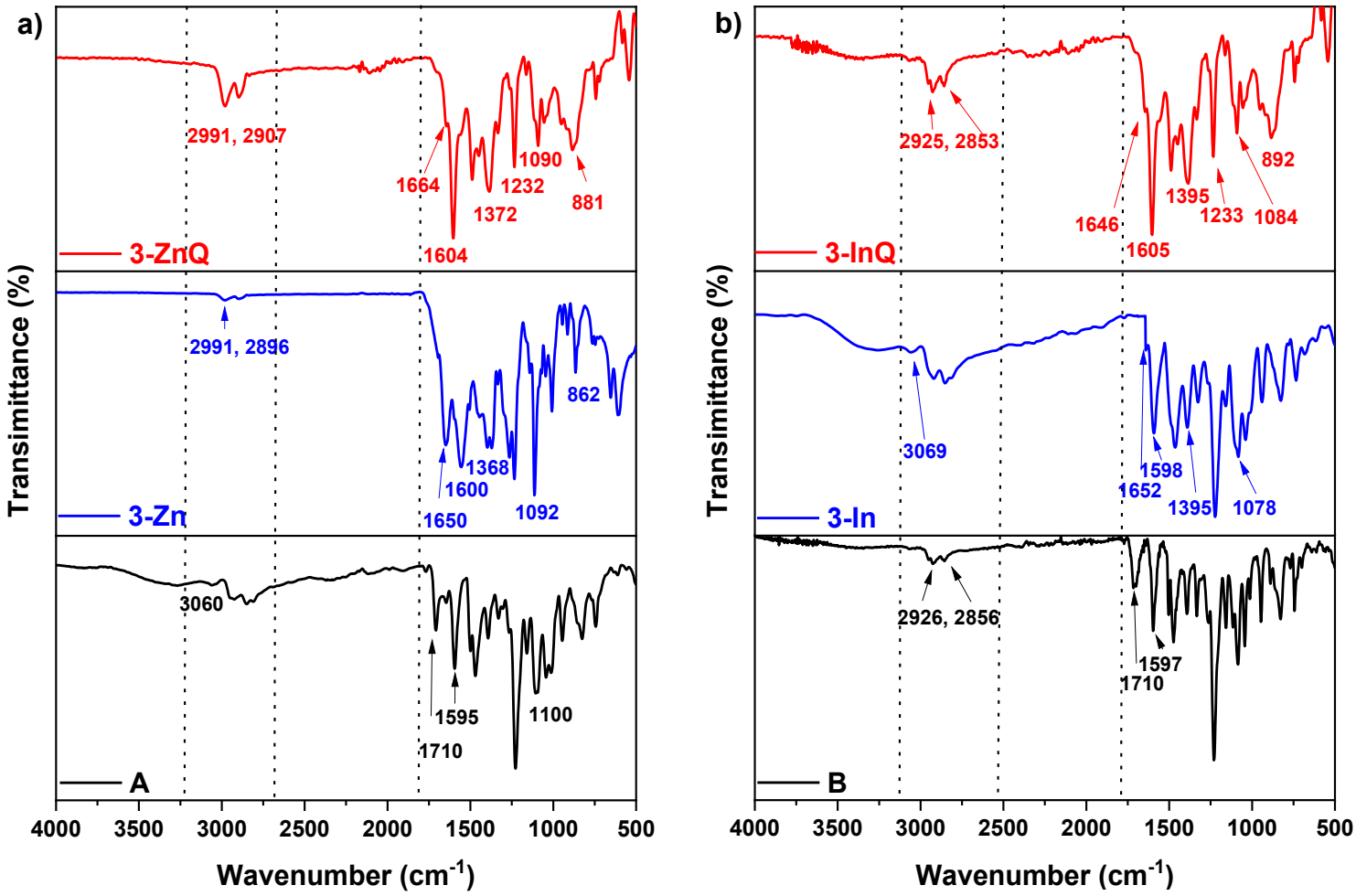

Figure 3.2: Infrared spectra of a) zinc (II) and b) indium (III) phthalocyanines.

In the ^{1}H NMR spectra of **3-Zn** and **3-In**, the imine group was observed as a singlet at 9.38-8.09 ppm, respectively, and the aromatic protons appeared at around 9.17-7.67 ppm for **3-Zn**. The singlet signal at around 2.78-2.77 ppm indicates the presence of methyl groups in compounds **3-ZnQ** and **3-InQ**. The mass spectra of **3** confirmed the proposed structures with the molecular ions at 1505.07 $[M+1]^{+}$ for **3-Zn**, 1555.29 $[M\text{-}Cl]^{+}$ for **3-In**, 390.73 $[M]^{4+}$ for **3-ZnQ** and 414.44 $[M+H]^{4+}$ for **3-InQ**.

3.2.2.2 Schiff base pyrrolidine phthalocyanines (4 and 5)

Similarly, the new pyrrolidine metallophthalocyanine derivatives **4-Zn**, **5-Zn**, **4-In**, and **5-In** were synthesized following the above mentioned synthetic route (**Scheme 3.4**). Briefly, 1-(2-aminoethyl)pyrrolidine or 1-(3-aminopropyl)pyrrolidine were reacted with previously synthesized zinc or indium tetracarbaldeyde substituted Pc (**A** = Zn or **B** = In) under Schiff base reaction conditions. The reaction resulted in the formation of the following complexes: **4-Zn**, **5-Zn**, **4-In**, and **5-In**, with complexes **4** and **5** containing ethyl and propyl alkyl chains, respectively. The cationic derivatives were obtained by reacting the neutral complexes with methyl iodide (CH_3I) in DMF, resulting in **4-ZnQ**, **4-InQ**, **5-ZnQ**, and **5-InQ**, respectively. High temperature of 120 ˚C was used in order to shorten the reaction times. These structures were confirmed and characterized by MALDI-TOF, elemental analysis, and ^{1}H NMR, all the data were in accordance with the proposed structures. MALDI-TOF confirmed the formation of the new complexes, m/z was observed at 1440.86 $[M]^{+}$ for **4-Zn**, 1527.36 $[M]^{+}$ and 1492.22 $[M\text{-}Cl]^{+}$ for **4-In**, 1496.14 $[M\text{-}H]^{+}$ for **5-Zn**, 1582.29 $[M\text{-}H]^{+}$ and 1547.47 $[M\text{-}Cl]^{+}$ for **5-In**. The methylation to form **4-ZnQ**, **4-InQ**, **5-ZnQ**, and

5-InQ was confirmed by the observation of the molecular ion peaks at m/z = 373.54 $[M-H]^{4+}$, 397.05 $[M]^{4+}$, (361.44 $[M-Cl]^{4+}$), 389.25 $[M]^{4+}$ and 412.71 $[M+2H]^{4+}$, respectively.

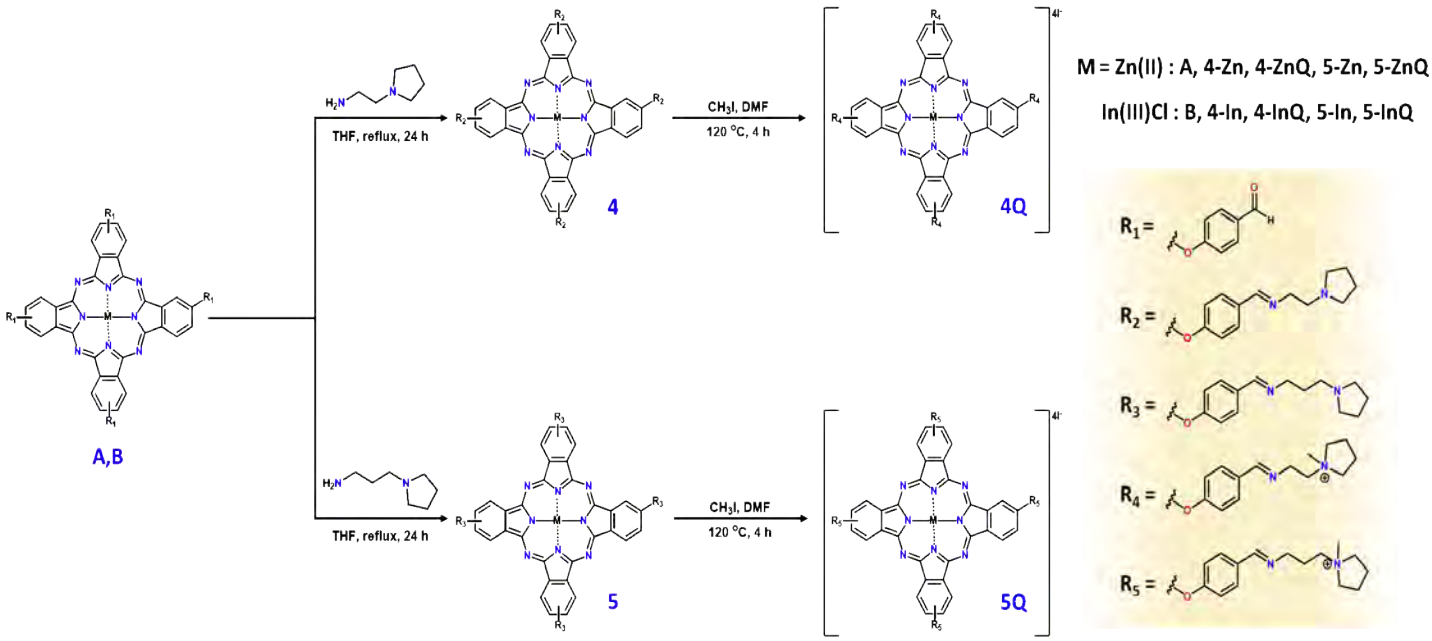

Scheme 3.4: Synthetic pathway for the preparation of complexes **4** and **5**.

3.2.3 Tris benzothiazole phthalocyanine (6)

The synthetic routes of complex **6** is shown in **Scheme 3.5**. These complexes were obtained by reacting 4-(3,4-dicyanophenoxy)benzoic acid phthalonitrile (**ii**) with phthalonitriles **i** or **v**, (the latter in a 5-fold excess to prevent the formation of undesired phthalocyanine derivatives). The dark green products were soluble in polar and apolar organic solvents such as chloroform, THF, DMF, and DMSO. Alhough complexes **6-ZnQ** and **6-InQ** are cationic, the Pcs were only partially soluble in water. All new compounds were characterized by the combination of ^{1}H NMR, MALDI-TOF, UV-Vis spectral data, and elemental analysis, all of which confirmed the proposed structures. Elemental analysis results agreed with reports that some phthalocyanines are isolated as hydrates

[178]. The MPcs (**6-Zn, 6-In, 6-ZnQ,** and **6-InQ**) gave signals that integrated with the expected number of protons in the proposed structure and a singlet peak was observed downfield (11.58 and 11.49 ppm for compound **6-Zn** and **6-In**) attributed to the COOH proton, however, the carboxylic proton signal for complex **6-ZnQ** and **6-InQ** was not detected due to deprotonation. The mass spectra data further confirmed the formation of the new MPcs. The molecular ion peaks for complexes **6-Zn** and **6-In** were obtained at m/z of 1208.11 and 1293.05, corresponding to $[M+1]^+$ and $[M]^+$, respectively. Complexes **6-ZnQ** and **6-InQ** mass spectral peaks were observed at 420.48 and 446.00, correlating with $[M+3]^{3+}$ and $[M]^{3+}$, respectively, confirming the presence of three positive charges.

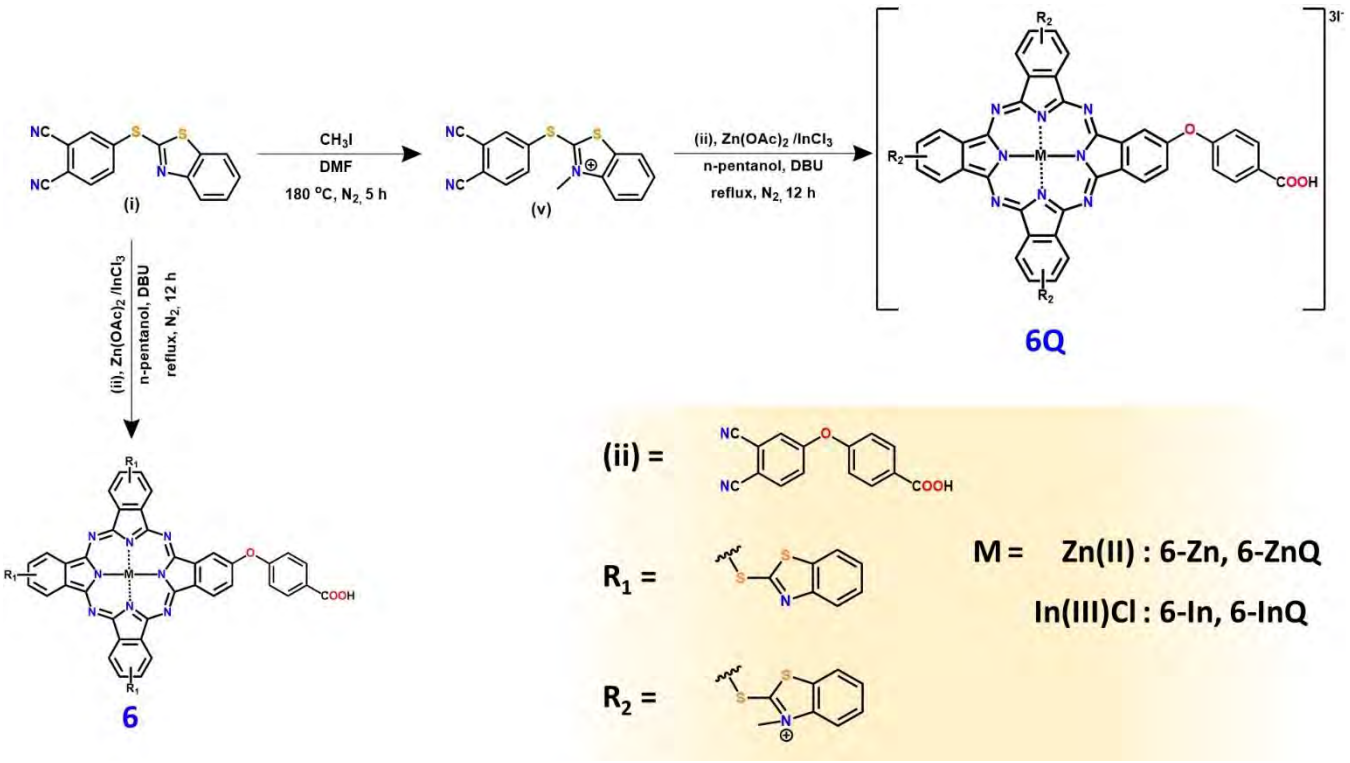

Scheme 3.5: Synthesis of neutral and cationic metallophthalocyanine **6**.

3.2.4 Tris morpholino phthalocyanines (7)

The general synthetic route for the syntheses of asymmetric morpholino metallophthalocyanine **7** is shown in **Scheme 3.6**. Briefly, the statistical cross-condensation of 4-morpholinophthalonitrile (**iv**) and 4-(3,4-dicyanophenoxy)benzoic acid (**ii**) (4:1 mol ratio) was carried out in pentanol, in the presence of metal salt (zinc (II) acetate or indium (III) chloride) and DBU under inert conditions. The complexes formed were purified by column chromatography. The MPcs (**7-Zn** and **7-In**) were further N-methylated using dimethyl sulphate in DMF, producing cationic asymmetrical MPcs, **7-ZnQ** and **7-InQ,** respectively. All the new MPcs derivatives were characterized using various spectroscopic methods (^{1}H NMR, FT-IR, mass, and UV-vis) and elemental analysis. ^{1}H NMR showed characteristic macrocyclic ring peaks upfield and CH_2 peaks downfield, confirming the formation of the proposed structure. The quaternized compounds (**7-ZnQ** and **7-InQ**) showed an additional sharp peak downfield, with the integral matching the expected value, confirming successful methylation. The mass spectra of compounds **7-Zn** and **7-In** confirmed the presence of the target compounds. The molecular ion peaks were observed at 968.37 $[M+1]^+$ and 1054.08 $[M+1]^+$ m/z, for **7-Zn** and **7-In**, respectively. Cationic **7-ZnQ** and **7-InQ** did not ionize hence there is no MALDI-TOF spectral data.

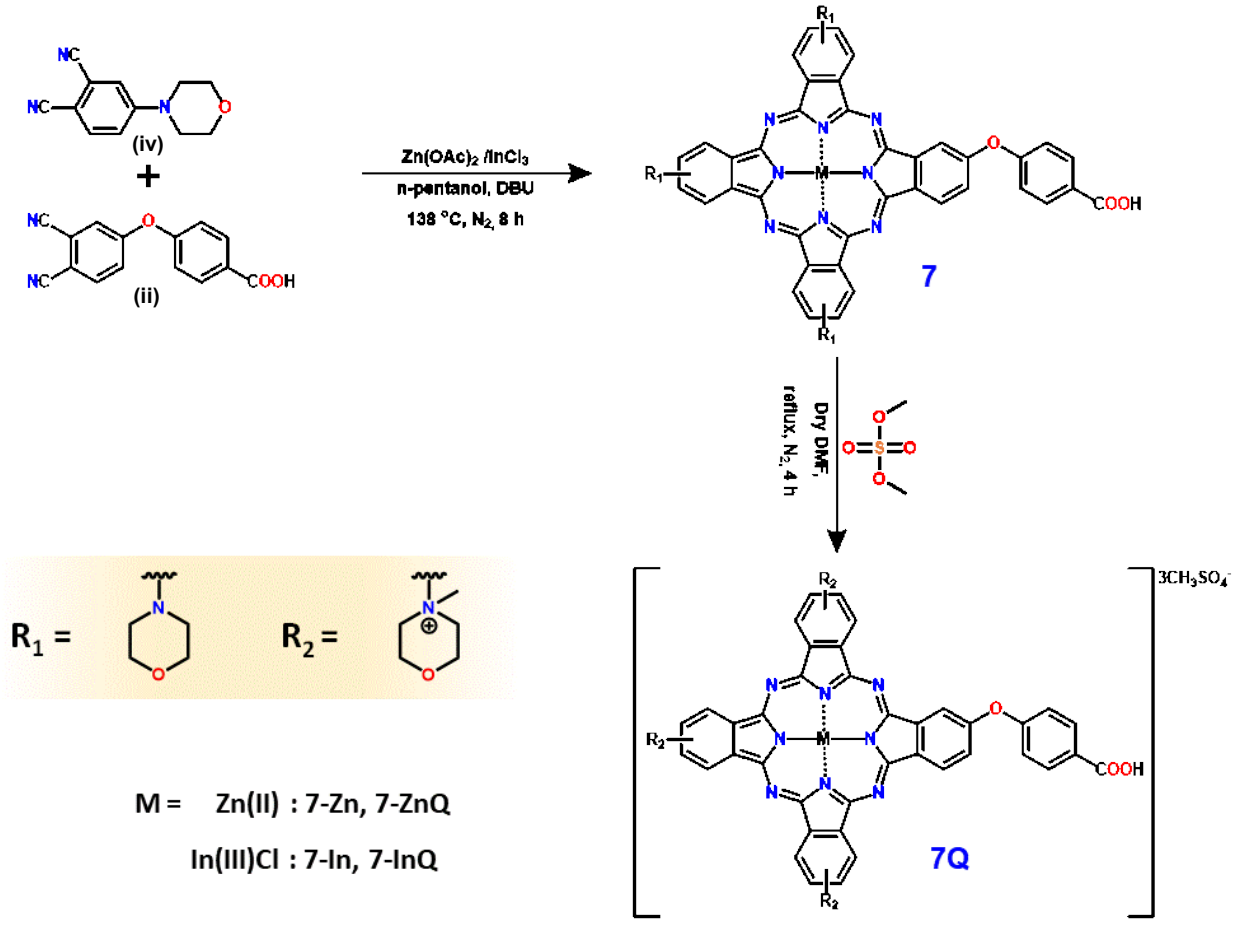

Scheme 3.6: Synthesis asymmetrical morpholino phthalocyanines **7** and their respective cationic derivatives.

The FT-IR spectra of the complexes **7-Zn**, **7-In**, **7-ZnQ,** and **7-InQ** showed similar trends (**Figure 3.3** (**7-Zn** and **7-ZnQ** used as examples)). The broad vibrational bands for carboxylic acid O-H were observed at 3331, 3377, 3373, 3313 cm^{-1} with the carboxylic acid C=O vibrational band observed at 1702, 1709, 1701, 1695 cm^{-1} for **7-Zn**, **7-In**, **7-ZnQ,** and **7-InQ**, respectively.

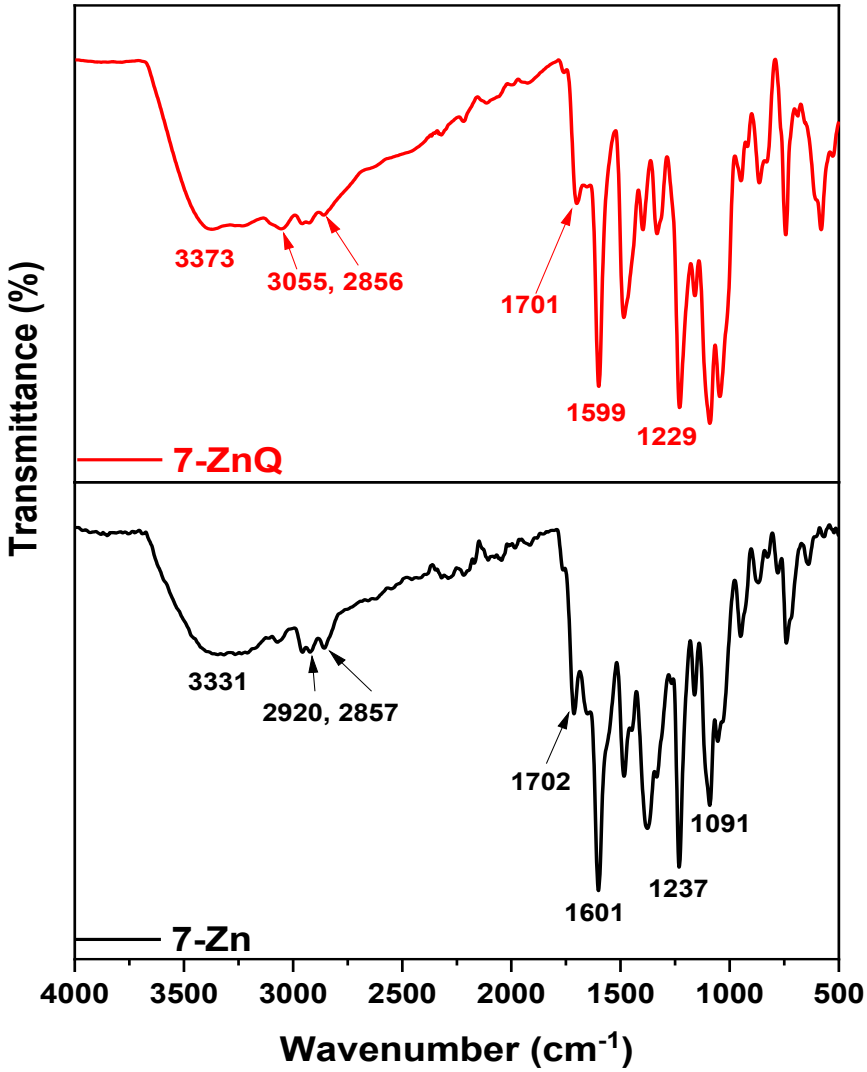

Figure 3.3: FT-IR of complexes **7-Zn** and **7-ZnQ**.

3.2.5 UV-Vis spectra

The UV-Vis spectra of complexes **1-Zn, 2-Zn, 1-In, 2-In, 1-ZnQ, 2-ZnQ, 1-InQ, 2-InQ**) showed a single sharp Q band typical of monomeric phthalocyanines **(Figure 3.4**) [179]. The UV-Vis of the H_2Pcs **1-H_2** and **2-H_2** (**Figure 3.4(a)**) showed characteristic split Q band at 775 and 745 nm for **1-H_2** and 739 and 709 nm in DMF for **2-H_2** (**Table 3.1**), respectively, confirming the structure to be of D_{2h} symmetry. However, Compounds **1-H_2** and **2-H_2** showed single Q bands in DMSO (**Figure 3.4**, insert), suggesting deprotonation of the inner pyrrolic H atoms in the Pc core and thus, symmetry change from D_{2h} to D_{4h} occurs due to basicity of these solvents [44].

Compounds **1-Zn** and **2-Zn** (**Figure 3.4(b)**) showed a Q-band at 747 and 717 nm and the compounds **1-In** and **2-In** (**Figure 3.4(c)**) showed the characteristic Q-band peak at 765 and 736 nm in DMSO (**Table 3.1**). The non-peripherally substituted compound **1-H_2**, **1-Zn** and **1-In** were redshifted compared to the peripherally substituted **2-H_2, 2-Zn,** and **2-In**. This large-scale redshift can be attributed to the linear combinations of the atomic orbitals coefficients at the non-peripheral positions of the highest occupied molecular orbital (HOMO) more significant than that of peripheral positions [180]. As a result, the HOMO level is destabilized more at the non-peripheral than at the peripheral position, resulting in the redshifting of the Q band in the former. For all Pcs, an additional peak was observed from the 485 nm region attributed to charge transfer [181].

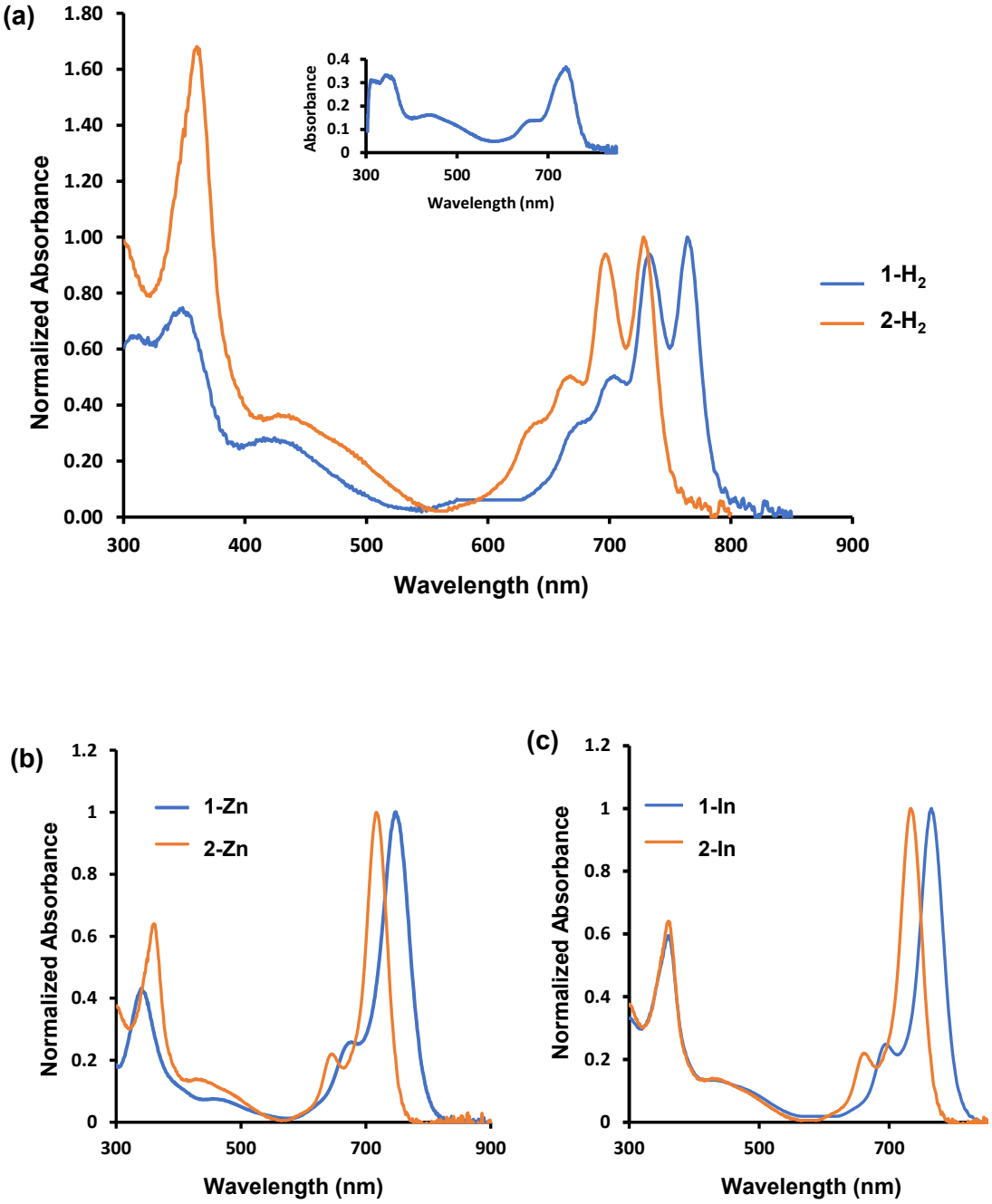

Figure 3.4: UV-vis spectra of a) **1-H₂** and **2-H₂** in DMF; b) **1-Zn** and **2-Zn**; c) **1-In** and **2-In** in DMSO. The insert in (a) is the spectrum of **2-H₂** in DMSO.

The Pcs were dissolved in THF, DCM and DMSO to examine the solvent effect as well the aggregation behaviour of the newly synthesized Pcs. All Pcs show no aggregation in the above-mentioned solvents, **Figure 3.5(a)**. With an increase in the polarity of the solvent (THF < DCM < DMSO) there was a spectral shift as shown in **Figure 3.5(a)**. Lambert-Beer's Law was obeyed in the concentration range of 5.5 × 10^{-6} to 3.5 ×10^{-5} mol/L (**Figure 3.5(b)** for **2-Zn** used as an example) in DMSO.

a)

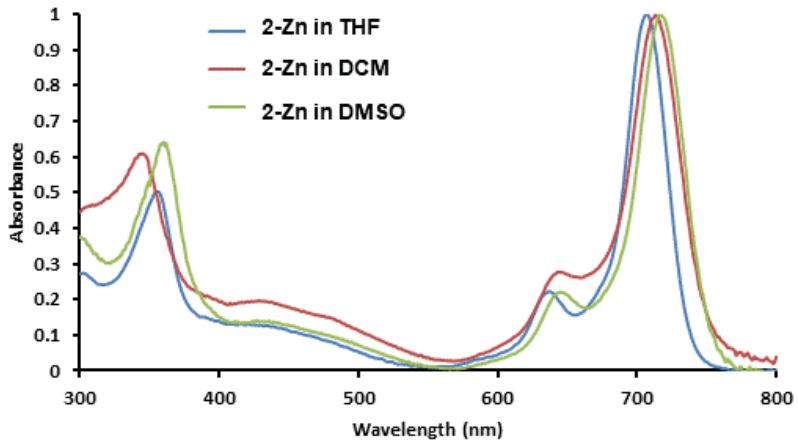

b)

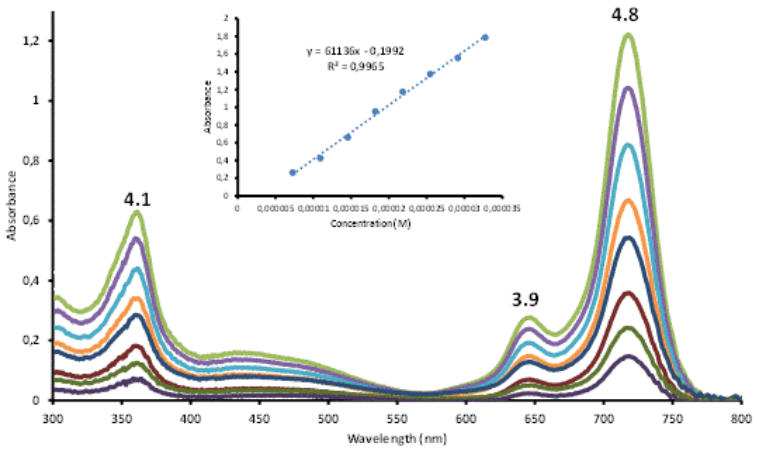

Figure 3.5: UV-vis spectra of **2-Zn** in (a) different solvents at concentration ~1.7 ×10^{-6} and (b) spectral changes of in DMSO at 6.5 x10^{-6} to 3.5 x10^{-5} mol/L (Insert: absorbance vs concentration graph).

Upon quaternization, the MPcs became blue-shifted (**Table 3.1**) in DMSO. This is due to the lowering of the electron donating ability of the nitrogen groups upon quaternization [182]. The quaternized derivatives (**1-ZnQ**, **2-ZnQ**, **1-InQ**, and **2-InQ**) were soluble in water but showed no sign of aggregation UV-vis spectrum in water. Water solubility and lack of aggregation are imperative for PACT applications.

The absorption spectra of complexes **3**-**5** also showed monomeric behaviour in DMSO corresponding to D_{4h} symmetry of metallophthalocyanines, **Figure 3.6**, mimicking the morpholine phthalocyanine above. The single and narrow Q-bands were observed in the visible region at 692 nm, 698 nm, 680 nm, 690 nm for **3-Zn**, **3-In**, **3-ZnQ** and **3-InQ**, respectively, **Table 3.1**. The Q-bands of the indium (III) Pc complexes were redshifted compared to the zinc (II) Pc complexes, this is ascribed to the nonplanar effect of the In (III) ion and its bigger atomic radius [183]. This was also observed for complexes **1** and **2**.

The electronic absorption spectra of the pyrrolidine Schiff base phthalocyanines observed intense absorption maxima between 678-682 nm for the ZnPc series (**Figure 3.6(b)**) and 691-697 nm for the InPc series (**Figure 3.6(c)**), **Table 3.1**. There was a minor difference between the absorbance peak for the ethyl pyrrolidine (**4-Zn**, **4-ZnQ**, **4-In**, and **4-InQ**) and the corresponding propyl pyrrolidine Schiff base Pcs (**5-Zn**, **5-ZnQ**, **5-In**, and **5-InQ**) suggesting that the extension of the alkyl chain had a small effect on the electron delocalization of the Pc rings. As was the case above, the indium-containing complexes (**4-In**, **5-In**, **4-InQ**, and **5-InQ**) were redshifted when compared to the zinc-containing complexes (**4-Zn**, **5-Zn**, **4-ZnQ**, and **5-ZnQ**). Comparing complexes **2-Zn**, **3-Zn**, **4-Zn**,

and **5-Zn** shows that **2-Zn** is highly red shifted. The same applies to indium bearing complexes suggesting the direct linkage of morpholine to the Pc macrocycle is responsible for the red shift.

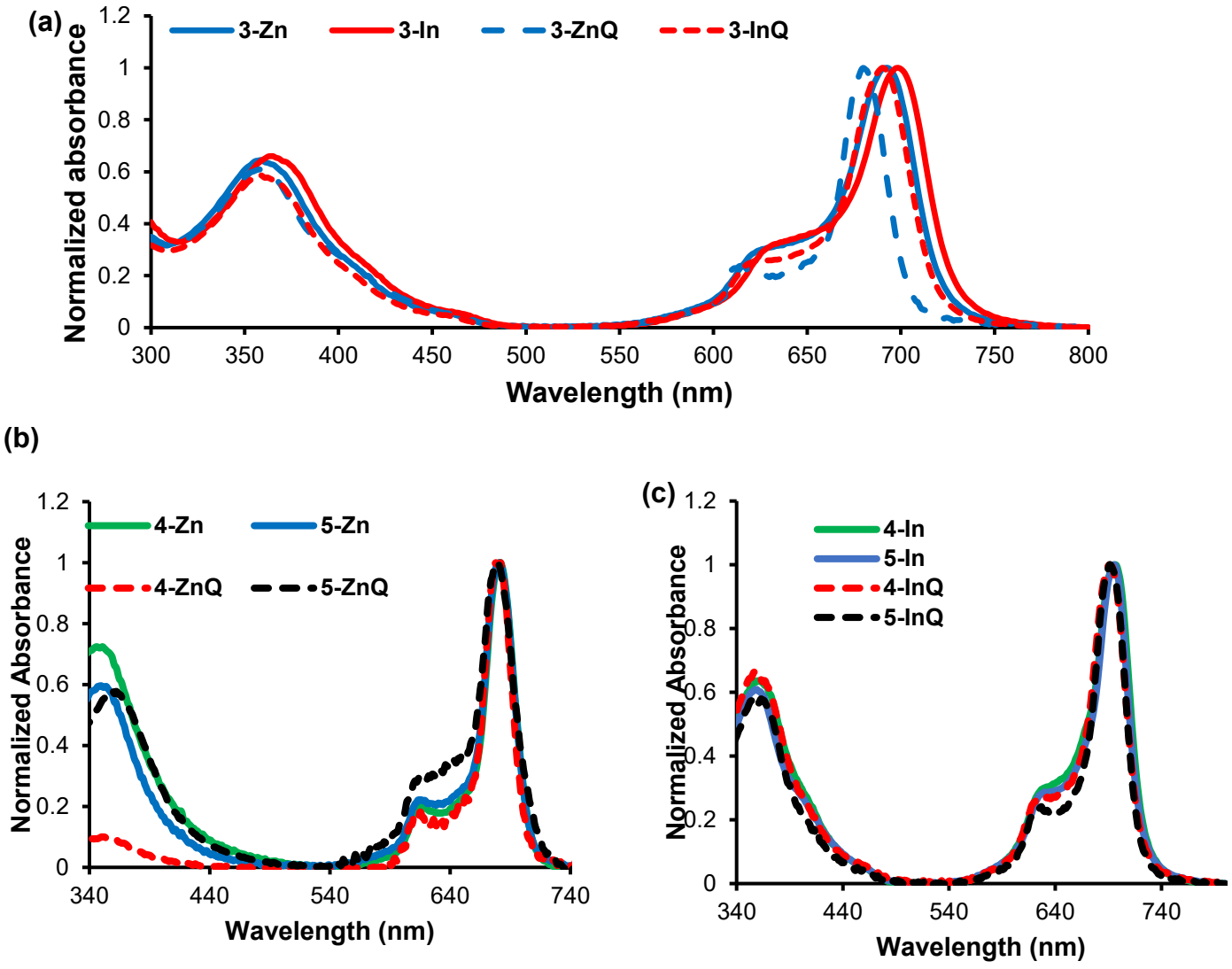

Figure 3.6: Normalized UV-vis absorption spectra of (a) complexes **3,** (b) Zn and (c) In Pcs derivatives of complexes **4** and **5,** all spectra were recorded in DMSO.

In aqueous media (5% DMSO, used for PACT), the neutral morpholino Pcs (**3-Zn**, **3-In**) showed an increase in the absorption of the band at around 650 nm (**Figure 3.7(a)**, **3-Zn** used as an example), resulting from the formation of cofacial H-type-like aggregates [184]. Although the cationic Pcs showed a more monomeric Q-band in aqueous media compared to the neutral Pcs, the absorption spectra appeared broad and showed some aggregation, **Figure 3.7(a)** (showing **3-ZnQ** as an example). Aggregation is undesirable for the intended application as aggregates tend to lead to photo-inactivity.

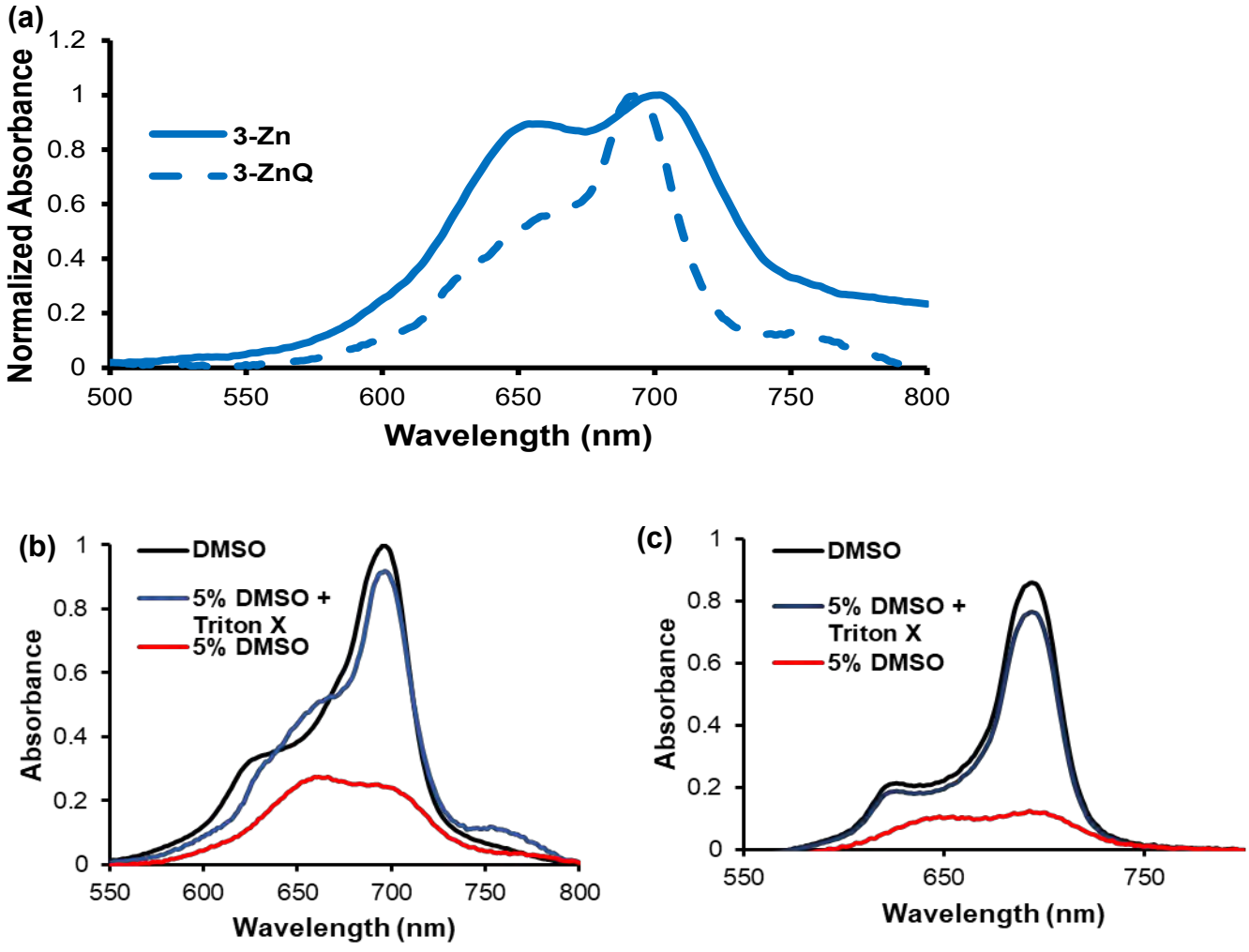

Figure 3.7: UV-Vis absorption spectra of (a) complex **3-Zn** and **3-ZnQ**, (b) **4-In**, and (c) **4-InQ** recorded in aqueous media (5% DMSO) and DMSO.

The electronic absorption spectra of **4-In** and **4-InQ** (used as examples) were also recorded in 5% DMSO (used in PACT studies) and the results are shown in **Figure 3.7 (b), (c)**. The Q band is broad and split with the high energy band being due to the aggregate and the low energy band being due to the monomer. For **4-In**, the aggregate peak is larger in intensity than the monomer peak, while the monomer peak is slightly higher than the aggregate peak for **4-InQ**. Thus, **4-In** is more aggregated than **4-InQ**. Both Pcs showed a drastic decrease in the absorption band in aqueous media with a redshifted monomeric band at 705 and 701 nm for **4-In** and **4-InQ**, respectively. Triton-X was added to break the aggregation and there was an increase in the absorbance of the monomeric band with the **4-InQ** retaining its original absorption profile, however, the **4-In** complex still showed some aggregates. Similar behaviour was observed in 5% DMSO for complex **5**.

The asymmetrical Pcs complex **6** and **7** showed largely monomeric behaviour with data listed in **Table 3.1** and the spectra for complex **6** is shown in **Figure 3.8(a)**. The Q-bands of tris-morpholino substituted Pcs **7-Zn** and **7-In** were blue-shifted by approximately 7 nm and 9 nm to that of tetra-morpholino substituted Pcs **2-Zn** and **2-In**, suggesting that the effect of the morpholine substitution is key in shifting the Q-bands to higher wavelengths, **Table 3.1**.

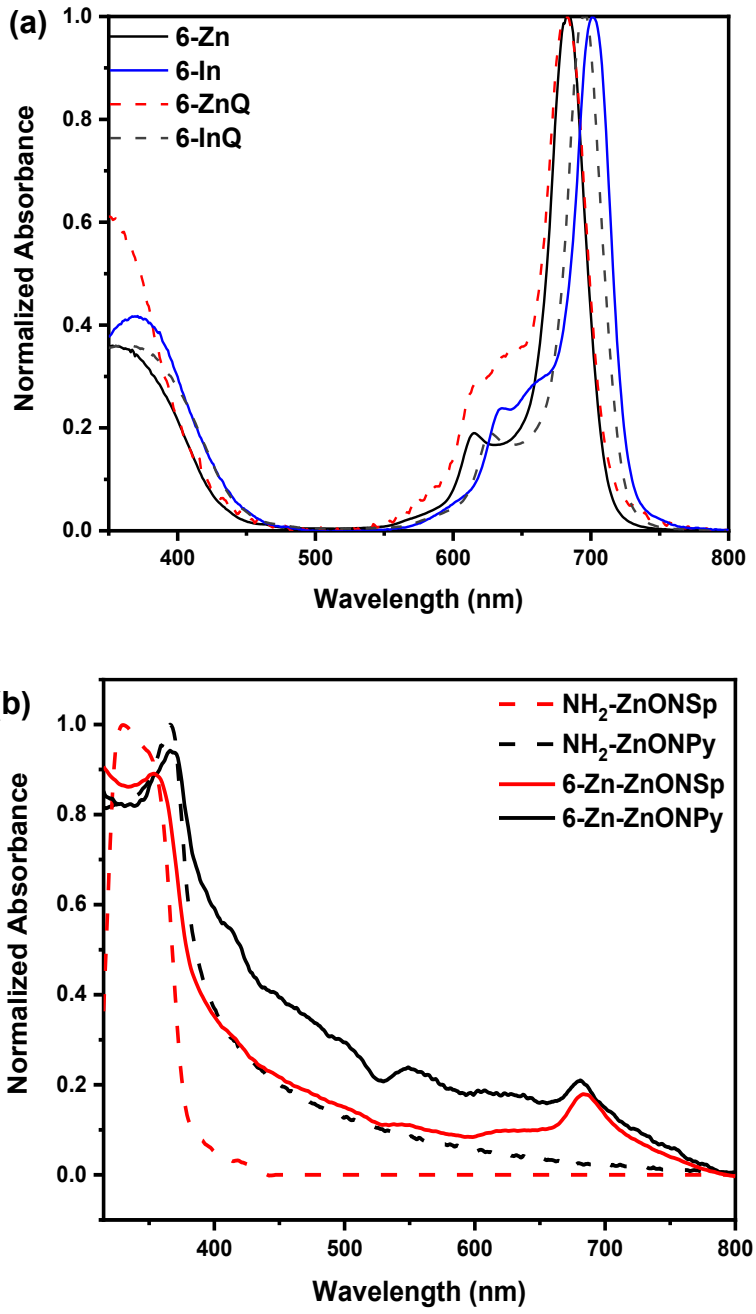

Figure 3.8: UV-Vis absorption spectra of (a) Pcs alone and (b) ZnONPs and nanoconjugates. All spectra were recorded in DMSO.

Table 3.1: Summary of the Q band values for all Pcs in DMSO unless stated otherwise.

Photosensitizer	Q band (λ_{max}) (nm)
1-H_2	775[a], 745[a] 773
1-Zn	747 750[b]
1-ZnQ	684 687[b]
1-In	765 768[b]
1-InQ	702 704[b]
2-H_2	739[a], 709[a] 738
2-Zn	717 719[b]
2-ZnQ	673 674[b]
2-In	736 739[b]

[a] values in DMF [b] values in aqueous media (5% DMSO, used in PACT)

Table 3.1 continues:

Photosensitizer	Q band (λ_{max}) (nm)
2-InQ	685 687[b]
3-Zn	692 702[b]
3-ZnQ	680 692[b]
3-In	698 710[b]
3-InQ	690 702[b]
4-Zn	681 690[b]
4-ZnQ	678 690[b]
4-In	694 705[b]
4-InQ	691 701[b]

[b] values in aqueous media (5% DMSO, used in PACT)

Table 3.1 continues:

Photosensitizer	Q band (λ_{max}) (nm)
5-Zn	682 692[b]
5-ZnQ	679 688[b]
5-InQ	691 700[b]
6-Zn	683 692[b]
6-In	702 710[b]
6-ZnQ	682 690[b]
6-InQ	695 703[b]
7-Zn	710 713[b]
7-In	727 730[b]

[b] values in aqueous media

Table 3.1 continues:

Photosensitizer	Q band (λ_{max}) (nm)
7-ZnQ	675 684[b]
7-InQ	689 698[b]

3.3 Zinc oxide nanoparticles and Pc-conjugates

3.3.1 Synthesis

The synthesis of bare zinc oxide nanospheres (ZnONSps) and zinc oxide nanopyramids (ZnONPys) was synthesized as reported in literature [**169**, **170**]. The functionalization of ZnONSps and ZnONPys with APTES was performed as shown in **Scheme 3.7.** The conjugation of complexes **6** to amino functionalized ZnONSps and ZnONPys was achieved by forming an amide using the -COOH moiety of the former and the -NH_2 moiety of the latter, **Scheme 3.8**. The representation in **Scheme 3.8** is just a dramatization not a true reflection of the number of Pcs linked to the NPs. All the nanoparticles and nanoconjugates were characterized using UV-vis, TEM, X-ray powder diffraction (XRD), and FT-IR techniques.

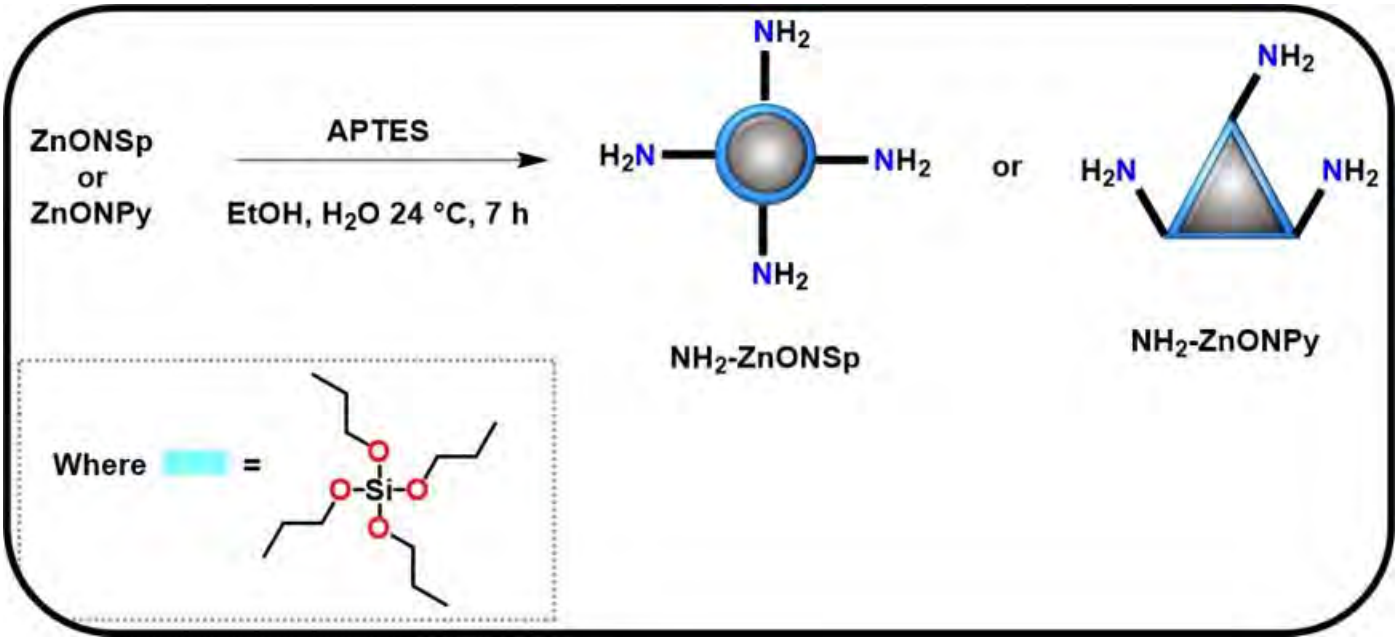

Scheme 3.7: Synthetic route of APTES capped ZnONSps and ZnONPys. APTES = (3-Aminopropyl)triethoxysilane.

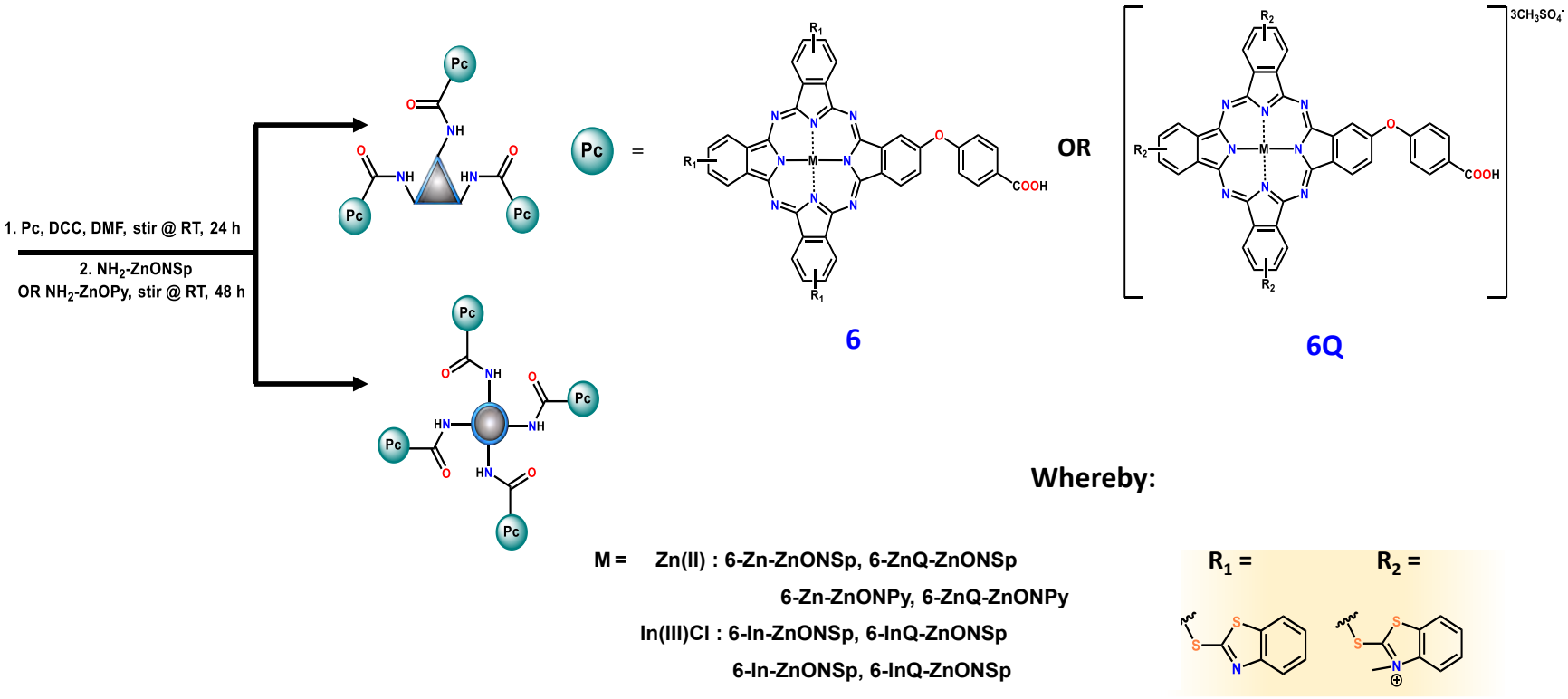

Scheme 3.8: Synthetic route for covalent linkage of phthalocyanine complex **6** with NH_2-ZnONSps and NH_2-ZnONPys.

3.3.2 UV-Vis spectra

The UV-vis spectra of NH_2-ZnONSps, NH_2-ZnONPys, **3**-ZnONSps, and **3**-ZnONPys are shown in **Figure 3.8**. The synthesized NH_2-ZnONSps and NH_2-ZnONPys showed distinct peaks at 330 nm and 367 nm, respectively, **Table 3.2**. The difference in absorbance of the two NPs is due to the size variation and morphology change. Upon conjugation to Pcs, the nanoconjugates retained both the NPs (**Figure 3.8a**) and Pc (**Figure 3.8b**) profiles. There were insignificant shifts in the Q band of the MPcs (**Figure 3.8a**), following conjugation, **Table 3.2**. The loading of the MPc complexes onto the ZnONPs was determined via thermogravimetric analysis (TGA) as reported before [**185**], and the values are summarized in **Table 3.2**. Overall, the MPc loading is slightly higher for the Pc-ZnONPys nanoconjugates than Pc-ZnONSps; this is attributed to the NH_2-ZnONPys having a larger size than NH_2-ZnONSps, as shown by TEM discussed later.

Table 3.2: The characterization data of synthesized phthalocyanine, **6** and nanoconjugates in DMSO.

Complex	Size (from TEM) (nm)	Pc Loading (µg/mg)	λ_{abs} (nm)
NH_2-ZnONSps	4.6	-	330
NH_2-ZnONPys	36.7[a]	-	367
6-Zn-ZnONSps	7.9	89	684 (683)
6-Zn-ZnONPys	38.4[a]	136	682 (683)
6-In-ZnONSps	8.4	92	702 (702)
6-In-ZnONPys	37.8[a]	130	700 (702)
6-ZnQ-ZnONSps	8.0	102	682 (682)
6-ZnQ-ZnONPys	38.8[a]	127	682 (682)
6-InQ-ZnONSps	8.8	99	697 (695)
6-InQ-ZnONPys	40.7[a]	134	693 (695)

[a] Edge/length [b] vaues in brackets are for Pcs alone

3.3.3 FT-IR spectra

The addition of the amine functional group on the nanoparticles and the formation of the amide bond between phthalocyanines and the modified NPs was investigated using the FT-IR spectra, and the spectra of ZnONPys, NH_2-ZnONPys, **6-In**, and **6-In**-ZnONPys are shown in **Figure 3.9**. The synthesized ZnONPys exhibited a broad peak at 3372 cm^{-1} related to the hydroxyl stretch. The peak at 1555 cm^{-1} is ascribed to C=O group while the peaks at 1406 cm^{-1} and 896 cm^{-1} are due to C-H bending. The presence of 3-

aminopropyltriethoxysilane in the NPs became apparent due to the appearance of distinct peaks observed at 3248 cm^{-1} (related to amine N-H stretch), 3137 cm^{-1} (related to amine N-H stretch), 2921 cm^{-1}(related to C-H stretch), 2855 cm^{-1} (related to C-H stretch), and 988 cm^{-1} (related to Si-O-Si stretch). The amide bond formation is supported by the appearance of a single peak at 3235 cm^{-1} related to a secondary amine stretch and the C=O shifting from 1713 cm^{-1} in complex **6-In** to 1705 cm^{-1} in the **6-In**-ZnONPys.

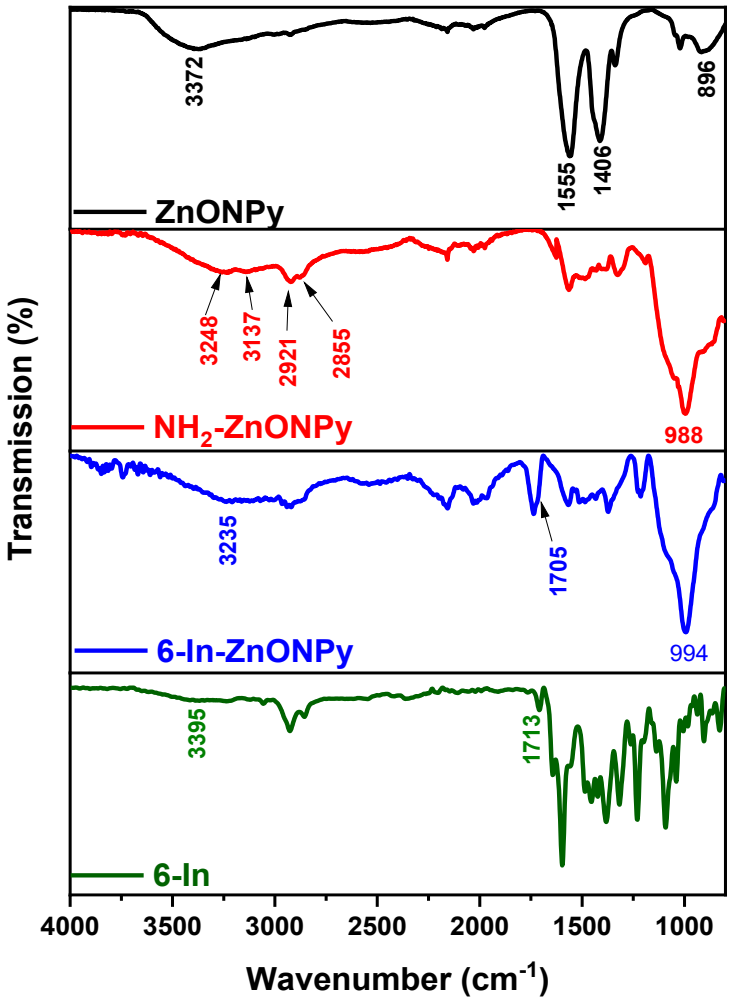

Figure 3.9: FTIR spectra of ZnONPys, NH_2-ZnONPys, **6-In**-ZnONPys and **6-In**.

3.3.4 X-ray photoelectron spectroscopy (XPS) analysis

The amide bond formation and chemical composition were confirmed via XPS analysis, as shown in **Figure 3.10**. The survey spectra (**Figure 3.10 (a)**) of NH_2-ZnONSps, **6-Zn,** and **6-Zn**-ZnONSps revealed the presence of Zn, C, O, N, and an additional Si peak for NH_2-ZnONSps and **6-Zn**-ZnONSps compounds, confirming the presence of the conjugate without any impurities. The high-resolution XPS N 1s spectra are shown in **Figure 3.10 b-d)**. As expected, the APTES-coated ZnONPs showed two peaks at 400.6 eV and 402.2 eV corresponding to $-NH_2$ and $-NH_3^+$, respectively, further confirming the successful self-assembling of APTES on the ZnONPs [**186**]. The nanoconjugate showed three distinct peaks at 399.8 eV, 401.1 eV, and 401.9 eV attributed to N-C (arising from **6-Zn**), N-H (arising from the NH_2-ZnONSps), and N-C=O, respectively. The amide peak (N-C=O) confirmed the link between amino-functionalized nanoparticles and carboxylic acid-containing phthalocyanine [**187**].

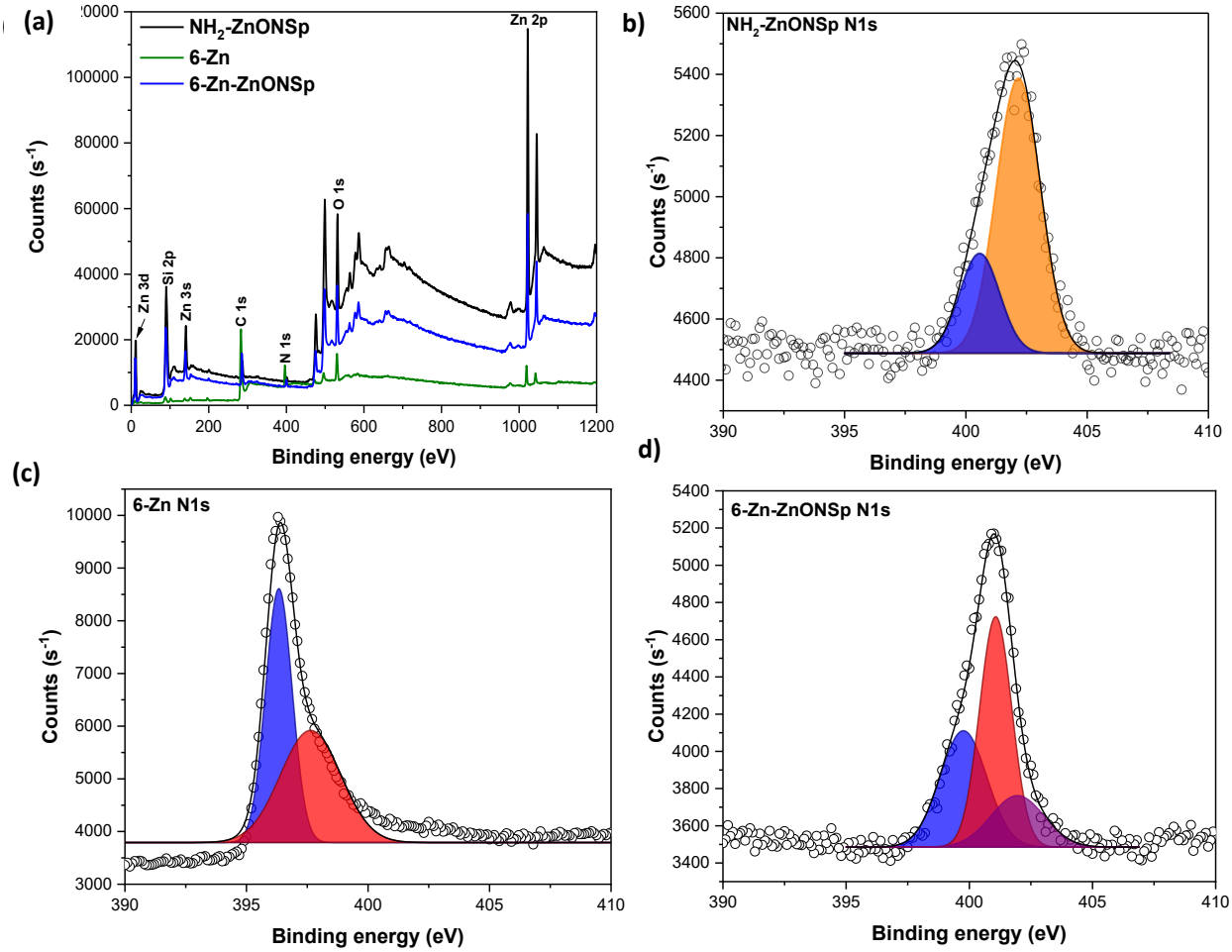

Figure 3.10: (a) XPS survey spectra of NH2-ZnONSps, **6-Zn**, and **6-Zn**-ZnONSps. N1s of (b) NH2-ZnONSps, (c) **6-Zn** and (d) **6-Zn**-ZnONSps.

3.3.5 Transmission electron microscopy (TEM)

The TEM micrographs (**Figure 3.11**) revealed the morphology of amino-capped ZnONSps, ZnONPys, and the average diameters or edge lengths (nm) are summarized in **Table 3.2**. The NH_2-ZnONSps were spherical and monodispersed (**Figure 3.11 (a)**) with an average diameter of 4.6 nm (as shown by the corresponding histogram). The NH_2-

ZnONPys were measured to have an average edge length of 36.7 nm. After conjugating to MPcs, there was a significant increase in diameter for the ZnONSps nanoconjugate due to the π -π interaction between the phthalocyanine core and the adjacent NPs. However, there was no significant change in the edge length of the ZnONPys nanoconjugate.

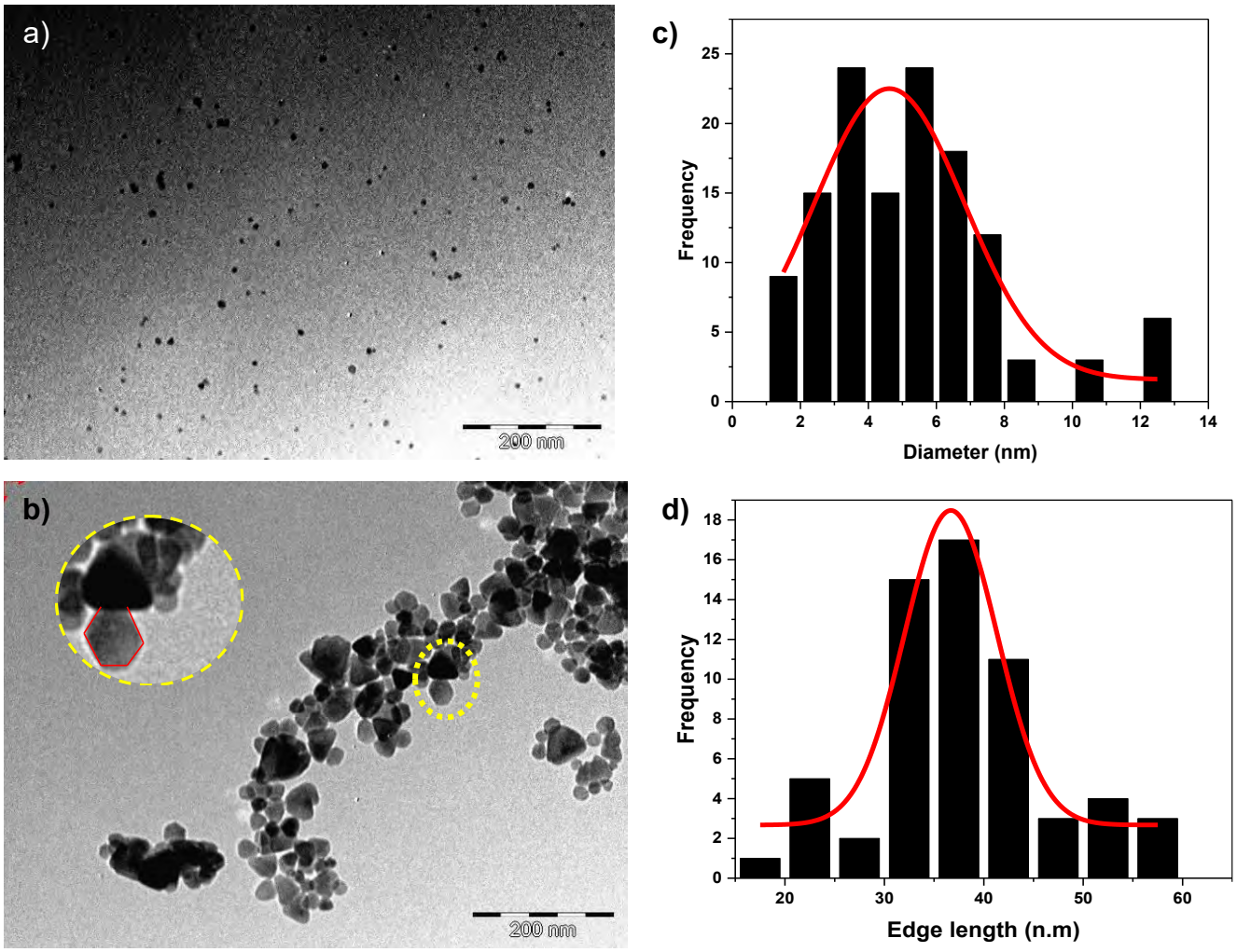

Figure 3.11: TEM images and corresponding histograms of APTES coated NH_2-ZnONSps (a, b) and NH_2-ZnONPys (c,d), insert: show the top and side view of the NH_2-ZnONPys.

3.5.6 XRD

The XRD patterns of ZnONPys, NH_2-ZnONPys, and **6-ZnQ**-ZnONPys were investigated. The ZnONPys showed the expected characteristic diffraction peaks of a ZnONPs at 100, 002, 101, 102, 110, 103, 200, 112, 004, and 202, respectively, **Figure 12(a)**. No other peaks were observed on the XRD pattern of ZnONPys, confirming the formation of pure phase ZnONPs. The same XRD patterns were observed for NH_2-ZnONPys and **6-ZnQ**-ZnONPys, with the **6-ZnQ**-ZnONPys conjugate revealing an additional broad peak at 2θ =17° attributed to the presence of the MPc. The broad peak is an indication of the amorphous nature of the MPcs. The ZnONSps series retained the same XRD pattern (not shown). However, all the ZnONPys peaks were narrower when compared to the ZnONSps, confirming the difference in the crystal structures.

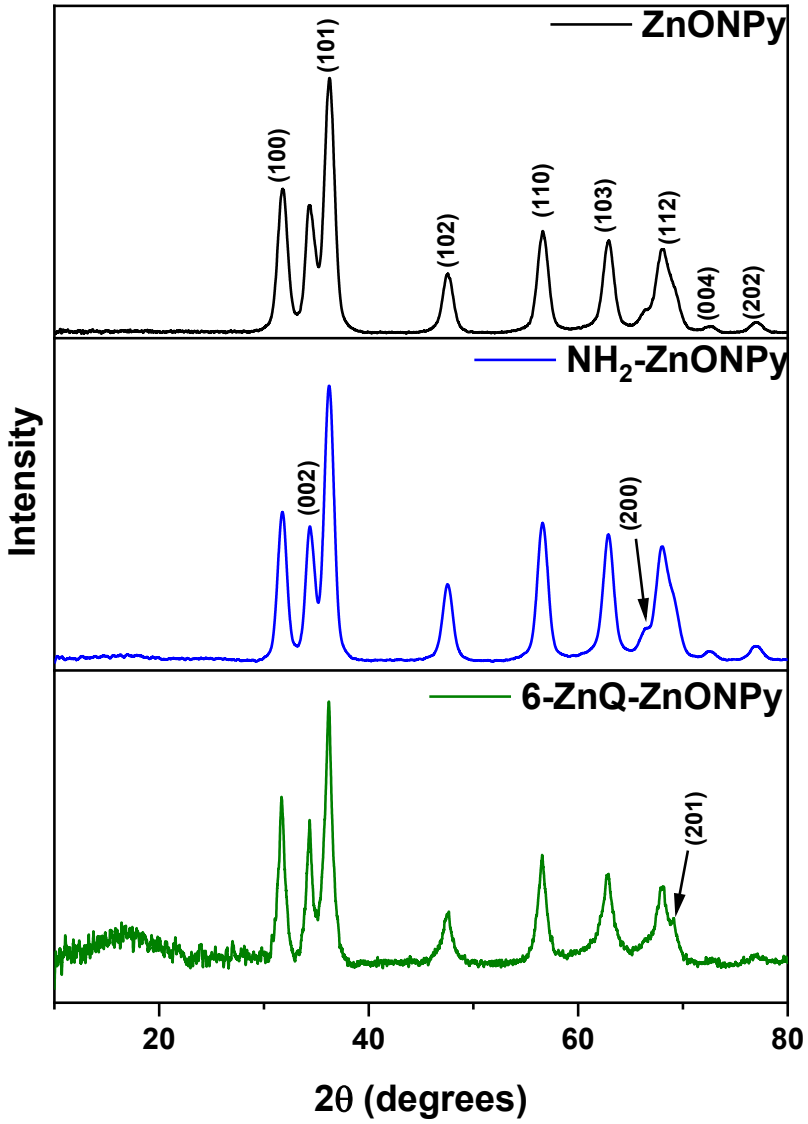

Figure 3.12: Powder XRD diffractograms of ZnONPys, NH_2-ZnONPys and **6-Zn**-ZnONPys.

3.4 Glass wool and Pc-conjugates

3.4.1 Synthesis

Commercial glass wool was functionalized with amine groups through the addition of APTES. The attachment of APTES to GW (**Scheme 3.9**) was achieved through self-assembly, as reported in the literature [188].

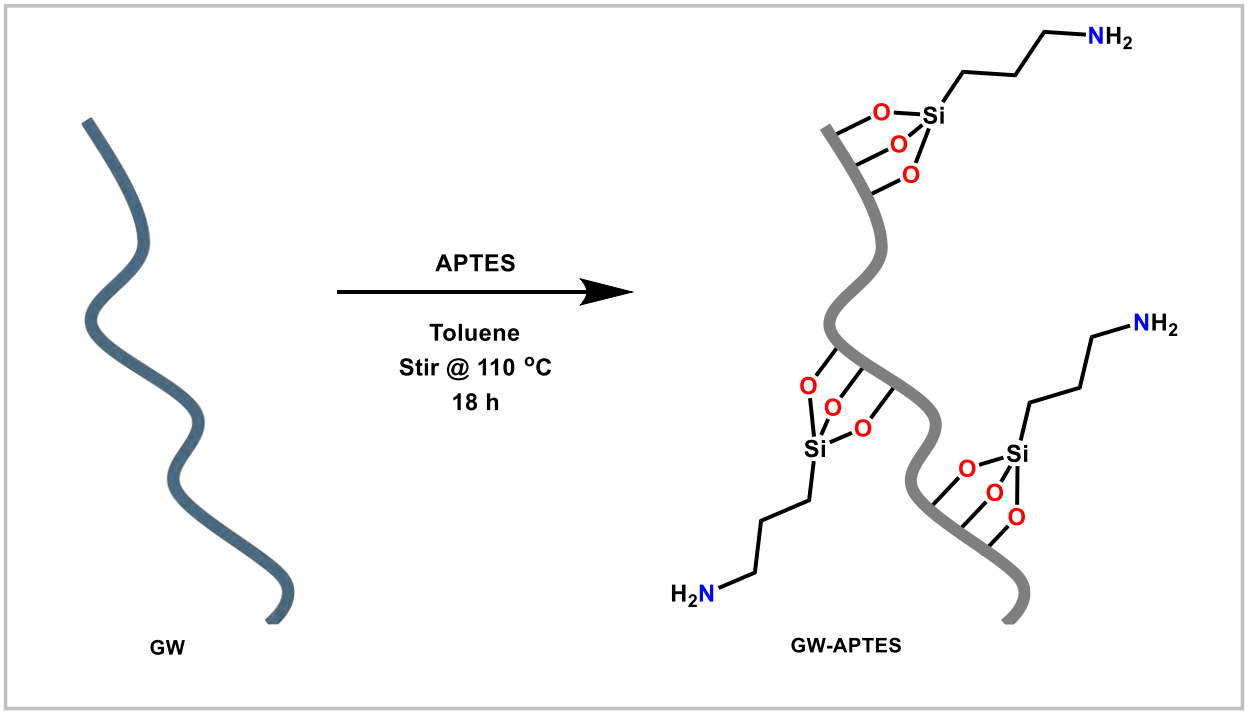

Scheme 3.9: Synthetic route illustrating the functionalization of glass wool with APTES.

The amount of APTES attached to GW was evaluated by ^{1}H NMR spectroscopy (**Figure 3.13**). Using the quantitative NMR method (and maleic acid as a standard), duplicates of each sample (GW-2-APTES, GW-4-APTES, and GW-8-APTES) were tested, as reported before [189]. GW-2-APTES showed no APTES content, meaning little or no APTES was attached to GW. For GW-4-APTES and GW-8-APTES, three individual signals

(multiplets) at 2.35-2.42, 1.29, and 0.27-0.23 ppm corresponding to the CH_2 peak present on the APTES can be distinguished. Quantitative analysis of the APTES content indicates that only in GW-4-APTES is APTES present in close to its monomeric form, and this is shown by the reproducible results as depicted by the integral (**Figure 3.13 B-C**). The GW-8-APTES support, however, exhibited less resolved peaks with high integrals (**Figure 3.13 D-E**), suggesting the presence of APTES in a polymerized form. Henceforth, only the results for GW-4-APTES (0.96 mg (2.8 WT%) of APTES in 34 mg of GW) will be discussed, and GW-4-APTES is referred to as APTES-GW.

(A) GW-2-APTES

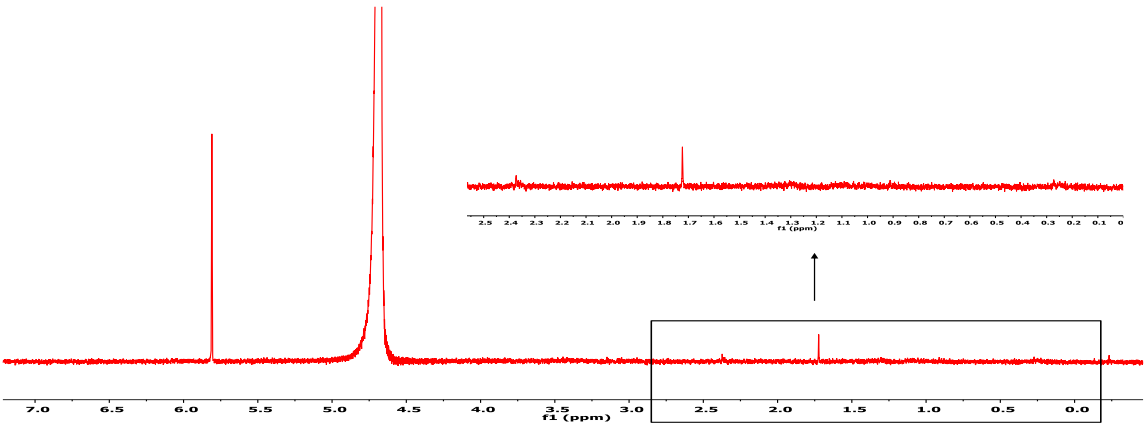

(B) GW-4-APTES – Trial 1

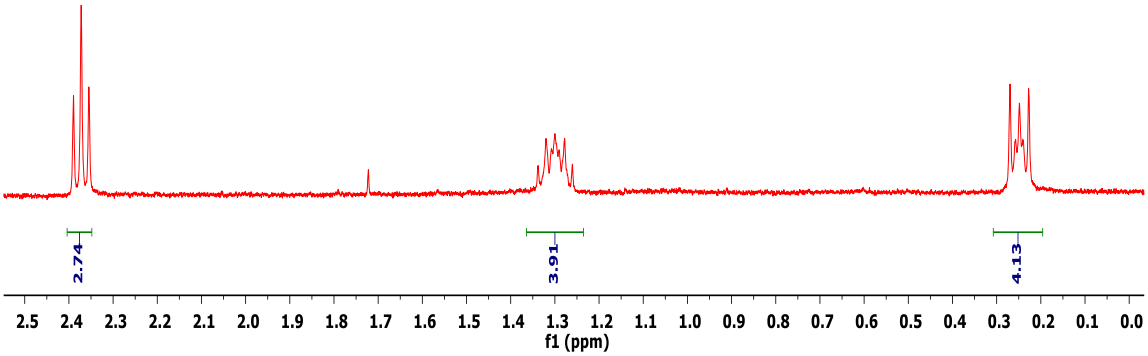

(C) GW-4-APTES – Trial 2

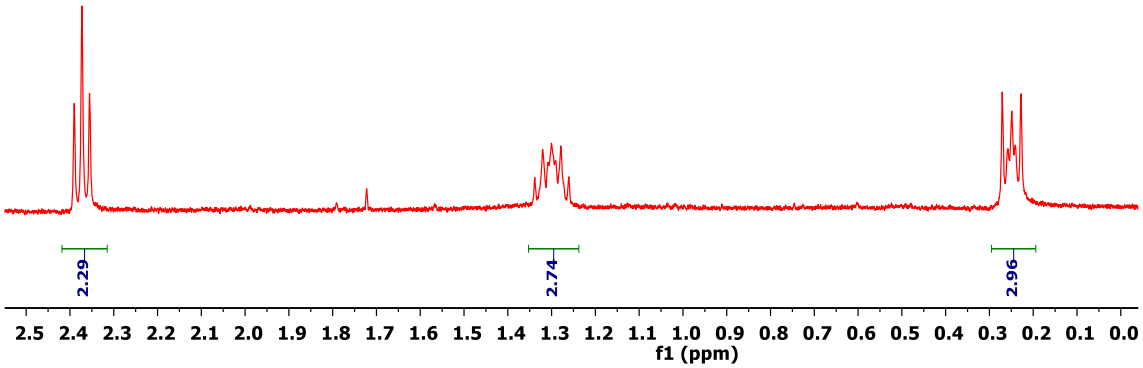

(D) GW-8-APTES – Trial 1

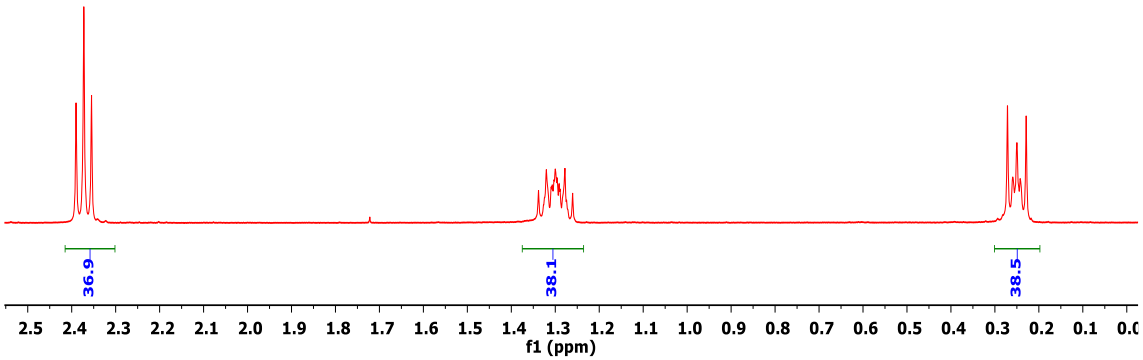

(E) GW-8-APTES – Trial 2

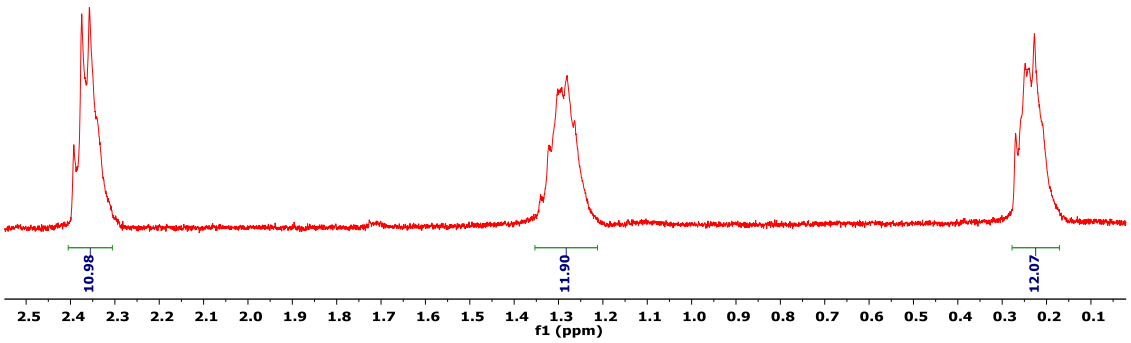

Figure 3.13: ^{1}H NMR spectra of (A) GW-2-APTES, (B-C) GW-4-APTES, trials 1 and 2, (D-E) GW-8-APTES, trials 1 and 2. Solvent = 0.4 M NaOD using 80 mM maleic acid as a standard.

The formation of **Pc-GW** was facilitated by the reaction between amino-containing glass wool and the COOH-containing Pc complex, **7-Zn**, **7-In**, **7-ZnQ**, **7-InQ**, **8-Zn**, **9-Zn**, and **10-Zn**, **Scheme 3.10.** The composites were characterized using solid-state UV-vis and SEM. The formation of the amide bond was confirmed via XPS and FTIR spectra. The loading of the Pcs onto the support was determined using TGA.

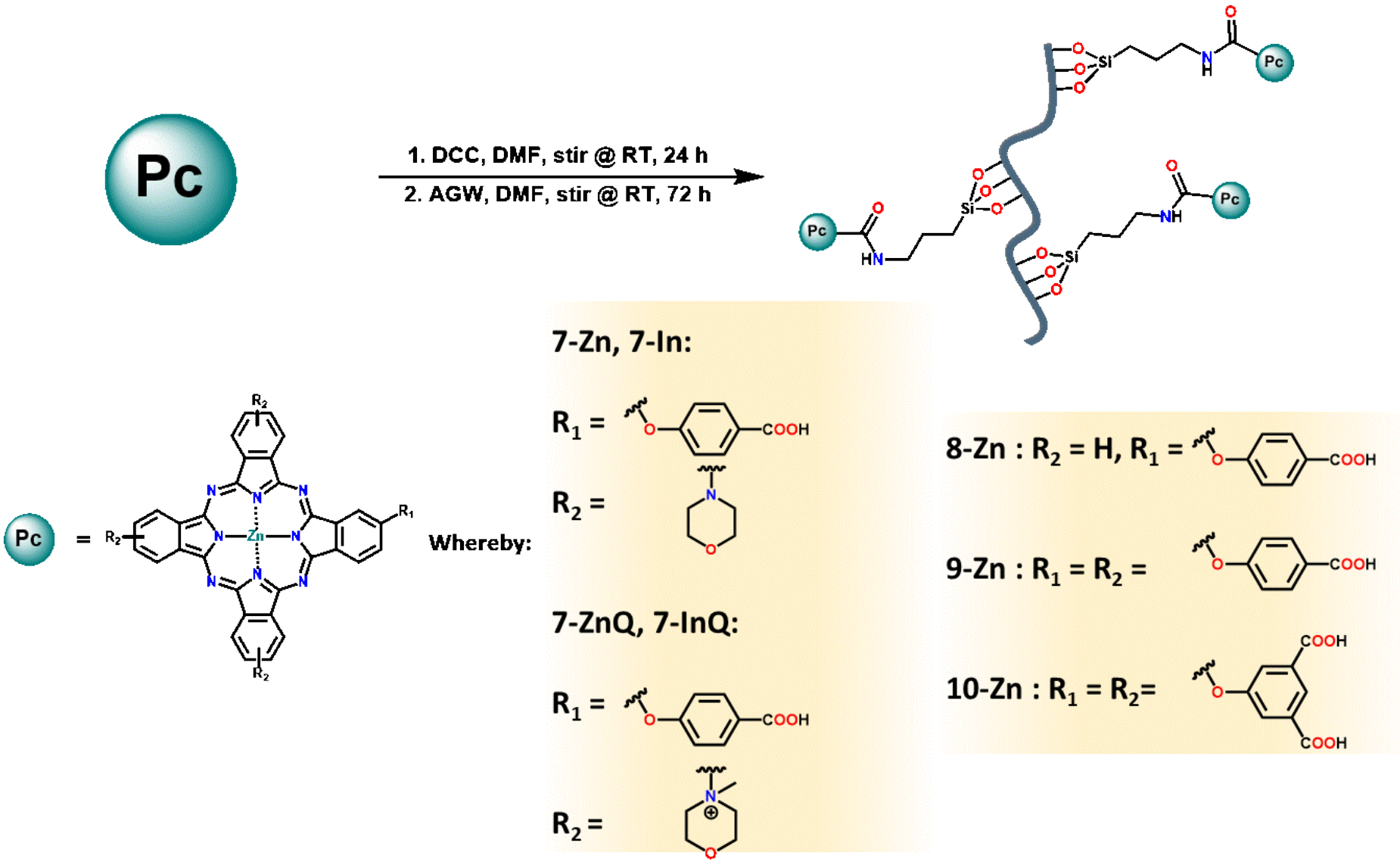

Scheme 3.10: Conjugation of glass wool to phthalocyanine through amide bond formation. AGW = APTES-GW.

3.4.2 Physical appearance of GW and conjugates

The physical appearance of untreated GW, APTES-GW, **8-Zn**-GW, **9-Zn**-GW, and **10-Zn**-GW is shown in **Figure 3.14**. The modified glass wool maintains a similar physical appearance as the pristine glass wool.

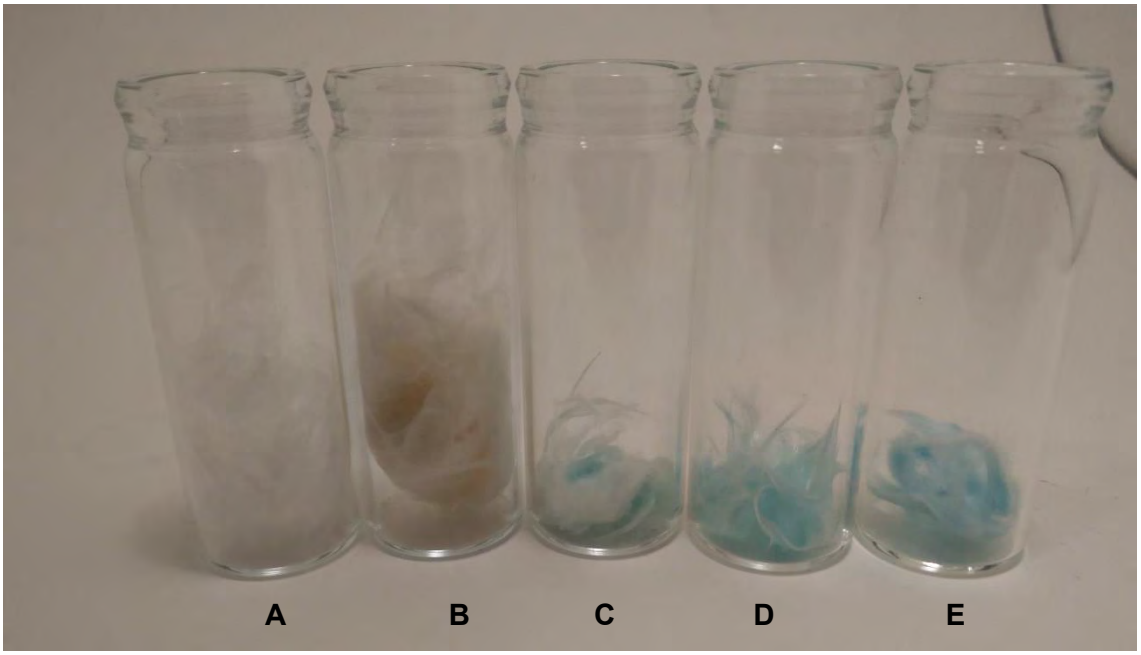

Figure 3.14: Glass wool images of (A) GW, (B) APTES-GW, (C) **8-Zn**-GW, (D) **9-Zn**-GW, and (E) **10-Zn**-GW.

3.4.3 SEM, and EDX

The morphologies of the glass wools were assessed by SEM, and the micrographs are presented in **Figure 3.15**. Pristine GW shows a glass fiber with small NaCl crystalline particles attached [110]. Upon modification, the GWs retain the same roughness and diameter of the glass fiber. Using ImageJ software, the diameters of the composite were measured, and the diameter of all Pc-GW conjugates was 9.25 μm. The estimated elemental composition for GW, APTES-GW, **10-Zn**, and **10-Zn**-GW was determined by EDS and is shown in **Figure 3.16**. EDX analysis shows that commercial glass wool contained various elements, including Na, Si, and Ca. Upon modification with APTES, there was evidence of N content and an increase in the intensity of Si, confirming the presence of APTES in the glass wool. The **10-Zn**-GW- spectrum shows an increased intensity of N (compared to APTES-GW) and a Zn peak, attributed to the conjugation of the zinc phthalocyanine.

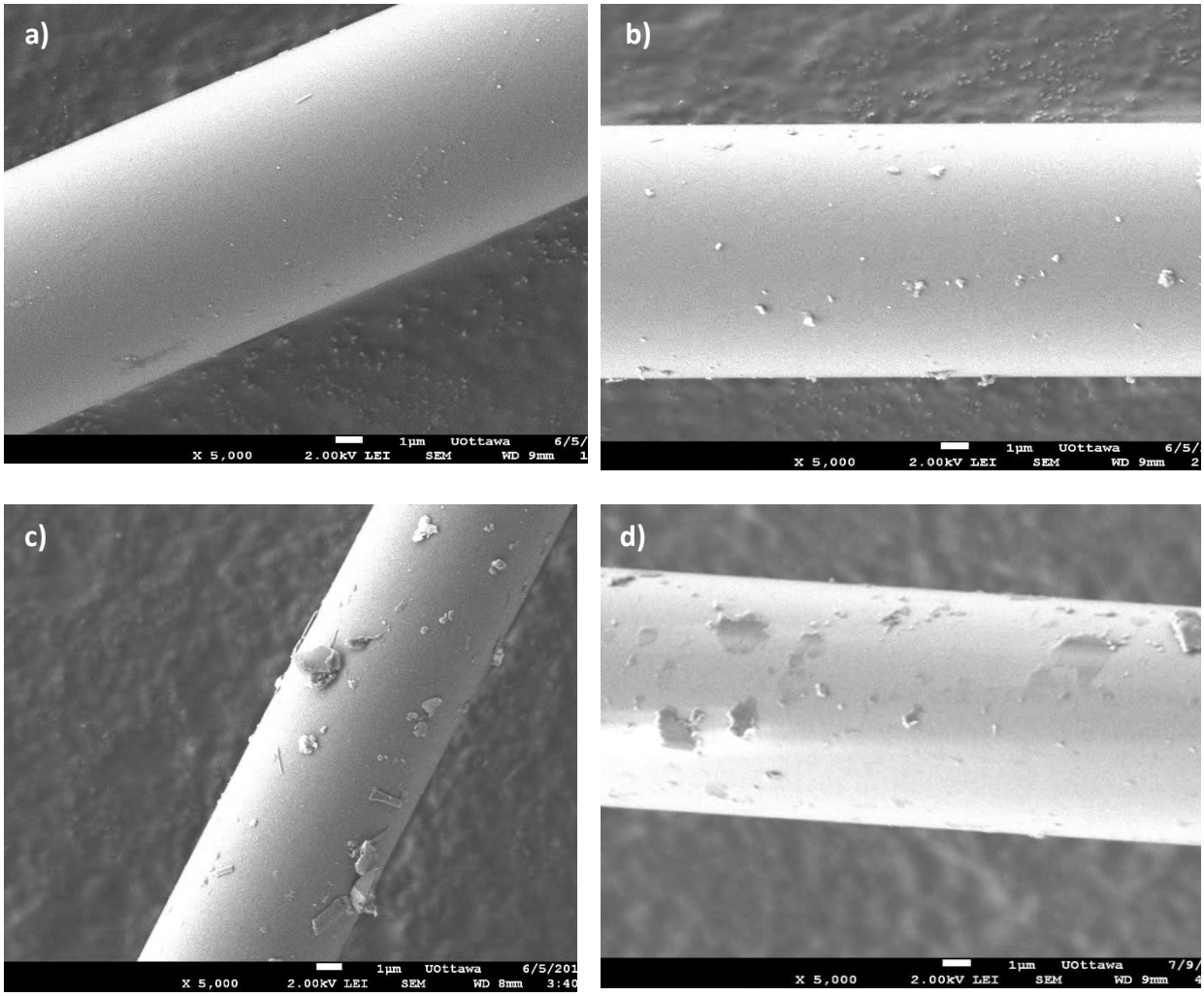

Figure 3.15: SEM micrographs for a) GW, b) APTES-GW, c) **8-Zn**-GW, and d) **9-Zn**-GW.

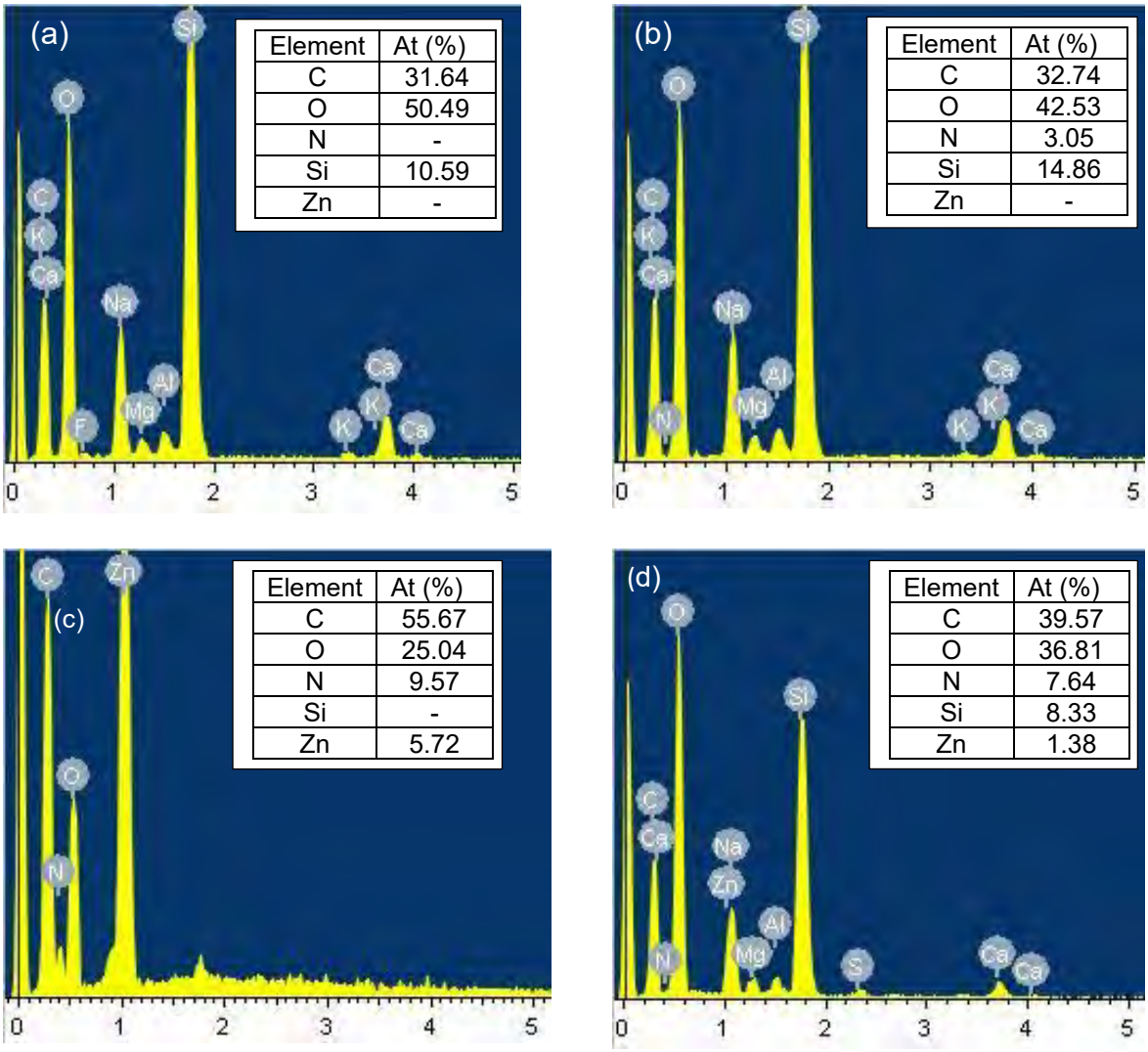

Figure 3.16: EDX spectra of (a) GW, (b) APTES-GW, (c) **10-Zn**, and (d) **10-Zn**-GW.

3.4.4 ToF-SIMS

ToF-SIMS was used to study the mass distribution of GW, APTES-GW, and **9-Zn**-GW, **Figure 3.17**. The positive mode was used to assess the intensities of CH_3O^+ (m/z = 31.03) and $C_3H_7^+$ (m/z = 43.09), which are characteristic peaks for APTES [**190**], and the negative mode was used to identify CN^- (m/z = 26.02) used as a marker for ZnPc [**191**]. As demonstrated in **Figure 3.17**, $C_3H_7^+$ ions were present in all samples and increased upon adding APTES and the **9-Zn**. CH_3O^+ ions had a higher intensity in APTES-GW and were well distributed on the glass wool, confirming the presence of APTES. The decrease in intensity (compared to APTES-GW) observed for both $C_3H_7^+$, and CH_3O^+ masses on **9-Zn**-GW is due to **9-Zn** covering some $C_3H_7^+$ / CH_3O^+ rich regions. The CN^- ions increased (compared to APTES-GW) by three folds following conjugating to CN^- rich **9-Zn**.

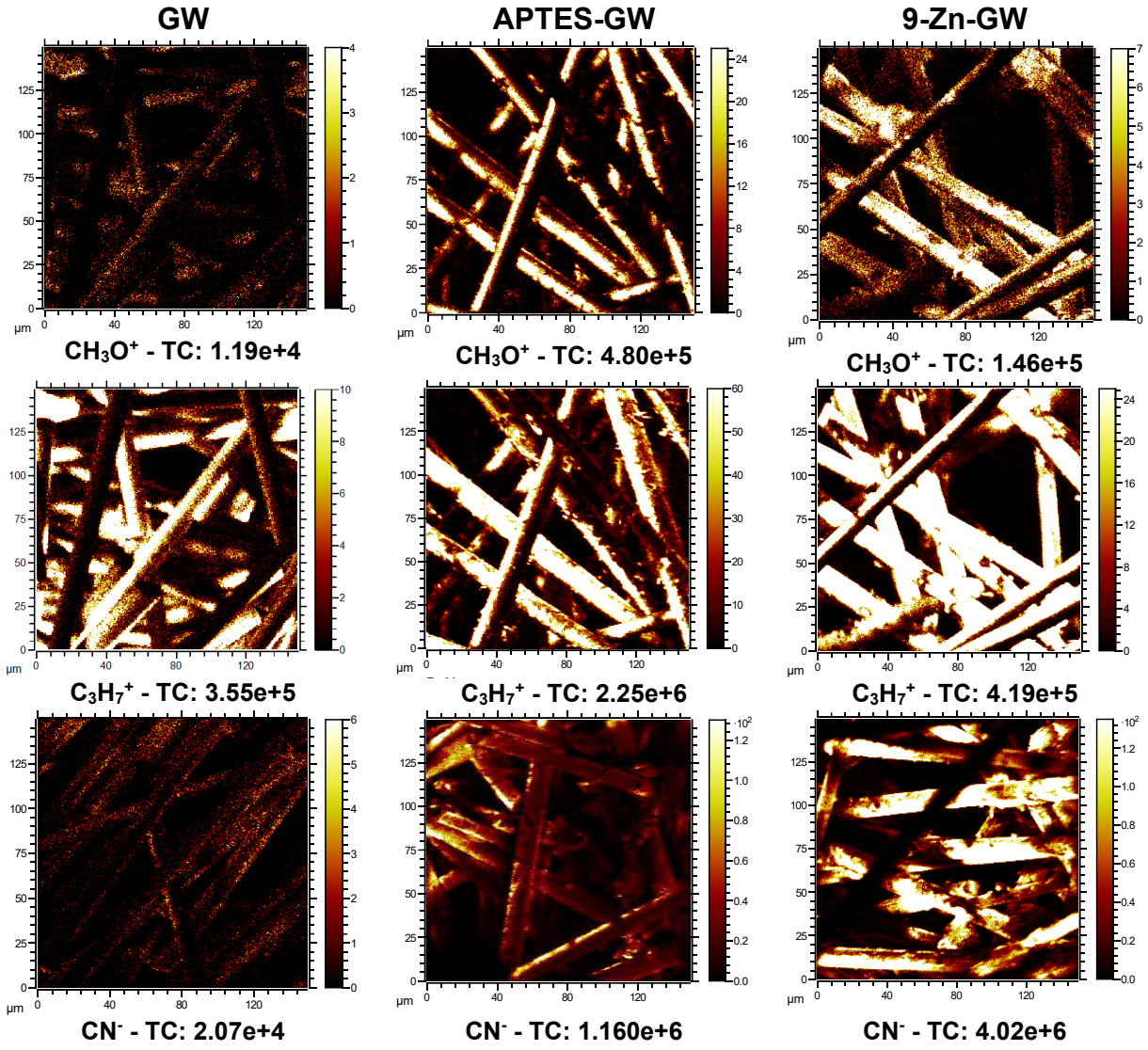

Figure 3.17: ToF-SIMS images of GW, APTES-GW, and **9-Zn**-GW. The image area was 150 µm×150 µm, and the total ion dose was ~1.79 × 10^{13} ions/cm^2.

3.4.5 XPS and FT-IR

XPS was used to analyze the chemical composition of the untreated and treated glass wool composites. The deconvoluted C1s and N1s spectra of GW, APTES-GW, **8-Zn**, and **8-Zn**-GW are shown in **Figure 3.18**. The C 1s of GW showed two signals at 282.7 and 283.9 eV corresponding to C-C and C-H bonds, respectively [192], while the N 1s depicted no signal complimenting the EDX results. The C 1s spectra of the APTES-GW showed an additional peak at 286.3 eV related to the C-N peak arising from the attachment of APTES to the glass wool [193]. The high-resolution N 1s spectrum for APTES-GW exhibited two peaks at 397.3 and 398.9 eV, assigned to $-NH_2$ and NH_3^+ [194], respectively. Typical C 1s and N 1s spectra were obtained for a carbonyl-containing Pc, whereby three peaks at 283.3 (C-C), 285.2 (C=N), and 287.1(COOR) eV were obtained for C1s, and two peaks at 397.9 (C-N=C), and 399.4 (N-H) eV were observed for N 1s [195, 196]. The high-resolution spectra were further used to prove the formation of an amide bond between the Pcs and APTES-GW. The deconvoluted N 1s spectrum for **8-Zn**-GW showed an additional peak at 400 eV, corresponding to the N-C=O bond. Similar trends were observed for the **7**-GW conjugates.

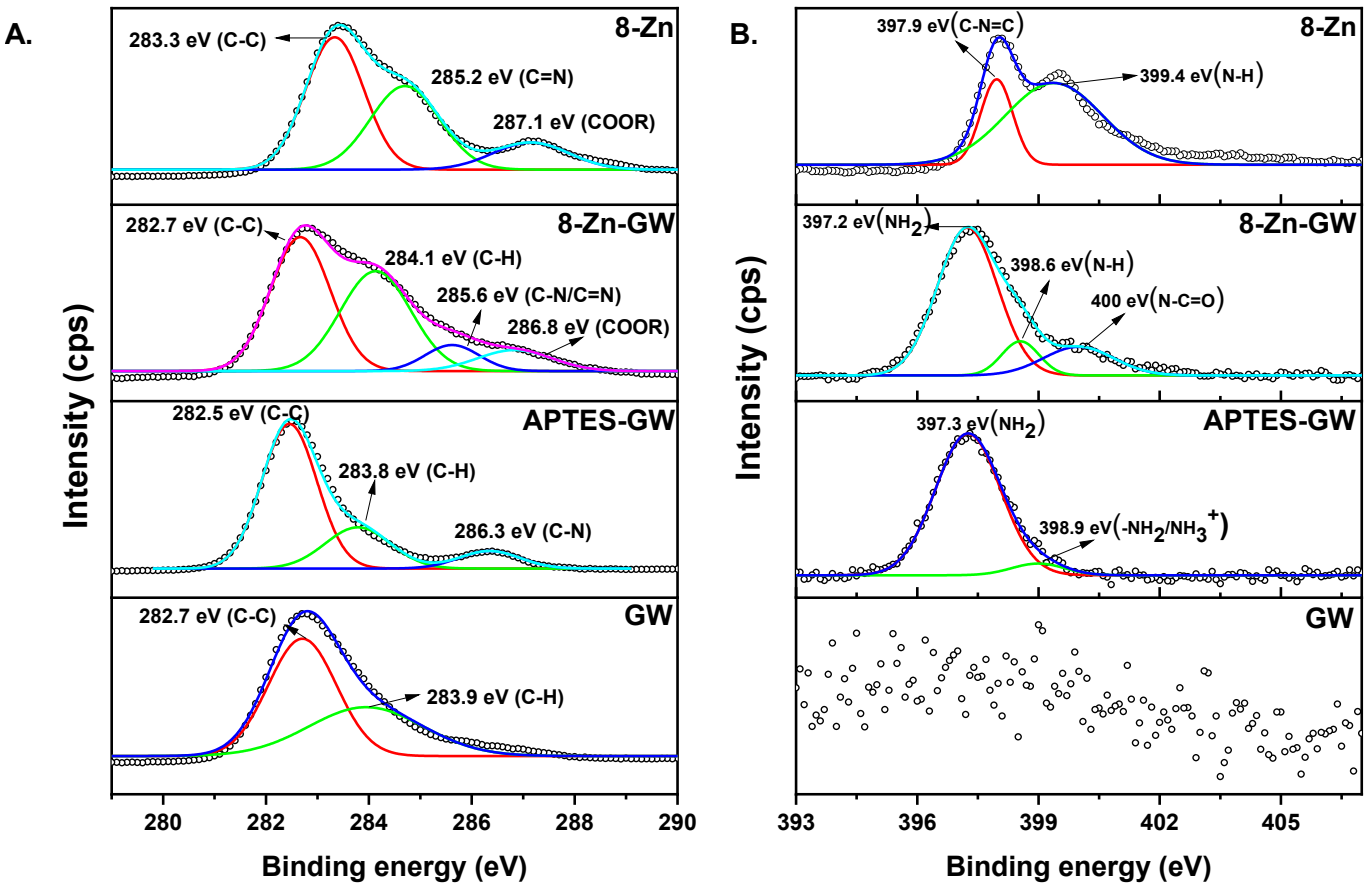

Figure 3.18: The deconvoluted (A.) C1s and (B.) N1s XPS spectra of GW, APTES-GW, **8-Zn**-GW, and **8-Zn**.

Furthermore, the FT-IR spectra of **7-Zn**, APTES-GW, and **7-Zn**-GW is shown in **Figure 3.19**. The APTES-GW composite showed peaks at 3362 cm^{-1}, and 3236 cm^{-1} respectively, corresponding to $-NH_2$. After the introduction of the Pc complex, the composite exhibited a peak at 1698 cm^{-1} related to the formation of an amide bond, complimenting the XPS results.

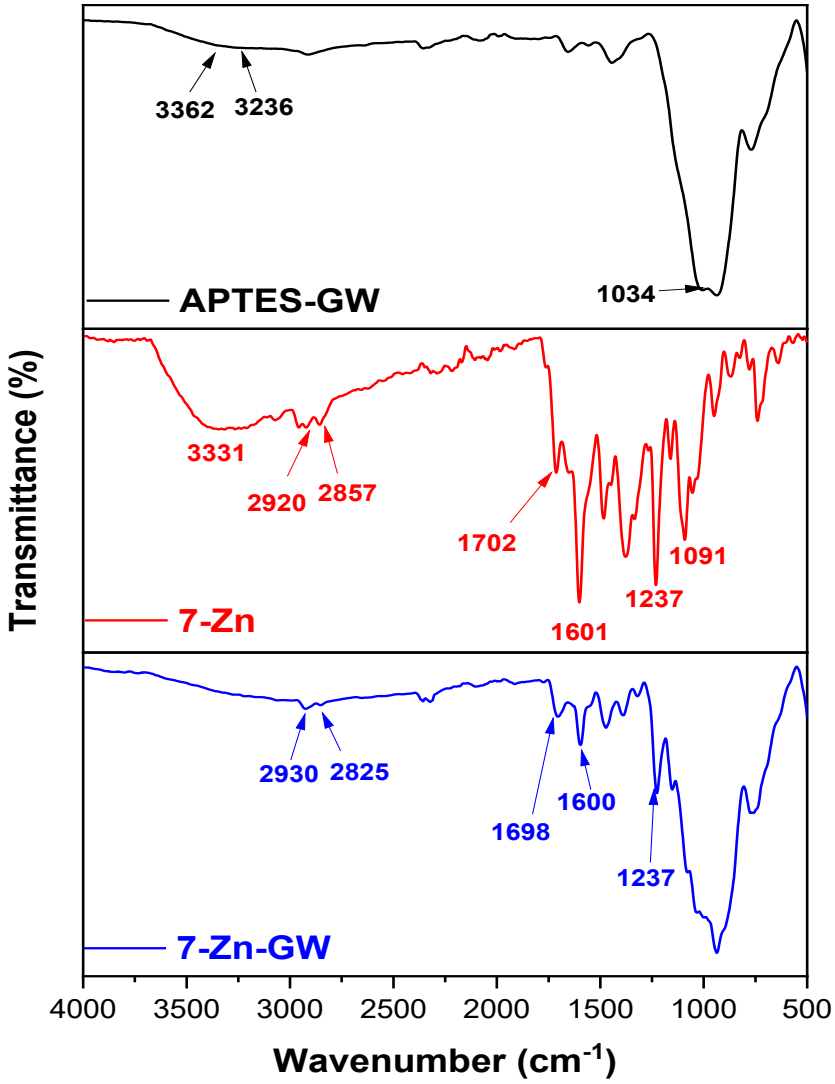

Figure 3.19: FT-IR spectra of **7-Zn**, APTES-GW, and **7-Zn**-GW.

3.4.6 TGA

The loading of the Pc complexes onto the glass wool was determined using the TGA method whereby the thermal decomposition profile of the Pc complexes was compared to the thermal decomposition of composites [197]. The TGA thermograms of APTES-GW (TGA profile for GW was similar to the APTES-GW; hence GW is not included in the plot), **8-Zn**, and **8-Zn**-GW are shown in **Figure 3.20(a)** in the range of 50-800 ºC under a nitrogen atmosphere. The glass wool was very stable, showing a minor weight loss of 1.22%. Upon conjugation, **8-Zn**-GW showed an increase in the weight loss (4.22%) due to the presence of the Pc. TGA was further used to estimate the loading of the Pc complexes onto each support, and the Pc loading values are listed in **Table 3.3**. **8-Zn**-GW and **9-Zn**-GW had slightly higher values of 3.65 and 3.34 mg of Pc/g of GW, while **10-Zn**-GW had a lower value of 1.84. The lower loading observed for **10-Zn**-GW may be due to aggregation. The **7**-GW conjugates had a much higher Pc loading of 34.9, 33.8, 34.5, and 33.2 mg/g of GW for **7-Zn**-GW, **7-ZnQ**-GW, **7-In**-GW, and **7-InQ**-GW, respectively. Both complexes **7** and **8** are asymmetrical, hence, it was unexpected that the support containing the bulkier substituents (**7**-GW) would result in a higher Pc loading values.

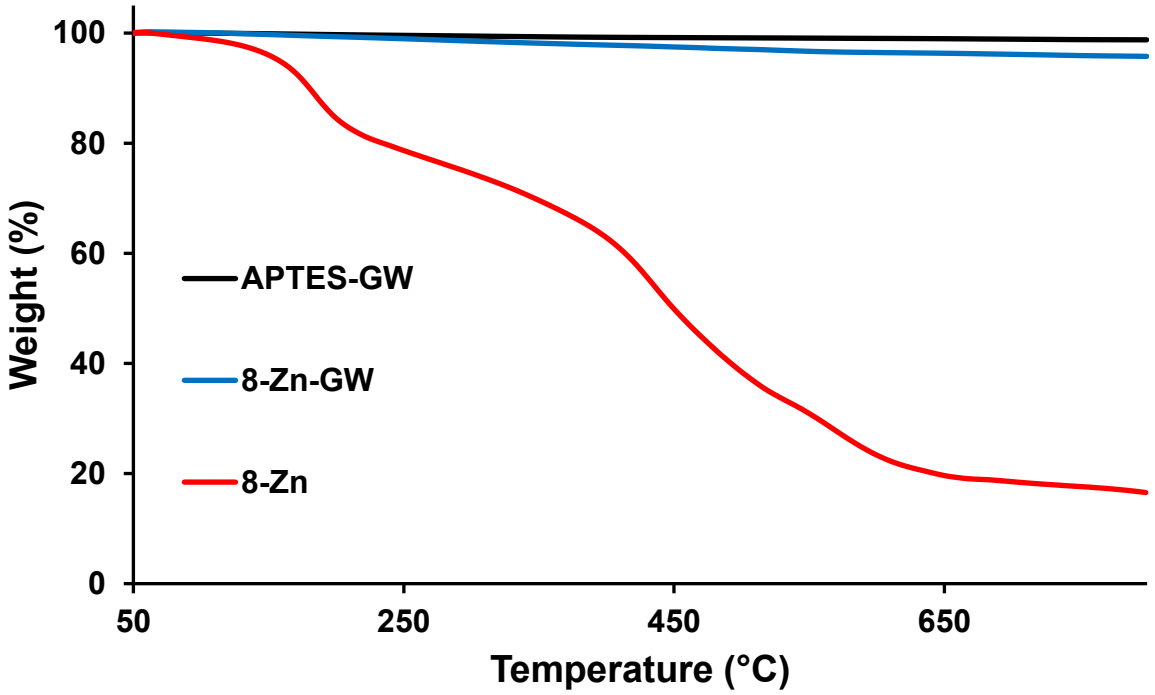

Figure 3.20: TGA thermograms of APTES-GW, **8-Zn**-GW, and **8-Zn**.

3.4.7 Solid-state UV-vis spectra

The solid-state UV-vis spectra of the composites were recorded to determine the profile of the phthalocyanine complexes anchored on the glass wool. As shown in **Figure 3.21** (**Table 3.3**), the spectra of the Pc-GW conjugates showed the characteristic phthalocyanine Q band, the Q band in the solid state is split due to aggregation, with the low energy peak being due to the monomer and the high energy peak being due to the aggregate. Aggregation is typical for Pcs in the solid state [198]. Redshifting of the Q band (the monomer peak) is also expected in the solid state compared to the solution [198]. Nevertheless, this redshifting is observed only for quaternized derivatives in **Figure 3.21(a)**, **Table 3.3**. Moreover, both **8-Zn**-GW and **9-Zn**-GW displayed a more pronounced Q band compared to **10-Zn**-GW. The broadening observed in the Q-band of **10-Zn**-GW can be attributed to the presence of aggregated phthalocyanines attached to the support, **Figure 3.21(b)**. APTES-GW (**Figure 3.21(b)**) showed a slight enhancement in absorbance compared to GW (**Figure 3.21(b)**) from 550 nm to 350 nm. After conjugation, the phthalocyanine profile is maintained for all conjugates.

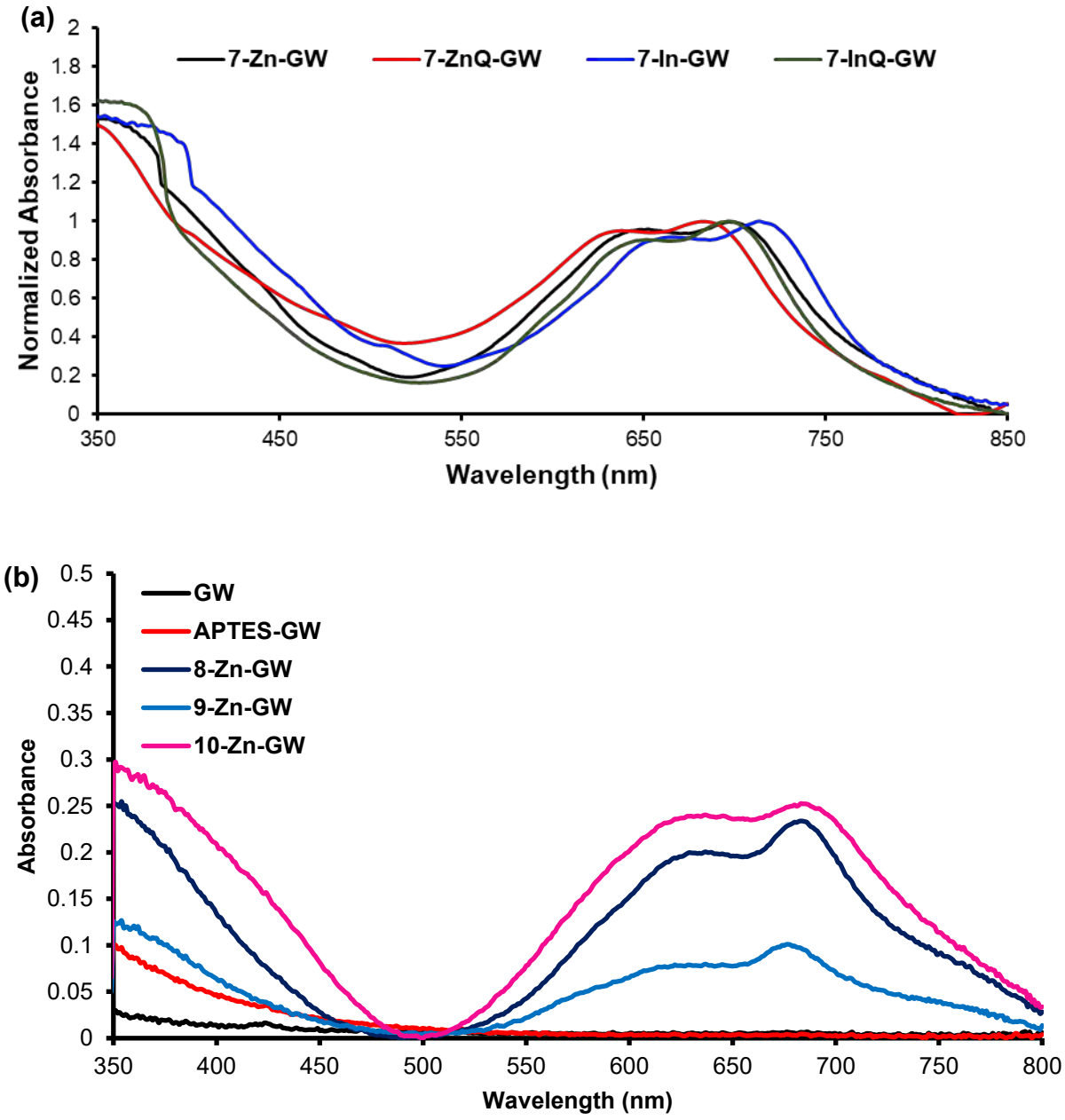

Figure 3.21: Solid-state UV-Vis spectra of (a) **7**-GW, and (b) **8-Zn**-GW, **9-Zn**-GW**, 10-Zn**-GW, GW, and APTES-GW.

Table 3.3: Summary of the characteristic properties of Pc-GW composites.

Sample	Loading (mg Pc/g Pc-GW) - TGA	λ_{max} (nm)[a]
7-Zn-GW	34.9	697 (710)
7-ZnQ-GW	33.8	682 (675)
7-In-GW	34.5	714 (727)
7-InQ-GW	33.2	697 (689)
8-Zn-GW	3.65	683 (674)
9-Zn-GW	3.34	680 (678)
10-Zn-GW	1.84	686 (680)

[a] Values in brackets are for Pc alone in DMSO

3.5 Nanofiber and Pc-conjugates

3.5.1 Synthesis

Commercially available polyacrylonitrile (PAN) polymer was modified to provide the possibility of chemical linking with chitosan and phthalocyanines to improve antibacterial properties. PAN-COOH, was synthesized as reported in literature [171]. Then, PAN-COOH was reacted with hydrazine (for PAN-NH_2) or chitosan (for PAN-CS) to form an amide bond, separately, **Scheme 3.11**. PAN-NH_2 was conjugated to the asymmetrical morpholino Pcs, **7** to produce **7-Zn**-PAN, **7-ZnQ**-PAN, **7-In**-PAN, **7-InQ**-PAN, **Scheme 3.12**. Furthermore, PAN-CS was also conjugated to complex **7** resulting in **7-Zn**-PAN-CS, **7-ZnQ**-PAN-CS, **7-In**-PAN-CS, **7-InQ**-PAN-CS, **Scheme 3.12**.

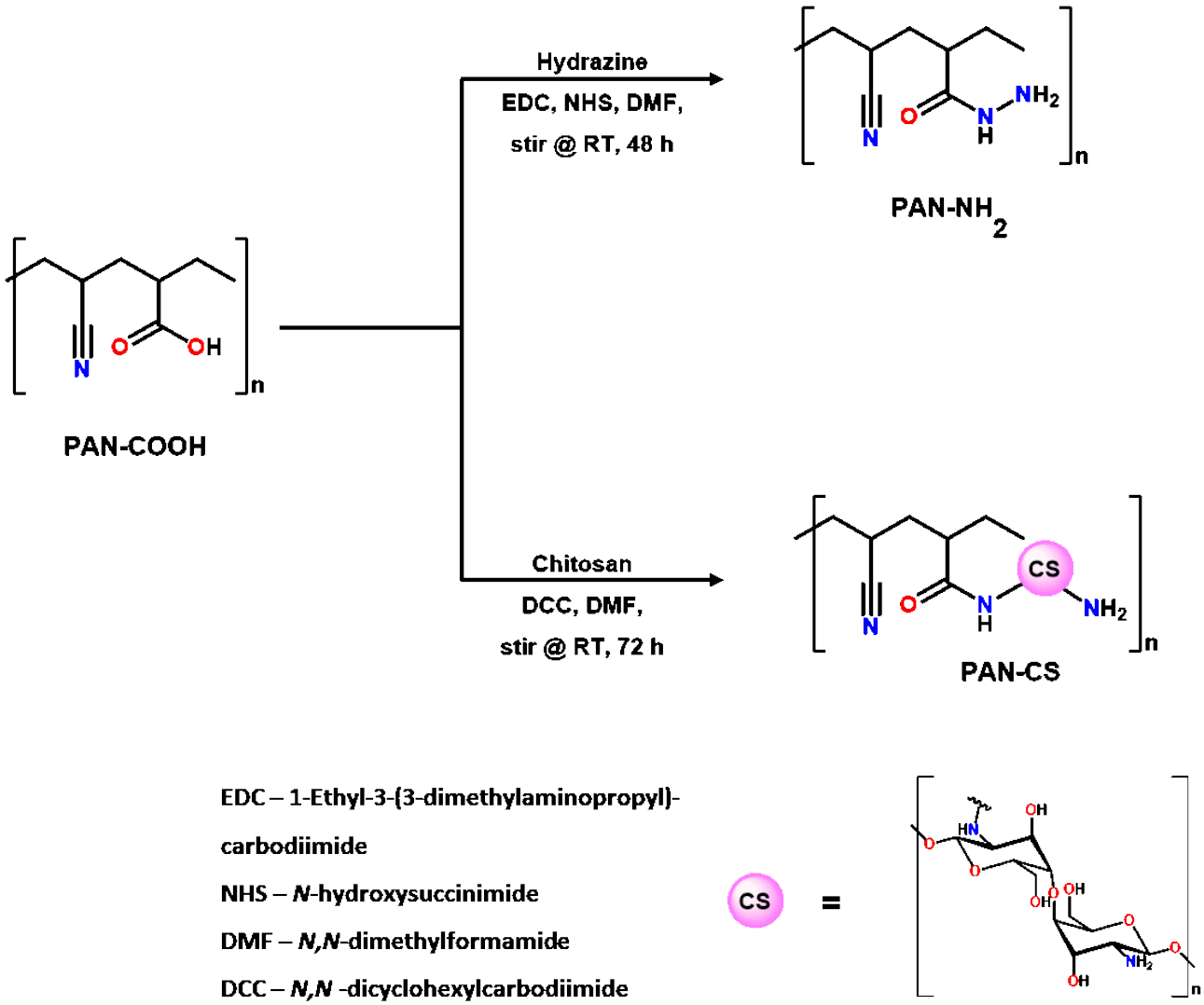

Scheme 3.11: Formation of PAN-NH_2 and PAN-CS polymers.

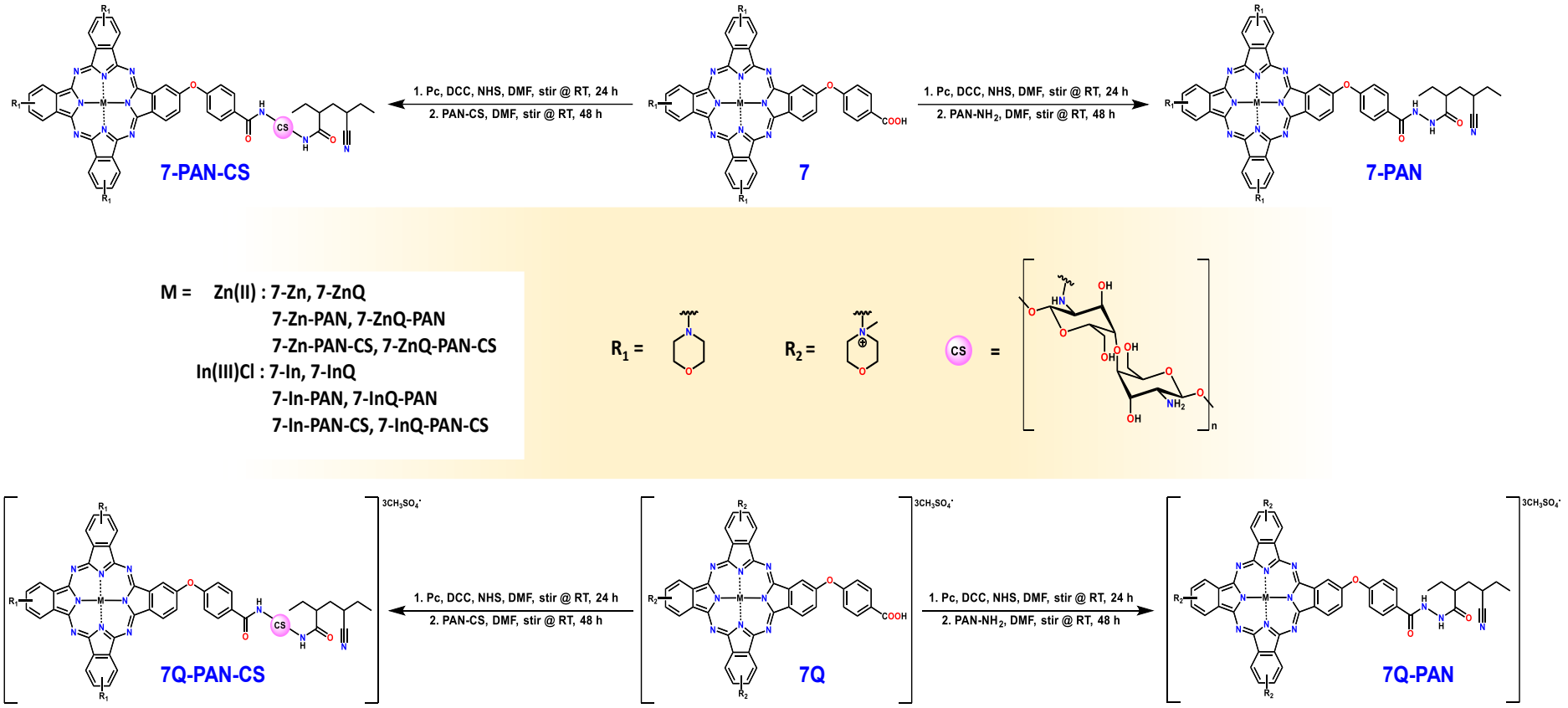

Scheme 3.12: Conjugation of complex **7** to PAN-NH_2 and PAN-CS.

3.5.2 FT-IR

FTIR analysis of the pristine and modified polymers was undertaken (**Figure 3.22**). **Figure 3.22(a)** represents the FTIR spectra of PAN, PAN-COOH, and PAN-NH_2. As expected, PAN revealed sharp peaks at 2934 cm^{-1} (attributed to -CH_2-), 2244 cm^{-1} (attributed to C≡N), and 1442 cm^{-1} (attributed to CH_2 and CH_3). The reduction in peak intensity of the C≡N band of PAN on forming PAN-COOH indicates successful hydrolysis. Moreover, PAN-COOH showed additional, broad peaks at 3317 cm^{-1} (attributed to -OH), 1702, and 1699 cm^{-1} (related to -C=O) due to the formation of -COOH. Amide bond formation between hydrazine and PAN-COOH (to form PAN-NH_2) was confirmed by the presence of -C=O at 1661 cm^{-1} and the two peaks at 3358 and 3207 cm^{-1} related to a free -NH_2.

Figure 3.22(b) represents the FT-IR spectra of PAN-COOH, CS, PAN-CS, and **7-Zn**-PAN-CS (used as an example). CS showed the expected peaks as previously reported; the peak at 1648 cm^{-1} shows the presence of an amine group [**199**]. The amide bond formation (to form PAN-CS) provided structural changes, which can be seen by the presence of amine stretch at 3325 cm^{-1}, nitrile peak at 2243 cm^{-1}, and C=O stretch at 1703 cm^{-1}. Upon conjugating PAN-CS to a Pc, the -NH_2 stretch of the former at 3325 cm^{-1} disappeared, and there was a broad peak at 3571 cm^{-1} attributed to Pcs. The peak at 1696 cm^{-1} shows the amide C=O bend confirming a covalent linkage. From the FT-IR spectra, **7-Zn**-PAN-CS maintained a similar profile to PAN-CS.

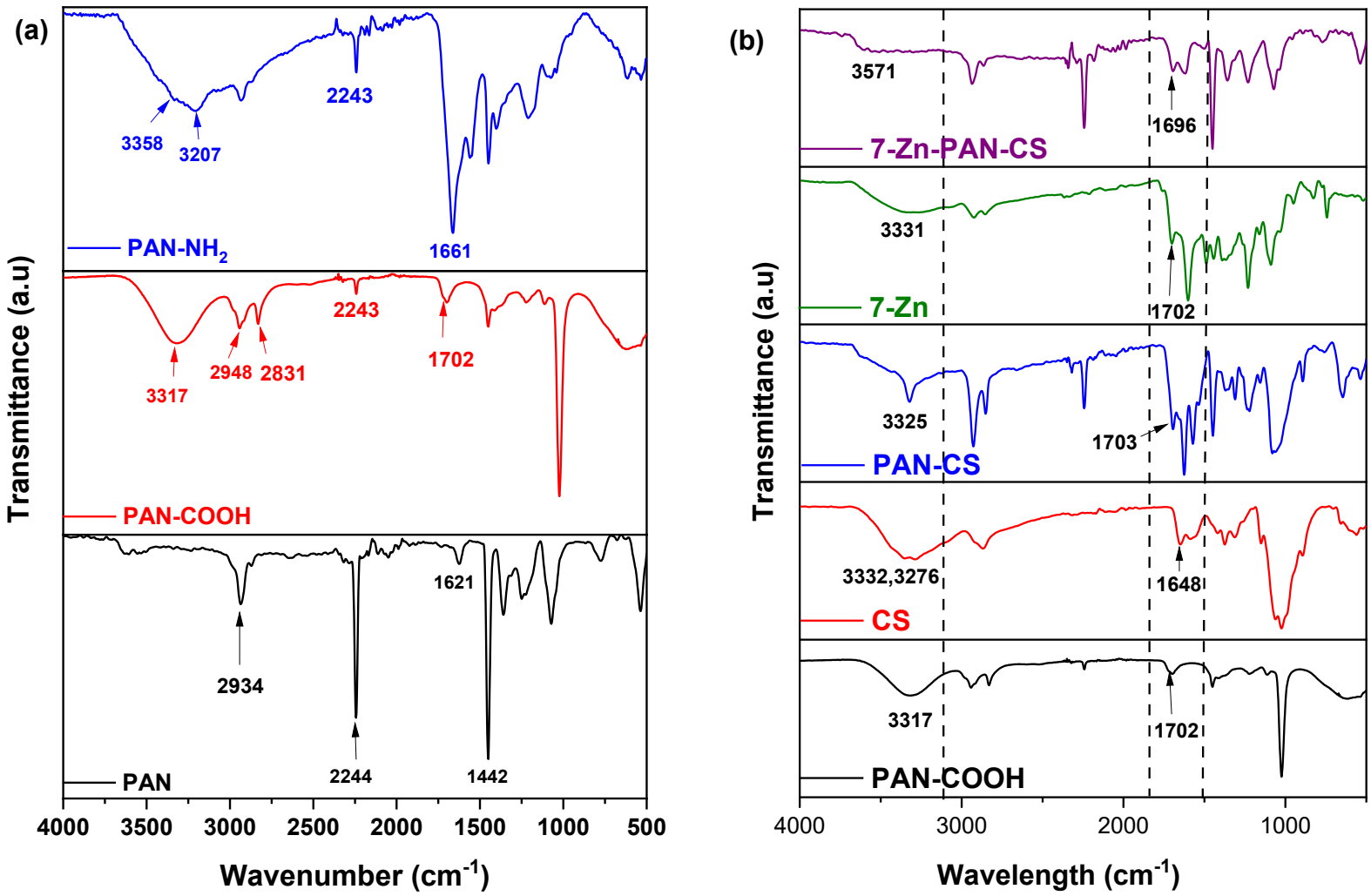

Figure 3.22: FT-IR spectra of (a) PAN, PAN-COOH, PAN-NH_2, and (b) PAN-COOH, CS, PAN-CS, **7-Zn**, and **7-Zn**-PAN-CS.

3.5.3 TGA

The loading quantities were determined via thermogravimetric analysis as reported before [185, 200]. Examples of the TGA plots are shown in **Figure 3.23**. The weight loss below 200 ºC could be from the loss of moisture [201]. The TGA curve of PAN-CS (same curve as PAN-NH_2) revealed a typical two-step degradation process of the PAN polymer, the polymer showed significant weigh loss from 298 °C due to loss of volatile gases and breaking of the PAN macromolecular chain [202, 203]. PAN-CS was more stable than the Pc (**7-Zn**) and **7-Zn**-PAN-CS for most of the heating temperature. As shown in **Table 3.4**, the loading amount are similar for conjugates ranging from 14.8 to 16.3 mg Pc/g **Pc-**PAN-CS and 50.7 to 52.8 mg Pc/g **Pc-**PAN. The quaternized Pcs had a slightly lower loading due to charge repulsion [204].

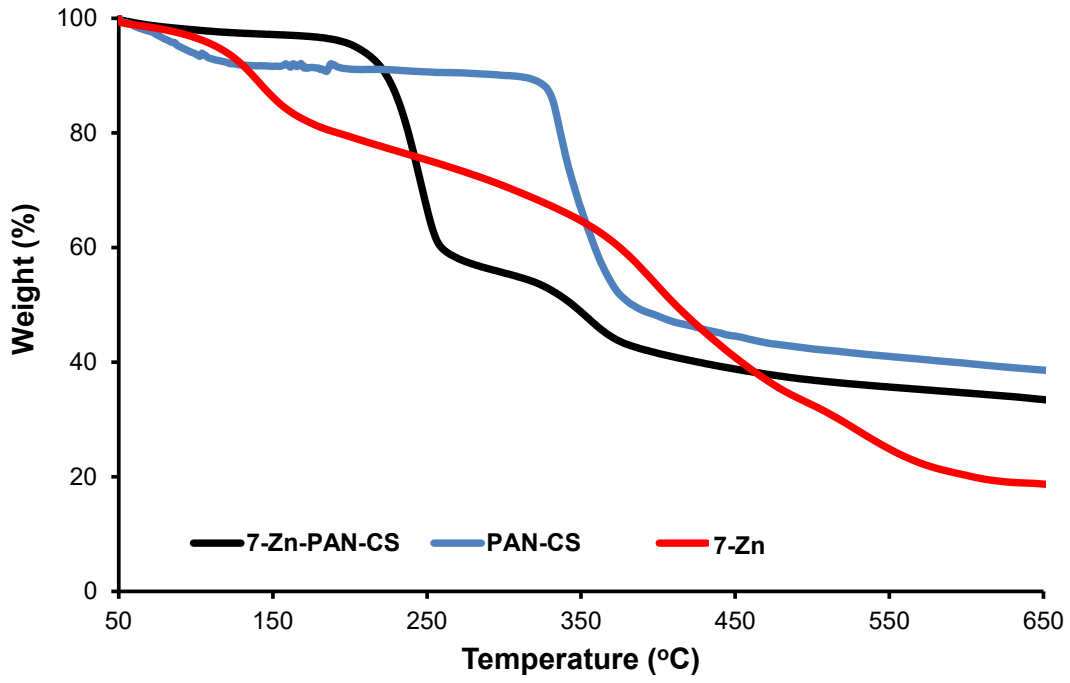

Figure 3.23: TGA thermograms of **7-Zn, PAN-CS**, and **7-Zn-PAN-CS**.

3.5.4 XPS

XPS was utilized to characterize the chemical composition of each sample. High-resolution C1s were used to support the formation of the initial amide bond between the amine groups from chitosan and the -COOH moiety from PAN-COOH and the spectra are shown in **Figure 3.24**. The spectrum of PAN-COOH shows four deconvoluted peaks at 283.3, 284.7, 287.1 and 288.9 eV, assigned to C-C, C-N, C=O, and -COOH. As expected, three peaks are obtained for chitosan found at 282.8, 284.3, and 285.7 eV related to C-C, C-N, and C-O [**205**]. After covalently linking CS to PAN-COOH to form PAN-CS, five peaks with an additional peak at 289.3 eV (attributed to the presence of the amide bond [**206**]. N1s was also used to identify the bonds formed and to compare the intensity of the two amide bonds formed. **Figure 3.24** shows the high-resolution N1s spectrum of **7-Zn**, PAN-CS, and **7-Zn**-PAN-CS. Complex **7-Zn** alone showed three deconvoluted peaks at 398.0, 399.4, and 401.0 eV related to N=C, -N- and -HN-C, while PAN-CS, two peaks were observed at 397.8 and 400.5 arising from the combination of N-H/N-C and O=C-N signals. The conjugate, **7-Zn**-PAN-CS, depicted three peaks at 397.9, 399.9 and 402.0 eV confirming the presence of N=C, -N/-HN-C and O=C-N. The initial amide bond formed found in PAN-CS, had an intensity of 1140 cps, after conjugating complex **7-Zn** to PAN-CS, the intensity of the amide bond increased to 2010 cps confirming the linkage since there is an increase in the amide bonds [**207**].

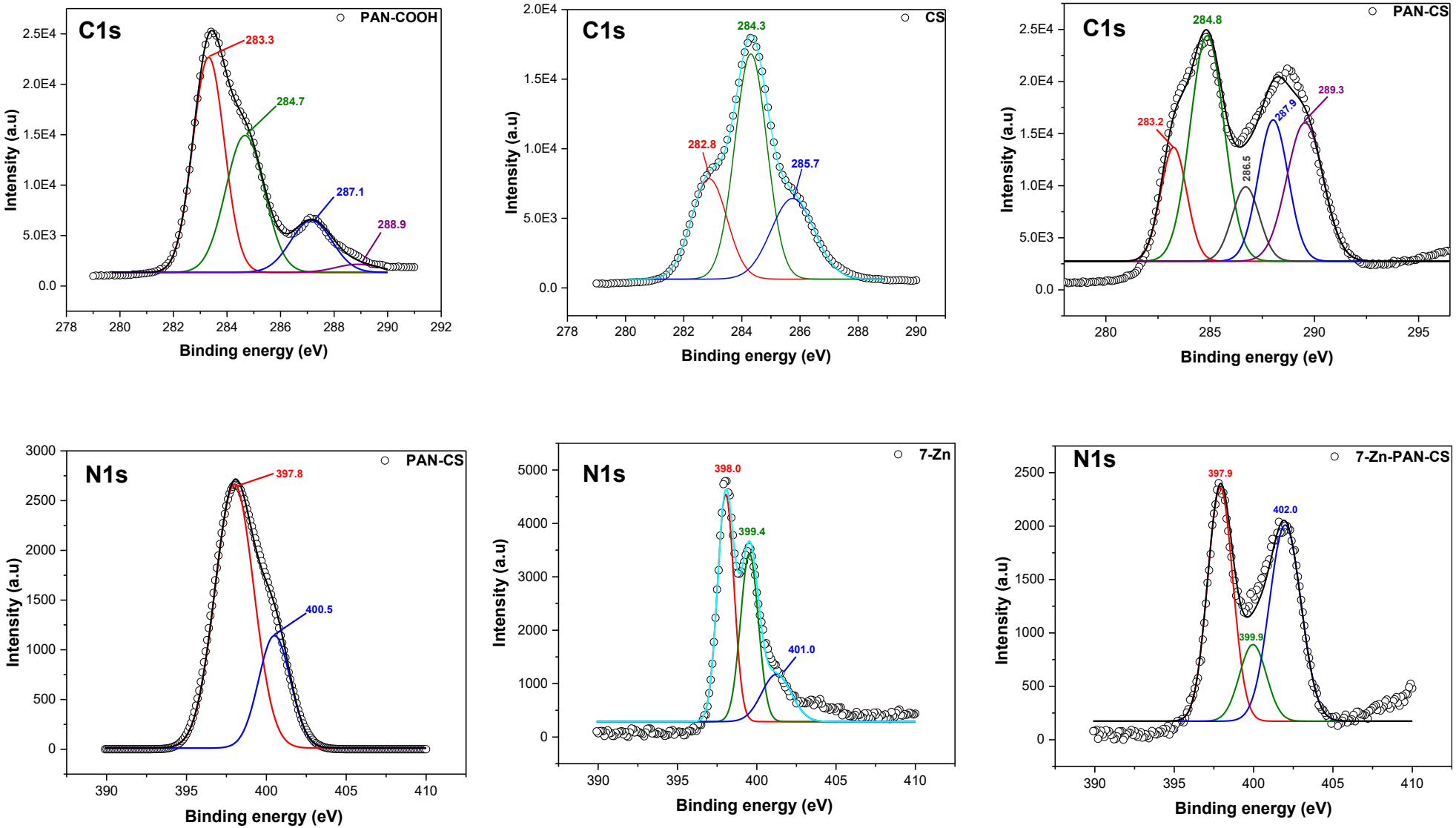

Figure 3.24: C1s spectra of PAN-COOH, Chitosan, PAN-Chitosan, and N1s spectra of PAN-CS, **7-Zn and 7-Zn**-PAN-Chitosan.

3.5.5 Scanning electron microscope (SEM)

The SEM images of the electrospun nanofibers are shown in **Figure 3.25**. The SEM images reveal that the nanofibers are cylindrical. The nanofiber diameter increased from an average diameter of 905 nm to 1175 nm after conjugating PAN-CS to complex **7-Zn**, a similar trend was observed for the remaining complexes and the results are summarized in **Table 3.4**. This increase indicates that the complexes are incorporated into the nanofibers. Furthermore, the micrographs show smooth unbranched nanofibers, typical of PAN nanofibers [208] and chitosan-based nanofibers [209].

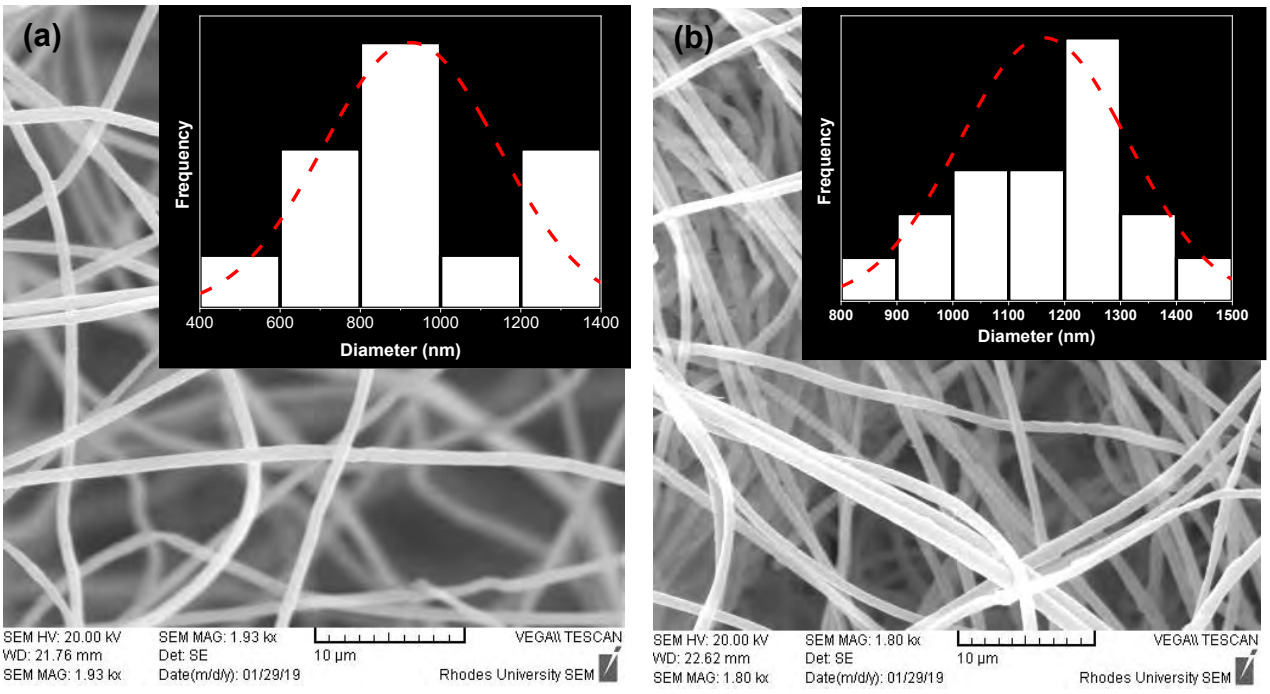

Figure 3.25: SEM micrographs of (a) PAN-CS and (b) **7-Zn**-PAN-CS.

3.5.6 BET

The N_2 adsorption-desorption isotherms were obtained via BET, the analysis shows a type IV IUPAC classification [210]. As an example, the adsorption-desorption isotherms of complex **7-Zn**, PAN-CS and **7-Zn**-PAN-CS are depicted in **Figure 3.26** and shows that the N_2 adsorption of **7-Zn**-PAN-CS was higher than that of PAN-CS and complex **7-Zn**. Moreover, surface area results reveals that the surface area of PAN-CS increased by 1.8% after conjugating with complex **7-Zn**. There is no significant difference between the surface areas of **7-ZnQ**-PAN-CS, **7-In**-PAN-CS**,** and **7-InQ**-PAN-CS compared to **7-Zn**-PAN-CS, the results are shown in **Table 3.4**. The Pc-PAN-CS nanofibers had a higher surface area when compared to PAN-Pc nanofibers (**Table 3.4**).

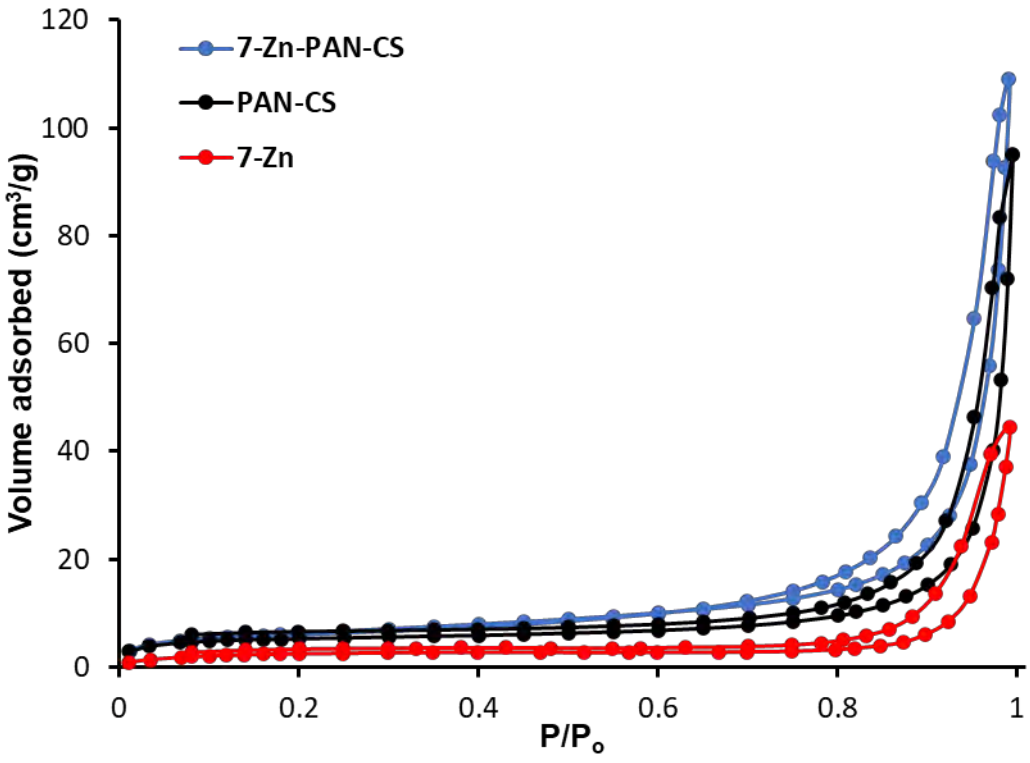

Figure 3.26: N_2 adsorption and desorption isotherms.

3.5.7 Solid-state UV-Vis spectra

Solid-state UV-Vis spectroscopy was used to characterize the electronic absorption properties of the Pc containing electrospun nanofibers between λ = 550 and 800 nm, shown in **Figure 3.27**. As stated above, compared to the complexes in solution, the nanofibers show a broad, bathochromically shifted Q-bands in some cases, these differences are expected in solid-state [**198**, **211**].

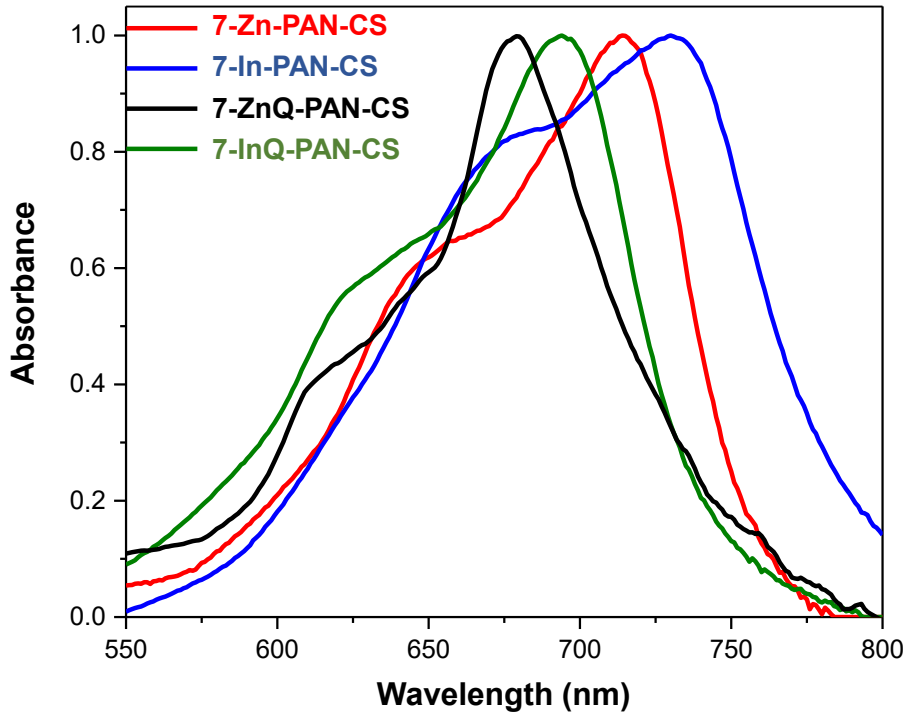

Figure 3.27: a) Solid-state UV-Vis spectrum of **7-Zn**-PAN-CS, **7-In**-PAN-CS, **7-ZnQ**-PAN-CS, and **7-InQ**-PAN-CS.

Table 3.4: Summary of the characteristic properties of Pc-PAN, and Pc-PAN-CS conjugates.

Sample	Loading (mg Pc/g Pc-PAN or Pc-PAN-CS)	Average fiber diameter (nm) (SEM)	Surface area (m^2/g) (±0.05)	λ_{max} (nm)[a]
PAN	-	784	17.5	-
PAN-CS	-	905	21.4	-
7-Zn-PAN	52.3	955	18.9	710 (710)
7-Zn-PAN-CS	15.2	1175	21.8	714 (710)
7-ZnQ-PAN	52.8	823	19.3	675 (675)
7-ZnQ-PAN-CS	14.8	1120	21.7	679 (675)
7-In-PAN	50.7	1001	19.1	727 (727)
7-In-PAN-CS	16.3	1005	21.6	731 (727)
7-InQ-PAN	51.1	913	18.6	689 (689)
7-InQ-PAN-CS	15.5	1135	21.7	694 (689)

[a] Values in brackets are for Pcs alone in DMSO

3.6 Summary of chapter

This chapter focuses on the synthesis and characterization of Pcs, ZnONPs, nanofibers, glass wool and their conjugates. The characterization of Pcs involved various analytical techniques such as ^{1}H NMR, mass spectrometry, UV-Vis spectroscopy, FTIR spectroscopy, and elemental analysis. These techniques were utilized to confirm the presence of substituted Pcs and their respective structures. The unmetalled Pcs (**1-H$_2$**, **2-H$_2$**) showed a split Q-band in DMF, while all metalated Pcs exhibited a monomeric Q-band in DMSO.

The ZnONPs showed a characteristic diffraction pattern, including peaks at 100, 002, 101, 102, 110, 103, 200, 112, 004, and 202. The TEM micrographs confirmed the spherical and pyramidal morphologies of ZnONSps and ZnONPys, respectively. The ZnONSps (<10 nm) were smaller in comparison to the ZnONPys (<40 nm), however the latter nanoparticles had a higher Pc loading than the former.

The supports, nanofibers and glass wool showed cylindrical surfaces. However, in comparison to the nanofiber, the glass wool had a rougher surface. The average diameter was determined using SEM and it was found that the GW was 10 times larger than that of the nanofibers.

The covalent linkages of all the conjugates (**6**-ZnONSps, **6**-ZnONPys, PAN-CS, **7**-PAN, **7**-PAN-CS, **7**-GW, **8-Zn**-GW, **9-Zn**-GW, and **10-Zn**-GW) were confirmed through XPS and FT-IR. The absorption properties of conjugates was assessed using UV-Vis spectroscopy for the nanoparticle conjugates and solid-state UV-vis spectroscopy for nanofibers and glass wool conjugates.

Chapter 4

Photophysical and Photochemical Properties

4. Photophysical and Photochemical Properties

This chapter delves into the photophysical and photochemical characteristics of the complexes and soluble conjugates employed in this thesis. Furthermore, it examine the singlet oxygen generation properties of the photoactive supports.

4.1 Fluorescence spectra, quantum yields (Φ_F), and lifetimes (τ_F)

Fluorescence quantum yield refers to the ratio of emitted fluorescence photons to absorbed excitation photons [212]. Fluorescence quantum yields of all fluorophores were determined by the comparative method (equation 4.1 [212]), using ZnPc as a standard (Φ_F^{Std} = 0.2) [41]

$$\Phi_F = \Phi_F^{Std} \frac{F\, A^{Std}\, n^2}{F^{Std} A\, (n^{Std})^2} \quad (4.1)$$

where F and F^{Std} represent the areas under the emission curves of the sample and standard, respectively. A and A^{Std} correspond to the absorbances of the sample and standard, while n and n^{Std} are the refractive indices of the solvents used for sample and standard, respectively. To mitigate inner filter effects, the absorbance at the excitation wavelength was maintained at approximately 0.05. At least three independent experiments were performed for the quantum yield determinations. Both the sample and the standard were excited at the same relevant wavelength.

The fluorescence lifetime measures the average time during which fluorophores remain in the excited singlet state and the values were obtained using the time-correlated single-photon counting (TCSPC) setup.

4.1.1 Fluorescence excitation and emission spectra

The fluorescence absorption, excitation, and emission spectra of **3-ZnQ** is shown in **Figure 4.1** as an example for other fluorophores, as all complexes and conjugates showed similar behaviour in DMSO. The excitation spectra closely resembled the absorption spectra, and both were mirror images of the emission spectra in DMSO, **Figure 4.1**. The proximity of the wavelength of the Q-band absorption and excitation spectra suggests that the nuclear configurations of the ground and excited states remain similar and are not affected by the excitation in DMSO.

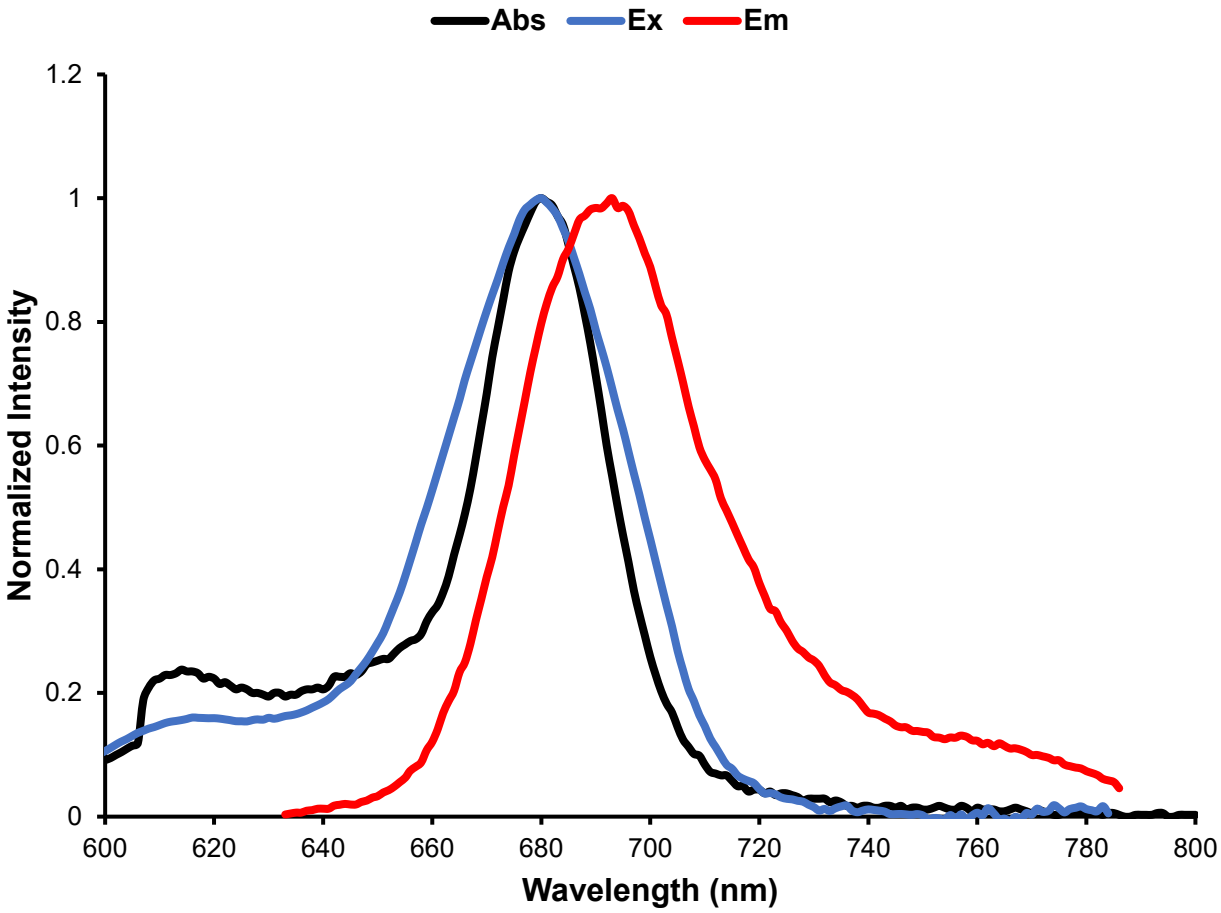

Figure 4.1: Absorption, excitation, and emission spectra of **3-ZnQ** in DMSO.

4.1.2 Fluorescence quantum yield and lifetime

The fluorescence quantum yields (Φ_F) were determined using a comparative method and equation 4.1. The fluorescence lifetimes (τ_F) were obtained through the TCSPC method. **Figure 4.2** illustrates the fluorescence decay curve for **3-ZnQ**, which served as a representative of all the photosensitizers studied. This curve was used for the determination of the τ_F values.

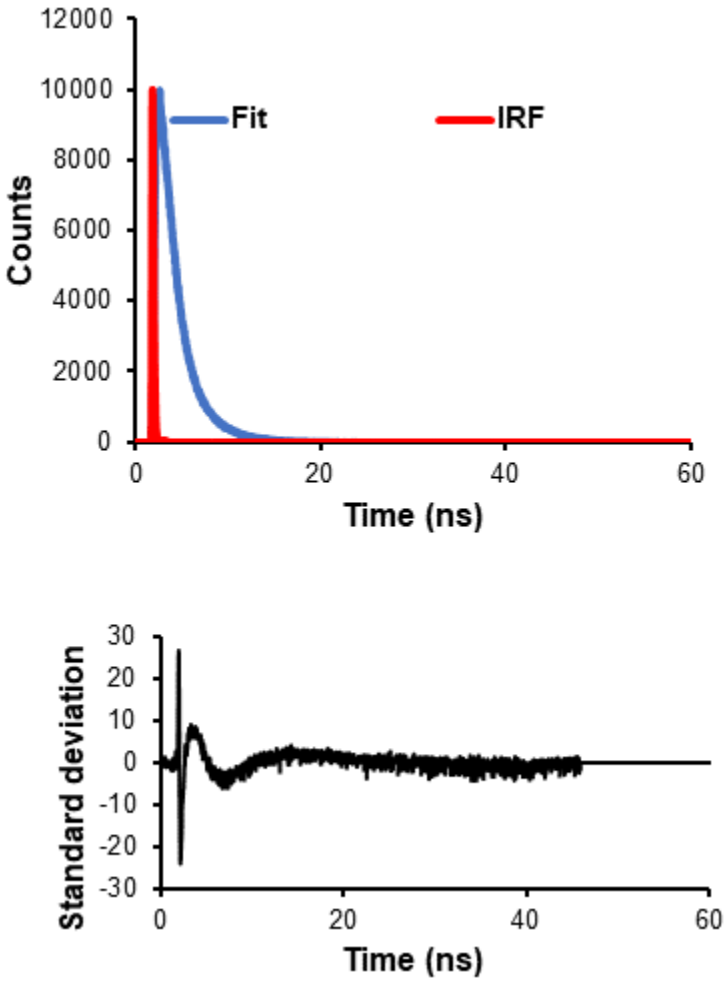

Figure 4.2: The fluorescence decay curve and fitting of **3-ZnQ** in DMSO and the fitting residue for decay curve. IRF: instrument response function.

The Φ_F and τ_F values for the various photosensitizers studied are presented in **Table 4.1**. The phthalocyanines alone displayed mono-exponential decay, while the **6**-ZnONSps and **6**-ZnONPys conjugates exhibited bi-exponential decays, indicating the presence of two distinct lifetimes, however, only the average lifetimes are represented in **Table 4.1**.

Table 4.1: Fluorescence quantum yield and lifetime parameters of the photosensitizers in DMSO.

Photosensitizer	Φ_F	τ_F (ns)
1-H_2	0.08	2.08
2-H_2	0.09	5.48
1-Zn	<0.01	1.86
2-Zn	0.01	2.34
1-In	<0.01	1.48
2-In	<0.01	1.97
1-ZnQ	0.19	1.92
2-ZnQ	0.24	2.84
1-InQ	0.01	1.69
2-InQ	0.02	2.31
3-Zn	0.06	2.04
3-In	0.02	1.52
3-ZnQ	0.18	2.87
3-InQ	0.11	2.32
4-Zn	0.03	2.66
5-Zn	0.02	2.60
4-In	0.01	2.24
5-In	<0.01	1.47
4-ZnQ	0.14	3.59

Table 4.1 continues:

Photosensitizer	Φ_F	τ_F (ns)
5-ZnQ	0.12	3.38
4-InQ	0.08	2.87
5-InQ	0.06	2.78
6-Zn	0.18	2.96
6-In	0.08	2.04
6-ZnQ	0.12	2.46
6-InQ	0.03	1.58
6-Zn-ZnONSps	0.05	1.82
6-In-ZnONSps	0.02	1.54
6-ZnQ-ZnONSps	<0.01	1.23
6-InQ-ZnONSps	<0.01	1.02
6-Zn-ZnONPys	0.03	1.57
6-In-ZnONPys	<0.01	1.21
6-ZnQ-ZnONPys	0.03	0.92
6-InQ-ZnONPys	<0.01	0.78
7-Zn	0.02	2.97
7-In	<0.01	2.58
7-ZnQ	0.17	5.15
7-InQ	0.08	4.98
8-Zn	0.16	2.88

Table 4.1 continues:

Photosensitizer	Φ_F	τ_F (ns)
9-Zn	0.09	1.68
10-Zn	0.06	1.52

This thesis discusses the impact of various factors on the fluorescence properties of MPcs photosensitizers, including the central metal, quaternization, nanoparticles, and symmetry. A summary of the investigation is provided below:

Effects of central metal:

Complexes **1-H₂** and **2-H₂** showed higher Φ_F values of 0.08 and 0.09 respectively, compared to the metalled Pcs, **1-Zn**, **1-In**, **2-Zn** and **2-In**. Indium Pcs produced lower Φ_F than zinc Pcs due to the heavier indium atom favouring intersystem crossing to the forbidden triplet state [49]. This is known as the heavy atom effect. Heavy atoms promote intersystem crossing to populate the triplet state through the spin orbit coupling, which is most prevalent in atoms whose nuclei are large and enhances the kinetics of both radiative and non-radiative transitions between states with different spin, hence lowering fluorescence quantum yields and lifetimes. This trend was observed consistently across all metalated complexes.

Effects of quaternization:

The quaternized compounds **1-ZnQ**, **1-InQ**, **2-ZnQ**, and **2-InQ**, had an intense fluorescence emission, with higher Φ_F values of 0.19, 0.01, 0.24, and 0.02, respectively.

The methylated complexes showed an enhancement in the Φ_F and τ_F values, and this increase is due to the lone pairs being used in the quaternization resulting in less fluorescence quenching. This trend was observed consistently across all quaternized complexes.

Effects of nanoparticles:

Complex **6** was covalently attached to two distinct zinc oxide nanoparticles: ZnONSps and ZnONPys. This conjugation resulted in a decrease in Φ_F due to the heavy atom effect of the NPs [213]. The average τ_F in **Table 4.1** were consistent with the Φ_F values, as the unconjugated complexes exhibited longer τ_F values than the conjugated complexes. This further supports the efficient promotion of intersystem crossing to the triplet state for the conjugates.

Effects of symmetry:

The effect of symmetry was assessed by comparing asymmetrical complex **7** with three morpholine showed no significant difference and no clear trend in the Φ_F and τ_F values compared to symmetrical complex **2** (**Table 4.1**). Asymmetrical **8-Zn** containing a single oxo spacer exhibited significantly higher Φ_F and τ_F values of 0.16 and 2.88 ns, compared to symmetrical **9-Zn** and **10-Zn** with four oxo bridges.

4.2 Triplet quantum yield (Φ_T) and lifetimes (τ_T)

The triplet quantum yield quantifies the efficiency of transitions from the singlet excited state to the triplet state. The triplet quantum yields were determined in DMSO using a comparative method and ZnPc as a standard (Φ_T = 0.65 [214]). The assessment was carried out using Equations 4.2

$$\Phi_T = \Phi_T^{std} \frac{\Delta A_T . \varepsilon_T^{std}}{\Delta A_T^{std} . \varepsilon_T} \quad (4.2)$$

where Φ_T^{std} is the triplet quantum yield of the standard, ΔA_{std} and ΔA_s are the changes in the triplet state absorbances of the standard and the sample, respectively, ε_T and ε_T^{std} are the triplet state molar extinction coefficients for the sample and the standard, respectively. The ε_T and ε_T^{std} are calculated using the equations 4.2a and 4.2b respectively.

$$\varepsilon_T = \varepsilon_s \frac{\Delta A_T}{\Delta A_s} \quad (4.2a)$$

$$\varepsilon_{T(std)} = \varepsilon_{s(std)} \frac{\Delta A_{T(std)}}{\Delta A_{s(std)}} \quad (4.2b)$$

where ε_s and $\varepsilon_{s(std)}$ are the molar extinction coefficients in the ground sates for the sample and standard, respectively. The ΔA_s and $\Delta A_{s(std)}$ are the changes in the absorbance in the ground states for the sample and standard, respectively.

Each complex underwent a 15 min deaeration process using argon gas and the crossover wavelength between each sample and standard was employed as the laser excitation wavelength. A laser flash photolysis set-up was utilized to acquire the transient

absorption and decay curves. These curves were subsequently employed to calculate the triplet quantum yield (Φ_T) and triplet lifetime (τ_T) in DMSO.

The typical transient absorption and triplet decay curves of MPcs and their conjugates are shown in **Figure 4.3** using **2-ZnQ** as an example. A broad where there was a broad T_1- T_n triplet absorption peak was evident at 480 nm, consistent with the finding from the literature [215]. Nitrogen-containing substituents directly bound to the Pcs ring have been reported to quench the triplet state [216], hence no Φ_T values in **Table 4.2** are recorded for the tetra morpholine-substituted complexes, **1** and **2**, since there was no signal. In contrast, the introduction of the methyl groups to the nitrogen atoms improved the signal quality (**Figure 4.3(a)**) with the Φ_T values of **1-ZnQ**, **1-InQ**, **2-ZnQ**, and **2-InQ** were determined to be 0.71, 0.66, 0.92, and 0.87, respectively, **Table 4.2**. The non-peripheral Pcs (complex **1**) had higher values than peripheral Pcs (complex **2**), corresponding to the low fluorescence quantum yields for the former. The extension of the alkyl chain complex **5** (compared to complex **4**) showed minor increase in the Φ_T values. Upon linking complex **6** to the ZnONPs resulted in an increase in the Φ_T values, attributed to the heavy-atom influence of ZnONPs, facilitating intersystem crossing to the triplet state. There was no clear influence of shape of the ZnONPs on the Φ_T values.

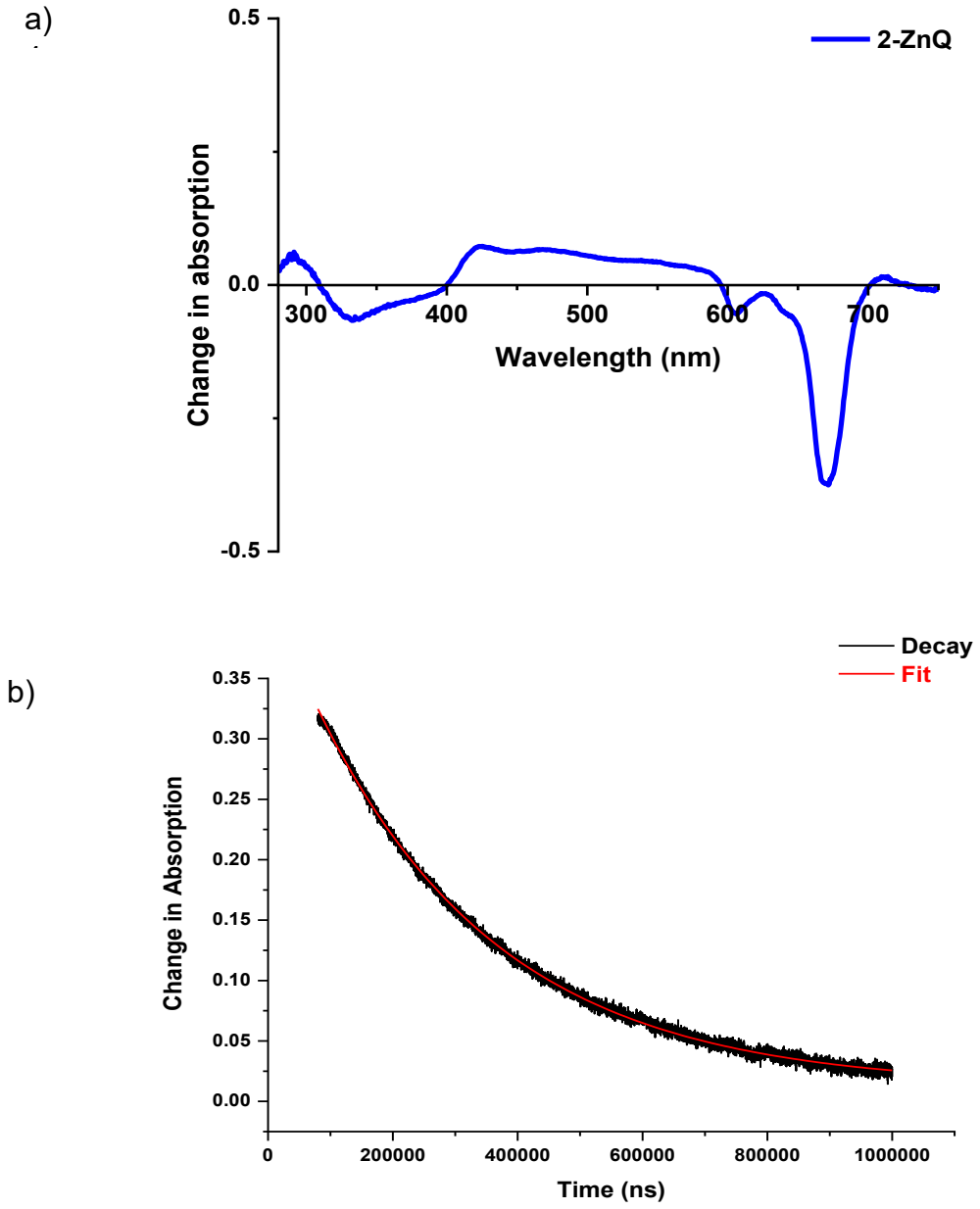

Figure 4.3: (a) Transient differential spectrum and (b) corresponding triplet decay curve of complex **2**-ZnQ in DMSO.

Typically, complexes with higher fluorescence quantum yields are expected to exhibit lower triplet quantum yields, as these processes compete with each other. As a result, cationic Pcs with higher Φ_F displayed lower triplet quantum yields when compared to the neutral Pcs. The heavier central atom, indium, yielded a greater conversion to the triplet state than the corresponding zinc complexes due to the enhanced intersystem crossing discussed earlier, leading to an increase in the triplet quantum yields.

Triplet state lifetimes (τ_T) were studied to confirm the population of the triplet state. The triplet decay curve obeyed second-order kinetic law, **Figure 4.3(b)**, primary due triplet-triplet recombination [217]. This decay behavior is typical for Pc complexes and conjugates and the corresponding values are summarized in **Table 4.2**. This thesis unveiled two distinct trends. The first trend was observed in complexes **1-ZnQ**, **1-InQ**, **2-ZnQ**, **2-InQ** and **6** (and its conjugates), where the efficient spin-orbit coupling (the heavy atom effect) resulted in the shortened triplet lifetimes and increased triplet quantum yields [218]. In contrast, the Schiff base complexes **3-5** and the asymmetrical complex **7** revealed a second trend. In these cases, higher triplet quantum yields were accompanied by longer triplet lifetimes. This observation suggests that these complexes are less effective at dissipating the energy of the excited triplet state compared to complexes **1-ZnQ**, **1-InQ**, **2-ZnQ**, **2-InQ**, and **6**. The triplet quantum yield and lifetime for complexes **8-10** were not studied**.**

Table 4.2: Triplet quantum yield and lifetime parameters of the photosensitizers in DMSO.

Photosensitizer	Φ_T	τ_T (ns)
1-H_2	-	-
2-H_2	-	-
1-Zn	-	-
2-Zn	-	-
1-In	-	-
2-In	-	-
1-ZnQ	0.71	112
2-ZnQ	0.66	292
1-InQ	0.92	76
2-InQ	0.87	92
3-Zn	0.62	132
3-In	0.75	210
3-ZnQ	0.52	88
3-InQ	0.59	112
4-Zn	0.55	147
5-Zn	0.59	154
4-In	0.61	192
5-In	0.63	202
4-ZnQ	0.48	157

Table 4.2 continues:

Photosensitizer	Φ_T	τ_T (ns)
5-ZnQ	0.52	177
4-InQ	0.59	218
5-InQ	0.59	216
6-Zn	0.58	258
6-In	0.63	223
6-ZnQ	0.52	271
6-InQ	0.60	249
6-Zn-ZnONSps	0.67	207
6-In-ZnONSps	0.70	135
6-ZnQ-ZnONSps	0.62	228
6-InQ-ZnONSps	0.68	182
6-Zn-ZnONPys	0.69	177
6-In-ZnONPys	0.72	112
6-ZnQ-ZnONPys	0.65	212
6-InQ-ZnONPys	0.70	135
7-Zn	0.50	185
7-In	0.68	248
7-ZnQ	0.45	152
7-InQ	0.52	212

4.3. Singlet oxygen quantum yields (Φ_Δ) and photostability

4.3.1 Singlet oxygen quantum yields in solution

The singlet oxygen quantum yield denotes the quantity of singlet oxygen ($^1O_2$ molecules) produced for each absorbed photon by a photosensitizer. In the context of this study, the Φ_Δ value for soluble photosensitizer solutions were determined using a comparative approach as previously outlined in literature [**219**]. This method involved employing unsubstituted ZnPc (Φ_Δ = 0.67 [**219**] in DMSO, as well as ClAlPcSmix (Φ_Δ = 0.42 [**41**]) in aqueous media as standards. 1,3-Diphenylisobenzofuran (DPBF) and anthracene-9,10-bis-methylmalonate (ADMA) were used as quenchers in DMSO and in aqueous media, respectively.

In the experimental procedure, equal volumes of the photosensitizer solution (sample or standard, each with an approximate absorbance of 1.5) and the quencher solution (with an approximate absorbance of 2) were mixed in the dark. Subsequently, the mixtures were exposed to light with a wavelength corresponding to the crossover wavelength of the sample and standard. The degradation of the quencher following successive irradiation cycles was then tracked using UV-Vis spectroscopy, and the Φ_Δ values were calculated employing Equation 4.3

$$\Phi_\Delta = \Phi_\Delta^{std} \frac{R.I_{abs}^{std}}{R^{std}.I_{abs}} \tag{4.3}$$

where Φ_Δ^{std} is the singlet oxygen quantum yield for the standard, R and R^{std} are the DPBF or ADMA photobleaching rates in the presence of Pc complexes, nanoconjugates under

investigation, as well as the standard, respectively. I_{abs} and I_{abs}^{std} are the rates of light absorption by the Pc complexes, nanoconjugates and standard, respectively.

The degradation profiles of DPBF and ADMA for complexes **1-Zn** and **1-ZnQ** are shown in **Figure 4.4** as representatives. The Q-band were unaltered while the quenchers degraded over the irradiation period. In the absence of the photosensitizers and light, the absorption profile of DPBF at 417 nm and ADMA at 380 nm remained unchanged. The Φ_Δ values are summarized in **Table 4.3**. As shown in **Table 4.3**, the Φ_Δ in DMSO followed the same trend as the Φ_T as the Φ_Δ is generated from the triplet state. Therefore, all complexes with higher Φ_T exhibited higher Φ_Δ values except for the ZnONPs nanoconjugates. The decrease in the Φ_Δ observed may be due to the screening effect introduced by the capping agent on the ZnONPs, which may have inhibited the interaction between molecular oxygen and the excited triplet state of the nanoconjugates [220]. The Φ_Δ values for **8-10** were determined in DMSO to confirm the photoactivity of the compounds, and the values obtained were between 0.24-0.44.

The Φ_Δ values in aqueous media, however, were reduced compared to DMSO, **Table 4.3**. The reduction of the Φ_Δ values in aqueous media relative to DMSO alone is due to oxygen having a higher solubility in many organic solvents compared to water [221] and the quenching effect brought by water molecules on the singlet oxygen generation [41]. Additionally, in aqueous media, Φ_Δ values of cationic Pcs were relatively higher than for neutral Pcs due to the latter demonstrating a higher degree of aggregation in this environment than the former. The Φ_Δ values of H_2Pcs could not be obtained due insolubility in aqueous media, hence no values were reported. In both media, the central

metal ion showed a significant effect on the Φ_{Δ} values. The indium (III) containing Pcs were the most efficient photosensitizers compared to the zinc (II) containing Pcs, due to the heavy atom effect discussed above. This effect is known to enhance the triplet state population, resulting in increase in singlet oxygen yields [**49**].

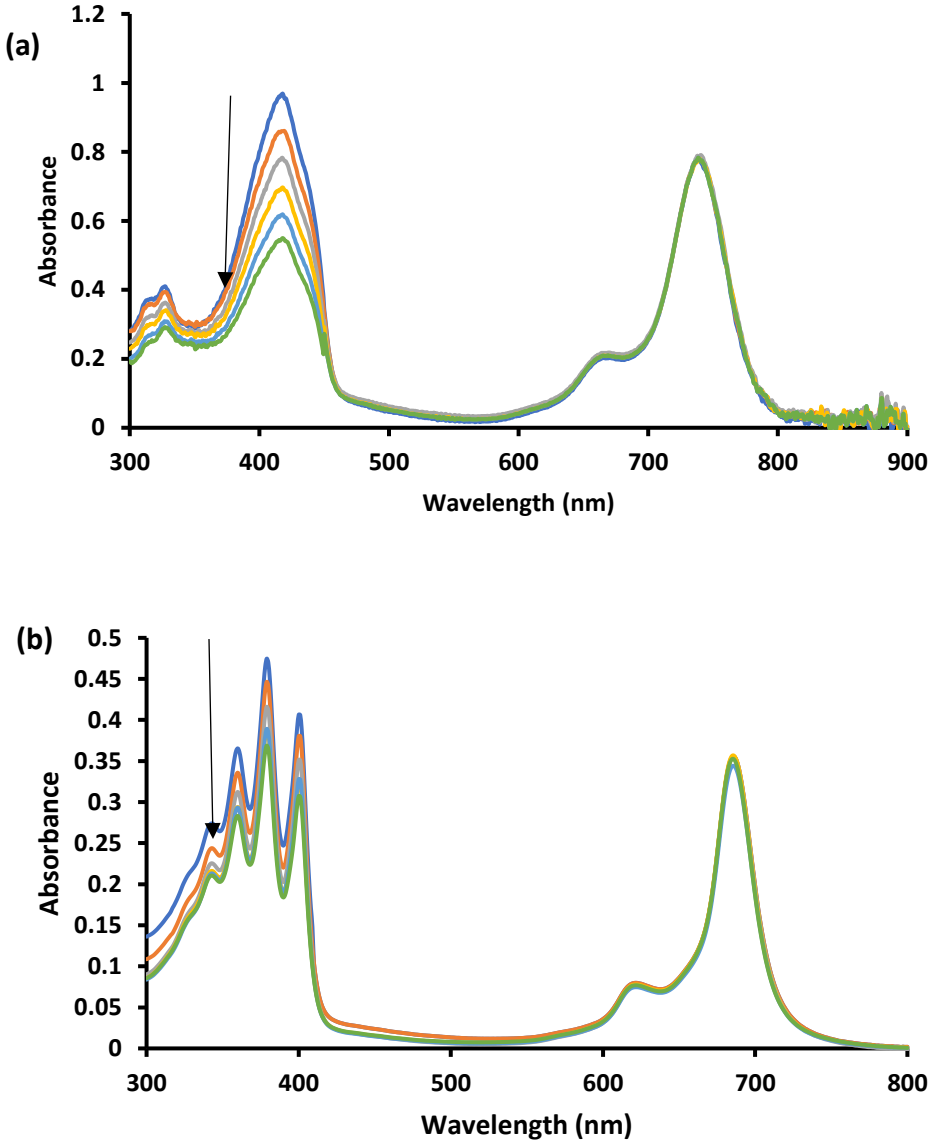

Figure 4.4: Absorption changes of (a) DBPF in the presence **1-Zn** in DMSO and (b) ADMA by **1-ZnQ** complex in water.

Table 4.3: Singlet quantum yield and photostability of the Pc complexes and their conjugates, where Aq sol – aqueous solution.

Photosensitizer	Φ_Δ (in DMSO)	Φ_Δ (in aq sol)	%Pd	%Pd (in aq sol)
1-H_2	0.28	-	2.8	-
2-H_2	0.20	-	3.2	-
1-Zn	0.54	0.01	2.1	4.7
2-Zn	0.47	0.02	2.5	5.2
1-In	0.68	<0.01	2.3	4.9
2-In	0.63	<0.01	2.9	5.4
1-ZnQ	0.58	0.26	2.9	18.7
2-ZnQ	0.50	0.23	3.6	18.9
1-InQ	0.66	0.38	3.1	18.0
2-InQ	0.62	0.32	3.9	18.4
3-Zn	0.61	0.03	1.2	4.6
3-In	0.68	0.05	1.3	4.3
3-ZnQ	0.48	0.18	3.5	16.2
3-InQ	0.56	0.20	2.7	15.5
4-Zn	0.48	0.07	1.0	2.4
5-Zn	0.50	0.08	0.8	1.3
4-In	0.53	0.10	1.5	2.9
5-In	0.54	0.12	1.1	2.0

Table 4.3 continues:

Photosensitizer	Φ_Δ (in DMSO)	Φ_Δ (in aq sol)	%Pd	%Pd (in aq sol)
4-ZnQ	0.40	0.20	1.8	4.1
5-ZnQ	0.41	0.22	1.2	2.9
4-InQ	0.50	0.22	2.4	3.2
5-InQ	0.52	0.24	1.5	2.4
6-Zn	0.55	0.08	3.0	3.0
6-In	0.58	0.10	3.3	3.0
6-ZnQ	0.46	0.21	4.1	11.7
6-InQ	0.54	0.25	4.3	11.0
6-Zn-ZnONSps	0.44	0.03	2.4	5.2
6-In-ZnONSps	0.52	0.05	2.7	5.4
6-ZnQ-ZnONSps	0.40	0.17	3.6	8.4
6-InQ-ZnONSps	0.49	0.20	2.9	6.7
6-Zn-ZnONPys	0.50	0.05	2.1	4.6
6-In-ZnONPys	0.49	0.06	2.5	5.0
6-ZnQ-ZnONPys	0.42	0.18	3.3	7.8
6-InQ-ZnONPys	0.54	0.23	2.5	6.9
7-Zn	0.42	0.21	1.9	5.2
7-In	0.60	0.23	2.0	4.9

Table 4.3 continues:

Photosensitizer	Φ_Δ (in DMSO)	Φ_Δ (in aq sol)	%Pd	%Pd (in aq sol)
7-ZnQ	0.40	0.24	4.2	12.8
7-InQ	0.55	0.28	3.4	12.1
8-Zn	0.40	-	-	-
9-Zn	0.44	-	-	-
10-Zn	0.24	-	-	-

The effect of light and two free radical experiments were carried out to confirm the active species in the photodegradation of the chemical probes, DPBF and ADMA. Sodium azide (NaN_3, 0.01 M) and methanol (MeOH, 0.01 M) were added as singlet oxygen [222] and hydroxyl radicals [223] scavengers, respectively. The experiments were conducted both with or without light exposure, respectively. Complex **6-ZnQ** and **6-ZnQ**-ZnONPys were used as representative. As shown in **Figures 4.5a** and **4.5b**, complexes **6-ZnQ** and **6-ZnQ**-ZnONPys revealed very low activity in the dark. Upon the addition of NaN_3 and MeOH, there was a significant inhibition in the photodegradation activity of DPBF, suggesting that both singlet oxygen and hydroxyl radical were involved in the oxidation reaction. However, for complex **6-ZnQ** the changes in the presence of MeOH were minor, confirming singlet oxygen as the main reactive oxygen species. The same trend was observed for ADMA studies.

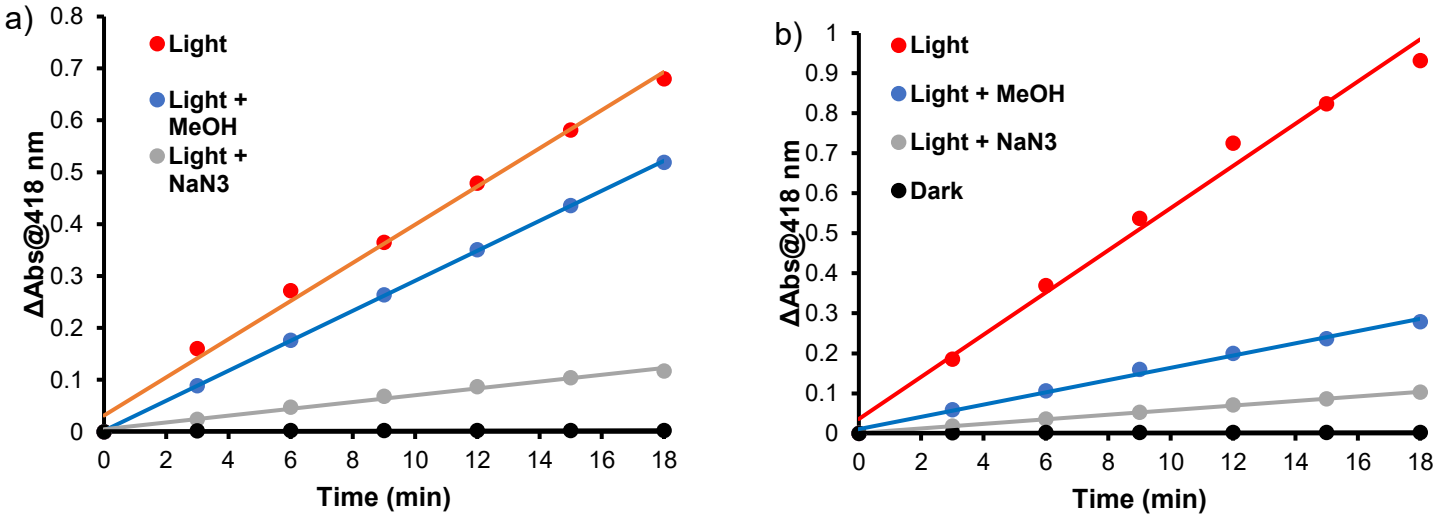

Figure 4.5: Photodegradation of DPBF by (a) **6-ZnQ** and (b) **6-ZnQ**-ZnONPys in the presence or absence of different scavengers and light.

As a complimentary technique, electron paramagnetic resonance spectroscopy (EPR) was used to monitor the ability to generate ROS under illumination for **6-ZnQ** and **6-ZnQ**-ZnONPys.TEMPO and DMPO were used as spin trapping agents for singlet oxygen and hydroxyl radical, respectively. The EPR results (**Figure 4.6**) followed the same trend observed above. The EPR spectra showed a typical triplet signal of TEMPO (**Figure 4.6a**), confirming the photo-generation of singlet oxygen of both complex **6-ZnQ** and **6-ZnQ**-ZnONPys. The hydroxyl radicals were effectively scavenged by DMPO in the presence of **6-ZnQ**-ZnONPys, and the EPR spectrum (**Figure 4.6b**) revealed four weak characteristic peaks with an intensity ratio of 1:2:2:1. However, no signal was detected

with complex **6-ZnQ**, indicating that linking the phthalocyanines to the ZnONPs produces different reactive oxygen species, which may be essential in the inactivation of micro-organisms.

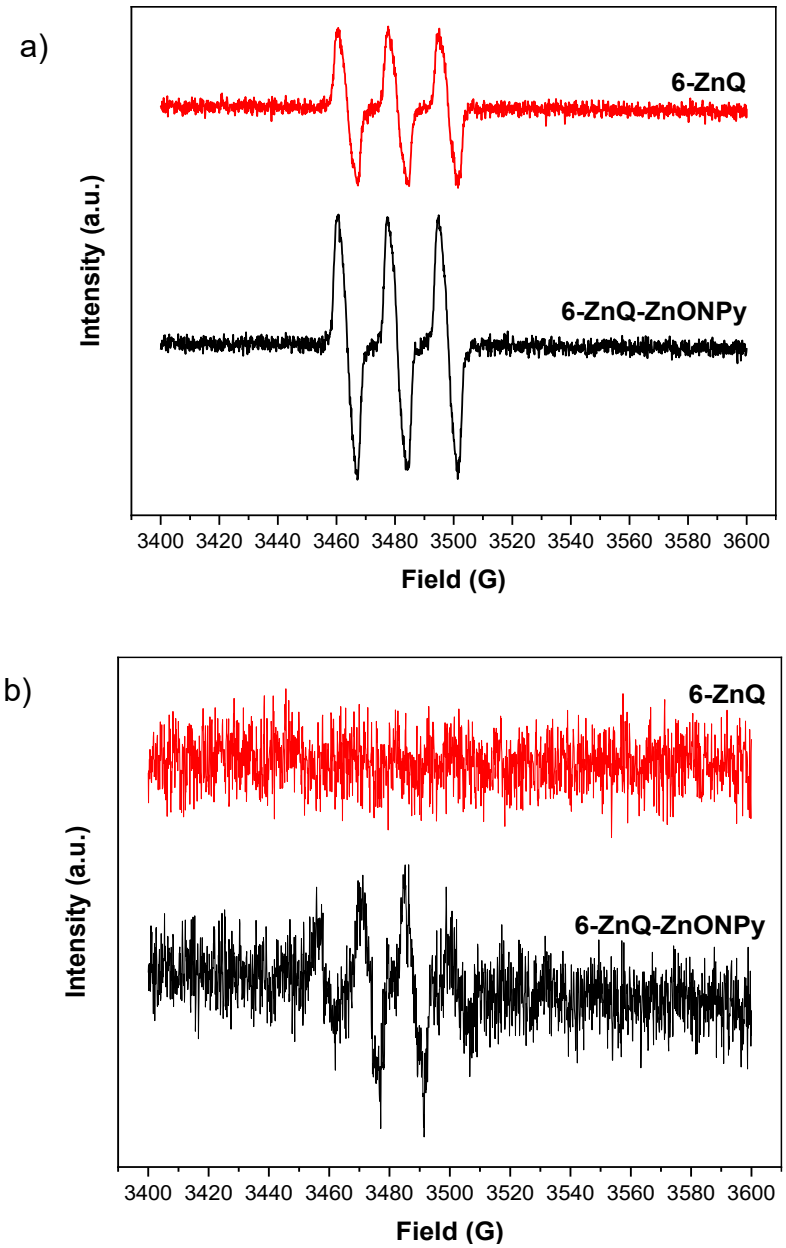

Figure 4.6: EPR spectra of **6-ZnQ** and **6-ZnQ**-ZnONPys mixed with a) TEMPO and b) DMPO under light.

Ensuring the photostability of sensitizers against photo-induced changes is of utmost significance for their practical use such as PACT and photodegradation of pollutants. To assess the photostability of the complexes and nanoconjugates, each photosensitizer was exposed to light for 1 h in both DMSO and aqueous solution. The formation or disappearance of bands were monitored via UV-Vis absorption at 15 min intervals, **Figure 4.7** shows the spectra of **3-Zn** in DMSO, as an example. The photodecomposition percentages (%Pd) of the Q-band are quantified and listed in **Table 4.3**. In DMSO, all complexes showed a good photostability, with %Pd less than 5%. Conversely, in aqueous media, the susceptibility to light was evident, leading to an increased in the photodecomposition percentage, as outlined in **Table 4.3**. However, the Pcs and nanoconjugates were still relatively stable with percentage degradation of less than 20% in aqueous media hence this stability renders them suitable for use in application. The lower photodecomposition rates are observed in DMSO due to its coordinating properties which reduce the photooxidation rates of Pcs [**224**].

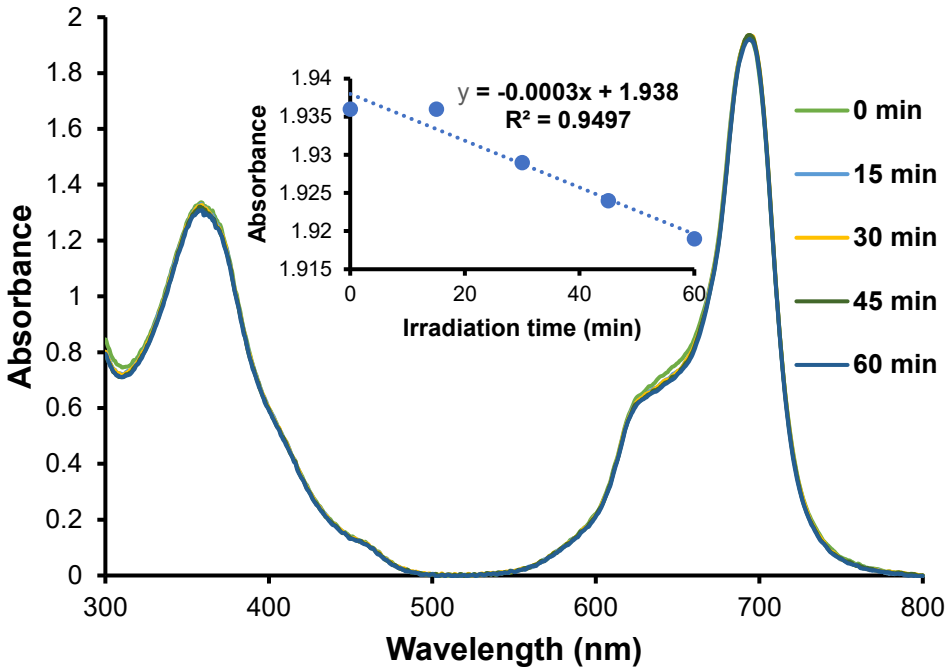

Figure 4.7: Photodegradation of **3-Zn** in DMSO at 15 min. Insert: Absorbance versus time plot of **3-Zn**.

4.3.2 Singlet oxygen quantum yields on support

To determine the singlet oxygen quantum yield in nanofibers and glass wool, the absolute method was employed due to the absence of standards [225]. These experiments were conducted in unbuffered aqueous solutions, utilizing ADMA as a quencher. The degradation of ADMA was tracked at 380 nm [225]. The quantum yields (Φ_{ADMA}) were determined using Equation 4.4:

$$\Phi_{\text{ADMA}} = \frac{(C_0 - C_t)V}{\text{tI}_{\text{abs}}} \tag{4.4}$$

Here, C_o and C_t stand for the initial and final concentrations of ADMA respectively, V represents the volume of the solution, t signifies the irradiation time per cycle, and I_{abs} is defined by Equation 4.5

$$I_{abs} = \frac{\alpha A I}{\text{N}_\text{A}} \tag{4.5}$$

where α = 1 - 10 $^{-A(\lambda)}$, $A(\lambda)$ is the absorbance of the phthalocyanines on the support as determined by placing the modified support directly onto solid-state UV spectrophotometer, A is the irradiated area (0.20 cm^2), I is the intensity of light and N_A is Avogadro's constant. The light intensity measured refers to the light reaching the spectrophotometer cell, and it is expected that some of the light may be scattered, hence the Φ_Δ values of Pc complexes in the prepared materials are estimates. The singlet oxygen quantum yields (Φ_Δ) were calculated using Equation (4.6) [225]:

$$\frac{1}{\Phi_{\text{ADMA}}} = \frac{1}{\Phi_\Delta} + \frac{1}{\Phi_\Delta}\frac{k_d}{k_a}\frac{1}{[\text{ADMA}]} \tag{4.6}$$

where k_d is the decay constant of singlet oxygen, while k_a represents the rate constant of the reaction between ADMA and O_2 ($^1\Delta_g$). Φ_Δ is obtained from the plot of $1/\Phi_{ADMA}$ versus 1/[ADMA].

The singlet oxygen generation of the supports were assessed through monitoring of ADMA absorption at 380 nm. **Figure 4.8** displays the absorption intensity of ADMA at various irradiation times of **7-ZnQ**-PAN-CS and **7-ZnQ**-GW (used as examples). Control experiments were conducted in the dark and showed negligible changes (not presented). The absence of the Q-band validates that the immobilized Pcs did not leach out from nanofibers (**Figure 4.8a**) or glass wool (**Figure 4.8b**). The Φ_Δ values of modified nanofibers and glass wool are provided in **Table 4.4**.

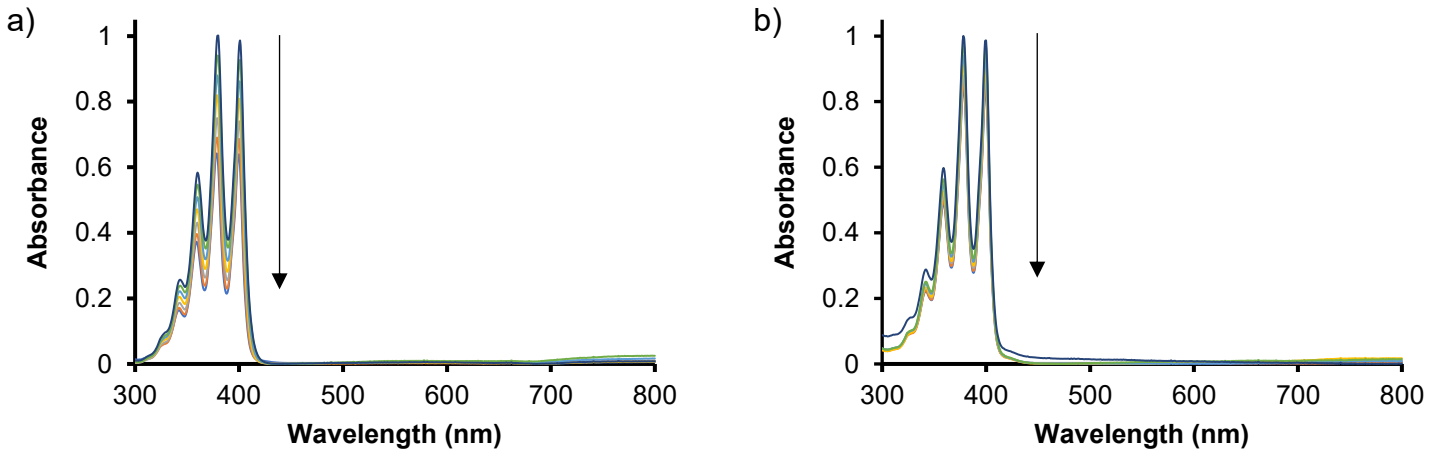

Figure 4.8: UV–vis spectral changes of ADMA in water in the presence of (a) **7-ZnQ-PAN** and (b) **7-ZnQ-GW** supports. Spectra were recorded at 15 min intervals.

Table 4.4: A summary of the singlet oxygen quantum yields for the modified nanofibers and glass wool in aqueous solution.

Pc-support conjugate	Φ_Δ	Loading mg/g
7-Zn-PAN	0.14 (0.35)	52.3
7-Zn-PAN-CS	0.18	15.2
7-Zn-GW	0.11 (0.17)	34.9
7-In-PAN	0.16 (0.40)	50.7
7-In-PAN-CS	0.18	16.3
7-In-GW	0.12 (0.18)	34.5
7-ZnQ-PAN	0.18 (0.45)	52.8
7-ZnQ-PAN-CS	0.21	14.8
7-ZnQ-GW	0.15 (0.23)	33.8
7-InQ-PAN	0.21 (0.53)	51.3
7-InQ-PAN-CS	0.24	15.5
7-InQ-GW	0.17 (0.26)	33.2
8-Zn(a)-GW	0.38 0.40[a]	3.65
9-Zn-GW	0.35 0.44[a]	3.34
10-Zn-GW	0.22 0.24[a]	1.84

[a]Values of unconjugated Pcs in DMSO and values in brackets are the Φ_Δ values generated with white light.

All modified supports exhibited reduced Φ_Δ values in comparison to the values observed in DMSO or aqueous media (for water-soluble complexes). This reduction may be attributed to the aggregation of MPcs in the solid state and the quenching effects of water [41]. The incorporation of chitosan into the polymer led to an increase in the Φ_Δ values due to improved hydrophilicity of the material [226], as indicated in **Table 4.4**. For comparison purpose, Complex **7** was also conjugated to glass wool, resulting in considerably lower Φ_Δ values for **7**-GW than for **7**-PAN, primarily due to the higher loading of Pc in the latter. The effect of loading was also observed for **8**-GW composites. The low Φ_Δ value for **10-Zn**-GW is due to the higher degree of aggregation discussed earlier. Both **8-Zn**-GW and **9-Zn**-GW showed less aggregation than **10-Zn**-GW, hence the comparable Φ_Δ values, with **8-Zn**-GW demonstrating higher Φ_Δ due to improved loading onto the glass wool. Furthermore, the Φ_Δ values of **7**-PAN and **7**-GW, were further assessed under both white light and red light, and the comparison is shown in **Figure 4.9a-b** and the Φ_Δ values given in **Table 4.4** (within brackets). The degradation of ADMA was significantly higher when exposed to white light compared to red light. This difference is attributed to the broader absorption range of white light (380-750 nm) in contrast to red light (660-750 nm). Correspondingly, white light produced higher Φ_Δ values compared to red light, and these values also aligned with the loading trends observed above. In addition, the studies were repeated without photocatalysts using white light (as shown in **Figure 4.9c**) to determine the effect of the short wavelengths. No significant changes were observed confirming that singlet oxygen generation primarily drives the photooxidation of ADMA. To further substantiate the role of singlet oxygen, the studies were repeated in the presence of NaN_3, a singlet oxygen inhibitor, and the efficacy of the photocatalyst to produce singlet

oxygen decreased (as shown in **Figure 4.9d,** using **8-Zn**-GW as an example), providing further evidence of the modified support ability to produce singlet oxygen.

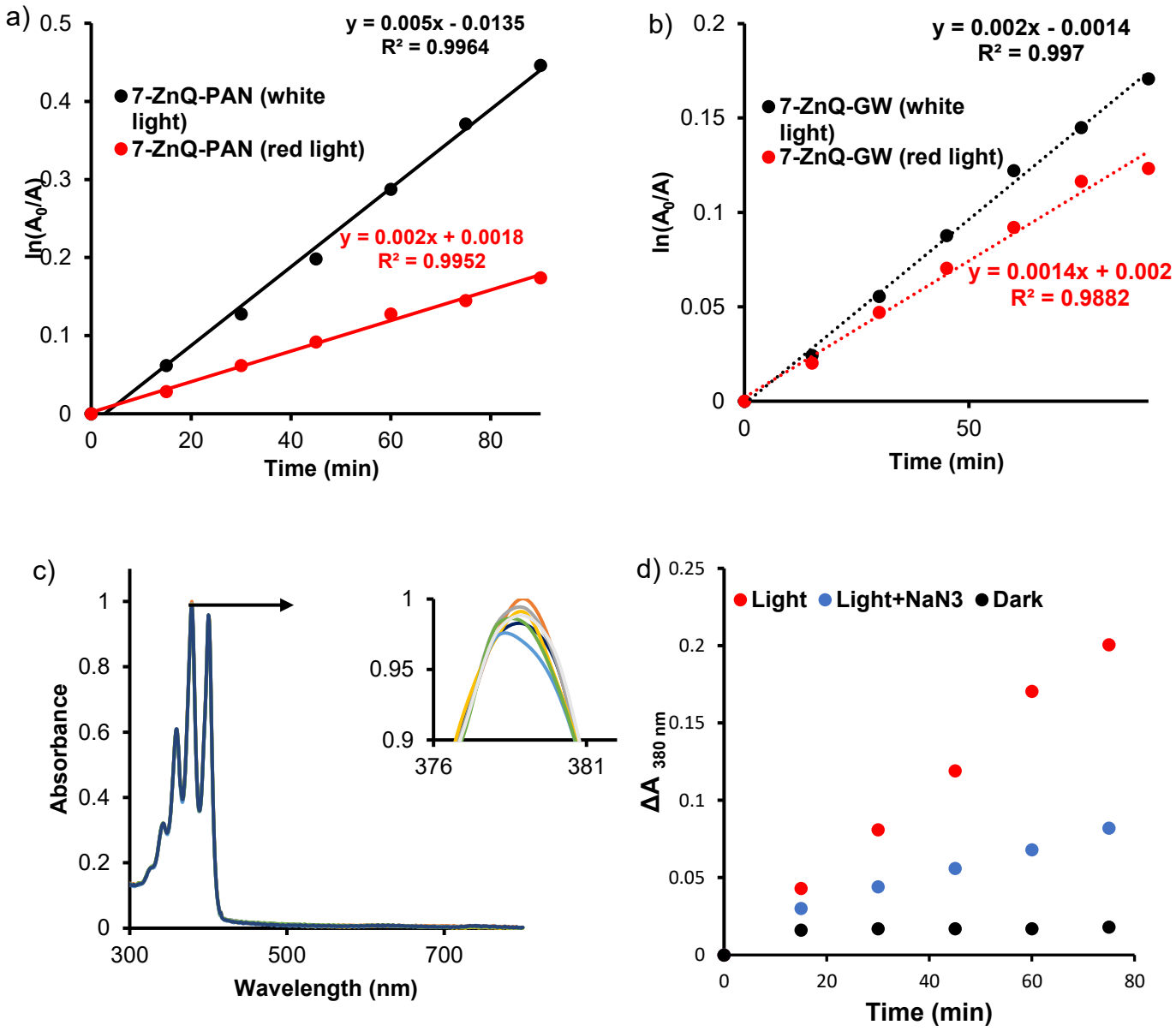

Figure 4.9: The comparison of degradation rates of ADMA by (a) **7-ZnQ-PAN** and (b) **7-ZnQ-GW** composite under irradiation by red and white light. UV–vis spectral changes of (c) ADMA alone when irradiated with white light, the spectra were recorded at 15 min intervals and (d) Plot of ΔA for ADMA (380 nm) when irradiated with light, in the presence of NaN_3, **8-Zn**-GW and in the dark.

4.4 Summary of chapter

The photophysical and photochemical characteristics of the Pc complexes and nanoconjugate were investigated, along with the singlet oxygen generating abilities of their corresponding nanofibers and glass wool supports. All the complexes and conjugates exhibited distinct characteristics attributed to the inherent properties of the photosensitizers, including factors such as the choice of central metal, substituents, symmetry, and conjugation with nanoparticles.

As expected, heavier central metals, such as indium when compared to zinc, demonstrated increased singlet oxygen generation due to a high Φ_T resulting from enhanced intersystem crossing to the triplet excited state, driven by spin-orbit coupling, hence the lower fluorescence quantum yields were observed. The extension of the alkyl chain and conjugation to ZnONPs resulted in an increase in the Φ_T. Notably, complexes with higher Φ_T exhibited higher Φ_Δ values with the exception being the ZnONPs nanoconjugates. The decrease in the Φ_Δ observed may be due to the screening effect introduced by the capping agent on the ZnONPs, which may have inhibited the interaction between molecular oxygen and the excited triplet state of the nanoconjugates.

All modified nanofibers and glass wools showed adequate singlet oxygen generation in aqueous solution with the loading capacity proving to be the determining fact in the generation of Φ_Δ. The introduction of chitosan into PAN nanofibers improved the Φ_Δ values due to improved hydrophilicity. As such, the modified support showed potential application in photodynamic antimicrobial chemotherapy.

Chapter 5

Photodynamic Antimicrobial Chemotherapy

5. Photodynamic Antimicrobial Chemotherapy (PACT)

In this chapter, the applications of synthesized phthalocyanines, nanoconjugates, and modified nanofibers and glass wool as PACT agents will be discussed. Complexes **1-3**,**6-7** were utilized in the photodynamic antimicrobial chemotherapy for planktonic forms of gram-positive *Staphylococcus aureus* (*S. aureus*), gram-negative *Escherichia coli* (*E. coli*), as well as *Candida albicans* (*C. albicans*) in aqueous solution. Complex **3** was also used the photoinactivation of *Klebsiella pneumoniae* (*K. pneumoniae)*, *Salmonella enterica* subspecies *enterica* serovar *Choleraesuis* (*S. choleraesuis*), vancomycin-resistant *Enterococcus faecium* (VREF), methicillin-sensitive and methicillin-resistant *Staphylococcus aureus* (MSSA and MRSA). Complex **4** and **5** were only applied to photoinactive MSSA and MRSA. Additionally, complex **6** and its corresponding nanoconjugates were applied in the PACT of biofilms. Complex **7** and **8-10** were immobilized onto support and the PACT activity of the support were assessed.

5.1 Photodynamic Antimicrobial Chemotherapy in solution

The PACT studies were carried out using a stock solution dissolved in 5% DMSO and further diluted with PBS to a final working concentration. DMSO was used to improve the solubility of non-water-soluble complexes. Preliminary blanks and controls were conducted to confirm the effect of 5% DMSO, there was negligible difference in the controls hence all studies are carried out in 5% DMSO. Control study was also performed using the light alone and the light alone had no effect in the cell death. Statistical analyses were evaluated using the one-way analysis of variance (ANOVA) and all the experiments were performed in triplicates. A p-value of <0.05 was considered significant.

5.1.1 Dark toxicity studies

The dark toxicity studies of complexes **1**-**10** were conducted to assess the effect of these complexes in the absence of light at various concentrations. Generally, the dark toxicity of all complexes was found to be dose-dependent, as illustrated in **Figure 5.1**, using **3-ZnQ** and **3-InQ** as examples. The neutral phthalocyanines (except for **1**-**3**, **7**) exhibited minimal toxicity against gram-positive and gram-negative bacteria (figure not shown). However, the dark toxicity slightly increased for water-soluble cationic complexes. This could be attributed to the presence of positive charge, which assists in orientating the Pc to disrupt the cellular function and organization of the microbial cell [227]. On the other hand, the morpholine-bearing phthalocyanines, complex **1**-**3** and **7**, displayed significant dark toxicity (figure not shown). This toxicity can be attributed to the presence of the morpholine group, which is known to inhibit ergosterol, a hormone that stimulates fungal growth [228]. The dark toxicity was enhanced in complexes when the morpholine group was directly attached to the Pc macrocycle (**1** and **2**). Complexes **3Q** showed an increase in dark toxicity with increasing concentration due to the influence of the imine and morpholine moiety (as shown in **Figure 5.1**). As mentioned earlier, compounds containing imine and morpholine groups exhibit antibacterial activities [53, 229].

Nevertheless, all micro-organisms exhibited > 62.1% cell viability (at 80 μM) with vancomycin-resistant *Enterococcus faecium* (VREF) being the most susceptible bacteria in the absence of light. The lengthening of the alkyl chain did not prove to have any effect on the dark toxicity rate for complexes **4** and **5**.

a)

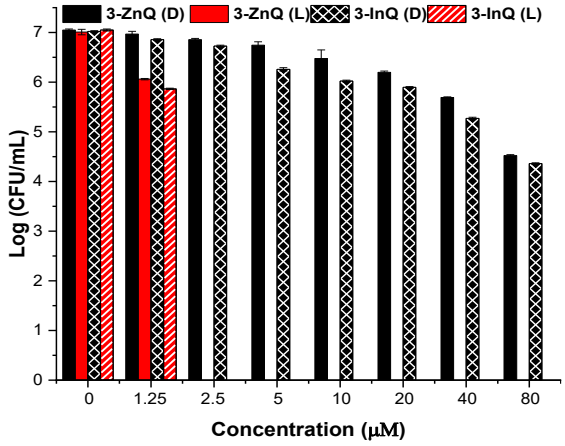
3-ZnQ (D)
3-ZnQ (L)
3-InQ (D)
3-InQ (L)
Log (CFU/mL)
Concentration (μM)
0
1.25
2.5
5
10
20
40
80

d)

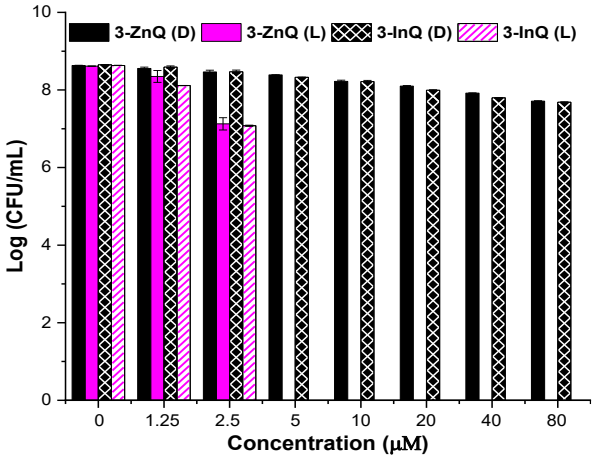
3-ZnQ (D)
3-ZnQ (L)
3-InQ (D)
3-InQ (L)
Log (CFU/mL)
Concentration (μM)
0
1.25
2.5
5
10
20
40
80

b)

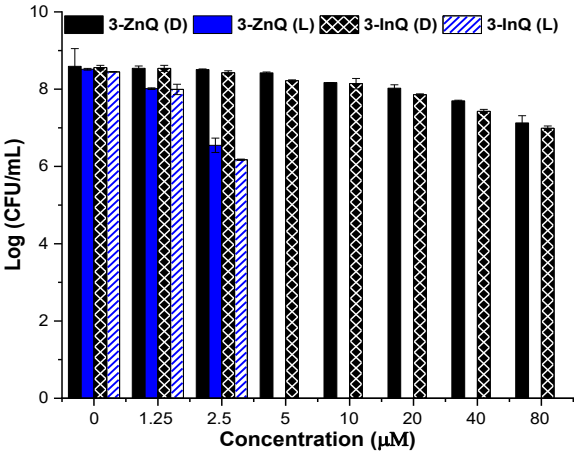
3-ZnQ (D)
3-ZnQ (L)
3-InQ (D)
3-InQ (L)
Log (CFU/mL)
Concentration (μM)
0
1.25
2.5
5
10
20
40
80

e)

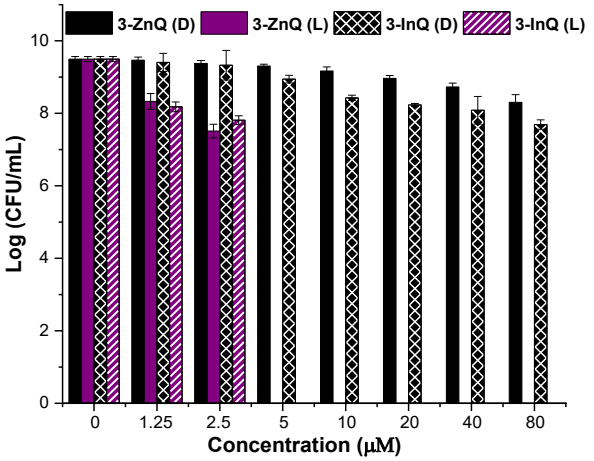
3-ZnQ (D)
3-ZnQ (L)
3-InQ (D)
3-InQ (L)
Log (CFU/mL)
Concentration (μM)
0
1.25
2.5
5
10
20
40
80

c)

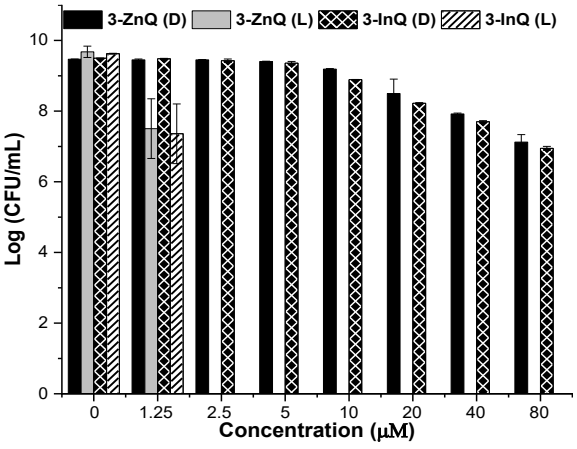
3-ZnQ (D)
3-ZnQ (L)
3-InQ (D)
3-InQ (L)
Log (CFU/mL)
Concentration (μM)
0
1.25
2.5
5
10
20
40
80

f)

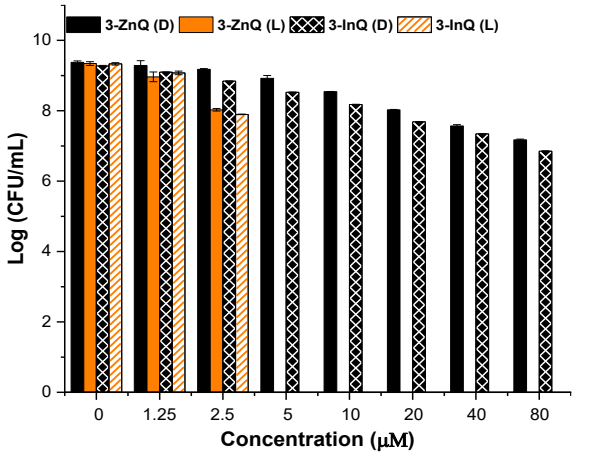
3-ZnQ (D)
3-ZnQ (L)
3-InQ (D)
3-InQ (L)
Log (CFU/mL)
Concentration (μM)
0
1.25
2.5
5
10
20
40
80

g)

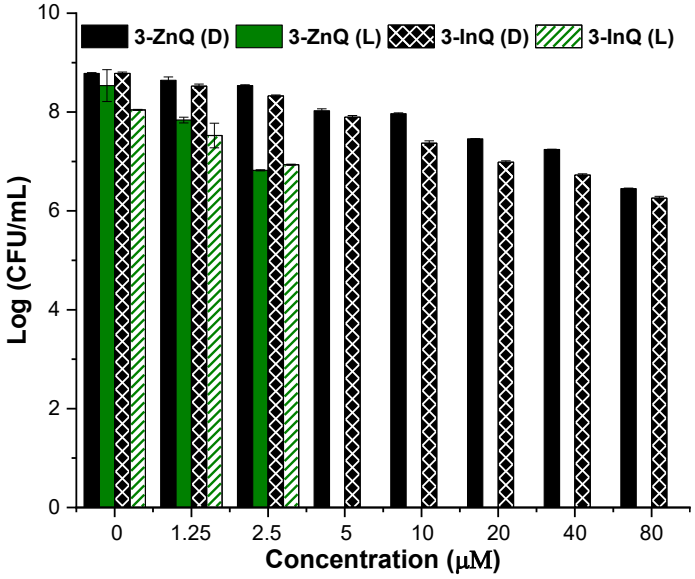

Figure 5.1: Concentration-dependent plots against gram-positive bacteria (a) VREF, (b) MRSA, (c) *S. aureus*, gram-negative bacteria (d) *K. pneumoniae*, (e) *S. choleraesuis* (c) *E. coli* and (f) *C. albicans* in the dark (D) and light (L, 108 J/cm^2, wavelength = 680/690 nm) using **3-ZnQ** and **3-InQ** as photosensitizers in 5% DMSO.

The activity of ZnONPs was assessed by varying the concentration against *S. aureus* and *E. coli*, and the results are shown in **Figure 5.2**. The nanoparticles alone showed dark toxicity which also increased with an increase in concentration (**Figure 5.2)**. ZnONPys had slightly higher dark toxicity compared ZnONSps. Despite the antimicrobial activity observed with ZnONPs, complete eradication of the microorganisms was not achieved. Therefore, the linkage to a photosensitizer might lead to enhanced activity.

In the dark, a noteworthy log reduction values of all conjugates against the three microorganisms (*S. aureus*, *E. coli* and *C. albicans*) was evident, which is attributed to

the antimicrobial properties of the ZnONPs. Conversely, phthalocyanines (**6**) exhibited no dark toxicity in the absence of ZnONPs.

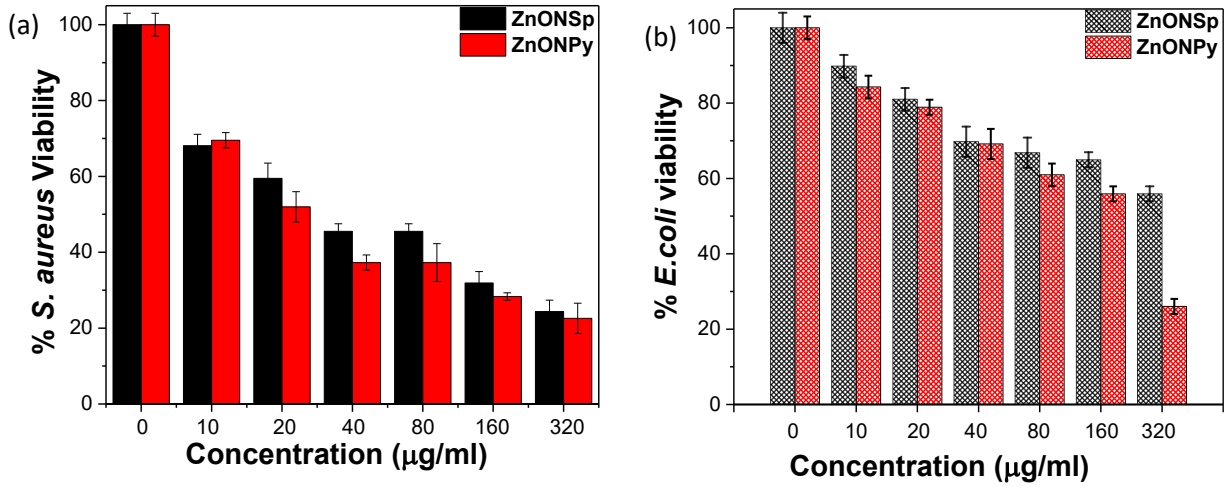

Figure 5.2: Dose-dependent antimicrobial effect of ZnONSps and ZnONPys against (a*) S. aureus* and (b) *E. coli*, the samples were incubated for 60 min in the dark.

5.1.2 PACT studies in solution

5.1.2.1 PACT of 1, 2, 6 and 7 against *S. aureus*, *E. coli* and *C. albicans* in planktonic form

Figure 5.3 is provided as an example for these studies, complexes **1**, **2**, and **7** were chosen since they contain morpholine which has antibacterial activity, hence will in comparing the microorganisms, **6** was chosen for the effect of nanoparticles. The PACT studies were initially conducted by varying concentrations of complexes **1** and **2** from 0.125 μM to 80 μM and were irradiated for 1 h. The lowest concentration achieving complete photo-eradication (log reduction ≥ 3) of the microbes was determined and defined as optimum values. The optimum concentration for complex **1** and **2** were found to be 0.5 μM for *S. aureus* and 2.5 μM for *E. coli* and *C. albicans*. The log reductions values are listed in **Table 5.1**. As expected from Φ_{Δ} values, the cationic Pcs (**1-ZnQ**, **2-ZnQ**, **1-ZnQ** and **2-InQ**) exhibited higher log reductions than their neutral derivatives against all three microorganisms. The hydrophilic nature of cationic Pcs promoted interaction between the dyes and cytoplasm of the microorganisms. Additionally, improved solubility enhanced the interaction between the dye and the microorganism. As a result, cationic complexes exhibited very high log reductions. In general, there was a moderate difference between the non-peripheral, peripheral, zinc and indium Pcs. The log reduction values in the presence of DMSO (≤ 5% DMSO) were not significantly different from the values in water alone for the quaternized derivatives (**Table 5.1**).

Table 5.1: Log reduction values for planktonic cells using different photosensitizers in aqueous media (5% DMSO) at 1 h irradiation, unless stated otherwise.

Photosensitizer	Φ_Δ (in aq sol)	Log reduction		
		S. aureus	*E. coli*	*C. albicans*
1-Zn	0.01	1.31	1.17	1.59
2-Zn	0.02	1.45	1.36	1.78
1-In	<0.01	1.28	1.03	1.36
2-In	<0.01	1.30	1.21	1.40
1-ZnQ	0.26	8.42 8.21[a]	9.90 9.43[a]	7.94 7.49[a]
2-ZnQ	0.23	8.37 8.19[a]	9.84 9.38[a]	7.87 7.34[a]
1-InQ	0.38	8.57 8.28[a]	9.92 9.41[a]	7.98 7.53[a]
2-InQ	0.32	8.48 8.22[a]	9.87 9.36[a]	7.92 7.37[a]
3-Zn	0.03	1.24	0.11	0.13
3-In	0.05	1.90	0.13	0.19
3-ZnQ	0.18	9.68	9.34	8.78
3-InQ	0.20	9.67	9.33	8.74
6-Zn	0.08	1.72	0.81	0.88
6-In	0.10	1.74	0.84	0.96
6-ZnQ	0.21	8.52	7.88	8.08

[a] values are in water

Table 5.1 continues:

Photosensitizer	Φ_{Δ} (in aq sol)	Log reduction (% reduction)		
		S. aureus	*E. coli*	*C. albicans*
6-InQ	0.25	8.48	7.88	8.10
6-Zn-ZnONSps[a]	0.03	2.28	1.74	1.69
6-In-ZnONSps[a]	0.05	2.30	1.77	1.71
6-ZnQ-ZnONSps[a]	0.17	8.48	7.94	8.30
6-InQ-ZnONSps[a]	0.20	8.54	7.90	8.32
6-Zn-ZnONPys[a]	0.05	3.72	1.93	2.34
6-In-ZnONPys[a]	0.06	3.77	2.01	2.38
6-ZnQ-ZnONPys[a]	0.18	8.41	7.98	8.36
6-InQ-ZnONPys[a]	0.23	8.45	7.98	8.40
7-Zn	0.21	8.07	2.24	7.60
7-In	0.23	8.05	2.73	7.61
7-ZnQ	0.24	8.11	7.90	7.63
7-InQ	0.28	8.13	7.92	7.64

[a]Studies were complete using 5 μg/mL for *S. aureus* and 10 μg/mL for both *E. coli* and *C. albicans*.

The effect of asymmetry was evaluated using complex **7** against *S. aureus*, *E. coli*, and *C. albicans*. The same optimal Pcs concentrations of 2.5 μM for *S. aureus* and 5 μM for *E. coli* and *C. albicans* were applied. The neutral Pcs (**7-Zn** and **7-In**) showed good photocytotoxicity (**Figure 5.3**) against *S. aureus* and *C. albicans* with log reduction values of 8.05-8.07 and 7.60-7.61, respectively, as summarized in **Table 5.1**. The addition of one carboxy phenoxy improved the solubility of **7-Zn** and **7-In** in aqueous solution compared to **2-Zn** and **2-In,** thus enhancing photo-antimicrobial activity. Neutral Pcs are known to be active against gram-positive bacteria due to their ability to penetrate the thick yet porous outer membrane layer [**85**, **230**]. Conversely, gram- negative bacteria are enveloped by non-lipids, lipopolysaccharide and selective porin-containing outer membranes, which are negatively charged, inhibiting the activity of neutral complexes [**231**, **232**]; hence, lower log values were obtained for *E. coli* when using complexes **7** (neutral). As expected, methylated Pcs (**7-ZnQ** and **7-InQ**) exhibited improved inactivation efficacy at a shorter time compared to the neutral Pcs, as shown in **Figure 5.3**. This improvement was attributed to an enhanced singlet oxygen quantum yield in aqueous media and the ability to penetrate all three microorganism's cell walls/membranes, **Table 5.1**.

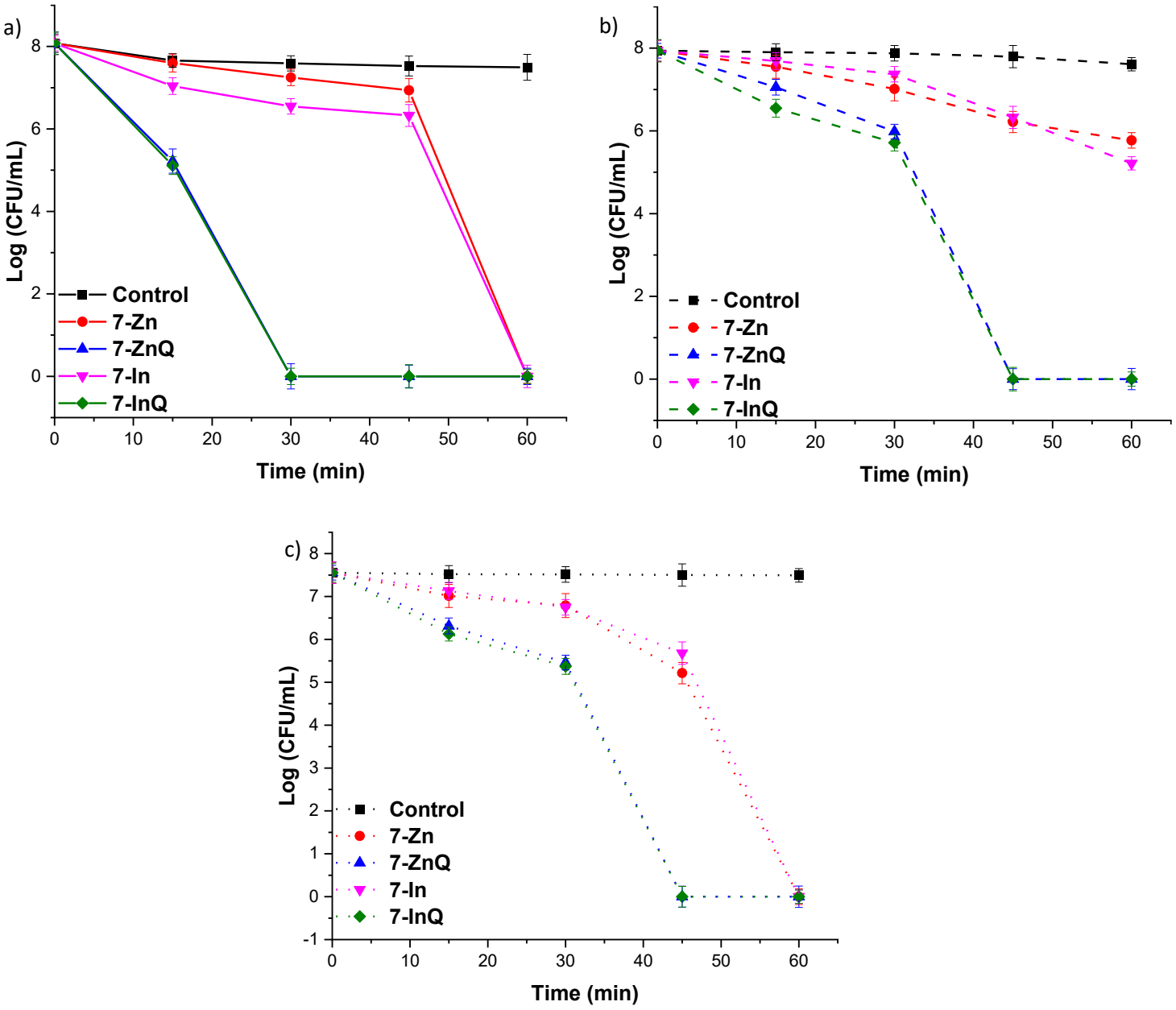

Figure 5.3: PACT activity time-correlated studies in aqueous solution (a) *S. aureus* (Pc = [2.5 μM]) b) *E. coli* (Pc = [5 μM]) and *C. albicans* (Pc = [5 μM]) in 5% DMSO.

The PACT studies for planktonic cells using complex **6** involved photosensitizer concentrations of 5 µg/mL for *S. aureus* and 10 µg/mL for both *E. coli* and *C. albicans*. The results for complex **6-ZnQ**, **6-ZnQ**-ZnONSps and **6-ZnQ**-ZnONPys conjugates are presented as examples in **Figure 5.4**(a)-(c)**.** Under light irradiation, the cationic complexes (**6-ZnQ** and **6-InQ**) and their conjugates successfully eradicated *S. aureus*, *E. coli*, and *C albicans* (**Figure 5.4**, **Table 5.1**) with log CFU values reaching close to or exceeding 8 for planktonic cells. The uncharged composites showed a reduction microorganism viability but were more effective than for Pcs alone. Log reduction values for uncharged composites generally remained lower than for the charged composites, corresponding with the low singlet oxygen quantum yield values in aqueous media for the former, **Table 5.1**. Complete eradication of *S. aureus* was achieved with an irradiation dose of 45 J/cm^2 using **6-ZnQ**-ZnONPys (**Figure 5.4**). A similar trend was observed for both *E. coli* and *C. albicans,* where the **6-ZnQ**-ZnONPys conjugate (**Figure 5.4** (b-c)) achieved a 0% cell survival when irradiated with 90 J/cm^2 intensity.

The biofilm studies were conducted with varying concentrations of 25, 50, 100, and 200 µg/mL for each nanocomposite. As expected, there was an enhancement in biofilm eradication with increasing nanocomposite concentration (**Figure 5.4** (d)-(f)). The phthalocyanines alone showed low activity against both *E. coli* and *C. albicans*. However, they displayed log CFU values of >3 against *S. aureus* at 200 µg/mL for cationic phthalocyanines (complexes **6-ZnQ** and **6-InQ**, **Table 5.2**). The nanoconjugates significantly improved the eradication of all three micro-organisms. Nevertheless, the log CFU values against *C. albicans* remained below 3 log CFU. The zinc oxide incorporated nanoconjugates can release zinc ions into the solution leading

to the termination of the microbes. The aforementioned results motivated the mixing of *S. aureus*, *E. coli*, and *C. albicans* to form a biofilm with a heterogeneous morphology. Subsequently, the antimicrobial activity of all nanocomposites was investigated (**Table 5.2**). The log reduction values decreased for all nanocomposites due to the complexity of the mixed biofilm. However, the **6-ZnQ** /**6-InQ**-ZnONPys nanocomposite showed promising potential in eradicating mixed species.

The morphology of the cell wall played a crucial role in affecting the antimicrobial activity of the nanocomposites. Cationic nanocomposites had greater efficacy owing to their capacity to penetrate the dense peptidoglycan layer in *S. aureus* and navigate through the intricate cell walls of *E. coli* and C*. albicans* cell walls [**233**]. Interestingly, the ZnONPys-containing conjugates had higher effectiveness than ZnONSps (except for *S. aureus*). This outcome was unexpected, given that ZnONSps are smaller and were anticipated to easily infiltrate the cell membrane. Overall, the highest PACT activity, as well as dark toxicity, was observed with ZnONPys and its nanoconjugates. This phenomenon might be attributed to the sharper nature of ZnONPys, enabling it to rupture the cell membrane, and the larger nanoparticle's capability to release the toxic Zn^{2+} ions.

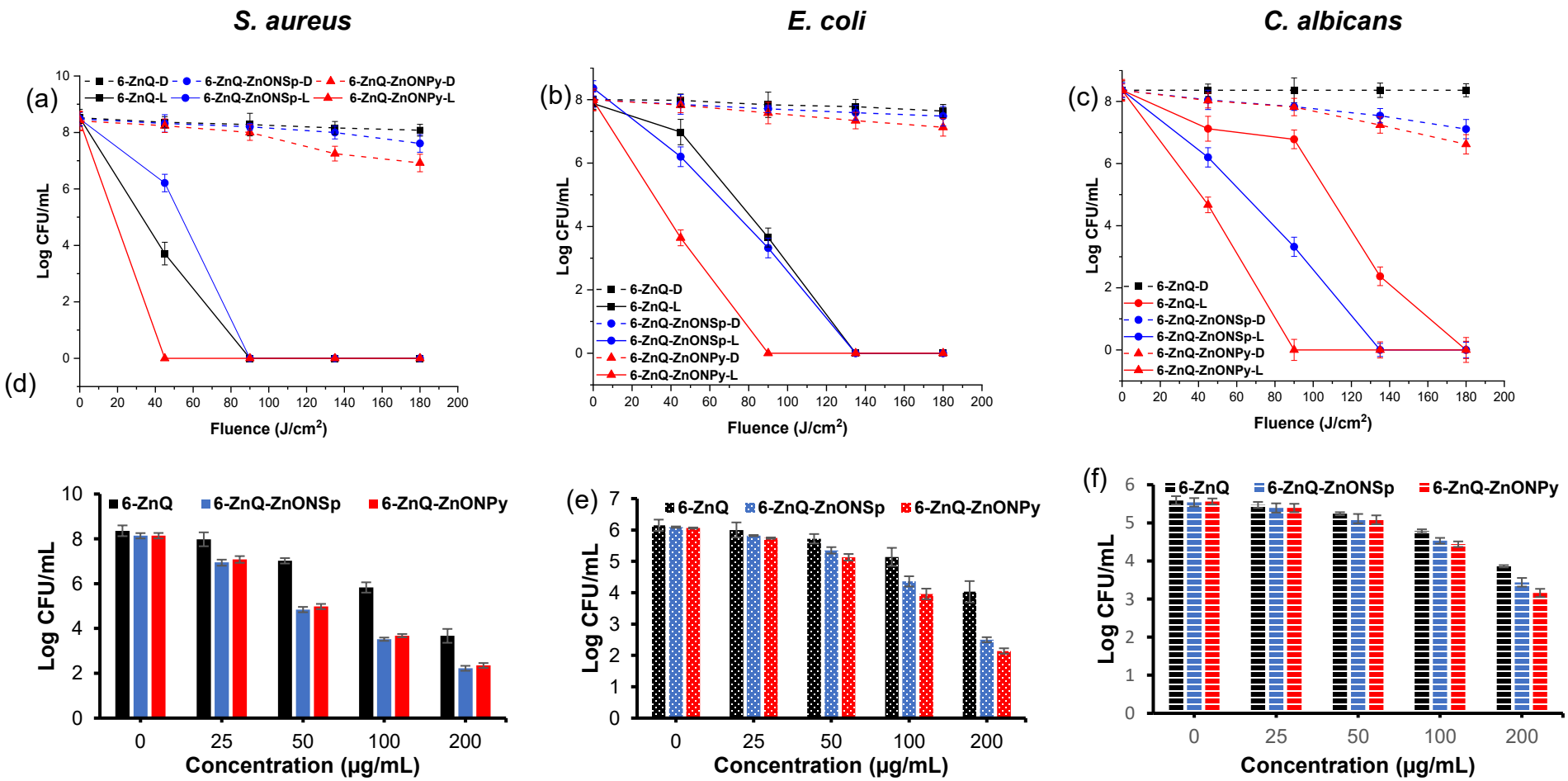

Figure 5.4: The photo antimicrobial activity of **6-ZnQ**, **6-ZnQ**-ZnONSps and **6-ZnQ**-ZnONPys on (a) *S. aureus*, (b) *E. coli* and (c) *C. albicans* planktonic cells (D= dark, L = light). Dose-dependent photo antimicrobial effect of complex **6, 6**-ZnONSps and **6**-ZnONPys on (d) *S. aureus*, (e) *E. coli* and (f) *C. albicans* biofilm. The experiments were irradiated for 60 min with Modulight 680 nm laser using concentrations of 5 µg/mL for *S. aureus* and 10 µg/mL for *E. coli* and *C. albicans* in 5% DMSO.

Table 5.2: Log reduction values of biofilms when treated with 200 µg/mL of each complex. The experiments were performed in aqueous solution at 108 kJ/cm^2.

Photosensitizer	Log reduction			
	S. aureus	*E. coli*	*C. albicans*	Mixture
6-Zn	2.25	1.17	0.11	0.05
6-In	2.29	1.18	0.14	0.07
6-ZnQ	4.69	2.12	1.73	1.05
6-InQ	4.66	2.12	1.79	1.08
6-Zn-ZnONSps	4.38	1.94	0.83	0.57
6-In-ZnONSps	4.41	2.00	0.84	0.63
6-ZnQ-ZnONSps	5.92	3.59	2.10	1.78
6-InQ-ZnONSps	5.95	3.62	2.12	1.81
6-Zn-ZnONPys	4.12	2.03	0.92	0.74
6-In-ZnONPys	4.08	2.07	0.95	0.78
6-ZnQ-ZnONPys	5.79	3.92	2.40	2.11
6-InQ-ZnONPys	5.84	3.95	2.43	2.13

5.1.2.2 PACT of 3 against various microorganisms

Complex **3** was not only used to assess the photodynamic effect of the morpholine Schiff base complexes and compared to cationic complexes **2**, but it was also employed to investigate other microorganisms. These complexes were tested against planktonic cells of various microorganism strains; gram-positive bacteria such as *S. aureus,* MRSA, VREF; gram-negative bacteria including *E. coli, K. pneumoniae, S. choleraesuis*; and fungi like *C. albicans*. The results for the light studies are summarized in **Table 5.3**.

The PACT results revealed complete eradication of the *S. aureus* and VREF populations when treated with 2.5 μM of **3-ZnQ** and **3-InQ**, while the rest of the microorganisms required 5 μM to achieve complete elimination. Using 5 μM, complexes **3-Zn** and **3-In** showed very low log reduction values of less than 2, **Table 5.3**. In contrast, **3-ZnQ** and **3-InQ** exhibited very high log reduction values of more than 7 for all micro-organisms (as shown in **Table 5.3**). The effectiveness of the cationic morpholine-containing complexes (**2** and **3**) was evaluated by varying the light dosage, as listed in **Table 5.4**. The cationic Schiff base Pcs (**3-ZnQ** and **3-InQ**) required more light energy than **2-ZnQ** and **2-InQ** to completely eradicate the microorganisms. When dealing with gram-positive bacteria, the light energy for **3-ZnQ** and **3-InQ** was doubled to 54 J/cm^2 (up from 27 J/cm^2 for **2-ZnQ** and **2-InQ**), except for MRSA, which necessitated a more intense light dosage of 108 J/cm^2, for **3-ZnQ** and **3-InQ**.

Interestingly, both the cationic Schiff base Pcs (**3-ZnQ** and **3-InQ**) and cationic non-Schiff base Pcs (**2-ZnQ** and **2-InQ**) contain the morpholine group. However, the Schiff base Pcs required a higher light energy to completely eradicate the microorganisms. This could be

attributed to the higher generation of singlet oxygen (Φ_Δ = 0.23 for **2-ZnQ** and Φ_Δ = 0.32 for **2-InQ**, in aqueous media). It has been reported that the width of the cell envelope is smaller than the diffusion length of singlet oxygen; thus, complexes **2-ZnQ** and **2-InQ** with higher singlet oxygen quantum yields in aqueous media, exhibit greater phototoxicity compared to **3-ZnQ** and **3-InQ** [234].

Table 5.3: Log reduction of planktonic cells and biofilms (in brackets) using 108 J/cm^2.

PS	Log reduction							
	SA	VREF	MRSA	KP	EC	SC	CA	Mixed
2-ZnQ	8.37 (4.15)	7.04 (4.08)	8.51 (5.45)	8.61 (4.15)	9.84 (4.34)	9.44 (4.44)	7.87 (4.02)	- (1.05)
2-InQ	8.48 (4.15)	7.02 (4.10)	8.50 (5.47)	8.62 (4.16)	9.87 (4.37)	9.46 (4.47)	7.92 (4.02)	- (1.11)
3-Zn	1.24 (0.32)	0.19 (0.02)	0.07 (0.01)	0.07 (0.08)	0.11 (0.01)	0.06 (0.02)	0.13 (0.48)	- (<0.01)
3-In	1.90 (0.32)	0.22 (0.03)	0.10 (0.01)	0.09 (0.08)	0.13 (0.02)	0.06 (0.05)	0.19 (0.50)	- (<0.01)
3-ZnQ	9.68 (4.15)	7.01 (4.04	8.52 (5.50)	8.61 (4.14)	9.34 (4.37)	9.48 (4.48)	8.78 (4.06)	- (1.05)
3-InQ	9.67 (4.14)	7.02 (4.08)	8.48 (5.48)	8.64 (4.16)	9.33 (4.37)	9.48 (4.44)	8.74 (4.06)	- (1.07)

SA = *S. aureus,* KP= *K. pneumoniae,* SC = *S. choleraesuis* and CA = *C. albicans.*

Both sets of cationic morpholine Pc complexes exhibit the ability to electrostatically attach to the outer membrane. To simulate the water/membrane interface, the lipophilicity of the complexes was determined using octanol: water partition coefficients (P_{ow}). The values were obtained using the shake-flask method [**235**], and the Log P_{ow} values are summarized in **Table 5.4**. Surprisingly, the cationic complexes containing both the imine and morpholine groups higher gave lipophilicity (positive log P_{OW}) and displayed a stronger affinity for membranes. This might be attributed to the presence of alkyl chains and their bulky nature. In contrast, the smaller complexes **2-ZnQ** and **2-InQ** appeared to be more hydrophilic (negative log P_{OW}).

Furthermore, both set of complexes (cationic **2** and **3**) were tested against mono-biofilms and mixed biofilms containing all microorganisms. Similar to the planktonic cell studies, the bactericidal effect was observed when using a combination of high concentration (200 μM) and higher light dosage (108 J/cm^2). The results are summarized in **Table 5.3**. For mono-biofilms, the cationic complexes demonstrated an acceptable biofilm reduction (log reduction > 3) for all microorganisms, **Table 5.3**. The neutral Pcs showed no significant activity against the mixed biofilms, and the cationic Pcs showed biofilm reduction of > 1 (cell viability of > 90%) at 108 J/cm^2.

Table 5.4: Fluence required for the complete eradication of each microorganism (planktonic) using 5 μM of each complex. Log partition coefficients of Pcs in octanol:water.

PS	Fluence (J/cm^2)							Log Pow
	SA	*VREF*	*MRSA*	KP	EC	SC	CA	
2-ZnQ	27	27	54	81	81	81	54	-0.28
2-InQ	27	27	54	81	81	81	54	-0.34
3-Zn	>108	>108	>108	>108	>108	>108	>108	-
3-In	>108	>108	>108	>108	>108	>108	>108	-
3-ZnQ	54	54	108	108	108	108	54	1.32
3-InQ	54	54	108	108	108	108	54	1.18

PS – Photosensitizer, SA – *S. aureus*, KP - *K. pneumoniae*, EC – *E. coli*, SC - *S. choleraesuis*, CA – *C. albicans*

5.1.2.3 PACT of 4 and 5 against MSSA and MRSA

The effect of alkyl chain extension in PACT was assessed using complexes **4** and **5** gram-positive methicillin-sensitive *Staphylococcus aureus* (MSSA) and methicillin-resistant *Staphylococcus aureus* (MRSA) bacteria strains. As expected, all neutral complexes (**4-Zn**, **5-Zn**, **4-In**, **5-In**) showed minimal phototoxicity levels. While the Φ_Δ values in aqueous media for **5-ZnQ**/**5-InQ** were comparable to **4-ZnQ**/**5-InQ**, the log reduction values for MRSA at 5 μM (**Table 5.5**) were found to be 2.65, 2.71, 8.48, 8.48 for **4-ZnQ**, **4-InQ**, **5-ZnQ,** and **5-InQ**, respectively. The decrease in the activity of **4-ZnQ** and **4-InQ** might be

influenced by the uptake of the compounds in MRSA, which will be discussed below. The log reduction values (> 8) reported in this study for both MSSA and MRSA using **5-ZnQ** and **5-InQ** surpass those reported for other cationic phthalocyanines containing quaternized pyridine substituents [**236**], where the value was 7 or less. This shows the significance of extending the alkyl chain to enhance uptake efficiency and highlight the utility of the pyrrolidine moiety in improving PACT activities.

Table 5.5: Summary of log reduction values results using a concentration of 5 μM for each complex and the diameters of zones of inhibition (in brackets) using 250 μM of each complex along with 50 μM of ampicillin and methicillin.

PS	Φ_{Δ} (in aq sol)	Log reduction	
		MSSA	MRSA
4-Zn	0.07	0.96 (0±0.0)	0.37 (0±0.0)
4-In	0.10	1.01 (0±0.0)	0.42 (0±0.0)
5-Zn	0.08	1.22 (0±0.0)	0.38 (0±0.0)
5-In	0.12	1.27 (0±0.0)	0.41 (0±0.0)
4-ZnQ	0.20	8.69 (20±0.1)	2.65 (36±0.1)
4-InQ	0.22	8.68 (22±0.1)	2.71 (40±0.2)
5-ZnQ	0.22	8.64 (20±0.3)	8.48 (46±0.5)
5-InQ	0.24	8.64 (32±0.5)	8.48 (46±0.2)
Ampicillin	-	- (228±0.2)	- (298±0.4)
Methicillin	-	- (144±0.3)	- (0±0.0)

The uptake studies revealed a gradual increase in the uptake of the complexes with an increase in concentration (0-250 μM), as depicted in **Figure 5.5**. Quaternized derivatives exhibited higher uptake compared to the corresponding unquaternized Pcs (**Figure 5.5(a,b)**). Neutral Pcs showed slower uptake due to their hydrophobic nature. Importantly, the time required to attain maximum uptake of **4-Zn**, **5-Zn**, **4-ZnQ**, and **5-ZnQ** by MSSA and MRSA was investigated using a concentration of 5 μM for each Pc complex. As shown in **Figure 5.5(c,d)**, all Pc complexes showed greater uptake in MSSA cells than in MRSA. Notably, **5-ZnQ** displayed higher uptake in both MSSA and MRSA compared to all other photosensitizers, achieving maximum uptake within 15 min of incubation for MSSA and within 30 min for MRSA. In contrast, the maximum uptake of **4-ZnQ** was observed within 30 min for both MSSA and MRSA. The extension of the alkyl chain contributed to the improvement in uptake efficiency. However, prior to conducting the dark and phototoxicity studies, all complexes were incubated for 30 min. Therefore, both **4-ZnQ** and **5-ZnQ** had already reached their maximum uptake. The slightly longer alkyl chain in **5-ZnQ** and **5-InQ** may have influenced the enhancement in the photodynamic inactivation against MRSA.

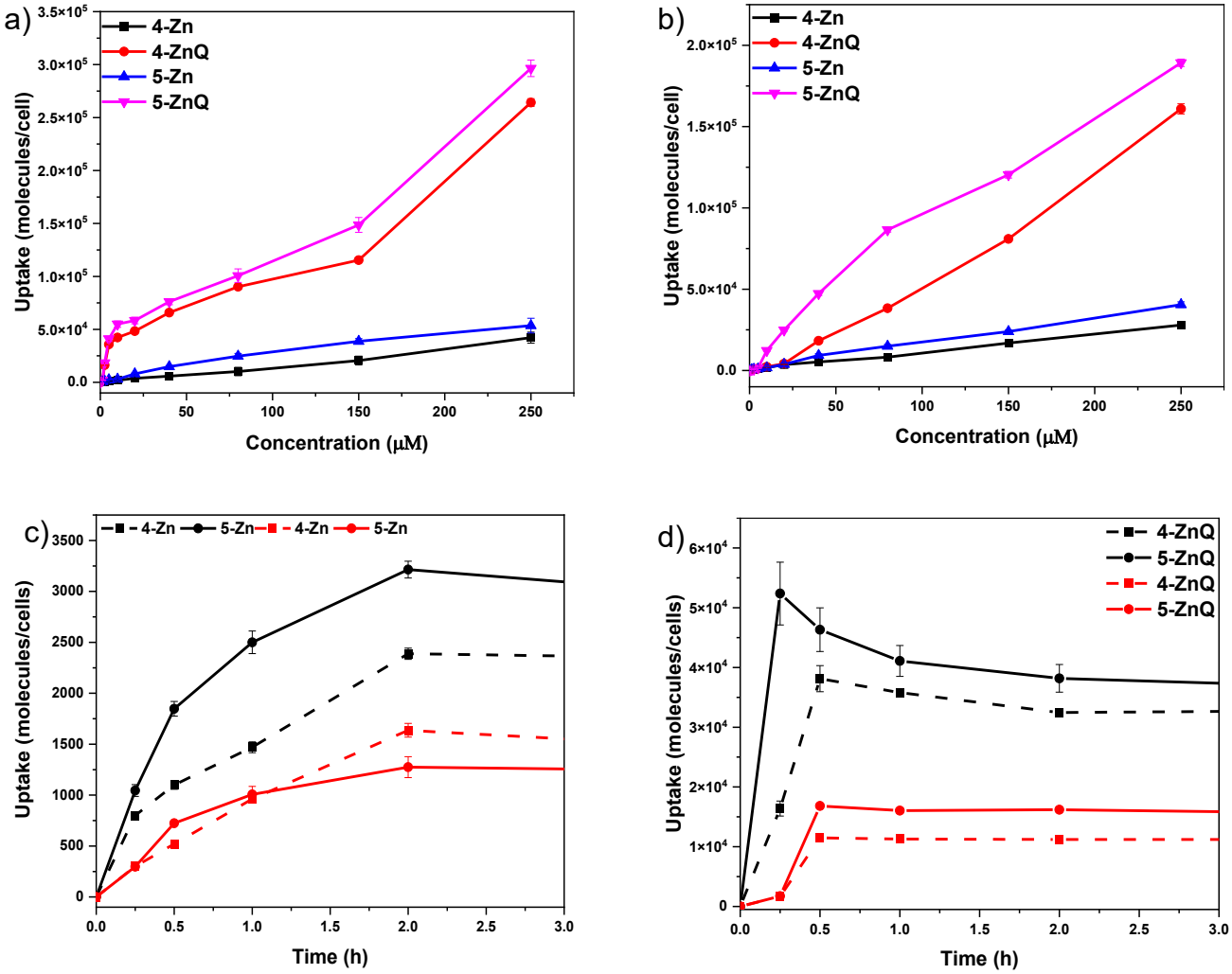

Figure 5.5: The quantity of **4-Zn**, **4-ZnQ**, **5-Zn**, and **5-ZnQ** taken up in a) MSSA and b) MRSA at varying concentrations after 1 h of incubation. Time-dependent uptake studies of c) neutral and d) cationic ZnPcs (5 μM) in MSSA (black) and MRSA (red).

Furthermore, the capacity of the Pcs to eliminate a thin bacterial film was evaluated using the disk diffusion method [**175**]. For this, 20 µL of each complex (250 µM) was loaded onto sterile test discs, which were then placed onto bacteria film. The agar plates were subsequently exposed to irradiation at 180 J/cm^2 for 1 h. Ampicillin and methicillin served as controls; ampicillin was employed as a positive control for both MSSA and MRSA, while methicillin was used as a positive control for MSSA and a negative control for MRSA. The results of the inhibition zone experiments for MSSA and MRSA are presented in **Figure 5.6** and the findings are summarized in **Table 5.5** (within brackets). Comparatively, the cationic Pcs showed an enhanced inhibition zone compared to the neutral Pcs. Interestingly, the sizes of the inhibition zones were larger for MRSA in comparison to MSSA. The newly synthesized Pcs complexes exhibited remarkable photodynamic antimicrobial activity against both methicillin-sensitive *Staphylococcus aureus* and methicillin-resistant *Staphylococcus aureus*.

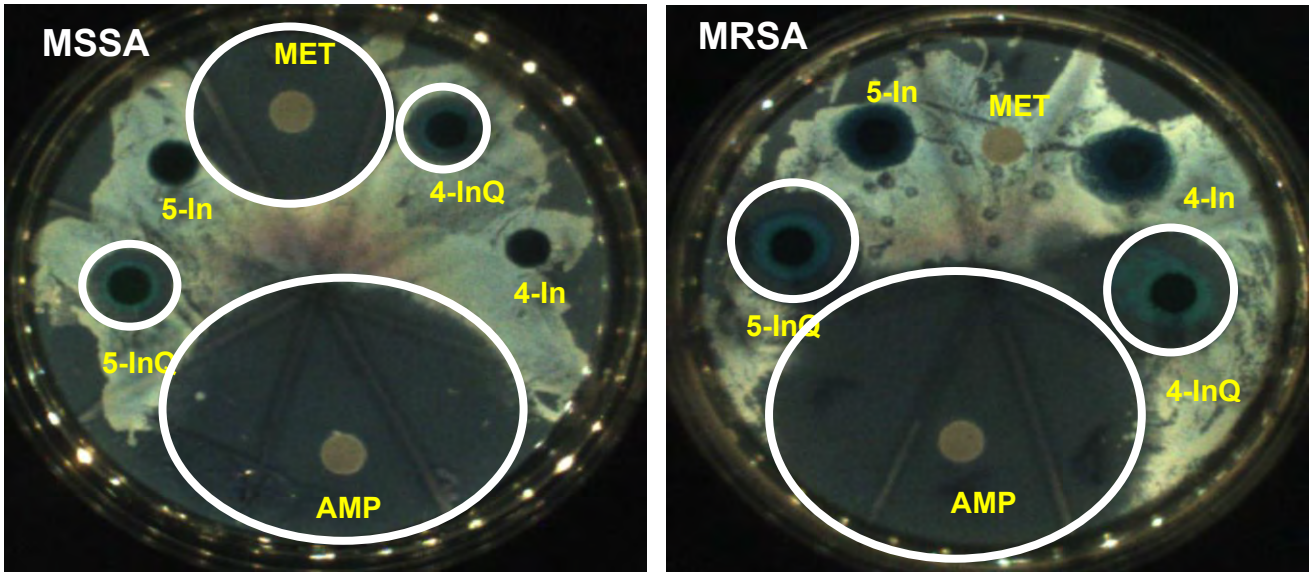

Figure 5.6: Zones of inhibition of MSSA and MRSA by; MET = methicillin, **4-InQ**, **4-In**, AMP = ampicillin, **5-InQ**, and **5-In**.

5.2 Photodynamic Antimicrobial Chemotherapy on support (Pc-PAN, Pc-PAN-CS and Pc-GW)

The Pc on supports were evaluated against microorganisms to assess their antifouling properties. Biological fouling of materials involves the absorption on micro-organisms into the surface. Herein, the antimicrobial properties of Pc-PAN, Pc-PAN-CS, and Pc-GW are reported.

5.2.1 PACT activity of Pc-PAN and Pc-PAN-CS

With complex **7** exhibiting positive antimicrobial activities for all three model microorganisms (*S. aureus*, *E. coli* and *C. albicans*), the investigation proceeded to the electrospinning of Pc-PAN and Pc-PAN-CS, using the same microorganisms. The dark studies were conducted and as depicted in **Figure 5.7 (a-c)**; the unmodified PAN

nanofibers showed no dark toxicity against any of the three microorganisms. In contrast, the pristine PAN-CS nanofibers demonstrated a decrease in cell survival, with *S. aureus* showing a higher cell death of 6.5 % compared to the PAN nanofibers.

Upon 1 h irradiation, the results obtained for Pc-PAN and Pc-PAN-CS are illustrated in **Figure 5.7(d-f)**, and the percentage reduction outcomes are summarized in **Table 5.6**. Across all microorganisms, the nanofibers containing chitosan exhibited enhanced efficacy, with a reduction in colony population following this trend: **7-InQ**-PAN-CS > **7-ZnQ**-PAN-CS > **7-InQ**-PAN > **7-ZnQ**-PAN > **7-In**-PAN-CS > **7-Zn**-PAN-CS > **7-In**-PAN > **7-Zn**-PAN.

Similar to the complexes in solution, nanofibers containing cationic Pcs showed significant PACT activity compared to neutral nanofibers due to the presence of positive charges. These positive charges attracted microorganisms to bind to the photoactive surface, thereby increasing the probability of interacting with the toxic singlet oxygen. The introduction of chitosan further enhanced activity of the cationic nanofibers, resulting in a reduction of over 90 % for both *S. aureus* and *C. albicans* and over 55% for *E. coli.* This improvement can be attributed to the enhanced hydrophilicity of the polymer and antimicrobial properties of chitosan. Notably, only against *S. aureus* was completely irradicated by **7-ZnQ-**PAN-CS and **7-InQ**-PAN-CS**,** with percent reduction of 100 % (**Figure 5.8**). This outcome arises from the absence of an outer membrane on the gram-positive bacteria, which permits singlet oxygen species to damage crucial lipids and proteins, consequently inducing cell death [237].

Table 5.6: Percentage reduction values for planktonic cells using different photosensitizers in aqueous media irradiated with red light unless stated otherwise.

Photosensitizer	Φ_{Δ} (in aq sol)	Percentage reduction		
		S. aureus	*E. coli*	*C. albicans*
7-Zn-PAN	0.14	57.5 (66.0)	11.9 (19.4)	37.3 (41.1)
7-Zn-PAN-CS	0.18	65.0	18.8	40.6
7-In-PAN	0.16	60.5 (69.6)	13.7 (21.7)	39.6 (44.1)
7-In-PAN-CS	0.18	68.8	20.6	41.9
7-ZnQ-PAN	0.18	91.7 (100)	52.3 (63.3)	75.9 (90.3)
7-ZnQ-PAN-CS	0.21	100	57.9	93.3
7-InQ-PAN	0.21	94.6 (100)	54.9 (67.1)	77.2 (94.3)
7-InQ-PAN-CS	0.24	100	58.8	94.6
7-Zn-GW	0.11	37.6 (45.7)	0.7 (7.6)	3.3 (12.6)
7-In-GW	0.12	43.8 (49.6)	2.9 (9.2)	7.7 (19.9)
7-ZnQ-GW	0.15	61.4 (72.6)	14.8 (25.2)	40.7 (51.1)
7-InQ-GW	0.17	66.8 (75.4)	17.3 (29.2)	31.2 (50.3)
8-Zn-GW	0.38	77.8	-	-
9-Zn-GW	0.35	75.3	-	-
10-Zn-GW	0.22	67.2	-	-

[a]Values in brackets are when irradiated with white light.

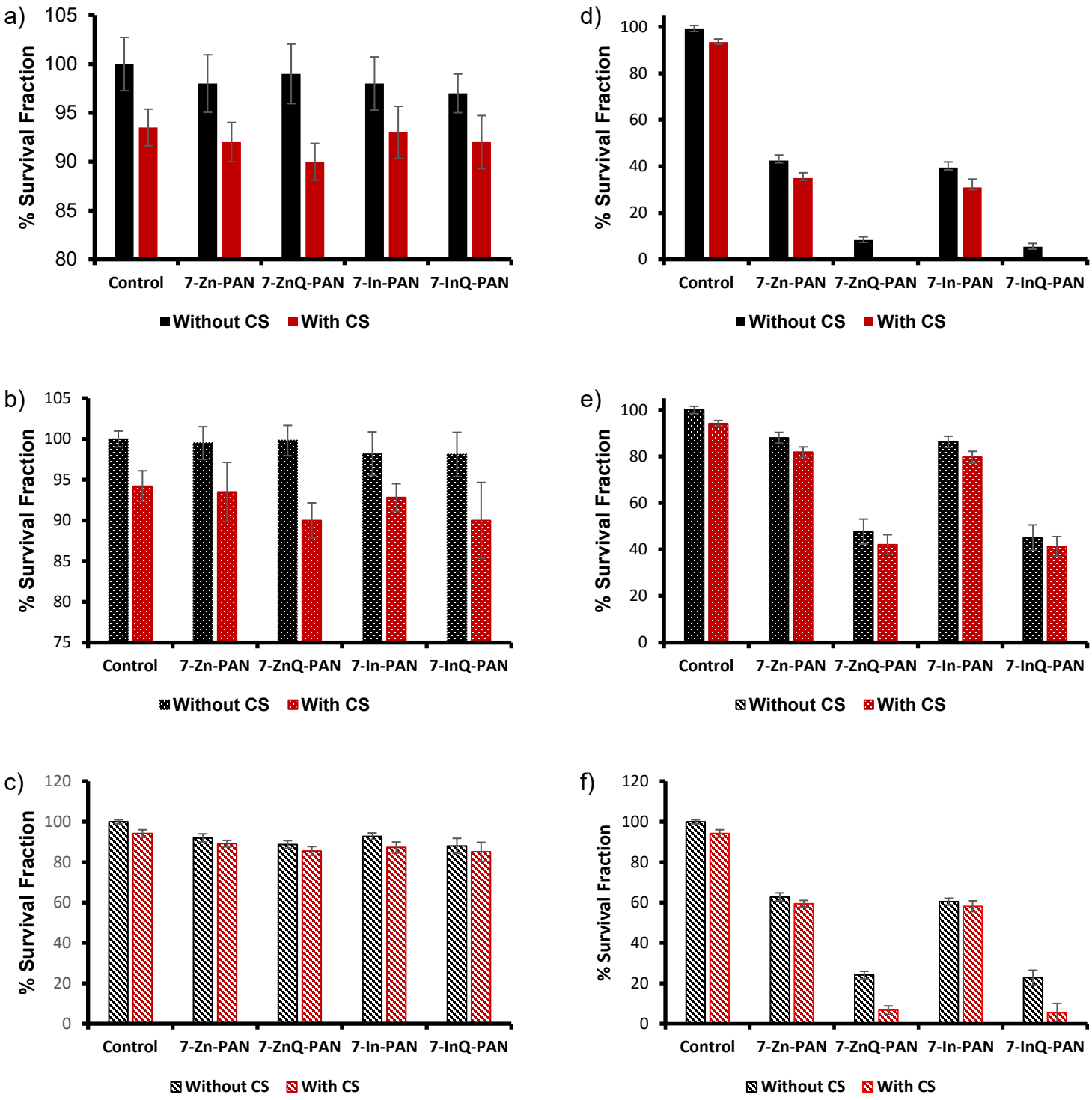

Figure 5.7: Dark toxicity studies on PAN fiber support (a) *S. aureus*, b) *E. coli* and c) *C. albicans* and PACT activity on PAN fiber support (d) *S. aureus*, e) *E. coli* and f) *C. albicans*.

5.2.2 PACT activity of Pc-GW

The photodynamic inactivation studies were also included complex **7** conjugated onto glass wool (Pc-GW). Studies using NH_2-GW and conjugates in the dark, showed no significant antimicrobial effect, hence the results are not reported. The PACT studies were conducted under both red and white light illumination and with Pc-PAN, for comparison. When illuminated with white light, the photoeradication trend was **7-InQ**-GW >**7-ZnQ-**GW > **7-In-**GW > **7-Zn-**GW (as shown in **Table 5.6** and **Figure 5.8**), which mirrors the trend observed for the nanofibers. As expected, the cationic composites exhibited higher microbial inactivation than neutral composites. This heightened activity stems from the electrostatic interaction between the positively charged composite and the negatively charged teichoic acids in *S. aureus*, the lipopolysaccharides in *E. coli* and the oligosaccharides in *C. albicans*. The combination of high singlet oxygen generation and positive charges showed effective photoirradiation of the microbes. PACT activity is more pronounced under white light due to its high singlet oxygen quantum yields. Moreover, the fabricated PAN nanofibers exhibit greater PACT activity compared to the glass wool composites, due to higher Φ_{Δ}, **Table 5.6**.

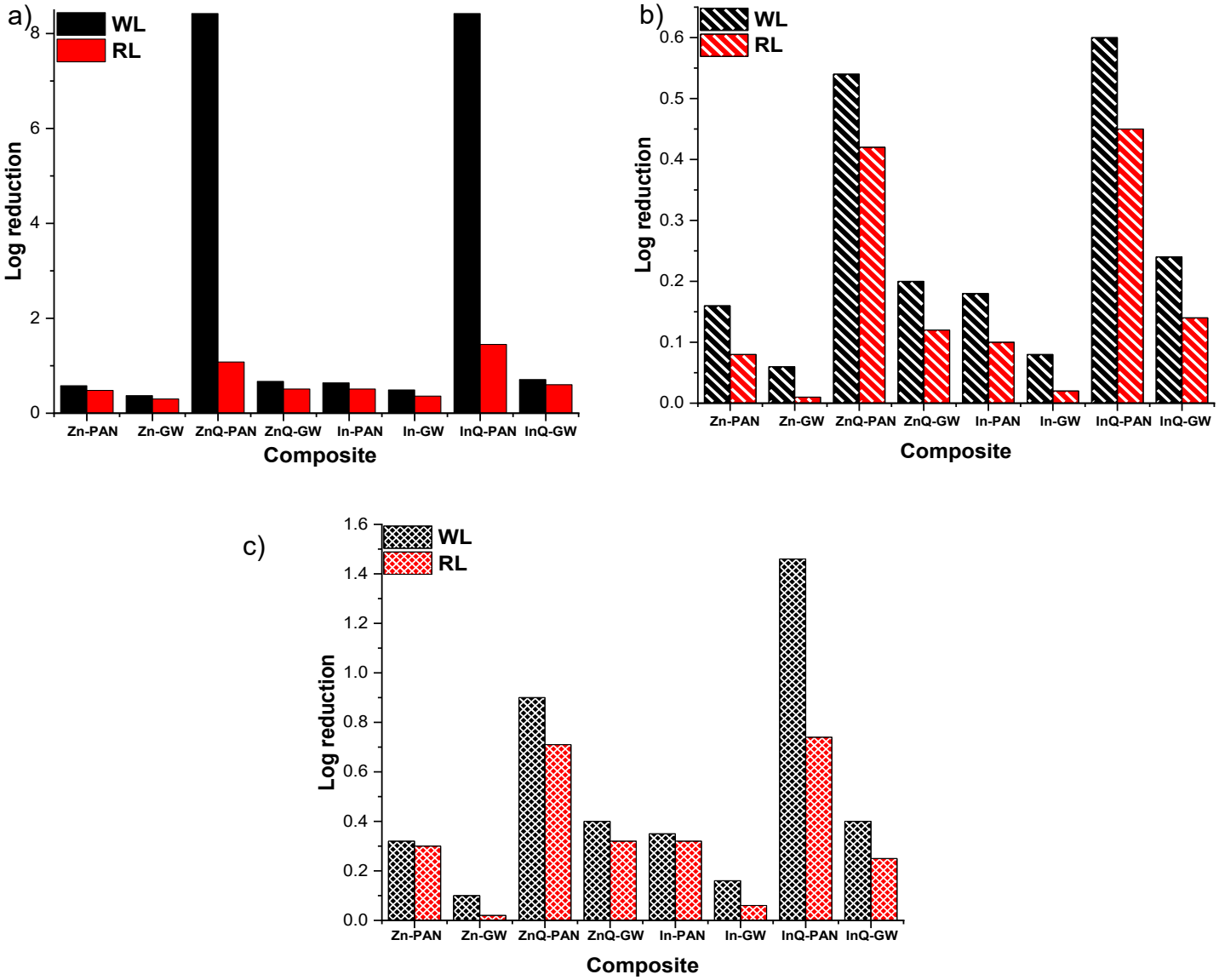

Figure 5.8: Log reduction of a) *S. aureus*, b) *E. coli*, and c) *C. albicans* of the composites (using complexes **7**) when irradiated with white light (WL, in black) and red light (RL, in red) for 60 mins.

The antibacterial activity of the neutral complexes **8-10** were investigated using *S. aureus* bacteria as a model micro-organism. While the studies were also completed using *E.coli* and *C.albicans*, all samples showed no significant antimicrobial activity; therefore, these results are not included. Photodynamic inactivation studies were performed using **8-Zn**-GW, **9-Zn**-GW, **10-Zn**-GW and GW. Upon illumination, the glass wools samples achieved reductions of 77.8 %, 75.3 %, and 67.2 % for **8-Zn**-GW, **9-Zn**-GW, and **10-Zn**-GW, respectively (as shown in **Table 5.6**). As expected, the unmodified GW demonstrated a low level of bacteria reduction (6 %) due to its lack of photoactivity. The slight inactivation observed may be attributed to diffusion effect. The enhanced inactivation efficacy for both **8-Zn**-GW and **9-Zn**-GW is attributed to their ability of sufficient singlet oxygen species when compared to **10-Zn**-GW. Overall, the percentage reduction for the Pc-GW was less than 99.99% which is less than desirable as it allows replication of the bacteria. This activity could be influenced by the presence of carboxylic groups attached to the Pcs. In water, these groups dissociate, resulting in negative charges on the glass wool surface. This charge difference induces repulsion between the photocatalyst and the negatively charge cell membrane [**238**].

5.3 Summary of chapter

The capacity of the phthalocyanine complexes to photoinactive microorganisms was explored. The PACT studies were conducted using various microorganisms including known antibiotic resistant bacteria such as MRSA and VREF. Generally, the cationic Pcs demonstrated high log reduction values when compared to their neutral counterpart due to improved solubility in aqueous media. There were no significant differences in the PACT activities of the zinc and indium complexes as well as alpha and beta substituted complexes. However, complex **2** was more efficient, requiring a lower dose compared to the Schiff base, complex **3**. The extension of the alkyl chain also proved to be essential in the enhancing of the PACT activity with complex **5** showing induced activity compared to complex **4**. The PACT activity of complex **6** and it nanoconjugates were investigated in both planktonic and biofilm forms, and **6**-ZnONPys had a higher efficacy.

Chapter 6

Photodegradation

6. Photodegradation

In addition to the PACT studies, the dual applicability of the Pc immobilized supports was assessed by photodegrading pollutants in water. Herein, in this chapter, the results are discussed.

6.1 Photocatalytic degradation of methyl orange using complexes 8-10 conjugated to glass wool

The phthalocyanines conjugated to glass wool were applied for methyl orange bleaching. For accuracy, the photocatalytic experiments were done in triplicate per Pc-GW sample. Complexes **8**-**10** were used as they contained multiple -COOH groups.

6.1.1 Adsorption in the dark

The methyl orange (MO) adsorption onto GW support was determined at 15 min intervals, and the percentage of adsorption is shown in **Figure 6.1**. Adsorption was calculated based on the decrease in the UV-Vis absorption profile of MO. In the initial 0-15 min period, a considerate amount of dye was adsorbed by the **8-Zn**-GW, **9-Zn**-GW, and **10-Zn**-GW conjugates. After 15 min, the adsorption rate stabilized. Therefore, the kinetics studies discussed below include a 15 min equilibrium period in the dark.

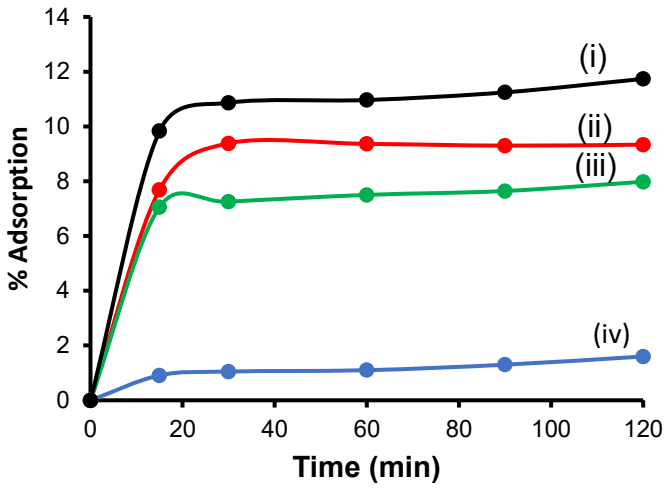

Figure 6.1: (a) Adsorption of methyl orange (3.3×10^{-5} M) over time in the presence of (i) **10-Zn**-GW, (ii) **9-Zn**-GW, (iii) **8-Zn**-GW, and (iv) GW.

6.1.2 UV-vis absorption spectroscopy studies

The photobleaching of methyl orange was conducted using pristine GW as a control and the complexes **8-10** conjugated glass wools at different concentrations. The studies were carried out using an MO solution at pH 7.2. The UV-vis absorption spectrum of MO shows two bands at 275 nm (band related to benzene rings) and 466 nm (related to the chromophore N=N) [239-241]. **Figure 6.2** illustrates the change in the absorption spectra of MO in the presence of GW, **8-Zn**-GW, **9-Zn**-GW, and **10-Zn**-GW at varying irradiation times. There was a rapid decrease of the 466 nm band, suggesting the decomposition of the azo bond and the formation of an amine-containing compound [242], along with a steady blue shift of the benzene ring absorption from 275 to approximately to 255 nm. Thus, these spectral changes are attributed to a photochemically induced process rather than surface adsorption of the dye.

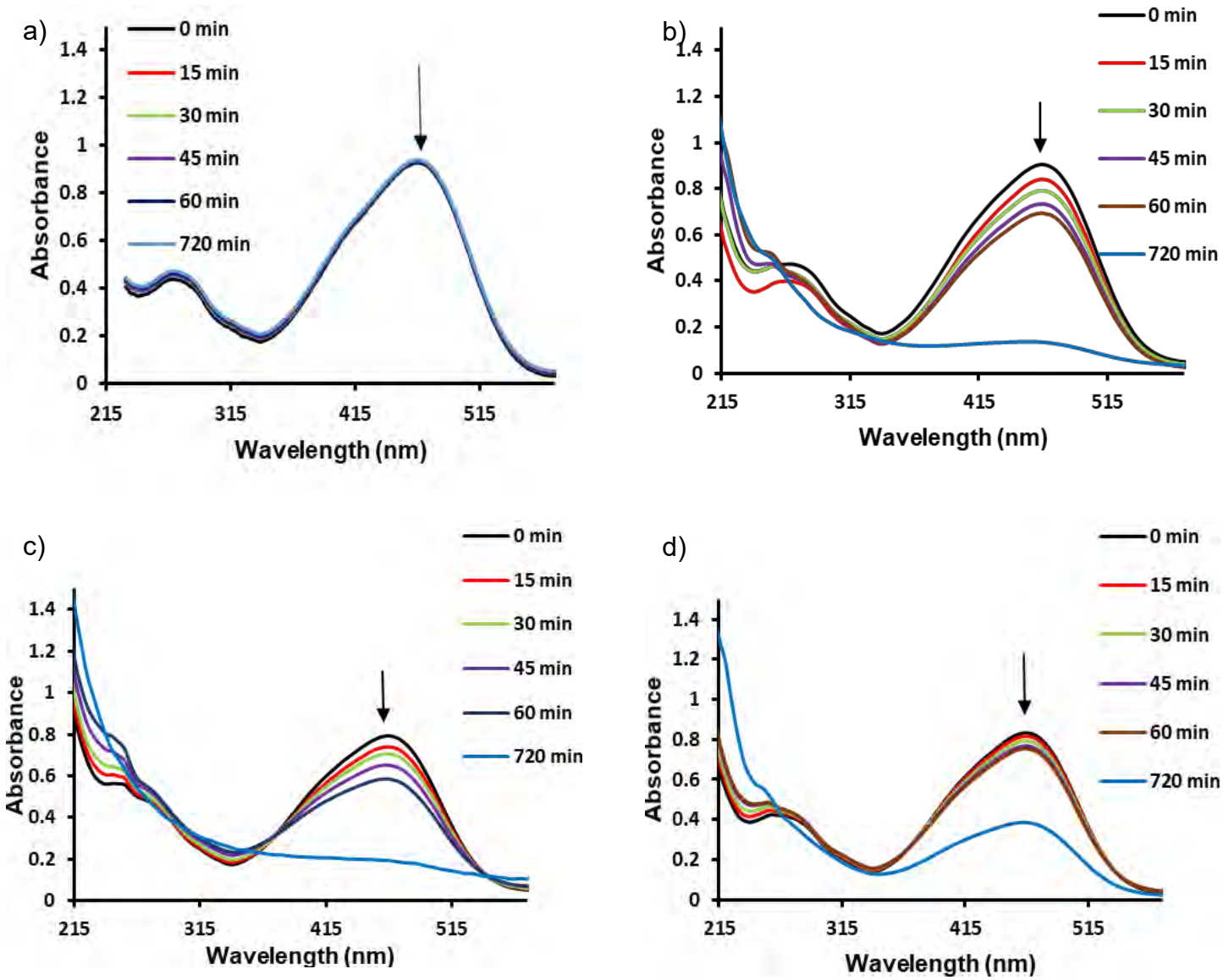

Figure 6.2: Time-dependent UV/Vis absorption analysis of photodegradation of methyl orange (3.3×10^{-5} M) in the presence of (a) GW, (b) **8-Zn**-GW, (c) **9-Zn**-GW, (d) **10-Zn**-GW at pH 7.2, irradiance = 450 mW/cm^2.

6.1.3 Kinetic study

The kinetic study of the photobleaching of MO at different initial concentrations (1.65×10^{-5} M, 3.30×10^{-5} M, 4.95×10^{-5} M, 6.60×10^{-5} M, and 8.25×10^{-5} M) was conducted in the presence of 20 mg of **8-Zn**-GW, **9-Zn**-GW, and **10-Zn**-GW. The linear kinetic plots indicate that the reactions follow pseudo-first-order kinetics, as shown in **Figure 6.3(a)**. The initial rates increased with the increase in MO concentration for both **8-Zn**-GW and **9-Zn**-GW, while the opposite trend was observed for **10-Zn**-GW, as detailed in **Table 6.1**. The initial rates for **8-Zn**-GW ($\Phi_\Delta = 0.38$) and **9-Zn**-GW ($\Phi_\Delta = 0.35$) are comparable, while **10-Zn**-GW ($\Phi_\Delta = 0.22$) showed a lower rate due to its lower singlet oxygen quantum yields, **Table 6.1**. The k_{obs} values decreased with increased MO concentrations, indicating that the photocatalytic activity of the employed photocatalysts decreases as the amount of MO increases. Notably, the **10-Zn**-GW conjugate more than doubled the half-life of both **8-Zn**-GW and **9-Zn**-GW, further supporting the efficiency of the latter conjugates in degrading the pollutant. It is worth mentioning that the k_{obs} values (and % efficiencies) are highly dependent on the concentration of the analyte. The values in this work are comparable to those reported in literature and even better in some cases, **Table 6.2** [243-246].

a)

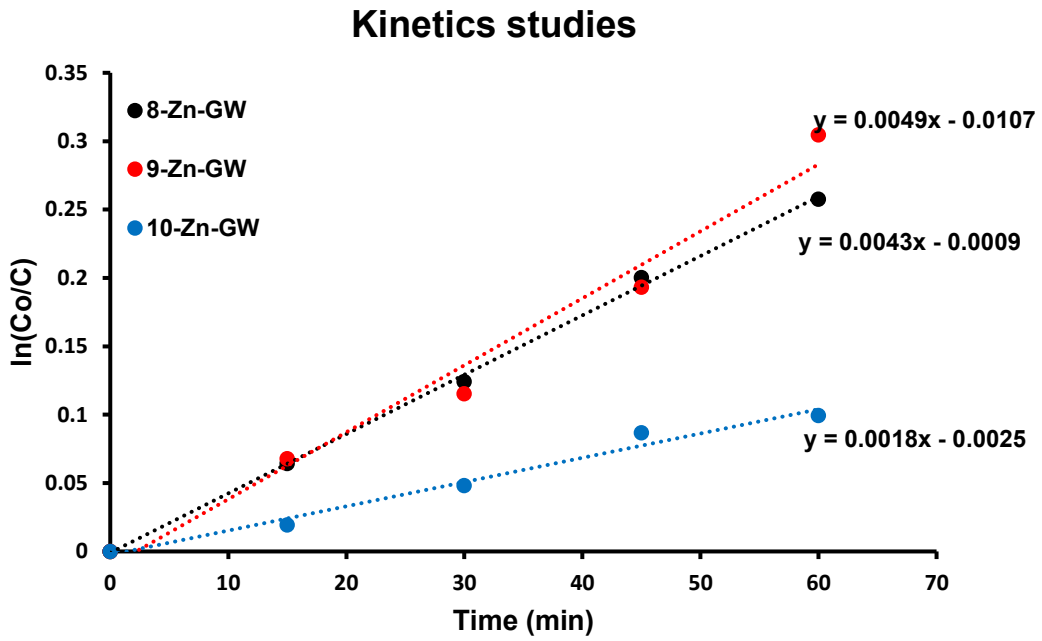

b)

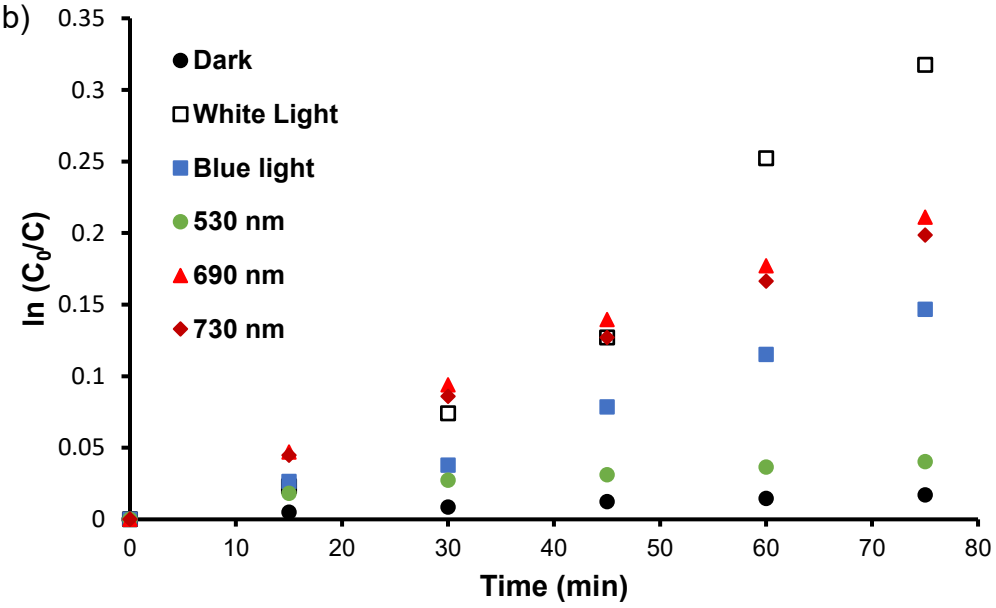

Figure 6.3: Time-dependent photodegradation of MO (3.3×10^{-5} M) upon (a) irradiation with red light (Modulight-690 nm) in the presence of each Pc-GW composite and (b) irradiation with varying light in the presence of **8-Zn**-GW.

Furthermore, the degradation of methyl orange (3.3×10^{-5} M) by the Pc-GW conjugates was investigated under different light sources, namely, white light (λ~380-750 nm), blue light (λ~450-495 nm), Thorlabs M530L3 LED (λ ~ 530 nm), Thorlabs M730L3 LED (λ ~ 730 nm) and Modulight 7710-690 RHO laser system (λ ~ 690 nm). For comparison, each light source was adjusted to an irradiance of 110 mW/cm^{2,} and the change in MO concentration is presented in **Figure 6.3(b)**. From the results, the order of degradation activity was white light > 690 nm > 730 nm > blue light > 530 nm. The lack of Pc absorption intensity at 530 nm resulted in a lower degradation activity, while the combination of all the wavelengths (white light) produced the maximum degradation activity. This observation was important to establish the potential practical applications of the Pc-GW nanocomposites in the presence of solar radiations.

Table 6.1: Photo-degradation of methyl orange using **8-Zn**-GW, **9-Zn**-GW, and **10-Zn**-GW.

[MO]×10^{-5} (mol/L)	k_{obs} (10^{-3} min^{-1})			Rate (10^{-7} mol L^{-1} min^{-1})			$t_{1/2}$ (min)		
	8-Zn-GW	9-Zn-GW	10-Zn-GW	8-Zn-GW	9-Zn-GW	10-Zn-GW	8-Zn-GW	9-Zn-GW	10-Zn-GW
1.65	8.1	7.8	5.0	1.34	1.29	0.83	86	89	139
3.30	4.9	4.3	1.8	1.62	1.42	0.59	141	161	385
4.95	3.8	3.4	0.9	1.88	1.68	0.45	182	204	770
6.60	3.2	2.5	0.4	2.11	1.65	0.26	217	277	1733
8.25	2.8	2.1	0.1	2.31	1.73	0.08	248	330	6931

6.1.4. Catalyst reusability

The stability of the conjugated Pc is imperative for these applications. Therefore, the photodegradation process was repeated three times, with each experiment carried out under the same conditions. After each experiment, the photocatalysts were washed, air-dried, and reused. The degradation efficiency after the third cycle was 78 % for **8-Zn**-GW and 82 % for **9-Zn**-GW but lowered to 63 % for **10-Zn**-GW when using an MO concentration of 3.30×10^{-5} mol/L. The decrease in activity may be due to the permanent adsorption of the products onto the support.

Furthermore, the integrity of the reused glass wool conjugates was assessed via SEM and solid-state UV-vis. After the final catalytic cycle, the photocatalysts were washed, air-dried, and prepared for analysis. The SEM micrographs (**Figure 6.4 (a-b)**) showed that the Pc-GW conjugates retained their structural integrity, and the solid-state UV-vis (**Figure 6.4 (c)**) showed no significant change after three photodegradation cycles. Due to this stability, the Pc-GW composite could be used for sustainable methyl orange degradation. The photodegradation of methyl orange using Pc based catalysts has been reported to yield poly(catechol) and 2-amino-5(3-hydroxy-4-oxo-cyclohexa-2,5-dienylideneamino)-benzene sulphonic acid as degradation products [**247**], using direct injection into ion trap mass spectrometer fitted with an electrospray ionization (ESI-MS).

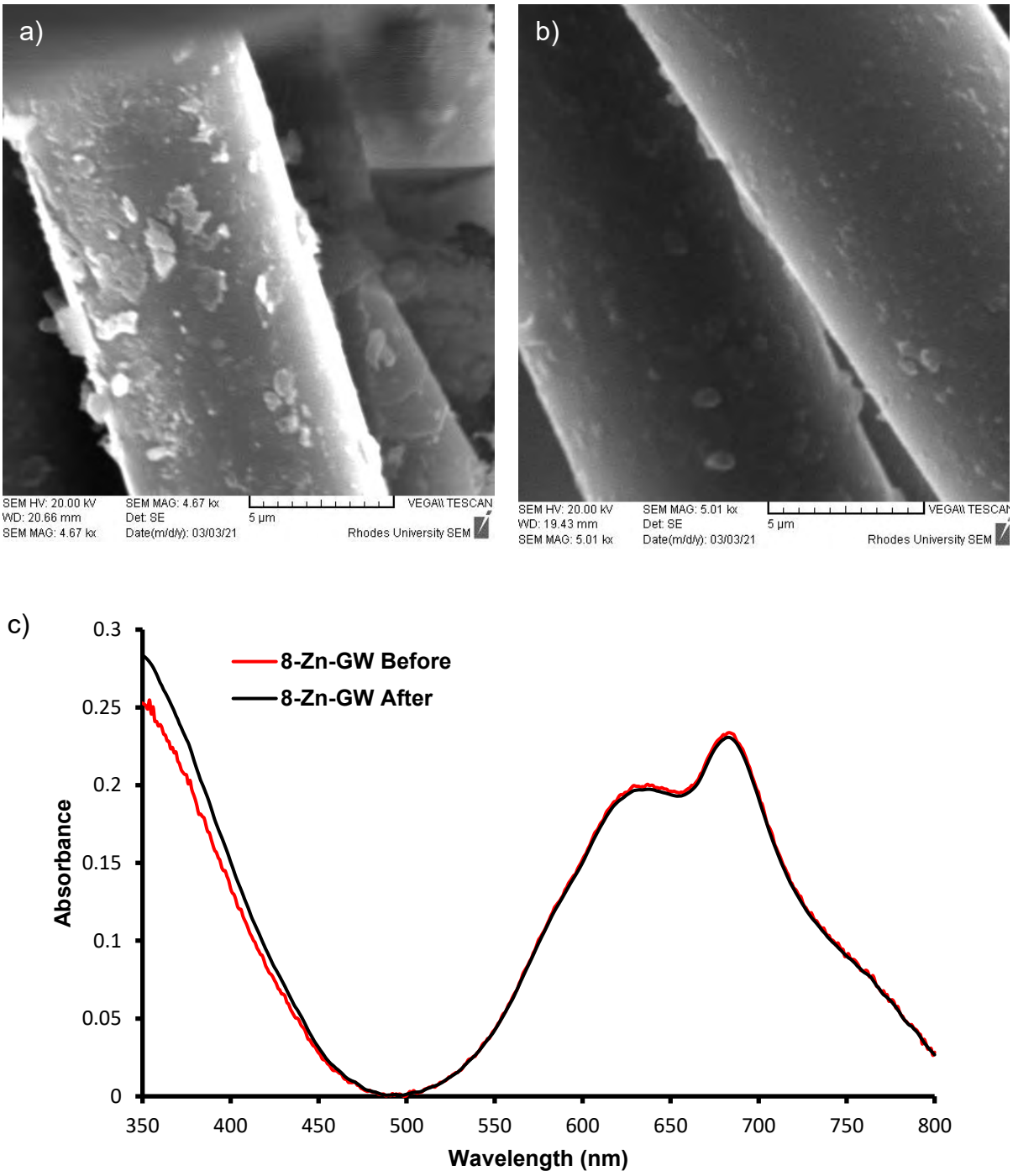

Figure 6.4: SEM images of (a) **8-Zn**-GW and (b) **10-Zn**-GW and (c) Solid-state UV-vis spectra of **8-Zn**-GW after three cycles.

Table 6.2: Comparison of Pc-GW conjugates with literature for the degradation of methyl orange

Catalyst	k_{obs}/min^{-1} (% efficiency)	[MO] ($\times 10^{-5}$) M	Ref
(ZnMIPPc)-ZnO nanofibers	0.0099	2.80	[243]
FeTPP/TiO2/CPVC	0.0049	50 m/L	[244]
3-TCbZnPc/PS	0.00253	2.31	[245]
ZnTCPC-Au@SiO_2	0.0094	2.58	[246]
8-Zn-GW	0.0049 (100%)	3.30	This work
9-Zn-GW	0.0043 (93%)		This work
10-Zn-GW	0.0018 min^{-1} (44%)		This work

ZnMIPPc = (2-[5-(phenoxy)-isophthalic acid]- 9(10),16(17),23(24)-tri-tert-butyl phthalocyaninato, CPVC = Chlorinated polyvinyl chloride.

6.2 Photocatalytic degradation of methyl orange, 4-chlorophenol, methylene blue using 7-PAN and 7-GW

Based on the ability to degrade MO using complexes **8-10** conjugated to glass wool, all **7**-PAN and **7**-GW conjugates were evaluated against three pollutants, and the studies were replicated three times. These studies were conducted to compare the two supports and to assess the photocatalytic activity under red and white light.

6.2.1 Adsorption studies

Figure 6.5 displays the absorption spectra of MO, methylene blue (MB), and 4-chlorophenol (4-CP). As previously mentioned, the observed peak for MO is due to

the azo bond [240]. For MB, the peaks 613 and 664 nm are consistent with those reported previously [248]. The spectrum for 4-CP exhibits two characteristic bands at 244 and 300 nm [249].

The adsorption of model dyes, MO, MB, and 4-CP, on the composites was investigated. Ten milligrams of **7**-PAN and **7**-GW composites were added to a 3 mL solution containing the pollutant dye at concentrations of 20, 40, and 80 μM. For the adsorption studies, the reaction vessel was kept in the dark, and the absorption spectra were recorded after a 15 min period. A similar procedure was followed for the photodegradation studies; however, for these studies, the reaction vessel was irradiated with either white or red light. For comparison, the photocatalytic studies of NH_2-PAN and NH_2-GW (without photocatalysts) were also assessed. However, no degradation activity was observed, and therefore, the results are not presented.

The dye adsorption of the respective composite was examined. As shown in **Figure 6.5(i-vi)** (using **7-ZnQ**-PAN and **7-ZnQ**-GW as examples), the glass wool support exhibited minor adsorption of all dyes. However, the PAN nanofibers showed a high adsorption affinity for the MB dye over a of 60 min period. For the MB dye alone, the adsorption capacity, *Q* (mg/g), was determined using equation 6.1:

$$Q = \frac{(C_0 - C_t) \times V}{1000 \times m} \tag{6.1}$$

where c_0 and c_t (mg/L) represent the initial and final concentrations (determined from absorption studies) at time *t*, *V* is the volume of the solution (mL), and *m* is the mass of the adsorbent (g), and the corresponding values are presented in **Table 6.3**.

The neutral nanofibers **7-Zn**-PAN, and **7-In**-PAN, showed higher adsorption capacity (6.88 and 6.32 mg/g) for MB compared to the cationic nanofibers; **7-ZnQ**-PAN, and **7-**

InQ-PAN (5.85 and 5.14 mg/g). The decrease in adsorption capacity for the latter two may be attributed to the repulsion between the positively charged dye and the material of the same charge. NH_2-PAN alone displayed the highest adsorption for MB, while NH_2-GW and its derivates showed minimal adsorption properties towards all three dyes. The adsorption of MB reached a stable state after 40 min. Consequently, all composites were allowed to react with each dye for 40 min in the dark before conducting light studies.

Table 6.3: Adsorption capacity of each composite in the presence of methylene blue.

Composite	Q (mg/g)
NH_2-PAN	9.72
7-Zn-PAN	6.88
7-ZnQ-PAN	5.85
7-In-PAN	6.32
7-InQ-PAN	5.14

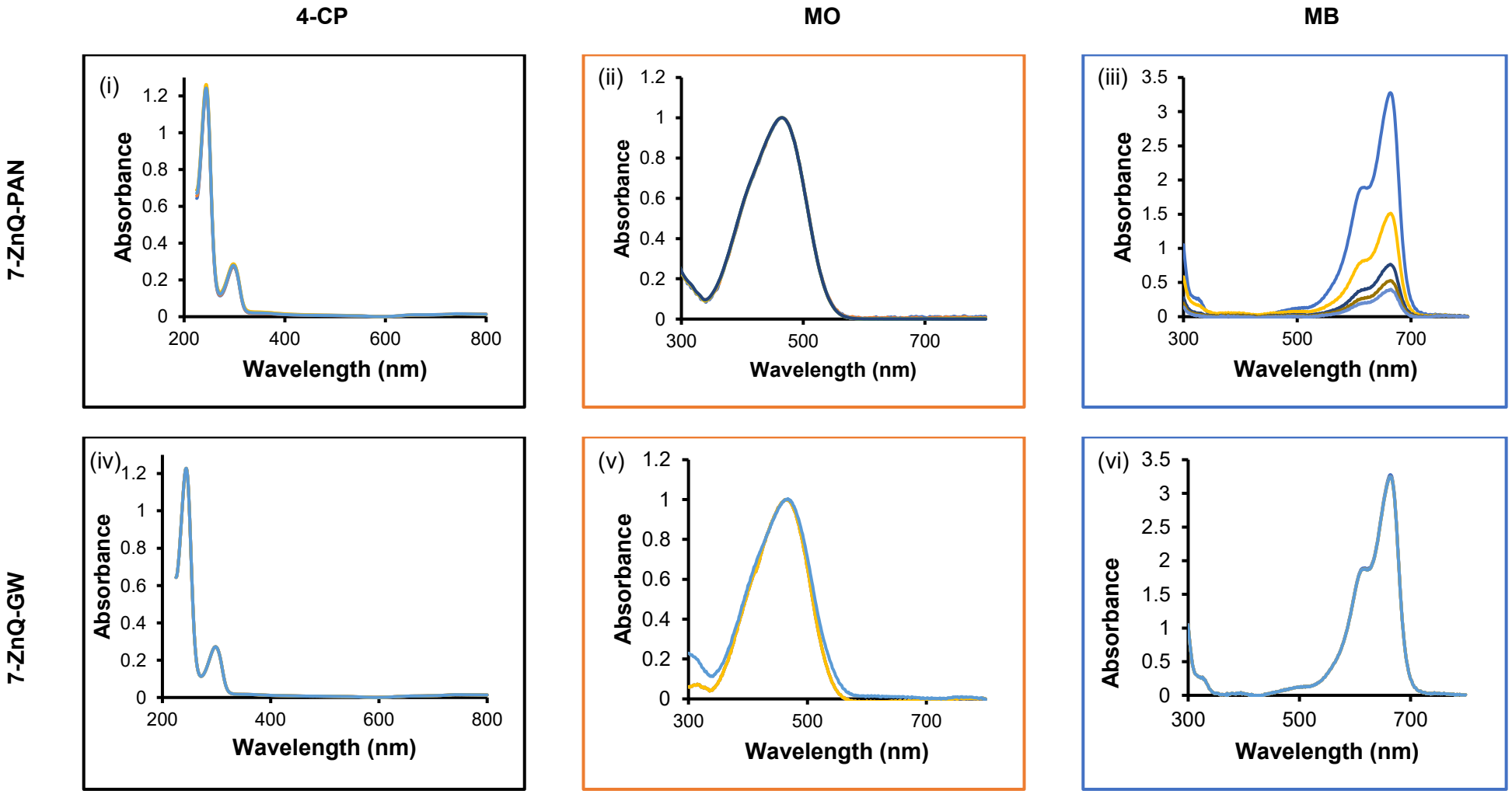

Figure 6.5: UV-vis absorption spectra of 4-CP, MO and MB dyes at 15 min intervals for 60 min, both in the absence of light and in the presence of photosensitizers: (i) **7-ZnQ-PAN** in 4-CP, (ii) **7-ZnQ-PAN** in MO, (iii) **7-ZnQ-PAN** in MB, (iv) **7-ZnQ-GW** in 4-CP (v) **7-ZnQ-GW** in MO, (vi) **7-ZnQ-GW** in MB, with an initial concentration of dyes at 40 µM.

6.2.2 Photocatalytic activity

The degradation profile of 4-CP, MO, and MB at pH 7.2 in the presence of **7-InQ**-PAN under white light is illustrated in **Figure 6.6 (a-c)**. Each dye showed changes in the UV-vis spectrum after 15 min of irradiation, with MB being completely degraded in the presence of Pc-PAN. The removal of Pc-PAN in the case of MB is enhanced due to the combination of photodegradation and adsorption processes. The photodegradation of 4-CP, and MB using Pc-based catalysts has been reported to produce benzoquinone and water, respectively [**115**, **250**]. The photostability of the pollutants alone was examined using the two lights and irradiated at 15 min intervals. As expected, the red light did not alter the profile of 4-CP and MO, while MB showed a slight decomposition as judged by decrease of its prominent peak. A minor deviation of the absorption maxima of all three pollutants was observed when irradiated with white light (spectra not shown).

The photocatalytic reactions followed a pseudo-first-order kinetics, as shown in **Figure 6.6 (d-f)**. The calculated k_{obs} values and the half-lives are summarized in **Tables 6.4-6.6**. Overall, the k_{obs} values were concentration-dependent. At high concentrations, the mean distance between the target dye and the catalyst is shorter, increasing the rate at which singlet oxygen molecules interact with the pollutants. The trend in removal efficiency (k_{obs} values) was MB > MO > 4-CP. This was further supported by the half-life values whereby **7-InQ**-PAN at an initial concentration of 80 µM resulted in lower half-life values of 11, 32, and 60 min (for MB, MO and 4-CP, respectively) when using white light. The Pc-anchored nanofibers exhibited higher kinetic rates and lower half-life values compared to the Pc-anchored glass wools, corresponding to Φ_{Δ}

values. The photodegradation rate (k_{obs}) of 4-CP, MO, and MB for **7-InQ**-PAN were 1.9, 2.8 and 36.9 times higher than **7-InQ**-GW at an initial concentration of 80 µM.

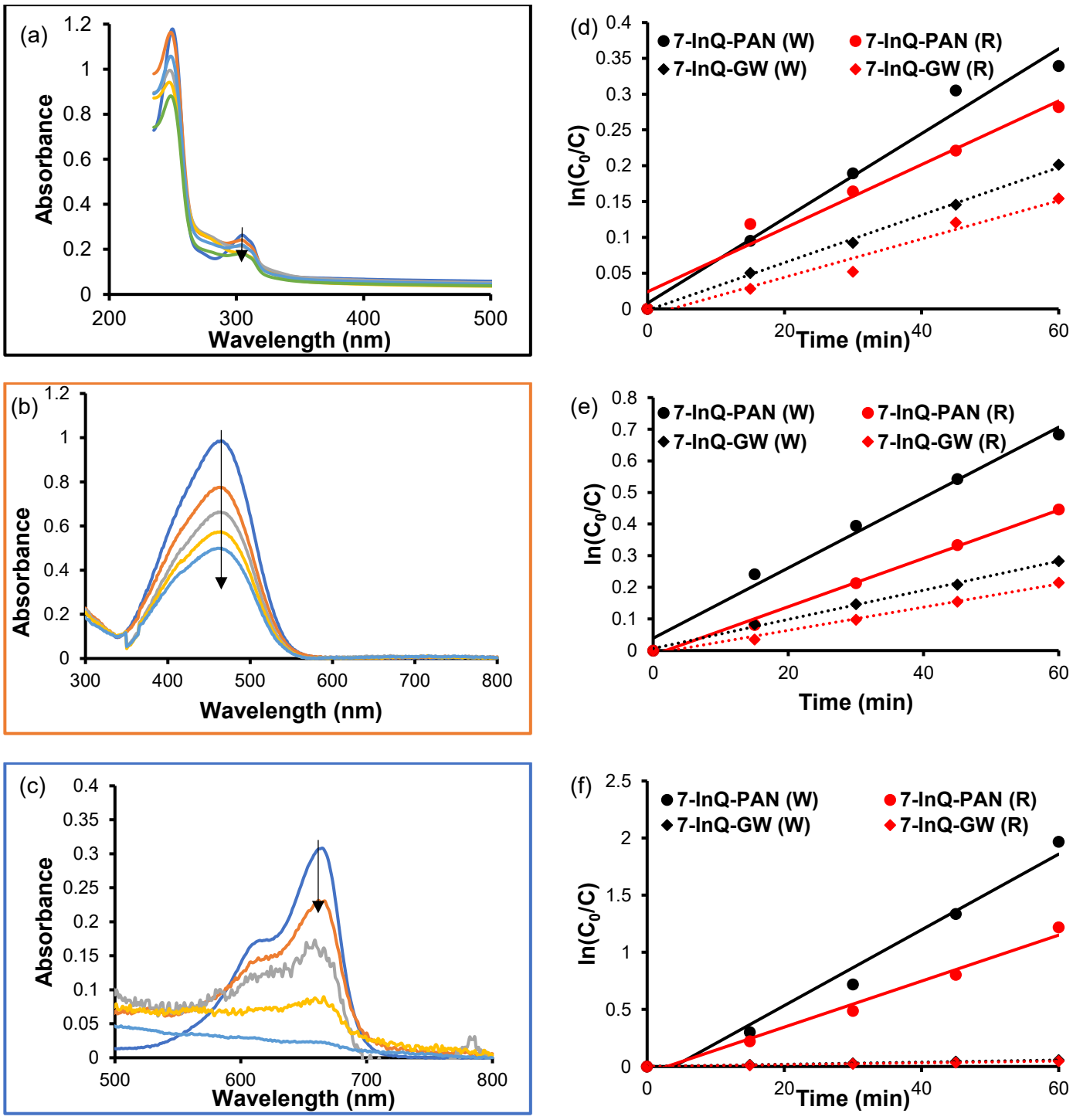

Figure 6.6: The degradation profile of a) 4-CP, b) MO and c) MB by **7-InQ**-PAN (under white light). Plots of ln(C_o/C) vs time for degradation of d) 4-CP, e) MO and f) MB by **7-InQ**-PAN and **7-InQ**-GW at white (W) and red (R) light irradiation. Initial concentration of dye 40 µM.

The rate of 4-CP degradation by the nanofibers was comparable to the studies performed by Mafukidze et al. (at an initial dye concentration of 67 μM) under red light irradiation by Pc-membrane catalyst with a rate constant of 0.0047 min^{-1} [**115**]. When comparing the asymmetrical conjugated composites used in this work, the photodegradation of MO (at an initial dye concentration of 82 μM) using **8-Zn-**GW catalysts showed a kinetic rate was 0.0028 min^{-1} under red light irradiation. For complex **7**, an improved efficiency (at an initial dye concentration of 80 μM) was observed for the cationic glass wool composites, **7-ZnQ**-GW (at k_{obs} = 0.0057 min^{-1}) and **7-InQ**-GW (at k_{obs} = 0.0077 min^{-1}), due to improved electrostatic interaction with the pollutants. Thus, literature data suggest that the Pc-PAN and Pc-GW catalysts have higher photocatalytic activity than the reported composites.

Moreover, the effect of pH was carried out using the best-performing neutral and cationic photocatalysts, **7-Zn**-PAN and **7-ZnQ**-PAN. The concentration of the dyes used was 80 μM. The photodegradation studies were conducted at pH 3, 5, 7.2, 9, and 11. Hydrochloric acid and sodium hydroxide were used to adjust the pH. According to **Figure 6.7**, **7-InQ**-PAN gave maximum photocatalytic rates at pH conditions of 11, 9, and 3 for 4-CP, MO, and MB, respectively. The increase in the photocatalytic rates for 4-CP and MO in basic conditions may be attributed to the deprotonation of both dyes [**148**, **251**]. The anionic dyes form a strong electrostatic attraction with the cationic surface enhancing the degradation process. However, at higher pH, MB showed the lowest degradation due to both the dye and composite having the same charges, promoting more repulsion, and thus reducing photocatalytic rates. The neutral **7-In**-PAN, performed best at pH = 7.2, 3, and 5 for 4-CP, MO, and

MB. It has been reported before that MO and MB degrade faster in acidic conditions [252, 253].

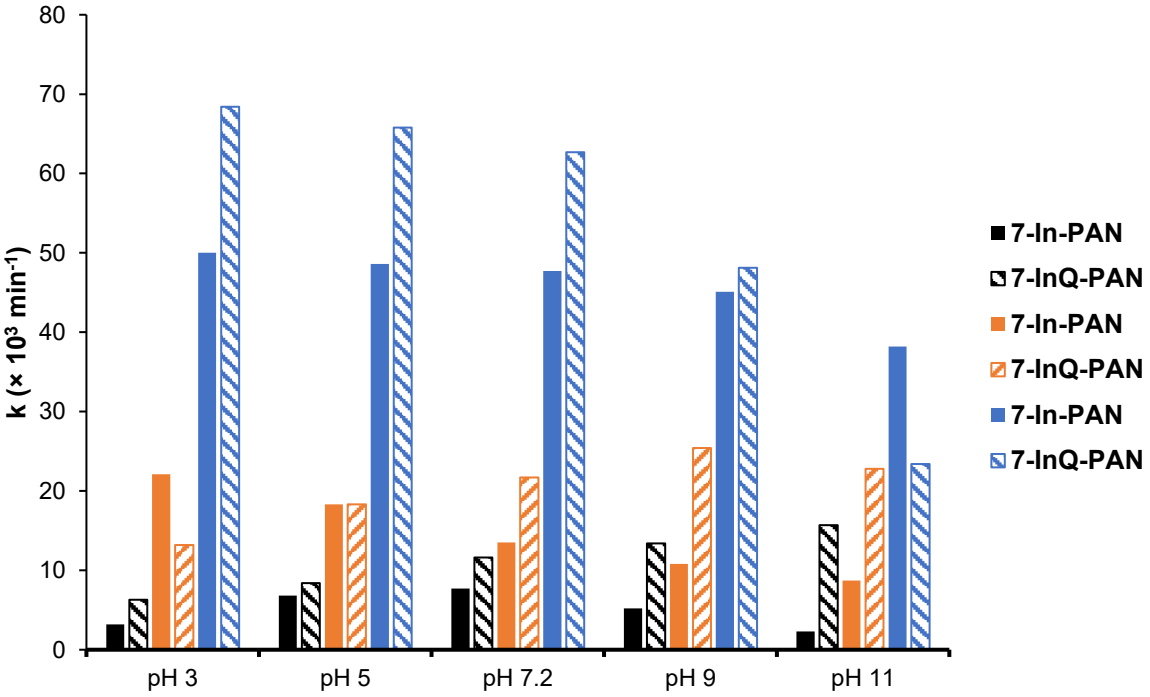

Figure 6.7: Influence of pH on the degradation kinetics of 4-CP (black bars), MO (orange bars), and MB (blue bars) using **7-InQ**-PAN and **7-InQ**-PAN at an initial dye concentration of 80 µM.

The reusability of all the composites was evaluated. After the experiment, the composites were washed, dried and reused. The studies were repeated twice. **Figure 6.8** illustrates the degradation efficiency after recycling. The efficiency of the PAN composite (**7-InQ**-PAN used as an example in **Figure 6.8a**) decreased after each cycle for MB. This decrease is due to dyes permanently adsorbing onto the surface, subsequently exposing fewer photoactive sites. However, the GW (**7-InQ**-GW used as an example, **Figure 6.8b**) showed no significant changes in its photodegradation

efficiency for all dyes. The morphology of both composites did not significantly change after three cycles (**Figure 6.8c-d**).

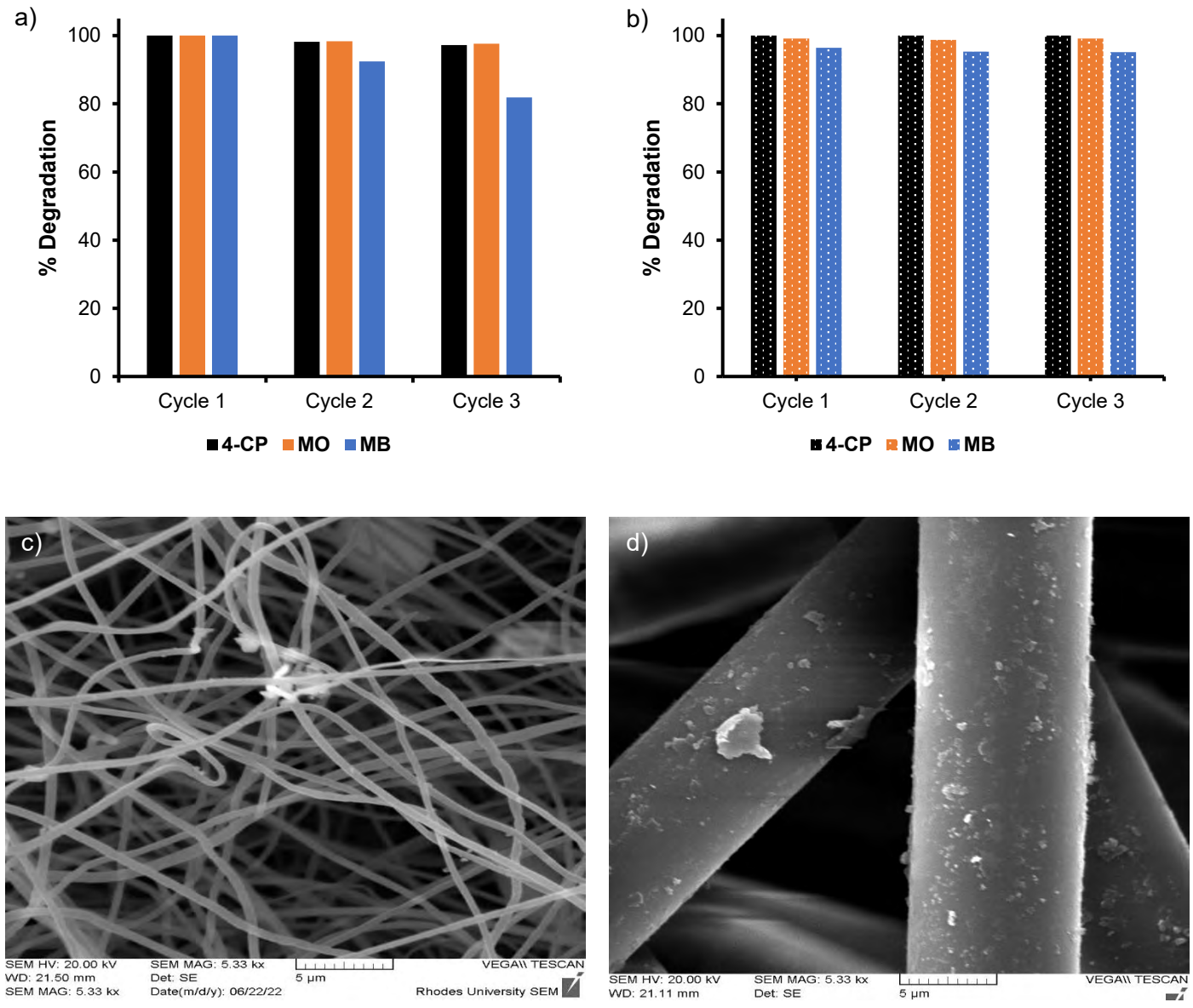

Figure 6.8: Photodegradation activity of dyes (80 µM) with recycled composites a) **7-InQ**-PAN and b) **7-InQ**-GW and the SEM micrographs of the reused (cycle 3) catalysts c) **7-InQ**-PAN and d) **7-InQ**-GW.

Table 6.4: Pseudo-first order kinetic parameters for the degradation (using white light) of the dyes at an initial concentration of 20 μM. Values in brackets are when using red light.

Composite	k_{obs} (min^{-1})			$t_{1/2}$ (min)		
	4-CP	MO	MB	4-CP	MO	MB
7-Zn-PAN	0.0018 (0.0014)	0.0029 (0.0025)	0.0124 (0.0078)	385 (495)	239 (277)	56 (89)
7-Zn-GW	0.0005 (0.0005)	0.0011 (0.0007)	0.0003 (0.0002)	1386 (1386)	630 (990)	2310 (3466)
7-ZnQ-PAN	0.0027 (0.0017)	0.0042 (0.0035)	0.0142 (0.0102)	257 (408)	165 (198)	49 (68)
7-ZnQ-GW	0.0010 (0.0008)	0.0018 (0.0011)	0.0004 (0.0003)	693 (866)	385 (630)	1733 (2310)
7-In-PAN	0.0020 (0.0017)	0.0036 (0.0026)	0.0136 (0.0092)	347 (408)	193 (267)	51 (75)
7-In-GW	0.0007 (0.0006)	0.0014 (0.0010)	0.0004 (0.0002)	990 (1155)	495 (693)	1733 (3466)
7-InQ-PAN	0.0031 (0.0024)	0.0061 (0.0042)	0.0174 (0.0106)	224 (289)	114 (165)	40 (65)
7-InQ-GW	0.0017 (0.0015)	0.0028 (0.0018)	0.0007 (0.0005)	408 (462)	248 (385)	990 (1386)

Table 6.5: Pseudo-first order kinetic parameters for the degradation (using white light) of the dyes at an initial concentration of 40 μM. Values in brackets are when using red light.

Composite	k_{obs} (min^{-1})			$t_{1/2}$ (min)		
	4-CP	MO	MB	4-CP	MO	MB
7-Zn-PAN	0.0032 (0.0023)	0.0054 (0.0047)	0.0222 (0.0154)	217 (301)	128 (147)	31 (45)
7-Zn-GW	0.0011 (0.0008)	0.0018 (0.0011)	0.0005 (0.0004)	630 (866)	385 (630)	1386 (1733)
7-ZnQ-PAN	0.0048 (0.0037)	0.0084 (0.0067)	0.0274 (0.0183)	144 (187)	83 (103)	25 (38)
7-ZnQ-GW	0.0022 (0.0018)	0.0032 (0.0025)	0.0007 (0.0005)	315 (385)	217 (277)	990 (1386)
7-In-PAN	0.0042 (0.0031)	0.0068 (0.0051)	0.0246 (0.0167)	165 (224)	102 (136)	28 (42)
7-In-GW	0.0016 (0.0013)	0.0026 (0.0019)	0.0006 (0.0005)	433 (533)	267 (365)	1155 (1386)
7-InQ-PAN	0.0059 (0.0044)	0.0110 (0.0076)	0.0332 (0.0201)	117 (158)	63 (91)	21 (34)
7-InQ-GW	0.0033 (0.0027)	0.0046 (0.0037)	0.0009 (0.0008)	210 (533)	151 (187)	770 (866)

Table 6.6: Pseudo-first order kinetic parameters for the degradation (using white light) of the dyes at an initial concentration of 80 μM. Values in brackets are when using red light.

Composite	k_{obs} (min^{-1})			$t_{1/2}$ (min)		
	4-CP	MO	MB	4-CP	MO	MB
7-Zn-PAN	0.0058 (0.0040)	0.0107 (0.0091)	0.0426 (0.0290)	120 (173)	65 (76)	16 (24)
7-Zn-GW	0.0021 (0.0016)	0.0032 (0.0019)	0.0010 (0.0009)	330 (433)	217 (365)	693 (770)
7-ZnQ-PAN	0.0088 (0.0066)	0.0164 (0.0127)	0.0510 (0.0348)	79 (105)	42 (55)	14 (20)
7-ZnQ-GW	0.0038 (0.0031)	0.0057 (0.0043)	0.0012 (0.0010)	182 (224)	122 (161)	578 (693)
7-In-PAN	0.0077 (0.0058)	0.0135 (0.0099)	0.0477 (0.0317)	90 (120)	51 (70)	15 (22)
7-In-GW	0.0029 (0.0024)	0.0042 (0.0030)	0.0011 (0.0010)	239 (289)	165 (231)	630 (693)
7-InQ-PAN	0.0116 (0.0083)	0.0217 (0.0147)	0.0627 (0.0376)	60 (84)	32 (47)	11 (18)
7-InQ-GW	0.0061 (0.0047)	0.0077 (0.0061)	0.0017 (0.0014)	114 (147)	90 (114)	408 (495)

6.3 Summary of photodegradation studies and comparison with PACT

The Pc-anchored supports, **7**-PAN, **7**-PAN-CS, **7**-GW and **8-10**-GW were investigated for their antimicrobial activity. The introduction of chitosan improved the antimicrobial properties of the PAN supports. All **8-10**-GW supports and the neutral **7**-GW showed less than desirable PACT activity while cationic **7**-GW had improved activity. This further highlighted the importance of positive charges.

Additionally, the supports were used to photodegrade pollutants. Complexes **8-10** conjugated to GW demonstrated successful degradation of MO. The photodegradation efficiencies of neutral and cationic Pc-PAN and Pc-GW were compared. Pc-PAN was more efficient in the removal of MB owing to its effective adsorption and photodegradation capabilities. This however meant the support has a lower reusability rate when compared to Pc-GW. With the exception of Pc-PAN, all the other support showed good reusability after three cycles. The success of the PACT and photodegradation studies highlight potential application of the photocatalysts in the removal of microorganisms and degradation of organic pollutants.

Chapter 7

Conclusions

7. Conclusions

This work presents for the first time the synthesis of a range of phthalocyanines incorporating Hydrogen (H_2), Zinc (Zn) and Indium (In) elements, alongside an exploration of their photophysicochemical properties. A successful introduction of morpholine, Schiff base morpholine and pyrrolidine substituents on zinc and indium phthalocyanines was achieved, as well as asymmetric morpholine and mercaptobenzothiazole on phthalocyanines. All nitrogen containing phthalocyanines were quaternized to provide positive charges while the carboxylic acid containing phthalocyanine were prepared to enable easy covalent attachment to amino-functionalized nanoparticles and supports. PAN, PAN-chitosan modified nanofibers and glass wool were prepared and conjugated to phthalocyanines for practical use in water treatment for the removal of microorganisms and organic pollutants.

The formation of phthalocyanine were confirmed using various techniques including mass spectroscopy which reveal the expected masses for photosensitizers. The morphology, sizes of nanoparticles or supports and their conjugates was carried out using techniques such as Energy-Dispersive X-ray Spectroscopy (EDX), Transmission Electron Microscopy (TEM), and X-ray Diffraction (XRD). The conjugation of phthalocyanine to nanoparticle and supports via the amide bond was verified by X-ray Photoelectron Spectroscopy (XPS).

Singlet oxygen generation properties of the phthalocyanine were influenced by the central metal and charge. The presence of nanoparticles and supports had a notable impact in the singlet oxygen generation properties. In general, the incorporation of nanoparticles and supports to phthalocyanine led to a minor decrease of the singlet oxygen quantum yield. Pc-PAN-CS, however, exhibited an increase in the singlet

oxygen quantum yield, this may be attributed to the increase hydrophilicity of the support.

This research delved into the evaluation of Photodynamic Antimicrobial Chemotherapy of various microorganisms. The PACT studies were assessed in planktonic and biofilm forms. The results indicated that the cationic phthalocyanines exhibited high log reductions values against all microorganisms. The studies revealed that the proximity of the quaternized group to the macrocycle plays a crucial role in the efficiency of the phthalocyanines as complex **2** was more efficient than Schiff base complex **3**. Interestingly, the shorter chain containing phthalocyanines (**4**) was less efficient that longer chain containing phthalocyanines (**5**). The pyramidal zinc oxide nanoparticles conjugated phthalocyanines exhibited higher log reduction values against biofilms compared to the spherical derivatives. In supports, Pc-PAN and Pc-GW showed good photoeradication of microbes when conjugated to cationic Pcs, however, the Pc-PAN-CS showed excellent antimicrobial activity with a 100 % population reduction of *S. aureus* and > 90 % for *C. albicans*. Even when Pcs are on support, the PACT studies remained highly depended on surface charge for antimicrobial activity.

Furthermore, Pc-PAN and Pc-GW were used to investigate the photodegradation of 4-chlorophenol, methyl orange and methylene blue. The composites with high singlet oxygen generation demonstrated rapid photodegradation of pollutants. The PAN nanofiber exhibited adsorption properties against methylene blue which contributed to the efficiency of the removal of the dye. The supports were recycled and reused; the Pc-GW maintained percentage degradation rate of > 90 % for all dyes while the rate for Pc-PAN decreased due to permanent adsorption.

Looking ahead, the quaternized Pcs explored in this thesis display promise for antimicrobial inactivation of microorganisms in solution and conjugated to nanoparticles and supports, suggesting potential applications in water purification. Future research could extend the study by incorporating nanoparticles and phthalocyanines to the same support for potential application in the removal of biofilms and photodegradation of other environmental pollutants. Additionally, the supports developed could be further investigated by designing a prototype resembling a real-life water tank and testing its efficacy using contaminated water samples.

References

1. Haseena, M., Malik, M. F., Javed, A., Arshad, S., Asif, N., Zulfiqar, S., & Hanif, J. (2017). Water pollution and human health. *Environ Risk Assess Remediat, 1*, 16. 10.4066/2529-8046.100020
2. Schwarzenbach, R. P., Egli, T., Hofstetter, T. B., Von Gunten, U., & Wehrli, B. (2010). Global water pollution and human health. *Annu Rev Environ Resour*, *35*, 109. 10.1146/annurev-environ-100809-125342
3. Liyanage, C. P., & Yamada, K. (2017). Impact of population growth on the water quality of natural water bodies. *Sustainability*, *9*, 1405. https://doi.org/10.3390/su9081405
4. Verma, R., Vinoda, K. S., Papireddy, M., & Gowda, A. N. S. (2016). Toxic pollutants from plastic waste-a review. *Procedia Environ Sci*, *35*, 701. https://doi.org/10.1016/j.proenv.2016.07.069
5. Ahmed, S., & Ismail, S. (2018). Water pollution and its sources, effects & management: a case study of Delhi. *Int J Curr Adv Res*, *7*, 10436. https://doi.org/10.24327/ijcar.2018
6. Zamora-Ledezma, C., Negrete-Bolagay, D., Figueroa, F., Zamora-Ledezma, E., Ni, M., Alexis, F., & Guerrero, V. H. (2021). Heavy metal water pollution: A fresh look about hazards, novel and conventional remediation methods. *Environ Technol Innov*, *22*, 101504. https://doi.org/10.1016/j.eti.2021.101504
7. Chung, K. T. (2016). Azo dyes and human health: A review. *J Environ Sci Health C Environ Carcinog Ecotoxicol Rev*, *34*, 233. https://doi.org/10.1080/10590501.2016.1236602

8. Cheng, D., Ngo, H. H., Guo, W., Chang, S. W., Nguyen, D. D., Liu, Y. Wei Q., Wei, D. (2020). A critical review on antibiotics and hormones in swine wastewater: Water pollution problems and control approaches. *J Hazard Mater*, *387*, 121682. https://doi.org/10.1016/j.jhazmat.2019.121682
9. Tao, T., Xin, K.L. (2014). Public health: a sustainable plan for China's drinking water. *Nature*, 511, 527. https://doi.org/10.1038/511527a
10. Anju, A., Ravi, S., P., & Bechan, S. (2010). Water pollution with special reference to pesticide contamination in India. *J Water Resour Prot*, *2*, 432. 10.4236/jwarp.2010.25050
11. Crini, G., & Lichtfouse, E. (2019). Advantages and disadvantages of techniques used for wastewater treatment. *Environ Chem Lett*, *17*, 145. https://doi.org/10.1007/s10311-018-0785-9
12. Malaeb, L., & Ayoub, G. M. (2011). Reverse osmosis technology for water treatment: State of the art review. *Desalination*, 267, 1. https://doi.org/10.1016/j.desal.2010.09.001
13. Duran Romero, D. A., de Almeida Silva, M. C., M. Chaúque, B. J., & D. Benetti, A. (2020). Biosand filter as a point-of-use water treatment technology: influence of turbidity on microorganism removal efficiency. *Water*, *12*, 2302. https://doi.org/10.3390/w12082302
14. Katuri, K. P., Ali, M., & Saikaly, P. E. (2019). The role of microbial electrolysis cell in urban wastewater treatment: integration options, challenges, and prospects. *Curr Opin Biotechnol*, *57*, 101. https://doi.org/10.1016/j.copbio.2019.03.007

15. Santhosh, C., Velmurugan, V., Jacob, G., Jeong, S. K., Grace, A. N., & Bhatnagar, A. (2016). Role of nanomaterials in water treatment applications: a review. *Chem Eng J*, *306*, 1116. https://doi.org/10.1016/j.cej.2016.08.053
16. Lever, A. P. (1965). The phthalocyanines. *Adv Inorg Chem Radiochem*, 7, 27. https://doi.org/10.1016/S0065-2792(08)60314-3
17. Fukuda, T., & Kobayashi, N., Electronic absorption spectra-phthalocyanianes, in: Kadish, K.M., Smith, K.M., & Guilard R. (Eds), Handbook Porphyrin Science, World Scientific Press, Singapore, 2010, Vol 9, pp. 650.
18. Peisert, H., Knupfer, M., Schwieger, T., Auerhammer, J. M., Golden, M. S., & Fink, J. (2002). Full characterization of the interface between the organic semiconductor copper phthalocyanine and gold. *J Appl Phys*, *91,* 4872. https://doi.org/10.1063/1.1459620
19. Sorokin, A. B. (2013). Phthalocyanine metal complexes in catalysis. *Chem Rev*, *113*, 8152. https://doi.org/10.1021/cr4000072
20. Basova, T., Hassan, A., Durmuſ, M., Gürek, A. G., & Ahsen, V. (2016). Liquid crystalline metal phthalocyanines: Structural organization on the substrate surface. *Coord Chem Rev, 310*, 131. https://doi.org/10.1016/j.ccr.2015.11.005
21. Wu, H., Chen, Z., Zhang, J., Wu, F., He, C., Wang, B., Wu, Y., & Ren, Z. (2016). Stably dispersed carbon nanotubes covalently bonded to phthalocyanine cobalt (II) for ppb-level H_2S sensing at room temperature. *J Mater Chem A Mater, 4,* 1096. https://doi.org/10.1039/C5TA09213B
22. Kaya, E. N., Tuncel, S., Basova, T. V., Banimuslem, H., Hassan, A., Gürek, A. G., Ahsen, V., & Durmuş, M. (2014). Effect of pyrene substitution on the

formation and sensor properties of phthalocyanine-single walled carbon nanotube hybrids. *Sens Actuators B Chem, 199,* 277. https://doi.org/10.1016/j.snb.2014.03.101

23. Saral Özdemir, P., & Özgüney, A. T. (2017). Chemical structures of phthalocyanine based dyestuffs and their useage in production of functional textiles. Pamukkale *Univ Muh Bilim Derg, 23,* 809. https://dx.doi.org/10.5505/pajes.2016.77200
24. Islam, Z. U., Tahir, M., Syed, W. A., Aziz, F., Wahab, F., Said, S. M., Sarker, M. R., Ali, S. H. M., & Sabri, M. F. M. (2020). Fabrication and photovoltaic properties of organic solar cell based on zinc phthalocyanine. *Energies, 13,* 962. https://doi.org/10.3390/en13040962
25. Ray, A. K., Mukherjee, D., & Sarkar, S., Phthalocyanines: A Class of Organic Photoconductive Materials, in: Capper, P., Willoughby, A., Kasap, S. O. (Eds), Photoconductivity and Photoconductive Materials: Fundamentals, Techniques and Applications, Wiley, United Kingdom, 2022, Vol 2, pp. 831. https://doi.org/10.1002/9781119579182.ch21
26. Ragoussi, M. E., Cid, J. J., Yum, J. H., de la Torre, G., Di Censo, D., Grätzel, M., Nazeeruddin, M. K., & Torres, T. (2012). Carboxyethynyl Anchoring Ligands: A Means to Improving the Efficiency of Phthalocyanine-Sensitized Solar Cells. *Angew Chem Int Ed Engl, 51,* 4375. https://doi.org/10.1002/anie.201108963
27. Nene, L. C., Managa, M., & Nyokong, T. (2019). Photo-physicochemical properties and in vitro photodynamic therapy activity of morpholine-substituted

Zinc (II)-Phthalocyanines π-π stacked on biotinylated graphene quantum dots. *Dyes Pigm, 165,* 488. https://doi.org/10.1016/j.dyepig.2019.03.002

28. Wainwright, M. (1998). Photodynamic antimicrobial chemotherapy (PACT). *J Antimicrob Chemother, 42*, 13. https://doi.org/10.1093/jac/42.1.13
29. Mack, J., & Kobayashi, N. (2011). Low symmetry phthalocyanines and their analogues. *Chem Rev*, *111*, 281. https://doi.org/10.1021/cr9003049
30. Byeon, C. C., McKerns, M. M., Sun, W., Nordlund, T. M., Lawson, C. M., & Gray, G. M. (2004). Excited state lifetime and intersystem crossing rate of asymmetric pentaazadentate porphyrin-like metal complexes. *Appl Phys Lett*, 84, 5174. https://doi.org/10.1063/1.1763983
31. Nemykin, V., Dudkin, S., Dumoulin, F., Hirel, C., Gurek, A., & Ahsen, V. (2014). Synthetic approaches to asymmetric phthalocyanines and their analogues. *Arkivoc*, 142. http://doi.org/10.3998/ark.5550190.p008.412
32. Idowu, M. A., Xego, S., Arslanoglu, Y., Mark, J., Antunes, E., & Nyokong, T. (2018). Photophysicochemical behaviour and antimicrobial properties of monocarboxy Mg (II) and Al (III) phthalocyanine-magnetite conjugates. *Spectrochim Acta A Mol Biomol Spectrosc, 193*, 407. https://doi.org/10.1016/j.saa.2017.12.052
33. Leznoff, C. C., & Hall, T. W. (1982). The synthesis of a soluble, unsymmetrical phthalocyanine on a polymer support. *Tetrahedron Lett, 23*, 3023. https://doi.org/10.1016/S0040-4039(00)87523-1

34. Akkurt, H. Y. Y., Okur, A. I., & Gül, A. (2012). Unsymmetrical phthalocyanines with cyclopalladated azo functions. *J Porphyr Phthalocyanines*, 16, 192. https://doi.org/10.1142/S1088424612004525

35. Kobayashi, N., Kondo, R., Nakajima, S., & Osa, T. (1990). New route to unsymmetrical phthalocyanine analogs by the use of structurally distorted subphthalocyanines. *J Am Chem Soc, 112,* 9640. https://doi.org/10.1021/ja00182a034.

36. Dilber, G., Nas, A., Pişkin, M., & Durmuş, M. (2022). Asymmetrically tetra-substituted phthalocyanine derivatives: synthesis, photophysical and photochemical properties. *Transit Met Chem*, *47,* 157. https://doi.org/10.1007/s11243-022-00499-3

37. Fukuda, T., Ono, K., Homma, S., & Kobayashi, N. (2003). A phthalocyanine producing green, ocher, and red colors depending on the central metals. *Chem Lett, 32,* 736. https://doi.org/10.1246/cl.2003.736

38. Martynov, A. G., Mack, J., May, A. K., Nyokong, T., Gorbunova, Y. G., & Tsivadze, A. Y. (2019). Methodological survey of simplified TD-DFT methods for fast and accurate interpretation of UV–vis–NIR spectra of phthalocyanines. *ACS Omega*, *4*, 7265. https://doi.org/10.1021/acsomega.8b03500

39. Sanusi, K., Antunes, E., & Nyokong, T. (2014). Optical nonlinearities in non-peripherally substituted pyridyloxy phthalocyanines: a combined effect of symmetry, ring-strain and demetallation. *Dalton Trans*, *43*, 999. https://doi.org/10.1039/C3DT52462K

40. Dilber, G., Altunparmak, H., Nas, A., Kantekin, H., & Durmuş, M. (2019). The peripheral and non-peripheral 2H-benzotriazole substituted phthalocyanines: Synthesis, characterization, photophysical and photochemical studies of zinc derivatives. *Spectrochim Acta A Mol Biomol Spectrosc*, *217*, 128. https://doi.org/10.1016/j.saa.2019.01.095
41. Ogunsipe, A., Chen, J. Y., & Nyokong, T. (2004). Photophysical and photochemical studies of zinc (II) phthalocyanine derivatives—effects of substituents and solvents. *New J Chem*, *28*, 822. https://doi.org/10.1039/B315319C
42. Locklin, J., Shinbo, K., Onishi, K., Kaneko, F., Bao, Z., & Advincula, R. C. (2003). Ambipolar organic thin film transistor-like behavior of cationic and anionic phthalocyanines fabricated using layer-by-layer deposition from aqueous solution. *Chem Mater*, *15*, 1404. https://doi.org/10.1021/cm021073f
43. Gouterman, M., Optical Spectra and Electronic Structure of Porphyrins and Related Rings, in: Dolphin, D. (Ed), The Porphyrins, Academic Press, New York, 1978, Vol 3, pp. 1.https://doi.org/10.1016/b978-0-12-220103-5.50008-8.
44. Stillman, M.J., & Nyokong, T., Phthalocyanines - Properties and Applications, in: Lever, A.B.P., & Leznoff, C.C. (Eds), Porphriyn Handbook, VCH, New York, 1989, Vol 1, pp. 133.
45. Mack, J., & Stillman, M. J. (2001). Assignment of the optical spectra of metal phthalocyanines through spectral band deconvolution analysis and ZINDO calculations. *Coord Chem Rev*, *219*, 993. https://doi.org/10.1016/S0010-8545(01)00394-0

46. Rio, Y., Rodriguez-Morgade, M. S., & Torres, T. (2008). Modulating the electronic properties of porphyrinoids: a voyage from the violet to the infrared regions of the electromagnetic spectrum. *Org Biomol Chem*, *6*, 1877. https://doi.org/10.1039/B800617B

47. Claessens, C. G., Hahn, U. W. E., & Torres, T. (2008). Phthalocyanines: From outstanding electronic properties to emerging applications. *Chemical Rec*, *8*, 75. https://doi.org/10.1002/tcr.20139

48. Alberto, M. E., De Simone, B. C., Mazzone, G., Sicilia, E., & Russo, N. (2015). The heavy atom effect on Zn (II) phthalocyanine derivatives: a theoretical exploration of the photophysical properties. *Phys Chem Chem Phys*, *17*, 23595. https://doi.org/10.1039/C5CP03833B

49. Azenha, E. G., Serra, A. C., Pineiro, M., Pereira, M. M., De Melo, J. S., Arnaut, L. G., Formosinho, S.J., & Gonsalves, A. M. d'A. R. (2002). Heavy-atom effects on metalloporphyrins and polyhalogenated porphyrins. *Chem Phys*, *280*, 177. https://doi.org/10.1016/S0301-0104(02)00485-8

50. Gorman, A., Killoran, J., O'Shea, C., Kenna, T., Gallagher, W. M., & O'Shea, D. F. (2004). In vitro demonstration of the heavy-atom effect for photodynamic therapy. *J Am Chem Soc*, *126*, 10619. https://doi.org/10.1021/ja047649e

51. Li, Y., Pritchett, T. M., Huang, J., Ke, M., Shao, P., & Sun, W. (2008). Photophysics and nonlinear absorption of peripheral-substituted zinc phthalocyanines. *J Phys Chem A*, *112*, 7200. https://doi.org/10.1021/jp7108835

52. Kimura, M., Nakada, K., Yamaguchi, Y., Shirai, K. H. H., & Kobayashi, N. (1997). Dendritic metallophthalocyanines: synthesis and characterization of a zinc (II)

phthalocyanine [8] 3-arborol. *Chem Commun*, 1215. https://doi.org/10.1039/A701263B

53. Bektaş, H., Ceylan, Ş., Demirbaş, N., Alpay-Karaoğlu, Ş., & Sökmen, B. B. (2013). Antimicrobial and antiurease activities of newly synthesized morpholine derivatives containing an azole nucleus. *Med Chem Res*, *22*, 3629. https://doi.org/10.1007/s00044-012-0318-1
54. Rego, Y. F., Queiroz, M. P., Brito, T. O., Carvalho, P. G., de Queiroz, V. T., de Fátima, Â., & Macedo Jr, F. (2018). A review on the development of urease inhibitors as antimicrobial agents against pathogenic bacteria. *J Adv Res*, *13*, 69. https://doi.org/10.1016/j.jare.2018.05.003
55. Hong, C. Y., Kim, Y. K., Chang, J. H., Kim, S. H., Choi, H., Nam, D. H., Kim, Y. Z., & Kwak, J. H. (1997). Novel Fluoroquinolone Antibacterial Agents Containing Oxime-Substituted (Aminomethyl) pyrrolidines: Synthesis and Antibacterial Activity of 7-(4-(Aminomethyl)-3-(methoxyimino) pyrrolidin-1-yl)-1-cyclopropyl-6-fluoro-4-oxo-1, 4-dihydro [1, 8] naphthyridine-3-carboxylic Acid (LB20304), *J Med Chem*, *40*, 3584. https://doi.org/10.1021/jm970202e
56. Li Petri, G., Raimondi, M. V., Spanò, V., Holl, R., Barraja, P., & Montalbano, A. (2021). Pyrrolidine in drug discovery: a versatile scaffold for novel biologically active compounds. *Top Curr Chem*, *379*, 1. https://doi.org/10.1007/s41061-021-00347-5
57. Azam, M. A., & Suresh, B. (2012). Biological activities of 2-mercaptobenzothiazole derivatives: a review. *Sci Pharm*, *80*, 789. https://doi.org/10.3797/scipharm.1204-27

58. Kuznetsova, A., Domingues, P. M., Silva, T., Almeida, A., Zheludkevich, M. L., Tedim, J., Ferreira, M. G. S. & Cunha, A. (2017). Antimicrobial activity of 2-mercaptobenzothiazole released from environmentally friendly nanostructured layered double hydroxides. *J Appl Microbiol*, *122*, 1207. https://doi.org/10.1111/jam.13433

59. Sen, P., & Nyokong, T. (2019). A novel axially palladium (II)-Schiff base complex substituted silicon (IV) phthalocyanine: Synthesis, characterization, photophysicochemical properties and photodynamic antimicrobial chemotherapy activity against Staphylococcus aureus. *Polyhedron*, *173*, 114135. https://doi.org/10.1016/j.poly.2019.114135

60. Şahal, H., Pişkin, M., Organ, G. A., Öztürk, Ö. F., Kaya, M., & Canpolat, E. (2018). Zinc (II) phthalocyanine containing Schiff base containing sulfonamide: synthesis, characterization, photophysical, and photochemical properties. *J Coord Chem*, *71*, 3763. https://doi.org/10.1080/00958972.2018.1524140

61. Kömerik, N. U. L. G. U. L., Nakanishi, H., MacRobert, A. J., Henderson, B., Speight, P., & Wilson, M. (2003). In vivo killing of Porphyromonas gingivalis by toluidine blue-mediated photosensitization in an animal model. *Antimicrob Agents Chemother*, *47*, 932. https://doi.org/10.1128/AAC.47.3.932-940.2003

62. Li, K., Lei, W., Jiang, G., Hou, Y., Zhang, B., Zhou, Q., & Wang, X. (2014). Selective photodynamic inactivation of bacterial cells over mammalian cells by new triarylmethanes. *Langmuir*, *30*, 14573. https://doi.org/10.1021/la5028724

63. Rosseti, I. B., Chagas, L. R., & Costa, M. S. (2014). Photodynamic antimicrobial chemotherapy (PACT) inhibits biofilm formation by Candida albicans, increasing

both ROS production and membrane permeability. *Lasers Med Sci*, *29*, 1059. https://doi.org/10.1007/s10103-013-1473-4

64. Castano, A. P., Demidova, T. N., & Hamblin, M. R. (2004). Mechanisms in photodynamic therapy: part one—photosensitizers, photochemistry and cellular localization. *Photodiagnosis Photodyn Ther*, *1*, 279. https://doi.org/10.1016/S1572-1000(05)00007-4
65. Anas, A., Sobhanan, J., Sulfiya, K. M., Jasmin, C., Sreelakshmi, P. K., & Biju, V. (2021). Advances in photodynamic antimicrobial chemotherapy. *J Photochem Photobiol C Photochem Rev*, *49*, 100452. https://doi.org/10.1016/j.jphotochemrev.2021.100452
66. Sobczyński, J., & Polski, A., Nanocarriers for photosensitizers for use in antimicrobial photodynamic therapy, in: Ficai, A., & Grumezescu, A. M. (Eds), Nanostructures for Antimicrobial Therapy, Elsevier, Amsterdam, 2017, pp. 481. https://doi.org/10.1016/B978-0-323-46152-8.00021-4
67. Huang, L., Xuan, Y., Koide, Y., Zhiyentayev, T., Tanaka, M., & Hamblin, M. R. (2012). Type I and Type II mechanisms of antimicrobial photodynamic therapy: an in vitro study on gram-negative and gram-positive bacteria. *Lasers Surg Med*, *44*, 490. https://doi.org/10.1002/lsm.22045
68. Jimenez-Mancilla, N. P., Aranda-Lara, L., Morales-Avila, E., Camacho-Lopez, M. A., Ocampo-García, B. E., Torres-García, E., Estrada-Guadarrama, J. A., Santos-Cuevas, C. L. & Isaac-Olivé, K. (2021). Electron transfer reactions in rhodamine: Potential use in photodynamic therapy. *J Photochem Photobiol A Chem*, *409*, 113131. https://doi.org/10.1016/j.jphotochem.2021.113131

69. Spikes, J. D., Photosensitization, in: Smith, K. C. (Ed), The Science of Photobiology, Springer, Boston, 1989, pp. 79.
70. Gürek, A. G., & Hirel, C., Recent Developments of Synthetic Techniques for Porphyrins, Phthalocyanines and Related Systems, in: Nyokong, T., & Ahsen V. (Eds), Photosensitizers in medicine, environment, and security, Springer Science & Business Media, Berlin, 2012, pp. 47.
71. Wainwright, M. (1996). Non-porphyrin photosensitizers in biomedicine. *Chem Soc Rev*, *25*, 351. https://doi.org/10.1039/CS9962500351
72. World Health Organization (2017, February 27). *WHO Publishes List of Bacteria for Which New Antibiotics are Urgently Needed*. https://www.who.int/en/news-room/detail/27-02-2017-who-publishes-list-of-bacteria-for-which-new-antibiotics-are-urgently-needed.
73. Stefani, S., Chung, D. R., Lindsay, J. A., Friedrich, A. W., Kearns, A. M., Westh, H., & MacKenzie, F. M. (2012). Meticillin-resistant Staphylococcus aureus (MRSA): global epidemiology and harmonisation of typing methods. *Int J Antimicrob Agents*, *39*, 273. https://doi.org/10.1016/j.ijantimicag.2011.09.030
74. McCarthy, H., Rudkin, J. K., Black, N. S., Gallagher, L., O'Neill, E., & O'Gara, J. P. (2015). Methicillin resistance and the biofilm phenotype in Staphylococcus aureus. *Front Cell Infect Microbiol*, *5*, 1. https://doi.org/10.3389/fcimb.2015.00001
75. Rice, L. B. (2001). Emergence of vancomycin-resistant enterococci. *Emerg Infect Dis*, *7*, 183. https://doi.org/10.3201%2Feid0702.010205

76. Munteanu, A. C., & Uivarosi, V. (2021). Ruthenium complexes in the fight against pathogenic microorganisms. an extensive review. *Pharmaceutics*, *13*, 874. https://doi.org/10.3390/pharmaceutics13060874

77. Fesel, P. H., & Zuccaro, A. (2016). β-glucan: Crucial component of the fungal cell wall and elusive MAMP in plants. *Fungal Genet Biol*, *90*, 53. https://doi.org/10.1016/j.fgb.2015.12.004

78. Radzig, M. A., Nadtochenko, V. A., Koksharova, O. A., Kiwi, J., Lipasova, V. A., & Khmel, I. A. (2013). Antibacterial effects of silver nanoparticles on gram-negative bacteria: influence on the growth and biofilms formation, mechanisms of action. *Colloids Surf B Biointerfaces*, *102*, 300. https://doi.org/10.1016/j.colsurfb.2012.07.039

79. Ramage, G., Martínez, J. P., & López-Ribot, J. L. (2006). Candida biofilms on implanted biomaterials: a clinically significant problem. *FEMS Yeast Res*, *6*, 979. https://doi.org/10.1111/j.1567-1364.2006.00117.x

80. Osifeko, O. L., Durmuş, M., & Nyokong, T. (2015). Physicochemical and photodynamic antimicrobial chemotherapy studies of mono-and tetra-pyridyloxy substituted indium (III) phthalocyanines. *J Photochem Photobiol A Chem*, *301*, 47. https://doi.org/10.1016/j.jphotochem.2014.12.011

81. Galstyan, A., Schiller, R., & Dobrindt, U. (2017). Boronic acid functionalized photosensitizers: a strategy to target the surface of bacteria and implement active agents in polymer coatings. *Angew Chem Int Ed Engl*, *56*, 10362. https://doi.org/10.1002/anie.201703398

82. Gao, Y., Mai, B., Wang, A., Li, M., Wang, X., Zhang, K., Liu, Q., Wei, S., & Wang, P. (2018). Antimicrobial properties of a new type of photosensitizer derived from phthalocyanine against planktonic and biofilm forms of Staphylococcus aureus. *Photodiagnosis Photodyn Ther*, *21*, 316. https://doi.org/10.1016/j.pdpdt.2018.01.003

83. Openda, Y. I., & Nyokong, T. (2021). Enhanced photo-ablation effect of positively charged phthalocyanines-detonation nanodiamonds nanoplatforms for the suppression of Staphylococcus aureus and Escherichia coli planktonic cells and biofilms. *J Photochem Photobiol A Chem*, *411*, 113200. https://doi.org/10.1016/j.jphotochem.2021.113200

84. Cavalcante, L. L. R., Tedesco, A. C., Takahashi, L. A. U., Curylofo-Zotti, F. A., Souza-Gabriel, A. E., & Corona, S. A. M. (2020). Conjugate of chitosan nanoparticles with chloroaluminium phthalocyanine: Synthesis, characterization and photoinactivation of Streptococcus mutans biofilm. *Photodiagnosis Photodyn Ther*, *30*, 101709. https://doi.org/10.1016/j.pdpdt.2020.101709

85. Dharmaratne, P., Wang, B., Wong, R. C., Chan, B. C., Lau, K. M., Ke, M. R., Lau, C. B. S., Ng, D. K. P., Fung, K. P., & Ip, M. (2020). Monosubstituted tricationic Zn (II) phthalocyanine enhances antimicrobial photodynamic inactivation (aPDI) of methicillin-resistant Staphylococcus aureus (MRSA) and cytotoxicity evaluation for topical applications: in vitro and in vivo study. *Emerg Microbes Infect*, *9*, 1628. https://doi.org/10.1080/22221751.2020.1790305

86. Mapukata, S., Nwahara, N., & Nyokong, T. (2020). The photodynamic antimicrobial chemotherapy of Stapphylococcus aureus using an asymmetrical

zinc phthalocyanine conjugated to silver and iron oxide based nanoparticles. *J Photochem Photobiol A Chem*, *402*, 112813. https://doi.org/10.1016/j.jphotochem.2020.112813

87. Osifeko, O. L., & Nyokong, T. (2014). Applications of lead phthalocyanines embedded in electrospun fibers for the photoinactivation of Escherichia coli in water. *Dyes Pigm*, *111*, 8. https://doi.org/10.1016/j.dyepig.2014.05.010
88. Tunçel, A., Öztürk, İ., Ince, M., Ocakoglu, K., Hoşgör-Limoncu, M., & Yurt, F. (2019). Antimicrobial photodynamic therapy against Staphylococcus aureus using zinc phthalocyanine and zinc phthalocyanine-integrated TiO2 nanoparticles. *J Porphyr Phthalocyanines*, *23*, 206. https://doi.org/10.1142/S1088424619500238
89. George, L., Hiltunen, A., Santala, V., & Efimov, A. (2018). Photo-antimicrobial efficacy of zinc complexes of porphyrin and phthalocyanine activated by inexpensive consumer LED lamp. *J Inorg Biochem*, *183*, 94. https://doi.org/10.1016/j.jinorgbio.2018.03.015
90. Gharpure, S., Akash, A., & Ankamwar, B. (2020). A review on antimicrobial properties of metal nanoparticles. *J Nanosci Nanotechnol*, *20*, 3303. https://doi.org/10.1166/jnn.2020.17677
91. Buzea, C., Pacheco, I. I., & Robbie, K. (2007). Nanomaterials and nanoparticles: sources and toxicity. *Biointerphases*, *2*, MR17. https://doi.org/10.1116/1.2815690
92. Sirelkhatim, A., Mahmud, S., Seeni, A., Kaus, N. H. M., Ann, L. C., Bakhori, S. K. M., Hasan, H., & Mohamad, D. (2015). Review on zinc oxide nanoparticles:

antibacterial activity and toxicity mechanism. *Nanomicro Lett*, *7*, 219. https://doi.org/10.1007/s40820-015-0040-x

93. Tan, P., Li, H., Wang, J., & Gopinath, S. C. (2021). Silver nanoparticle in biosensor and bioimaging: Clinical perspectives. *Biotechnol Appl Biochem*, *68*, 1236. https://doi.org/10.1002/bab.2045
94. Bustamante-Torres, M., Romero-Fierro, D., Estrella-Nuñez, J., Arcentales-Vera, B., Chichande-Proaño, E., & Bucio, E. (2022). Polymeric composite of magnetite iron oxide nanoparticles and their application in biomedicine: a review. *Polymers*, *14*, 752. https://doi.org/10.3390/polym14040752
95. Gajbhiye, S., & Sakharwade, S. (2016). Silver nanoparticles in cosmetics. *J Cosmet Dermatol Sci Appl*, *6*, 48. http://dx.doi.org/10.4236/jcdsa.2016.61007
96. Tsuzuki, T., & Wang, X. (2010). Nanoparticle coatings for UV protective textiles. *Res J Text Appar*, *14*, 9. https://doi.org/10.1108/RJTA-14-02-2010-B002
97. Shaba, E. Y., Jacob, J. O., Tijani, J. O., & Suleiman, M. A. T. (2021). A critical review of synthesis parameters affecting the properties of zinc oxide nanoparticle and its application in wastewater treatment. *Appl Water Sci*, *11*, 1. https://doi.org/10.1007/s13201-021-01370-z
98. Bezza, F. A., Tichapondwa, S. M., & Chirwa, E. M. (2020). Fabrication of monodispersed copper oxide nanoparticles with potential application as antimicrobial agents. *Sci Rep*, *10*, 16680. https://doi.org/10.1038/s41598-020-73497-z
99. Tietze, R., Zaloga, J., Unterweger, H., Lyer, S., Friedrich, R. P., Janko, C., Pottler, M., Durr, S., & Alexiou, C. (2015). Magnetic nanoparticle-based drug

delivery for cancer therapy. *Biochem Biophys Res Commun*, *468*, 463. https://doi.org/10.1016/j.bbrc.2015.08.022

100. Shirgholami, M. A., Nazari, A., & Mirjalili, M. (2015). Statistical optimization of self-cleaning technology and color reduction in wool fabric by nano zinc oxide and eco-friendly cross-linker. *Clean Technol Environ Policy*, *17*, 905. https://doi.org/10.1007/s10098-014-0842-4
101. Kumar, S., & Sahare, P. D. (2012). Effects of annealing on the surface defects of zinc oxide nanoparticles. *Nano*, *7*, 1250022. https://doi.org/10.1142/S1793292012500221
102. Li, M., Zhu, L., & Lin, D. (2011). Toxicity of ZnO nanoparticles to Escherichia coli: mechanism and the influence of medium components. *Environ Sci Technol*, *45*, 1977. https://doi.org/10.1021/es102624t
103. Zhang, L., Jiang, Y., Ding, Y., Povey, M., & York, D. (2007). Investigation into the antibacterial behaviour of suspensions of ZnO nanoparticles (ZnO nanofluids). *J Nanopart Res*, *9*, 479. https://doi.org/10.1007/s11051-006-9150-1
104. Lallo da Silva, B., Abuçafy, M. P., Berbel Manaia, E., Oshiro Junior, J. A., Chiari-Andréo, B. G., Pietro, R. C. R., & Chiavacci, L. A. (2019). Relationship between structure and antimicrobial activity of zinc oxide nanoparticles: An overview. *Int J Nanomedicine*, 9395. https://doi.org/10.2147/IJN.S216204
105. D'Agostino, A., Taglietti, A., Desando, R., Bini, M., Patrini, M., Dacarro, G., Cucca, L., Pallavicini, P., & Grisoli, P. (2017). Bulk surfaces coated with triangular silver nanoplates: Antibacterial action based on silver release and photo-thermal effect. *Nanomaterials*, *7*, 7. https://doi.org/10.3390/nano7010007

106. Seil, J. T., & Webster, T. J. (2012). Antimicrobial applications of nanotechnology: methods and literature. *Int J Nanomedicine*, *7*, 2767. https://doi.org/10.2147/IJN.S24805

107. Mapukata, S., Britton, J., Nwahara, N., & Nyokong, T. (2022). The photocatalytic properties of zinc phthalocyanines supported on hematite nanofibers for use against methyl orange and Staphylococcus aureus. *J Photochem Photobiol A Chem*, *424*, 113637. https://doi.org/10.1016/j.jphotochem.2021.113637

108. Zakria, H. S., Othman, M. H. D., Kamaludin, R., Kadir, S. H. S. A., Kurniawan, T. A., & Jilani, A. (2021). Immobilization techniques of a photocatalyst into and onto a polymer membrane for photocatalytic activity. *RSC Adv*, *11*, 6985. https://doi.org/10.1039/D0RA10964A

109. Fu, G. B., Xie, R., Qin, J. W., Deng, X. B., Ju, X. J., Wang, W., Liu, Z., & Chu, L. Y. (2021). Facile fabrication of photocatalyst-immobilized gel beads with interconnected macropores for the efficient removal of pollutants in water. *Ind Eng Chem Res*, *60*, 8762. https://doi.org/10.1021/acs.iecr.1c00971

110. Elhage, A., Wang, B., Marina, N., Marin, M. L., Cruz, M., Lanterna, A. E., & Scaiano, J. C. (2018). Glass wool: a novel support for heterogeneous catalysis. *Chem Sci*, *9*, 6844. https://doi.org/10.1039/C8SC02115E

111. Ergün, A. B., Sevim, A. M., Kılıç, A., & Gül, A. (2021). Metallophthalocyanine/polyacrylonitrile nanofibers by solution blow spinning technique for enhanced photocatalytic activity by visible light. *J Appl Polym Sci*, *138*, 50115. https://doi.org/10.1002/app.50115

112. Guo, X., Zhou, X., Li, X., Shao, C., Han, C., Li, X., & Liu, Y. (2018). Bismuth oxychloride (BiOCl)/copper phthalocyanine (CuTNPc) heterostructures immobilized on electrospun polyacrylonitrile nanofibers with enhanced activity for floating photocatalysis. *J Colloid Interface Sci, 525*, 187. https://doi.org/10.1016/j.jcis.2018.04.028

113. Wang, F., Cao, S., Men, J., Lei, N., & Wang, R. (2020). Phthalocyanine-modified surfactant-encapsulated polyoxometalate and its self-assembly in solution. *Colloids Surf A Physicochem Eng Asp*, *601*, 125056. https://doi.org/10.1016/j.colsurfa.2020.125056

114. Liu, Y., Hao, M., Chen, Z., Liu, L., Liu, Y., Yang, W., & Ramakrishna, S. (2020). A review on recent advances in application of electrospun nanofiber materials as biosensors. *Curr Opin Biomed Eng*, *13*, 174. https://doi.org/10.1016/j.cobme.2020.02.001

115. Mafukidze, D. M., & Nyokong, T. (2021). Photocatalytic and solar radiation harvesting potential of a free-base porphyrin-zinc (II) phthalocyanine heterodyad functionalized polystyrene polymer membrane for the degradation of 4-chlorophenol. *J Photochem Photobiol A Chem*, *409*, 113142. https://doi.org/10.1016/j.jphotochem.2021.113142

116. Sun, Y., Zheng, W., Fu, S., & Singh, R. P. (2020). Immobilization of iron phthalocyanine on 4-aminopyridine grafted polystyrene resin as a catalyst for peroxymonosulfate activation in eliminating tetracycline hydrochloride. *Chem Eng J*, *391*, 123611. https://doi.org/10.1016/j.cej.2019.123611

117. Dahlin, R. L., Kasper, F. K., & Mikos, A. G. (2011). Polymeric nanofibers in tissue engineering. *Tissue Eng Part B Rev*, *17*, 349. https://doi.org/10.1089/ten.teb.2011.0238

118. Son, Y. J., Kim, W. J., & Yoo, H. S. (2014). Therapeutic applications of electrospun nanofibers for drug delivery systems. *Arch Pharm Res*, *37*, 69. https://doi.org/10.1007/s12272-013-0284-2

119. Blosi, M., Costa, A. L., Ortelli, S., Belosi, F., Ravegnani, F., Varesano, A., Tonetti, C., Zanoni, I., & Vineis, C. (2021). Polyvinyl alcohol/silver electrospun nanofibers: Biocidal filter media capturing virus-size particles. *J Appl Polym Sci*, *138*, 51380. https://doi.org/10.1002/app.51380

120. Sakib, M. N., Mallik, A. K., & Rahman, M. M. (2021). Update on chitosan-based electrospun nanofibers for wastewater treatment: A review. *Carbohydr Polym Technol Appl*, *2*, 100064. https://doi.org/10.1016/j.carpta.2021.100064

121. Ambekar, R. S., & Kandasubramanian, B. (2019). Advancements in nanofibers for wound dressing: A review. *Eur Polym J*, *117*, 304. https://doi.org/10.1016/j.eurpolymj.2019.05.020

122. Nain, A. S., Wong, J. C., Amon, C., & Sitti, M. (2006). Drawing suspended polymer micro-/nanofibers using glass micropipettes. *Appl Phys Lett*, *89*, 183105. https://doi.org/10.1063/1.2372694

123. Yan, J., Han, Y., Xia, S., Wang, X., Zhang, Y., Yu, J., & Ding, B. (2019). Polymer template synthesis of flexible BaTiO3 crystal nanofibers. *Adv Funct Mater*, *29*, 1907919. https://doi.org/10.1002/adfm.201907919

124. Dong, H., Paramonov, S. E., & Hartgerink, J. D. (2008). Self-assembly of α-helical coiled coil nanofibers. *J Am Chem Soc*, *130*, 13691. https://doi.org/10.1021/ja8037323

125. Zhao, J., Han, W., Chen, H., Tu, M., Zeng, R., Shi, Y., Cha, Z., & Zhou, C. (2011). Preparation, structure and crystallinity of chitosan nano-fibers by a solid–liquid phase separation technique. *Carbohydr Polym*, *83*, 1541. https://doi.org/10.1016/j.carbpol.2010.10.009

126. Huang, Z. M., Zhang, Y. Z., Kotaki, M., & Ramakrishna, S. (2003). A review on polymer nanofibers by electrospinning and their applications in nanocomposites. *Compos Sci Technol*, *63*, 2223. https://doi.org/10.1016/S0266-3538(03)00178-7

127. Elsabee, M. Z., Naguib, H. F., & Morsi, R. E. (2012). Chitosan based nanofibers, review. *Mater Sci Eng C*, *32*, 1711. https://doi.org/10.1016/j.msec.2012.05.009

128. Zeleny, J. (1914). The electrical discharge from liquid points, and a hydrostatic method of measuring the electric intensity at their surfaces. *Phys Rev*, *3*, 69. https://doi.org/10.1103/PhysRev.3.69

129. Anton, F. (1934). *U.S. Patent No. 1,975,504*. Washington, DC: U.S. Patent and Trademark Office.

130. Bhardwaj, N., & Kundu, S. C. (2010). Electrospinning: A fascinating fiber fabrication technique. *Biotechnol Adv*, *28*, 325. https://doi.org/10.1016/j.biotechadv.2010.01.004

131. Lee, Y.S., & Sun, J., Preparation of Functionalized Nanofibers and Their Applications, in: Kumar, A. (Ed), Nanofibers, IntechOpen, London, 2010. https://doi.org/10.5772/8150

132. Jayaraman, K., Kotaki, M., Zhang, Y., Mo, X., & Ramakrishna, S. (2004). Recent advances in polymer nanofibers. *J Nanosci Nanotechnol*, *4*, 52. https://doi.org/10.1166/jnn.2004.078

133. Bode-Aluko, C. A., Pereao, O., Kyaw, H. H., Al-Naamani, L., Al-Abri, M. Z., Myint, M. T. Z., Rossouw, A., Fatoba, O., Petrik, L., & Dobretsov, S. (2021). Photocatalytic and antifouling properties of electrospun TiO2 polyacrylonitrile composite nanofibers under visible light. *Mater Sci Eng B*, *264*, 114913. https://doi.org/10.1016/j.mseb.2020.114913

134. Fayemi, O. E., Ekennia, A. C., Katata-Seru, L., Ebokaiwe, A. P., Ijomone, O. M., Onwudiwe, D. C., & Ebenso, E. E. (2018). Antimicrobial and wound healing properties of polyacrylonitrile-moringa extract nanofibers. *ACS omega*, *3*, 4791. https://doi.org/10.1021/acsomega.7b01981

135. Tang, C., Bai, H., Liu, L., Zan, X., Gao, P., Sun, D. D., & Yan, W. (2016). A green approach assembled multifunctional Ag/AgBr/TNF membrane for clean water production & disinfection of bacteria through utilizing visible light. *Appl Catal B Environ*, *196*, 57. https://doi.org/10.1016/j.apcatb.2016.05.023

136. Mujtaba, M., Fernández-Marín, R., Robles, E., Labidi, J., Yilmaz, B. A., & Nefzi, H. (2021). Understanding the effects of copolymerized cellulose nanofibers and diatomite nanocomposite on blend chitosan films. *Carbohydr Polym*, *271*, 118424. https://doi.org/10.1016/j.carbpol.2021.118424

137. Sahariah, P., & Másson, M. (2017). Antimicrobial chitosan and chitosan derivatives: a review of the structure–activity relationship. *Biomacromolecules*, *18*, 3846. https://doi.org/10.1021/acs.biomac.7b01058

138. McKee, M. G., Wilkes, G. L., Colby, R. H., & Long, T. E. (2004). Correlations of solution rheology with electrospun fiber formation of linear and branched polyesters. *Macromolecules*, *37*, 1760. https://doi.org/10.1021/ma035689h

139. da Rosa, L. C., Santor, C. G., Lovato, A., da Rosa, C. S., & Güths, S. (2015). Use of rice husk and sunflower stalk as a substitute for glass wool in thermal insulation of solar collector. *J Clean Prod*, *104*, 90. https://doi.org/10.1016/j.jclepro.2015.04.127

140. Wang, F., Chen, Z., Wu, C., & Yang, Y. (2019). Prediction on sound insulation properties of ultrafine glass wool mats with artificial neural networks. *Appl Acoust*, *146*, 164. https://doi.org/10.1016/j.apacoust.2018.11.018

141. Batterman, S., Metts, T., & Kalliokoski, P. (2002). Diffusive uptake in passive and active adsorbent sampling using thermal desorption tubes. *J Environ Monit*, *4*, 870. https://doi.org/10.1039/B204835C

142. Nisnevitch, M., Kolog-Gulco, M., Trombka, D., Green, B. S., & Firer, M. A. (2000). Immobilization of antibodies onto glass wool. *J Chromatogr B Biomed Sci Appl*, *738*, 217. https://doi.org/10.1016/S0378-4347(99)00514-9

143. Steyn, B., Oosthuizen, M. C., MacDonald, R., Theron, J., & Brözel, V. S. (2001). The use of glass wool as an attachment surface for studying phenotypic changes in Pseudomonas aeruginosa biofilms by two-dimensional gel

electrophoresis. *PROTEOMICS Int Ed*, *1*, 871. https://doi.org/10.1002/1615-9861(200107)1:7%3C871::AID-PROT871%3E3.0.CO;2-2

144. Rueda-Marquez, J. J., Levchuk, I., Ibañez, P. F., & Sillanpää, M. (2020). A critical review on application of photocatalysis for toxicity reduction of real wastewaters. *J Clean Prod*, *258*, 120694. https://doi.org/10.1016/j.jclepro.2020.120694
145. Narayan, R. B., Goutham, R., Srikanth, B., & Gopinath, K. P. (2018). A novel nano-sized calcium hydroxide catalyst prepared from clam shells for the photodegradation of methyl red dye. *J Environ Chem Eng*, *6*, 3640. https://doi.org/10.1016/j.jece.2016.12.004
146. Khwannimit, D., Maungchang, R., & Rattanakit, P. (2022). Green synthesis of silver nanoparticles using Clitoria ternatea flower: an efficient catalyst for removal of methyl orange. *Int J Environ Anal Chem*, *102*, 5247. https://doi.org/10.1080/03067319.2020.1793974
147. Khan, I., Saeed, K., Zekker, I., Zhang, B., Hendi, A. H., Ahmad, A., Ahmad, S., Zada, N., Ahmad, H., Shah, L. A., Shah, T., & Khan, I. (2022). Review on methylene blue: its properties, uses, toxicity and photodegradation. *Water*, *14*, 242. https://doi.org/10.3390/w14020242
148. Madannejad, S., Rashidi, A., Sadeghhassani, S., Shemirani, F., & Ghasemy, E. (2018). Removal of 4-chlorophenol from water using different carbon nanostructures: a comparison study. *J Mol Liq*, *249*, 877. https://doi.org/10.1016/j.molliq.2017.11.089

149. Gupta, V. K., Jain, R., & Varshney, S. (2007). Removal of Reactofix golden yellow 3 RFN from aqueous solution using wheat husk—an agricultural waste. *J Hazard Mater*, *142*, 443. https://doi.org/10.1016/j.jhazmat.2006.08.048

150. Lin, L., Li, R. H., Li, Y., Xu, J., & Li, X. Y. (2017). Recovery of organic carbon and phosphorus from wastewater by Fe-enhanced primary sedimentation and sludge fermentation. *Process Biochem*, *54*, 135. https://doi.org/10.1016/j.procbio.2016.12.016

151. Kasperchik, V. P., Yaskevich, A. L., & Bil'Dyukevich, A. V. (2012). Wastewater treatment for removal of dyes by coagulation and membrane processes. *Pet Chem*, *52*, 545. https://doi.org/10.1134/S0965544112070079

152. Barragán, B. E., Costa, C., & Marquez, M. C. (2007). Biodegradation of azo dyes by bacteria inoculated on solid media. *Dyes Pigm*, *75*, 73. https://doi.org/10.1016/j.dyepig.2006.05.014

153. Mohan, S. V., Babu, V. L., & Sarma, P. N. (2007). Anaerobic biohydrogen production from dairy wastewater treatment in sequencing batch reactor (AnSBR): effect of organic loading rate. *Enzyme Microb Technol*, *41*, 506. https://doi.org/10.1016/j.enzmictec.2007.04.007

154. Gogate, P. R., & Pandit, A. B. (2004). A review of imperative technologies for wastewater treatment I: oxidation technologies at ambient conditions. *Adv Environ Res*, *8*, 501. https://doi.org/10.1016/S1093-0191(03)00032-7

155. Jüttner, K., Galla, U., & Schmieder, H. (2000). Electrochemical approaches to environmental problems in the process industry. *Electrochim Acta*, *45*, 2575. https://doi.org/10.1016/S0013-4686(00)00339-X

156. Ma, D., Yi, H., Lai, C., Liu, X., Huo, X., An, Z., Li, L., Fu, Y., Li, B., Zhang, M., Qin, L., Liu, S., & Yang, L. (2021). Critical review of advanced oxidation processes in organic wastewater treatment. *Chemosphere*, *275*, 130104. https://doi.org/10.1016/j.chemosphere.2021.130104

157. Bartolomeu, M., Neves, M. G. P. M. S., Faustino, M. A. F., & Almeida, A. (2018). Wastewater chemical contaminants: Remediation by advanced oxidation processes. *Photochem Photobiol Sci*, *17*, 1573. https://doi.org/10.1039/C8PP00249E

158. Zhang, X., Zhang, M., Liu, H., Gu, J., & Liu, Y. (2019). Environmental sustainability: a pressing challenge to biological sewage treatment processes. *Curr Opin Environ Sci Health*, *12*, 1. https://doi.org/10.1016/j.coesh.2019.05.006

159. Ghanbari, F., & Moradi, M. (2017). Application of peroxymonosulfate and its activation methods for degradation of environmental organic pollutants. *Chem Eng J*, *310*, 41. https://doi.org/10.1016/j.cej.2016.10.064

160. Zugle, R., Antunes, E., Khene, S., & Nyokong, T. (2012). Photooxidation of 4-chlorophenol sensitized by lutetium tetraphenoxy phthalocyanine anchored on electrospun polystyrene polymer fiber. *Polyhedron, 33*, 74. https://doi.org/10.1016/j.poly.2011.11.005

161. Jones, B., Britton, J., Mafukidze, D., & Nyokong, T. (2020). Photodegradation of 4-chlorophenol using Zn and In phthalocyanines substituted with pyrrole without hetero atoms linkers and supported on polyacrylonitrile electrospun fibres. *Polyhedron*, *178*, 114329 https://doi.org/10.1016/j.poly.2019.114329

162. Zugle, R., & Nyokong, T. (2013). Comparative phototransformation of environmental pollutants using metallophthalocyanines supported on electrospun polymer fibers. *J Appl Polym Sci, 128*, 1131. https://doi.org/10.1002/app.38381

163. Liu, G., Liu, S., Lu, Q., Sun, H., & Xiu, Z. (2014). BiVO 4/cobalt phthalocyanine (CoPc) nanofiber heterostructures: synthesis, characterization and application in photodegradation of methylene blue. Rsc Adv, 4, 53402. https://doi.org/10.1039/C4RA08759C

164. Liu, G., Liu, S., Lu, Q., Sun, H., & Xiu, Z. (2014). Iron (III) phthalocyanine/BiPO 4 heterostructured nanofibers: controllable fabrication and visible photocatalytic properties investigation. *J Nanopart Res*, *16*, 1. https://doi.org/10.1007/s11051-014-2685-7

165. Sen, P., Dege, N., & Yildiz, S. Z. (2017). Tri-nuclear phthalocyanine complexes carrying N/O donor ligands as hydrogen peroxide catalysts, and their bleaching activity measurements by an online spectrophotometric method. *J Coord Chem*, *70*, 2751. https://doi.org/10.1080/00958972.2017.1360490

166. Sen, P., Mack, J., & Nyokong, T. (2022). Indium phthalocyanines: Comparative photophysicochemical properties and photodynamic antimicrobial activities against Staphylococcus aureus and Escherichia coli. *J Mol Struct*, *1250*, 131850. https://doi.org/10.1016/j.molstruc.2021.131850

167. Jia, N., He, C., Wang, S., Song, W., Chen, Z., Zu, Y., Gao, Y., & Dong, Y. (2018). Effect of central metals and peripheral substituents on the third-order nonlinear optical properties of tetra-benzimidazole and benzothiazole

substituted phthalocyanines. *Opt Mater*, *76*, 81. https://doi.org/10.1016/j.optmat.2017.12.012

168. Kliesch, H., Weitemeyer, A., Müller, S., & Wöhrle, D. (1995). Synthesis of phthalocyanines with one sulfonic acid, carboxylic acid, or amino group. *Liebigs Ann Chem*, *1995*, 1269. https://doi.org/10.1002/jlac.1995199507168
169. Sun, B., & Sirringhaus, H. (2005). Solution-processed zinc oxide field-effect transistors based on self-assembly of colloidal nanorods. *Nano Lett*, *5*, 2408. https://doi.org/10.1021/nl051586w
170. Yang, M., Sun, K., & Kotov, N. A. (2010). Formation and assembly− disassembly processes of ZnO hexagonal pyramids driven by dipolar and excluded volume interactions. *J Am Chem Soc*, *132*, 1860. https://doi.org/10.1021/ja906868h
171. Jones, B., Mafukidze, D., & Nyokong, T. (2020). Fabrication of electrospun fibers from a porphyrin linked to polyacrylonitrile polymer for photocatalytic transformation of phenols. *J Mol Struct*, *1213*, 128191. https://doi.org/10.1016/j.molstruc.2020.128191
172. Ambroz, M., Beeby, A., MacRobert, A. J., Svensen, R. K., & Phillips, D. (1991). Preparative, analytical and fluorescence spectroscopic studies of sulphonated aluminium phthalocyanine photosensitizers. *J Photochem Photobiol B Biol*, *9*, 87. https://doi.org/10.1016/1011-1344(91)80006-4
173. Baghdadi, Y. N., Youssef, L., Bouhadir, K., Harb, M., Mustapha, S., Patra, D., & Tehrani-Bagha, A. R. (2020). The effects of modified zinc oxide nanoparticles

on the mechanical/thermal properties of epoxy resin. *J App. Polym Sci*, *137*, 49330. https://doi.org/10.1002/app.49330

174. Mafukidze, D. M., Mashazi, P., & Nyokong, T. (2016). Synthesis and singlet oxygen production by a phthalocyanine when embedded in asymmetric polymer membranes. *Polymer*, *105*, 203. https://doi.org/10.1016/j.polymer.2016.10.032
175. Balouiri, M., Sadiki, M., & Ibnsouda, S. K. (2016). Methods for in vitro evaluating antimicrobial activity: A review. *J Pharm Anal*, *6*, 71. https://doi.org/10.1016/j.jpha.2015.11.005
176. da Volta Soares, M., Oliveira, M. R., dos Santos, E. P., de Brito Gitirana, L., Barbosa, G. M., Quaresma, C. H., & Ricci-Júnior, E. (2011). Nanostructured delivery system for zinc phthalocyanine: preparation, characterization, and phototoxicity study against human lung adenocarcinoma A549 cells. *Int J Nanomed*, 227. https://doi.org/10.2147/IJN.S15860
177. Matshitse, R., Nwaji, N., Mananga, M., Prinsloo, E., Nyokong, T. (2018). Effect of number of positive charges on the photophysical and photodynamic therapy activities of quarternary benzothiazole substituted zinc phthalocyanine. *J Photochem Photobiol A Chem, 367,* 253. https://doi.org/10.1016/j.jphotochem.2018.08.033
178. Rusanova, J., Pilkington, M., Decurtins, S. (2002). A novel fully conjugated phenanthroline-appended phthalocyanine: Synthesis and characterisation. *Chem Commun, 9,* 2236. https://doi.org/10.1039/B206973C.
179. Yenilmez, H. Y., Özçeşmeci, İ., Okur, A. İ., & Gül, A. (2004). Synthesis and characterization of metal-free and metallo phthalocyanines with four pendant

naphthoxy-substituents. *Polyhedron*, *23*, 787. https://doi.org/10.1016/j.poly.2003.12.003

180. Soganci, T., Baygu, Y., Kabay, N., Gök, Y., & Ak, M. (2018). Comparative investigation of peripheral and nonperipheral zinc phthalocyanine-based polycarbazoles in terms of optical, electrical, and sensing properties. *ACS Appl Mater interfaces*, *10*, 21654. https://doi.org/10.1021/acsami.8b06206
181. Zhang, X. F., Li, X., Niu, L., Sun, L., & Liu, L. (2009). Charge transfer photophysics of tetra (α-amino) zinc phthalocyanine. *J Fluoresc*, *19*, 947. https://doi.org/10.1007/s10895-009-0494-7
182. Durmuş, M., Erdoğmuş, A., Ogunsipe, A., & Nyokong, T. (2009). The synthesis and photophysicochemical behaviour of novel water-soluble cationic indium (III) phthalocyanine. *Dyes Pigm*, *82*, 244. https://doi.org/10.1016/j.dyepig.2009.01.008
183. Chen, Y., Hanack, M., Blau, W. J., Dini, D., Liu, Y., Lin, Y., & Bai, J. (2006). Soluble axially substituted phthalocyanines: Synthesis and nonlinear optical response. *J Mater Sci*, *41*, 2169. https://doi.org/10.1007/s10853-006-5552-9
184. Doria, S., Lapini, A., Di Donato, M., Righini, R., Azzaroli, N., Iagatti, A., Caram, J.R., Sinclair, T.S., Cupellini, L., Jurinovich, S., Mennucci, B., Zanotti, G., Paoletti, A.M., Pennesi, G., & Foggi, P. (2018). Understanding the influence of disorder on the exciton dynamics and energy transfer in Zn-phthalocyanine H-aggregates. *Phys Chem Chem Phys*, *20*, 22331. https://doi.org/10.1039/C8CP02172D.

185. Loganathan, S., Valapa, R. B., Mishra, R. K., Puzazhenthi, G. & Thomas, S, Thermogravimetric Analysis for Characterization of Nanomaterials, in: Thomas, S., Thomas, R., Zachariah, A. K., & Mishra, R. K. (Eds), Thermal and rheological measurement techniques for nanomaterials characterization, Elsevier, Amsterdam, 2017, Vol 3, pp. 68.

186. Yang, Z., Chen, X., Li, S., Ma, W., Li, Y., He, Z., & Hu, H. (2020). Effective removal of Cr (VI) from aqueous solution based on APTES modified nanoporous silicon prepared from kerf loss silicon waste. *Environ Sci Pollut Res*, *27*, 10899. https://doi.org/10.1007/s11356-019-07427-6

187. Chen, C., Ma, Z., Zhou, S., Li, T., & Sun, X. (2017). Cobalt-Tetracarboxyl-Phthalocyanine Linked with Fe 3 O 4/Chitosan Microsphereas—Efficient Catalyst for Dye Degradation. *Catal Lett*, *147*, 2399. https://doi.org/10.1007/s10562-017-2149-7

188. Kyaw, H. H., Al-Harthi, S. H., Sellai, A., & Dutta, J. (2015). Self-organization of gold nanoparticles on silanated surfaces. *Beilstein J Nanotechnol*, *6*, 2345. https://doi.org/10.3762/bjnano.6.242

189. Kunc, F., Balhara, V., Brinkmann, A., Sun, Y., Leek, D. M., & Johnston, L. J. (2018). Quantification and stability determination of surface amine groups on silica nanoparticles using solution NMR. *Anal Chem*, *90*, 13322. https://doi.org/10.1021/acs.analchem.8b02803

190. Awsiuk, K., Budkowski, A., Psarouli, A., Petrou, P., Bernasik, A., Kakabakos, S., Rysz, J., & Raptis, I. (2013). Protein adsorption and covalent bonding to silicon nitride surfaces modified with organo-silanes: Comparison using AFM, angle-

resolved XPS and multivariate ToF-SIMS analysis. *Colloids Surf B Biointerfaces*, *110*, 217. https://doi.org/10.1016/j.colsurfb.2013.04.030

191. Kim, T. M., Whan Kim, J., Shim, H. S., & Kim, J. J. (2012). High efficiency and high photo-stability zinc-phthalocyanine based planar heterojunction solar cells with a double interfacial layer. *Appl Phys Lett*, *101*, 113301. https://doi.org/10.1063/1.4748123
192. Chen, X., Wang, X., & Fang, D. (2020). A review on C1s XPS-spectra for some kinds of carbon materials. *Fuller Nanotub Carbon Nanostruct*, *28*, 1048. https://doi.org/10.1080/1536383X.2020.1794851
193. Sun, W., Lu, X., Tong, Y., Lei, J., Nie, G., & Wang, C. (2014). A one-pot synthesis of a highly dispersed palladium/polypyrrole/polyacrylonitrile nanofiber membrane and its recyclable catalysis in hydrogen generation from ammonia borane. *J Mater Chem A*, *2*, 6740. https://doi.org/10.1039/C3TA15441F
194. Min, H., Girard-Lauriault, P. L., Gross, T., Lippitz, A., Dietrich, P., & Unger, W. E. (2012). Ambient-ageing processes in amine self-assembled monolayers on microarray slides as studied by ToF-SIMS with principal component analysis, XPS, and NEXAFS spectroscopy. *Analytical and bioanalytical chemistry*, *403*, 613-623. https://doi.org/10.1007/s00216-012-5862-5
195. Osifeko, O., & Nyokong, T. (2016). Synthesis and physicochemical properties of zinc and indium phthalocyanines conjugated to quantum dots, gold and magnetic nanoparticles. *Dyes Pigm*, *131*, 186. https://doi.org/10.1016/j.dyepig.2016.04.015

196. Ma, X., Luo, M., Yan, L., Tang, N., & Li, J. (2019). Preparation of a magnetically recyclable visible-light-driven photocatalyst based on phthalocyanine and its visible light catalytic degradation of methyl orange and p-nitrophenol. *New J Chem*, *43*, 9589. https://doi.org/10.1039/C9NJ01904A

197. Gulati, K., Aw, M. S., & Losic, D. (2012). Nanoengineered drug-releasing Ti wires as an alternative for local delivery of chemotherapeutics in the brain. *Int J Nanomedicine*, *7*, 2069. https://doi.org/10.2147/IJN.S29917

198. Alagna, L., Capobianchi, A., Casaletto, M. P., Mattogno, G., Paoletti, A. M., Pennesi, G., & Rossi, G. (2001). Effect of molecular packing on the solid state spectra of ruthenium phthalocyanine: anomalous behaviour of a monodimensional stacked assembly. *J Mater Chem*, *11*, 1928. https://doi.org/10.1039/B100041L

199. Queiroz, M. F., Teodosio Melo, K. R., Sabry, D. A., Sassaki, G. L., & Rocha, H. A. O. (2014). Does the use of chitosan contribute to oxalate kidney stone formation? *Mar Drugs*, *13*, 141. https://doi.org/10.3390/md13010141

200. Zhang, Y., Zhi, Z., Jiang, T., Zhang, J., Wang, Z., & Wang, S. (2010). Spherical mesoporous silica nanoparticles for loading and release of the poorly water-soluble drug telmisartan. *J Controlled Release*, *145*, 257. https://doi.org/10.1016/j.jconrel.2010.04.029

201. Qiao, M., Kong, H., Ding, X., Hu, Z., Zhang, L., Cao, Y., & Yu, M. (2019). Study on the changes of structures and properties of PAN fibers during the cyclic reaction in supercritical carbon dioxide. *Polymers*, *11*, 402. https://doi.org/10.3390/polym11030402

202. Lee, S., Kim, J., Ku, B. C., Kim, J., & Joh, H. I. (2012). Structural evolution of polyacrylonitrile fibers in stabilization and carbonization. *Adv Chem Engineer Sci, 2*, 275. http://dx.doi.org/10.4236/aces.2012.22032

203. Zhou, Y., Yu, H. Y., Gu, J. P., Zhu, J. Y., Zhu, M. H., Guan, Y., & Yao, J. M. (2018). Novel fabrication of modulated carpenterworm-like zinc oxide/polyacrylonitrile composite nanofibers for photocatalytic degradation of methylene blue dye. *J Taiwan Inst Chem Eng*, *91*, 548. https://doi.org/10.1016/j.jtice.2018.05.050

204. Boyer, C., Whittaker, M. R., Chuah, K., Liu, J., & Davis, T. P. (2010). Modulation of the surface charge on polymer-stabilized gold nanoparticles by the application of an external stimulus. *Langmuir*, *26*, 2721. https://doi.org/10.1021/la902746v

205. Yang, J., Duan, J., Zhang, L., Lindman, B., Edlund, H., & Norgren, M. (2016). Spherical nanocomposite particles prepared from mixed cellulose–chitosan solutions. *Cellulose*, *23*, 3105. https://doi.org/10.1007/s10570-016-1029-4

206. Ekiz, F., Oğuzkaya, F., Akin, M., Timur, S., Tanyeli, C., & Toppare, L. (2011). Synthesis and application of poly-SNS-anchored carboxylic acid: a novel functional matrix for biomolecule conjugation. *J Mater Chem*, *21*, 12337. https://doi.org/10.1039/C1JM12048D

207. Yu, Y. H., Lin, Y. Y., Lin, C. H., Chan, C. C., & Huang, Y. C. (2014). High-performance polystyrene/graphene-based nanocomposites with excellent anti-corrosion properties. *Polym Chem*, *5*, 535. https://doi.org/10.1039/C3PY00825H

208. Karbownik, I., Rac-Rumijowska, O., Fiedot-Toboła, M., Rybicki, T., & Teterycz, H. (2019). The preparation and characterization of polyacrylonitrile-polyaniline (PAN/PANI) fibers. *Materials, 12*, 664. https://doi.org/10.3390/ma12040664

209. Zhang, B., Zhang, Z. G., Yan, X., Wang, X. X., Zhao, H., Guo, J., Feng, J. Y., & Long, Y. Z. (2017). Chitosan nanostructures by in situ electrospinning for high-efficiency PM2. 5 capture. *Nanoscale*, *9*, 4154. https://doi.org/10.1039/C6NR09525A

210. Antilen, M., Förster, J. E., Del Confetto, S., Rodier, E., Fudym, O., Venezia, A. M., Deganello, G. & Escudey, M. (2004). Characterization of the porous structure of Chilean volcanic soils by nitrogen adsorption and mercury porosimetry. *J Chil Chem Soc*, *49*, 313. http://dx.doi.org/10.4067/S0717-97072004000400009

211. Rodriguez, M. E., Diz, V. E., Awruch, J., & Dicelio, L. E. (2010). Photophysics of zinc (II) phthalocyanine polymer and gel formulation. *Photochem Photobiol*, *86*, 513. https://doi.org/10.1111/j.1751-1097.2009.00702.x

212. Fery-Forgues, S., & Lavabre, D. (1999). Are fluorescence quantum yields so tricky to measure? A demonstration using familiar stationery products. *J Chem Educ*, *76*, 1260. https://doi.org/10.1021/ed076p1260

213. Cui, G., & Fang, W. H. (2013). State-specific heavy-atom effect on intersystem crossing processes in 2-thiothymine: A potential photodynamic therapy photosensitizer. *J Chem Phys*, *138*, 044315. https://doi.org/10.1063/1.4776261

214. Tran Thi, T. H., Desforge, C., Thiec, C., & Gaspard, S. (1989). Singlet-singlet and triplet-triplet intramolecular transfer processes in a covalently linked

porphyrin-phthalocyanine heterodimer. *J Phys Chem*, *93*, 1226. https://doi.org/10.1021/j100341a013

215. Ishii, K. (2012). Functional singlet oxygen generators based on phthalocyanines. *Coord Chem Rev*, *256*, 1556. https://doi.org/10.1016/j.ccr.2012.03.022

216. Zhang, X. F., Di, Y., & Zhang, F. (2009). Photoinduced single-and double-electron transfer in a photosynthetic model consisting of one-acceptor with four equally linked donors (D4–A). *J Photochem Photobiol*, *203*, 216. https://doi.org/10.1016/j.jphotochem.2009.02.009

217. Debacker, M. G., Deleplanque, O., Van Vlierberge, B., & Sauvage, F. X. (1988). A Laser Photolysis Study of Triplet Lifetimes and of Triplet–Triplet Annihilation Reactions of Phthalocyanins in DMSO Solutions (Etude des Durées de Vie du Triplet et des Réactions d'Annihilation Triplet–Triplet de Phthalocyanines dans le DMSO par Photolyse Laser). *Laser chem*, *8*, 1. https://doi.org/10.1155/LC.8.1

218. Darwent, J. R., Douglas, P., Harriman, A., Porter, G., & Richoux, M. C. (1982). Metal phthalocyanines and porphyrins as photosensitizers for reduction of water to hydrogen. *Coord Chem Rev*, *44*, 83. https://doi.org/10.1016/S0010-8545(00)80518-4

219. Kuznetsova, N. A., Gretsova, N. S., Derkacheva, V. M., Mikhalenko, S. A., Solov'eva, L. I., Yuzhakova, O. A., Kaliya, O.L, & Luk'yanets, E. A. (2002). Generation of singlet oxygen with anionic aluminum phthalocyanines in water. *Russ J Gen Chem*, *72*, 300. https://doi.org/10.1023/A:1015402524813

220. Chadwick, S. J., Salah, D., Livesey, P. M., Brust, M., & Volk, M. (2016). Singlet oxygen generation by laser irradiation of gold nanoparticles. *J Phys Chem C*, *120*, 10647. https://doi.org/10.1021/acs.jpcc.6b02005

221. Ramesh, H., Mayr, T., Hobisch, M., Borisov, S., Klimant, I., Krühne, U., & Woodley, J. M. (2016). Measurement of oxygen transfer from air into organic solvents. *J Chem Technol Biotechnol*, *91*, 832. https://doi.org/10.1002/jctb.4862

222. Wu, L., Li, A., Gao, G., Fei, Z., Xu, S., & Zhang, Q. (2007). Efficient photodegradation of 2, 4-dichlorophenol in aqueous solution catalyzed by polydivinylbenzene-supported zinc phthalocyanine. *J Mol Catal A Chem*, *269*, 183. https://doi.org/10.1016/j.molcata.2007.01.022

223. Devi, L. G., Kumar, S. G., Reddy, K. M., & Munikrishnappa, C. (2009). Photo degradation of Methyl Orange an azo dye by Advanced Fenton Process using zero valent metallic iron: Influence of various reaction parameters and its degradation mechanism. *J Hazard Mat*, *164*, 459. https://doi.org/10.1016/j.jhazmat.2008.08.017

224. Kuznetsova, N. A., & Kaliya, O. L. (2012). Oxidative photobleaching of phthalocyanines in solution. *J Porphyr Phthalocyanines*, *16*, 705. https://doi.org/10.1142/S1088424612300042

225. Spiller, W., Kliesch, H., Wöhrle, D., Hackbarth, S., Röder, B., & Schnurpfeil, G. (2012). Singlet oxygen quantum yields of different photosensitizers in polar solvents and micellar solutions. *J Porphyr Phthalocyanines*, *2*, 145. https://doi.org/10.1002/(SICI)1099-1409(199803/04)2:2%3C145::AID-JPP60%3E3.0.CO;2-2

226. Tang, F. X., Li, H. C., Ren, X. D., Sun, Y., Xie, W., Wang, C. Y., Zheng, B. Y. Ke, M. R. & Huang, J. D. (2018). Preparation and antifungal properties of monosubstituted zinc (Π) phthalocyanine-chitosan oligosaccharide conjugates and their quaternized derivatives. *Dyes Pigm*, *159*, 439. https://doi.org/10.1016/j.dyepig.2018.07.004

227. Ragàs, X., He, X., Agut, M., Roxo-Rosa, M., Gonsalves, A. R., Serra, A. C., & Nonell, S. (2013). Singlet oxygen in antimicrobial photodynamic therapy: photosensitizer-dependent production and decay in E. coli. *Molecules*, *18*, 2712. https://doi.org/10.3390/molecules18032712

228. Kathiravan, M. K., Salake, A. B., Chothe, A. S., Dudhe, P. B., Watode, R. P., Mukta, M. S., & Gadhwe, S. (2012). The biology and chemistry of antifungal agents: a review. *Bioorg Med Chem*, *20*, 5678. https://doi.org/10.1016/j.bmc.2012.04.045

229. Gibney, K. A., Sovadinova, I., Lopez, A. I., Urban, M., Ridgway, Z., Caputo, G. A., & Kuroda, K. (2012). Poly(ethylene imine)s as antimicrobial agents with selective activity. *Macromol Biosci*, *12*, 1279. https://doi.org/10.1002/mabi.201200052

230. Openda, Y. I., Matshitse, R., & Nyokong, T. (2020). A search for enhanced photodynamic activity against Staphylococcus aureus planktonic cells and biofilms: the evaluation of phthalocyanine–detonation nanodiamond–Ag nanoconjugates. *Photochem Photobiol Sci*, *19*, 1442. https://doi.org/10.1039/d0pp00075b

231. Kholikov, K., Ilhom, S., Sajjad, M., Smith, M. E., Monroe, J. D., San, O., & Er, A. O. (2018). Improved singlet oxygen generation and antimicrobial activity of sulphur-doped graphene quantum dots coupled with methylene blue for photodynamic therapy applications. *Photodiagnosis Photodyn Ther*, *24*, 7. https://doi.org/10.1016/j.pdpdt.2018.08.011

232. Oguz Er, A., Chen, J., Cesario, T. C., & Rentzepis, P. M. (2012). Inactivation of bacteria in plasma. *Photochem Photobiol Sci*, *11*, 1700. https://doi.org/10.1039/c2pp25135c

233. Mikula, P., Kalhotka, L., Jancula, D., Zezulka, S., Korinkova, R., Cerny, J., Marsalek, B., & Toman, P. (2014). Evaluation of antibacterial properties of novel phthalocyanines against Escherichia coli–comparison of analytical methods. *J Photochem Photobiol B Biol*, *138*, 230. https://doi.org/10.1016/j.jphotobiol.2014.04.014

234. Maisch, T., Hackbarth, S., Regensburger, J., Felgenträger, A., Bäumler, W., Landthaler, M., & Röder, B. (2011). Photodynamic inactivation of multi-resistant bacteria (PIB)–a new approach to treat superficial infections in the 21st century. *J Dtsc Dermatol Ges*, *9*, 360. https://doi.org/10.1111/j.1610-0387.2010.07577.x

235. Revuelta-Maza, M. Á., González-Jiménez, P., Hally, C., Agut, M., Nonell, S., de la Torre, G., & Torres, T. (2020). Fluorine-substituted tetracationic ABAB-phthalocyanines for efficient photodynamic inactivation of Gram-positive and Gram-negative bacteria. *Eur J Med Chem*, *187*, 111957. https://doi.org/10.1016/j.ejmech.2019.111957

236. Ribeiro, C. P., & Lourenco, L. M. (2021). Overview of cationic phthalocyanines for effective photoinactivation of pathogenic microorganisms. *J Photochem Photobiol C Photochem Rev*, *48*, 100422. https://doi.org/10.1016/j.jphotochemrev.2021.100422

237. Kashmiri, Z. N., & Mankar, S. A. (2014). Free radicals and oxidative stress in bacteria. *Int. J. Curr. Microbiol. Appl. Sci*, *3*, 34-40.

238. Datta, K. K. R., Kozak, O., Ranc, V., Havrdova, M., Bourlinos, A. B., Šafářová, K., Holá, K., Tománková, K., Zoppellaro, G., Otyepka, M., & Zbořil, R. (2014). Quaternized carbon dot-modified graphene oxide for selective cell labelling–controlled nucleus and cytoplasm imaging. *Chem Commun*, *50*, 10782. https://doi.org/10.1039/C4CC02637C

239. Simonenko, E., Gomonov, A., Rolle, N., & Molodkina, L. (2015). Modeling of H2O2 and UV oxidation of organic pollutants at wastewater post-treatment. *Procedia Eng*, *117*, 337. https://doi.org/10.1016/j.proeng.2015.08.170

240. Chen, S. L., Huang, X. J., & Xu, Z. K. (2011). Functionalization of cellulose nanofiber mats with phthalocyanine for decoloration of reactive dye wastewater. *Cellulose*, *18*, 1295. https://doi.org/10.1007/s10570-011-9572-5

241. Shen, T., Jiang, C., Wang, C., Sun, J., Wang, X., & Li, X. (2015). A TiO_2 modified abiotic–biotic process for the degradation of the azo dye methyl orange. *RSC Adv*, *5*, 58704. https://doi.org/10.1039/C5RA06686G

242. Sha, Y., Mathew, I., Cui, Q., Clay, M., Gao, F., Zhang, X. J., & Gu, Z. (2016). Rapid degradation of azo dye methyl orange using hollow cobalt

nanoparticles. *Chemosphere*, *144*, 1530. https://doi.org/10.1016/j.chemosphere.2015.10.040

243. Mapukata, S., & Nyokong, T. (2020). Development of phthalocyanine functionalised TiO_2 and ZnO nanofibers for photodegradation of methyl orange. *New J Chem*, *44*, 16340. https://doi.org/10.1039/D0NJ03326J
244. Shao, L., Xie, H., Mo, J., Yang, Z., Fan, Z., & Qi, C. (2012). Preparation of a novel nanofibrous mat–supported Fe (III) porphryin/TiO2 photocatalyst and its application in photodegradation of azo-dyes. *Environ Eng Sci*, *29*, 807. https://doi.org/10.1089/ees.2011.0260
245. Khoza, P., & Nyokong, T. (2014). Photocatalytic behavior of phthalocyanine-silver nanoparticle conjugates supported on polystyrene fibers. *J Mol Catal A Chem*, *395*, 34. https://doi.org/10.1016/j.molcata.2014.07.031
246. Yılmaz, Y. (2021). Preparation of a Phthalocyanine–Nanometal-Coated Silica Microparticle Conjugate as Heterogeneous Photocatalyst and Investigation of Its Photocatalytic Activity. *ChemistrySelect*, *6*, 7223. https://doi.org/10.1002/slct.202102129
247. Zugle, R., & Nyokong, T. (2013). Zinc (II) 2, 9, 16, 23-tetrakis [4-(N-methylpyridyloxy)]-phthalocyanine anchored on an electrospun polysulfone polymer fiber: Application for photosensitized conversion of methyl orange. *J Mol Catal A Chem*, *366*, 247. https://doi.org/10.1016/j.molcata.2012.10.001
248. Yu, X., Huang, L., Wei, Y., Zhang, J., Zhao, Z., Dai, W., & Yao, B. (2015). Controllable preparation, characterization and performance of Cu2O thin film and photocatalytic degradation of methylene blue using response surface

methodology. *Mater Res Bull*, *64*, 410. https://doi.org/10.1016/j.materresbull.2015.01.009

249. Bustos-Ramírez, K., Barrera-Díaz, C. E., De Icaza-Herrera, M., Martínez-Hernández, A. L., Natividad-Rangel, R., & Velasco-Santos, C. (2015). 4-chlorophenol removal from water using graphite and graphene oxides as photocatalysts. *J Environ Health Sci Eng*, *13*, 1. https://doi.org/10.1186/s40201-015-0184-0

250. Cabir, B., Yurderi, M., Caner, N., Agirtas, M. S., Zahmakiran, M., & Kaya, M. (2017). Methylene blue photocatalytic degradation under visible light irradiation on copper phthalocyanine-sensitized TiO2 nanopowders. *Mater Sci Eng B*, *224*, 9. https://doi.org/10.1016/j.mseb.2017.06.017

251. Mahmoudi, K., Hosni, K., Hamdi, N., & Srasra, E. (2015). Kinetics and equilibrium studies on removal of methylene blue and methyl orange by adsorption onto activated carbon prepared from date pits-A comparative study. *Korean J Chem Eng*, *32*, 274. https://doi.org/10.1007/s11814-014-0216-y

252. Youssef, N. A., Shaban, S. A., Ibrahim, F. A., & Mahmoud, A. S. (2016). Degradation of methyl orange using Fenton catalytic reaction. *Egypt J Pet*, *25*, 317. https://doi.org/10.1016/j.ejpe.2015.07.017

253. Alkaim, A. F., Aljeboree, A. M., Alrazaq, N. A., Baqir, S. J., Hussein, F. H., & Lilo, A. J. (2014). Effect of pH on adsorption and photocatalytic degradation efficiency of different catalysts on removal of methylene blue. *Asian J Chem*, *26*, 8445. http://dx.doi.org/10.14233/ajchem.2014.17908